GDAŃSK UNIVERSITY OF TECHNOLOGY

The author of the doctoral dissertation: **Bartłomiej Lemieszek**
Scientific discipline: **Automation, Electronics, Electrical engineering and Space Technologies**

DOCTORAL DISSERTATION

Title of doctoral dissertation: **Development and characterization of advanced materials for next generation solid oxide cells.**

Title of doctoral dissertation (in Polish): **Opracowanie i charakteryzacja zaawansowanych materiałów do nowej generacji ogniw ze stałym tlenkiem.**

Supervisor *signature*
Dr hab. Inż. Sebastian Molin

Gdańsk, year 2026

GDAŃSK UNIVERSITY OF TECHNOLOGY

STATEMENT

The author of the doctoral dissertation: Bartłomiej Lemieszek

I, the undersigned, declare that I am aware that in accordance with the provisions of Art. 27 (1) and (2) of the Act of 4th February 1994 on Copyright and Related Rights (Journal of Laws of 2021, item 1062), the university may use my doctoral dissertation entitled:
"Development and characterization of advanced materials for next generation solid oxide cells" for scientific or didactic purposes.[1]

Gdańsk,.....

signature of the PhD student

Aware of criminal liability for violations of the Act of 4th February 1994 on Copyright and Related Rights and disciplinary actions set out in the Law on Higher Education and Science(Journal of Laws 2021, item 478), as well as civil liability, I declare, that the submitted doctoral dissertation is my own work.

I declare, that the submitted doctoral dissertation is my own work performed under and in cooperation with the supervision of dr hab. inż. Sebastian Molin

This submitted doctoral dissertation has never before been the basis of an official procedure associated with the awarding of a PhD degree.

All the information contained in the above thesis which is derived from written and electronic sources is documented in a list of relevant literature in accordance with Art. 34 of the Copyright and Related Rights Act.

I confirm that this doctoral dissertation is identical to the attached electronic version.

Gdańsk,.....

signature of the PhD student

I, the undersigned, agree to include an electronic version of the above doctoral dissertation in the open, institutional, digital repository of Gdańsk University of Technology.

Gdańsk,.....

signature of the PhD student

[1] Art 27. 1. Educational institutions and entities referred to in art. 7 sec. 1 points 1, 2 and 4–8 of the Act of 20 July 2018 – Law on Higher Education and Science, may use the disseminated works in the original and in translation for the purposes of illustrating the content provided for didactic purposes or in order to conduct research activities, and to reproduce for this purpose disseminated minor works or fragments of larger works.

2. If the works are made available to the public in such a way that everyone can have access to them at the place and time selected by them, as referred to in para. 1, is allowed only for a limited group of people learning, teaching or conducting research, identified by the entities listed in paragraph 1.

GDAŃSK UNIVERSITY OF TECHNOLOGY

DESCRIPTION OF DOCTORAL DISSERTATION

The Author of the doctoral dissertation: Bartłomiej Lemieszek
Title of doctoral dissertation: Development and characterization of advanced materials for next generation solid oxide cells.

Title of doctoral dissertation in Polish: Opracowanie i charakteryzacja zaawansowanych materiałów do nowej generacji ogniw ze stałym tlenkiem.

Language of doctoral dissertation: English

Supervisor: Dr hab. Inż. Sebastian Molin

Date of doctoral defense:

Keywords of doctoral dissertation in Polish: Ogniwa ze stałym tlenkiem, korozja wysokotemperaturowa, powłoki ochronne, elektroda tlenowa, elektrochemia ciała stałego

Keywords of doctoral dissertation in English: Solid Oxide cells, High-temperature corrosion, protective coatings, oxygen electrode, solid-state electrochemistry

Summary of doctoral dissertation in Polish:

Niniejsza rozprawa doktorska przedstawia badania nad perspektywicznymi materiałami mogącymi stanowić alternatywę dla rozwiązań stosowanych obecnie w ogniwach paliwowych nowej generacji. W pracy skoncentrowano się na średnio- i niskotemperaturowych ogniwach paliwowych, czyli obszarze nadal słabo rozpoznanym, wymagającym dalszego rozwoju i stwarzającym nowe możliwości doboru materiałów dla SOC. Zbadano dwa potencjalne obszary zastosowania otrzymanych warstw. W pierwszym wykorzystano podwójne warstwy ochronne na metalicznych interkonektach w systemach SOC pracujących w 700 °C, oparte na nowym materiale spinelowym $CuMn_{1.7}Fe_{0.3}O_4$ oraz warstwach Y_2O_3 i Gd_2O_3 o grubości około 100 nm. Wykazano istotne ograniczenie przyrostu masy względem próbek referencyjnych oraz zwiększenie skuteczności blokowania dyfuzji chromu, stanowiącej główny czynnik ograniczający zastosowanie tego materiału. Drugi obszar badań dotyczył materiałów LSC ($La_{0.6}Sr_{0.4}CoO_{3-\delta}$) oraz PrO_x do niskotemperaturowych ogniw SOC pracujących ≤600 °C. Dla częściowo amorficznego LSC wykazano wzrost aktywności elektrochemicznej w 400 °C, związany ze zmniejszeniem średniego stopnia utlenienia kobaltu o 0,5 względem materiału krystalicznego. W przypadku PrO_x ustalono, że optymalna temperatura spiekania wynosi 500 °C. Wykazano współistnienie wielu faz PrO_x w materiale, co wpływa na efektywność elektrochemiczną materiału.

GDAŃSK UNIVERSITY OF TECHNOLOGY

Summary of doctoral dissertation in English:

This doctoral dissertation presents research on promising materials that could serve as alternatives in next-generation solid oxide cells to those currently used. The work focuses on intermediate- and low-temperature solid oxide cells, a still underexplored area that requires further development and offers new opportunities for selecting materials for SOCs. Two potential applications of the prepared layers were investigated. The first involved double protective coatings for metallic interconnects for SOC system operating at 700 °C, based on the novel spinel $CuMn_{1.7}Fe_{0.3}O_4$ and thin Y_2O_3 and Gd_2O_3 layers (~100 nm). The coatings significantly reduced mass gain compared with reference samples and improved chromium diffusion blocking, a key factor limiting the use of this material. The second area concerned LSC ($La_{0.6}Sr_{0.4}CoO_{3-\delta}$) and PrO_x materials for low-temperature oxygen electrodes operating at ≤600 °C. For partially amorphous LSC, higher electrochemical activity at 400 °C was observed, linked to a 0.5 decrease in the average cobalt oxidation state relative to the crystalline form. For PrO_x, the optimal annealing temperature was 500 °C, and the coexistence of multiple PrO_x phases was shown to influence electrochemical performance.

Acknowledgements

This work would not have been possible without the direct and indirect contributions of many people, and I am deeply grateful to each and every one of them.

I would like to express my sincere gratitude to my supervisor, Professor Sebastian Molin, for the insightful discussions and invaluable scientific guidance that made this work possible in the first place.

I would also like to thank the current and former staff members and PhD students of the Department of Functional Materials Engineering at the Faculty of Electronics, Electrical Engineering and Telecommunications. Without you, this work could not have been completed in such a friendly atmosphere. Beyond work itself, I have truly appreciated the chance to get to know you and to share so many good moments together. I sincerely hope there will be many more to come.

I would also like to thank Dr. Alexey Maximenko from the NCPS Solaris for the many hours of discussion and his invaluable assistance with the research. Many important aspects of this work would not have been possible without his contribution.

Furthermore, I would like to thank Dr. Marcin Urbanowicz from the IBIB PAN Institute, as well as the entire team, for the many meaningful scientific and personal conversations that helped shape me both as a person and as a scientist.

On a personal note, I would like to thank my wife, Joanna (you know best how much effort it took), and my immediate family for their patience, support, understanding, and for encouraging me to venture into places I had never imagined I would one day explore.

I would also like to thank my friends and acquaintances for their presence, support, and every moment we shared together. This work is also, thanks to you.

During this journey, I had the privilege of meeting many incredible people from KTU, WUT, AGH, and other Institutes. Some of them left me with invaluable insights and wise advice that I will never forget.

“It was good to have goals. They could bring you through tough times.”

Stephen King, *The Institute*

Contents

Abstract 9
Streszczenie 10
List of important symbols and abbreviations 11
1. Introduction 15
2. Fuel cells 18
3. SOCs history and generations 23
4. Principles of SOCs operation 25
4.1. Electrolyte 25
4.2. Fuel electrode 26
4.3. Oxygen electrode 27
4.4. Interconnects 28
5. Factors impacting SOCs performance 31
5.1. Activation polarisation 31
5.2. Ohmic Voltage Loss 32
5.3. Concentration Voltage Loss 32
6. Electrochemical impedance spectroscopy 35
7. Materials for SOCs 39
7.1. Electrolyte materials 39
7.2. Fuel electrode materials 42
7.3. Oxygen electrode materials 43
7.4. Interconnect coating materials 47
7.5. Current status and gaps of developed research topics 48
7.5.1. Protective coatings for metal interconnects based on rare-earth oxides and spinel $CuMn_2O_4$ and its derivatives 48
7.5.2. LSC- or PrO_x-based oxygen electrodes for low-temperature fuel cells 50
8. Objectives and hypothesis of the thesis 53
9. Materials preparation and measurement methods 56
9.1. Material synthesis and layer preparation 56
9.1.1. RE-oxide layer preparation 56
9.1.2. Spinel synthesis and deposition 57
9.1.3. LSC oxygen electrode deposition 58
9.1.4. PrO_x oxygen electrode deposition 59
9.1.5. Oxygen electrode prepared by infiltration CGO by LSC, PrOx and LSC:PrOx composite. 60
9.2. Measurement methods 60

9.2.1. Structural studies 60
9.2.2. Thermogravimetric measurements in high-temperature corrosion 70
9.2.3. Electrical and electrochemical measurements 72
10. List of publications included in the dissertation 80
10.1. Electrolytic deposition of reactive element thin films on Crofer 22 APU and evaluation of the resulting high-temperature corrosion protection properties at 700 °C–900 °C 82
10.2. $CuMn_{1.7}Fe_{0.3}O_4 – RE_2O_3$ (RE = Y, Gd) bilayers as protective interconnect coatings for solid oxide cells 98
10.3. Enhanced electrochemical performance of partially amorphous $La_{0.6}Sr_{0.4}CoO_{3-\delta}$ oxygen electrode materials for low-temperature solid oxide cells operating at 400 °C .. 119
10.4. Developing high-performance oxygen electrodes for intermediate solid oxide cells (SOC) prepared by $Ce_{0.8}Gd_{0.2}O_{2-\delta}$ backbone infiltration 141
10.5. Unveiling the Potential of Praseodymium Oxide as Efficient Oxygen Electrode for Low-Temperature Solid Oxide Cell Applications. 156
11. Conclusions 185
Other publication record in journals from the JCR list: 188
Conference attendance and lectures 189
List of Figures 191
List of Tables 193
12. Bibliography 194

Abstract

With growing energy demand, limited fossil fuel reserves, and the threat of global warming, the development of alternative energy sources is essential. Solid oxide fuel cells are among the most promising solutions because they provide stable energy independently of weather conditions and may become an important part of future smart grid systems. Research on materials for intermediate- and low-temperature solid oxide cells is essential, as this field remains underexplored and lower operating temperatures create new technological opportunities.

This doctoral dissertation investigates promising materials that could be used in next generation solid oxide cells. It focuses on two key areas: metallic interconnects and oxygen electrode materials. The first concerns high-temperature corrosion and improved chromium diffusion blocking, both crucial for electrical efficiency. The second addresses oxygen electrodes for operation ≤600 °C, where lower temperature increases polarization resistance and reduces cell performance. Corrosion studies examined 100 nm oxide coatings based on La_2O_3, Y_2O_3, Gd_2O_3, and CeO_2. Y_2O_3 and Gd_2O_3 showed the most promising protective properties and, when combined with $CuMn_{1.7}Fe_{0.3}O_4$ in double protective layers, enabled low area specific resistance after 4000 hours at 700 °C while improving chromium blocking. The second part of the work focused on LSC and PrO_x as oxygen electrode materials. LSC showed the highest electrochemical activity after annealing at 400 °C. Electrodes based on porous CGO scaffolds infiltrated with LSC achieved very low polarization resistance and an 8% higher power density than a commercial counterpart. Praseodymium oxide also proved to be an effective oxygen electrode material. A 200 nm PrO_x layer provided very low polarization resistance, with the best results after annealing at 500 °C. It also showed greater resistance to humidity and CO_2 than LSC and enabled a 40% increase in power density compared with a commercial solution.

Overall, the dissertation provides a strong basis for further research into new materials for intermediate- and low-temperature solid oxide cells.

Streszczenie

W obliczu rosnącego zapotrzebowania na energię, ograniczonych zasobów paliw kopalnych i zagrożenia globalnym ociepleniem rozwój alternatywnych źródeł energii staje się koniecznością. Ogniwa ze stałym tlenkiem (SOC) należą do najbardziej obiecujących rozwiązań, gdyż zapewniają stabilne dostawy energii niezależnie od warunków pogodowych i mogą stać się ważnym elementem przyszłych inteligentnych sieci energetycznych. Badania nad materiałami do średnio- i niskotemperaturowych SOC są szczególnie istotne, gdyż obszar ten pozostaje słabo zbadany, a obniżenie temperatury pracy otwiera nowe możliwości technologiczne.

Niniejsza rozprawa doktorska dotyczy obiecujących materiałów, które mogłyby zastąpić obecnie stosowane w ogniwach ze stałym tlenkiem. Skupia się na dwóch zagadnieniach: metalicznych interkonektach oraz materiałach elektrod tlenowych. Pierwsze obejmuje korozję wysokotemperaturową i poprawę blokowania dyfuzji chromu, kluczowe dla sprawności układu. Drugie dotyczy elektrod tlenowych pracujących ≤ 600 °C, gdzie obniżenie temperatury zwiększa opór polaryzacyjny i pogarsza pracę ogniwa. W badaniach korozyjnych analizowano powłoki tlenkowe o grubości 100 nm na bazie La_2O_3, Y_2O_3, Gd_2O_3 i CeO_2. Najlepsze właściwości ochronne wykazały Y_2O_3 i Gd_2O_3, które po połączeniu z $CuMn_{1.7}Fe_{0.3}O_4$ w podwójnych warstwach ochronnych umożliwiły uzyskanie niskiej rezystancji powierzchniowej po 4000 godzin utleniania w 700 °C oraz poprawę blokowania dyfuzji chromu. Druga część pracy dotyczyła materiałów LSC i PrO_x jako elektrod tlenowych. LSC wykazał najwyższą aktywność elektrochemiczną po spiekaniu w 400 °C. Elektrody oparte na porowatym szkielecie CGO, infiltrowane LSC, osiągnęły bardzo niski opór polaryzacyjny i o 8% wyższą gęstość mocy niż odpowiednik komercyjny. Tlenek prazeodymu również okazał się skutecznym materiałem elektrody tlenowej. Warstwa PrO_x o grubości 200 nm zapewniła bardzo niski opór polaryzacyjny, a najlepsze wyniki uzyskano po spiekaniu w 500 °C. Materiał ten wykazał większą odporność na wilgoć i CO_2 niż LSC oraz umożliwił wzrost gęstości mocy o 40% w porównaniu z rozwiązaniem komercyjnym.

Rozprawa stanowi solidną podstawę do dalszych badań nad nowymi materiałami do średnio- i niskotemperaturowych ogniw ze stałym tlenkiem.

List of important symbols and abbreviations

AFCs - alkaline fuel cells

ASR – Area specific resistance

BSD – backscattered electron detector

CAES - compressed air energy storage

CGO – Cerium Gadolinium oxide, $Ce_{1-x}Gd_xO_{2-\delta}$

CMFO - $CuMn_{1.7}Fe_{0.3}O_4$

DC – Direct current

DRT - Distribution of relaxation times

EDTA - ethylenediaminetetraacetic acid

EIS – Electrochemical Impedance Spectroscopy

EPD - electrophoretic deposition

EXAFS - Extended X-ray Absorption Fine Structure

FT – Fourier Transform

FTIR - Fourier Transform Infra-Red Spectroscopy

GIXRD – Grazing incidence X-ray diffraction

I-V – current-voltage characteristic

LSC - $La_{1-x}Sr_xCoO_{3-\delta}$

LSCF - $La_{1-x}Sr_xCo_{1-y}Fe_yO_{3-\delta}$

LSCM - $La_{0.75}Sr_{0.25}Cr_{0.5}Mn_{0.5}O_{3-\delta}$

LSCr - $La_{1-x}Sr_xCrO_3$

LSM - $La_{1-x}Sr_xMnO_{3-\delta}$

MCFCs - molten carbonate fuel cells

MCO - $MnCo_2O_4$

MIEC - mixed ionic–electronic conductors

Ni–YSZ – Nikiel - Yttria stabilised Zirconia composite

OCV – open circuit voltage

PCFCs - proton-conducting fuel cells

pCO_2 - partial pressure of carbon dioxide

PEM - proton exchange membrane

PEMFCs - proton exchange membrane fuel cells

pH_2O - partial pressure of water vapor

pO_2 – Oxygen partial pressure

PrO_x – Praseodymium oxide

RE-oxide – Rare Earth metal oxide

R_g – grain (bulk) resistance

R_{gb} – grain boundaries resistance

R_{ohm} – ohmic resistance

R_{pol} – polarisation resistance

SDC - samaria doped ceria, $Ce_{1-x}Sm_xO_{2-\delta}$

SED - secondary electron detector

SEM-EDS - Scanning Electron Microscopy with Energy Dispersive Spectroscopy

SFM - $Sr_2Fe_{1.5}Mo_{0.5}O_{6-\delta}$

SOC – Solid oxide cell

SOEC - solid oxide electrolysers

SOFC - solid oxide fuel cells

STF - $SrTi_{1-x}Fe_xO_{3-\delta}$

TEC - Thermal expansion coefficient

VdP - Van der Pauw method

XAFS - X-ray Absorption Fine Structure

XANES - X-ray Absorption Near Edge Spectroscopy

XAS - X-ray Absorption Spectroscopy

XPS - X-ray photoelectron spectroscopy

XRD - X-ray diffraction

YSZ – Yttria stabilised Zirconia

A – Electrode Area

A - pre-exponential factor in ASR

C - integration constant

d - interplanar spacing in Bragg's Law

d - thickness of the measured sample

E_a - activation energy

E(t) – excitation signal

E_0 – signal amplitude

f - frequency

f - correlation function

F - Faraday constant

I - current density

i_0 - exchange current density

I_0 - initial current intensity

I(t) – current response

I_x - current intensity after going through sample

k - Boltzmann's constant

k_p - the parabolic rate constant

n - the order of reflection

n_e – number of electrons transferred per reaction

P – power density

R - universal gas constant

R – resistance

R_s – measured ohmic resistance

T - temperature

t - oxidation time

U - measured cell voltage

Z – impedance

Z_0 – impedance modulus

β - transfer coefficient

Δm - the weight gain

η_{Act} - activation polarization

θ - diffraction angle

λ - X-ray wavelength in Bragg's Law

μ(E) - absorption coefficient

σ - electrical conductivity

τ – time value

ϕ – phase shift

ω – angular frequency

1. Introduction

Humans' natural curiosity and creative thinking abilities drove them to continually improve and invent new tools that made their work more efficient. This creativity, coupled with changing social demands, led to the Industrial Revolution of the 18th century and a radical increase in energy demand. During this time, global economies transitioned from wood to more calorific fossil fuels, including hard coal. Currently, human civilization is in the third industrial revolution and on the verge of transitioning to the fourth, in which artificial intelligence and machine learning will play an increasingly significant role. This will entail another significant increase in energy demand and require higher electricity production. According to a report by the Institute of Environmental Protection - National Research Institute with Centre for Climate and Energy Analysis, electricity demand in Poland alone will increase from 140 TWh in 2020 to 330–360 TWh by 2050 [1]. From a global perspective, the trend shown in Figure 1 indicates a rapid increase in electricity consumption. According to the projections, global electricity consumption is expected to rise from 154.6 PWh in 2020 to 231.8 PWh by 2050 [2]. It is also assumed that current oil, natural gas, and coal reserves are sufficient to meet global consumption needs for approximately 50, 50, and 132 years, respectively [2], [3]. This is the reason why alternative energy sources that don't rely on fossil fuels have been developed over the past few decades. Furthermore, continuous development of potentially zero-emission and renewable energy production methods brings us closer to achieving a Type 1 civilization on the Kardashev scale [4]. The planned energy mix for the energy transition will rely primarily on solar, wind, and nuclear power [5]. Other sources, such as hydropower, geothermal energy, and wave energy, may also be utilized locally [5]–[8]. However, because some of these sources are weather-dependent, ensuring a stable electricity supply remains a challenge, and the proposed diversification of sources may not fully resolve this issue. At present, producing hydrogen from surplus energy appears to be the one of the most interesting alternative for energy storage systems based on lithium-ion batteries for large-scale application and for long-term storage [9]. This can be achieved using solid oxide cells (SOCs), which operate in two modes: as solid

oxide fuel cells (SOFCs) that use hydrogen as fuel, and as solid oxide electrolysers (SOECs) that produce hydrogen from excess energy. This approach enables stored fuel to be used at any time, ensuring continuous operation regardless of weather conditions. A further advantage of SOEC technology is its high energy efficiency – 80 - 90% (Example - 83% efficiency for the system according to the report of the Institute for Sustainable Process Technology for industrial use cases) [10], [11] – for SOFC more thar 60% of efficiency, compared to 70–80% for low-temperature proton exchange membrane (PEM) or alkaline electrolysers [5]. This efficiency surpasses that of other storage methods, such as pumped-storage hydropower (70–85%) [12] and compressed air energy storage (CAES) (70–80% - for adiabatic CAES) [13], and is comparable to that of lithium-ion batteries (>85%) [14].

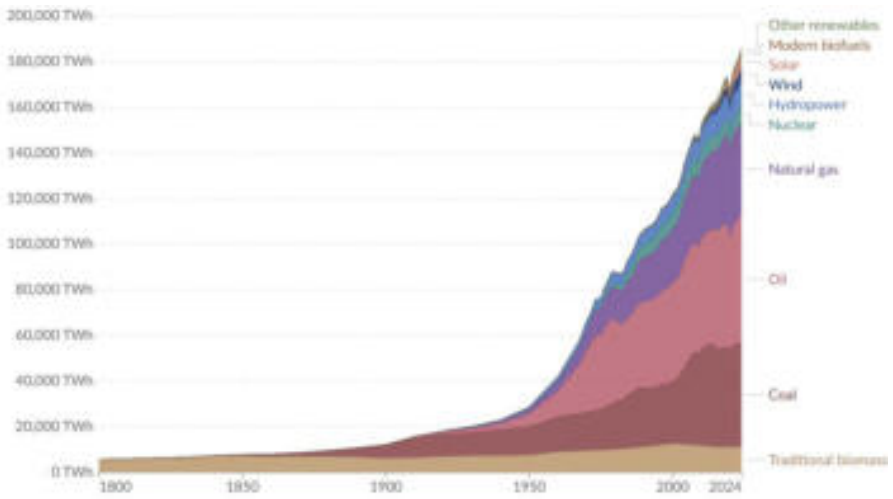


Figure 1. Global energy consumption by source of energy [3].

Hydrogen is the lightest, simplest, and most abundant element in the universe, accounting for an estimated 91.9% of its total atoms number [15]. A hydrogen atom consists of a nucleus containing a single proton and one electron. There are three naturally occurring isotopes of hydrogen: the most common form described above; deuterium, which has one neutron in addition to the proton; and tritium, which has two neutrons. There are also lesser known isotopes such as muon, muon helium, and positronium [16]. Under typical Earth-surface conditions, hydrogen is rarely found in nature as free molecular hydrogen. When it does occur in its free form, it is usually as diatomic hydrogen (H_2) - an odourless, colourless

gas present only in trace amounts in the atmosphere and sometimes in small proportions in natural gas or other geological gases. Most hydrogen on Earth is bound in inorganic and organic compounds, with water being the most abundant [17]. Producing hydrogen for use as a fuel or energy carrier therefore usually requires generating and/or purifying H_2 from hydrogen-containing feedstocks, which requires an energy input. Hydrogen has a high gravimetric energy density (143 MJ/kg, nearly three times higher than diesel or gasoline) but a very low volumetric energy density under standard conditions (0.01 MJ/dm^3 compared to 34.2 MJ/dm^3 for gasoline), as determined by Avogadro's law - one mole of gas occupies 22.4 dm^3 under standard conditions, and a mole of hydrogen has a mass of only 2 g [9], [18], [19]. To address this, hydrogen can be compressed to 700 bar (5.6 MJ/dm^3) or liquefied (10.1 MJ/dm^3), both requiring specialized technologies due to hydrogen's tendency to cause metal embrittlement and permeate most materials [9], [18]. Currently, hydrogen is produced via thermal methods such as steam methane reforming, biological processes, and electrochemical methods like water electrolysis. It is classified according to its production pathway:

- Gray hydrogen – from fossil fuels, without carbon capture;
- Blue hydrogen – from fossil fuels, with CO_2 capture;
- Turquoise hydrogen – from methane pyrolysis or waste plastic processing;
- Pink/Red/Purple hydrogen – from nuclear-powered electrolysis;
- Yellow hydrogen – from electrolysis powered directly by solar energy;
- Green hydrogen – from water electrolysis powered by renewable energy sources.

Efforts are underway to maximize the use and production of green hydrogen [20]. Hydrogen is widely used in the chemical, metallurgical, and food industries, and is gaining importance in the energy sector, where high-temperature solid oxide cells may become a leading technology for stable electricity generation in the future [21], [22].

2. Fuel cells

Storing energy in the form of hydrogen appears to be a highly promising alternative to today's standard methods. Fuel cells are commonly used to recover energy stored in chemical fuels. In general, fuel cells (FCs) are efficient and low-emission electrochemical devices that convert the chemical energy of a fuel directly into electrical energy (and heat). Compared with conventional combustion-based engines, they can achieve significantly higher efficiency and lower greenhouse-gas emissions, which is why they are widely regarded as one of the most promising energy-conversion technologies in the context of sustainable development. Fuel-cell technologies are commonly classified by electrolyte type and the ionic species transported through the electrolyte. Low-temperature fuel cells include PEMFCs (proton exchange membrane fuel cells), AFCs (alkaline fuel cells), and PAFCs (phosphoric acid fuel cells). High-temperature fuel cells include MCFCs (molten carbonate fuel cells), PCFCs (proton-conducting fuel cells), and SOFCs (solid oxide fuel cells). The basic division of fuel cells is shown in Figure 2.

The electrolyte determines both the operating temperature and the dominant ion-transport mechanism. In general, increasing the operating temperature can improve electrochemical kinetics and, in some cases, system efficiency, but it may also increase system complexity and the manufacturing costs of the cell and stack. For MCFC, PCFC, and SOFC systems, high overall efficiency can also result from the effective utilization of high-grade waste heat, for example for hot-water production or internal thermal management. In contrast, AFC, PAFC, and MCFC electrolytes are strongly corrosive, which can limit durability and complicate large-scale commercialization [23], [24]. Although several fuel cell technologies have electrolyzer counterparts, their reversibility and practical implementation differ considerably. The most established reversible systems are alkaline, PEM, and solid oxide technologies, with SOFC/SOEC being the most direct example of reversible, high-temperature operation. PEMFCs are usually less cost-effective for stationary power generation, while MCFCs and PAFCs remain more niche and are frequently less economically competitive [25].

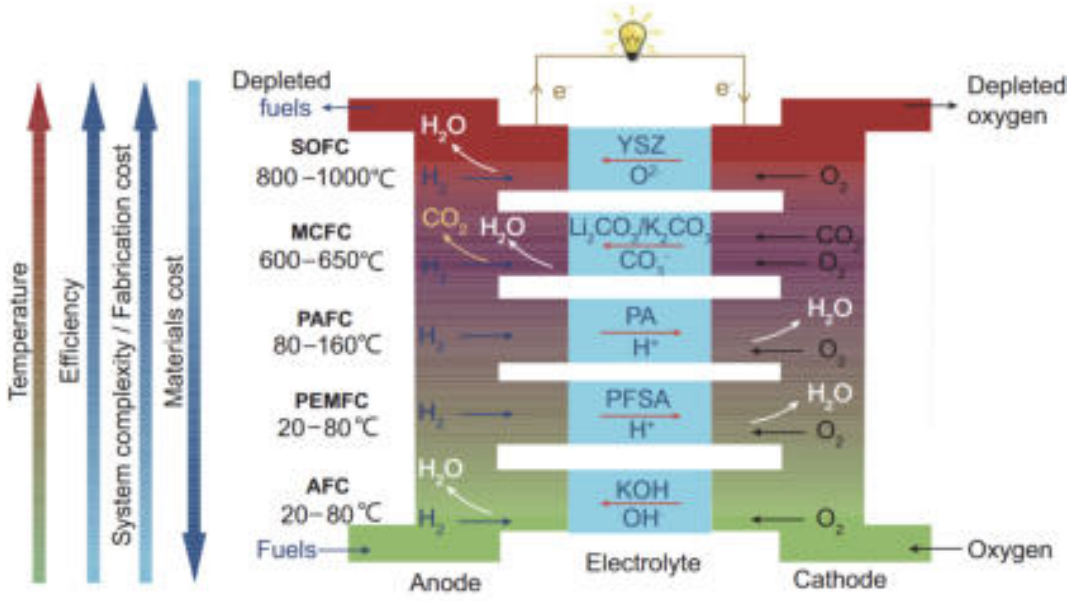


Figure 2. Overview of fuel cell types in relation to operating temperature, efficiency, system complexity, fabrication cost, and material cost [23].

PEMFCs use polymer proton-exchange membranes. State-of-the-art perfluorosulfonic acid (PFSA) membranes, such as Nafion, combined with platinum-based electrocatalysts, enable fast start-up, high power density, and low operating temperatures (typically ~80°C or below), as well as relatively straightforward installation and operation. PEMFCs are also the most mature fuel-cell technology for light-duty fuel-cell vehicles. Despite intensive research into non-noble electrocatalysts, many such catalysts perform satisfactorily mainly in alkaline environments, which has stimulated the development of anion-exchange membrane fuel cells (AEMFCs). However, developing anion-exchange membranes with high ionic conductivity and adequate chemical and mechanical stability remains a significant challenge. Although platinum resources are limited, Pt catalysts used in PEMFCs can generally be recovered and recycled at end-of-life. Consequently, Pt-based catalysts will likely remain important for the foreseeable future, and reducing Pt loading while maintaining or improving activity and durability is a key research direction. Catalyst performance can also be improved by using highly conductive nanostructured oxides or carbides as supports instead of conventional carbon-based carriers. SOFCs are based on ceramic components and, owing to their high operating temperatures (typically 700–900°C), do not require noble-metal catalysts. High temperature also enables

the use of a broad range of fuels—including hydrogen from reformate streams, natural gas, other hydrocarbons, and alcohol fuels—which is a major advantage relative to most other fuel cell types. For this reason, SOFCs are particularly well suited for stationary distributed generation in the kilowatt-to-megawatt range. Key technological challenges include thermal stability, resistance to thermal cycling, stack durability, and controllability at the system level. In solid-oxide devices, thermal-expansion mismatch between components can lead to mechanical stresses, instability, and degradation, especially during start-up and shut-down. Stack durability depends strongly on the activity and stability of electrode materials; however, gradual degradation due to contaminants in the fuel or air—and due to interactions with other system components such as metallic interconnects, seals, and current collectors—remains a major issue. Polarization-induced interfacial phenomena and their effects on microstructure and interface stability are also receiving increasing attention. A global trend in SOFC development is to reduce operating temperature to low levels of 500–600 °C, often referred to as low-temperature SOFC (LT-SOFC). The main advantages include lower manufacturing cost, a wider selection of materials for cell and stack construction, and improved thermal stability. Direct utilization of alcohol fuels also becomes more attractive in this temperature range. However, LT-SOFC development faces major challenges, primarily the reduced ionic conductivity of conventional electrolytes such as yttria-stabilized zirconia (YSZ) and increased polarization losses of electrode reactions—particularly oxygen reduction at the cathode [26]. A typical SOFC fuel cell structure is shown in Figure 3. Nevertheless, for hydrocarbon-fueled SOFC systems (e.g., natural-gas systems), lowering operating temperature below ~700–800°C may offer limited system-level benefits if internal or external reforming remains necessary. System lifetime is another critical aspect.

The IEA reports typical electrical efficiencies for SOFC systems of approximately 50–60%, and in some comparisons even 50–70% (HHV - Higher Heating Value). For MCFCs, reported values are typically around 43–47% or above 60% (HHV), depending on the source and system configuration. For PAFCs, typical values are around 40–42%, while stationary PEMFC systems are often reported at

approximately 30–40% or 32–49% (HHV) [27]. Higher electrical efficiency generally reduces the fuel cost per kWh produced, which can constitute a significant share of the total cost of electricity. However, the high operating temperatures of SOFCs and the associated need for high-temperature components and high-chromium steels can increase the overall system cost. SOFC systems often achieve among the lowest levelized electricity costs (LCOE) within stationary fuel-cell technologies, primarily due to their high electrical efficiency and their ability to operate on fuels such as natural gas.

For stationary SOFC systems, a lifespan of 40,000 hours is often assumed, although reported values in the literature vary widely depending on operating conditions and the definition of end-of-life. For other fuel cell types, typical ranges are approximately 5,000–8,000 hours for AFC, 20,000–60,000 hours for PEMFC, 30,000–80,000 hours for PAFC, and 20,000–40,000 hours for MCFC[28], [29].

Overall, SOFCs offer some of the highest electrical efficiency and among the best performance metrics across fuel cell technologies. They also provide a reasonable lifespan and can deliver relatively low electricity cost per kWh produced under suitable operating conditions. A major advantage of high-temperature fuel cells is their exceptional fuel flexibility. Moreover, the ability to switch between fuel-cell and electrolyzer operation (in reversible solid oxide systems) can be valuable for optimizing hydrogen-based energy storage and utilization. At the same time, high operating temperatures increase system complexity and, consequently, cost [30]. A key pathway to faster deployment may therefore lie in developing efficient materials and cell architectures that enable durable operation at lower temperatures. It is nevertheless widely assumed that improved materials and designs for SOFCs operating at lower temperatures—below 600°C (and in some studies even below 500°C)—could enable substantial cost reductions and accelerate commercialization and market uptake [31], [32].

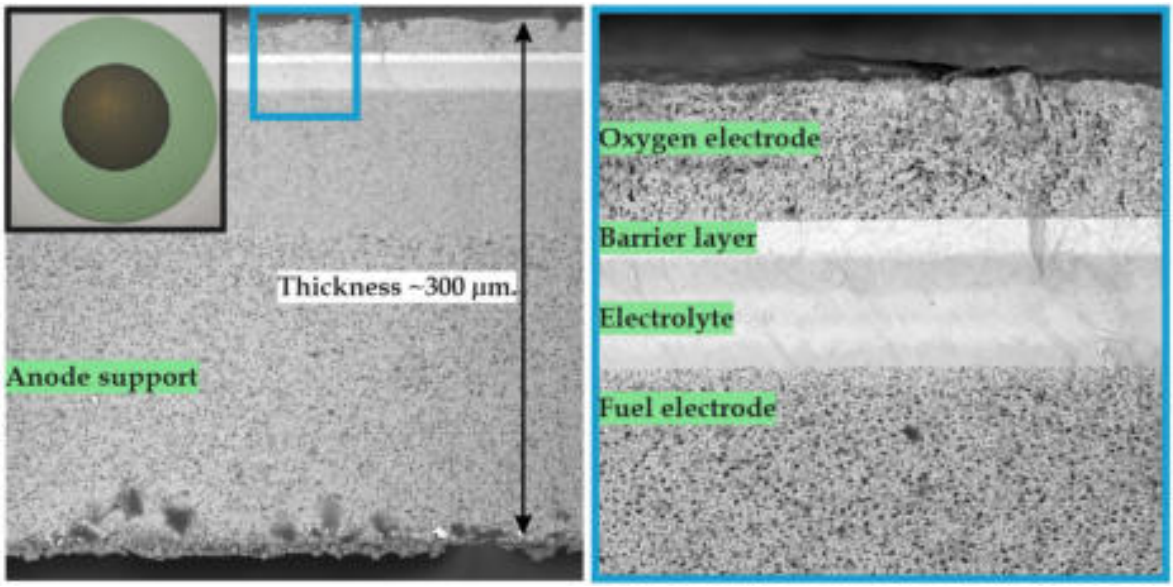


Figure 3. Cross-section of a modern anode-supported solid oxide cell (SOC), highlighting individual components – pictures taken by author.

3. SOCs history and generations

The origins of fuel cells date back to 1839, when Sir William Grove demonstrated an electrochemical cell using two platinum electrodes and dilute sulfuric acid as the electrolyte. The reactants, hydrogen and oxygen, was used to produce an electric current and water at room temperature. This experiment was the first to show that water electrolysis—a process already known at the time—could be reversible [33]. Less than a century later, Baur and Preis verified the feasibility of constructing a fuel cell based on a solid electrolyte, simultaneously demonstrating the ionic conductivity of oxygen ions. They employed zirconia (ZrO_2) stabilized with 15% yttria (YSZ) as the electrolyte and iron or carbon as the fuel electrode and magnetite (Fe_3O_4) as an oxygen electrodes. The cell, operated at 1000 °C, exhibited limited performance but initiated the continuous development of SOC technology [34]. Subsequent advances led to cells with significantly thinner YSZ electrolytes than those used by Baur and Preis and to the replacement of platinum electrodes with more affordable materials. Ni–YSZ cermets (cer-met – ceramic-metallic composite) were introduced on the fuel side, while the oxygen electrode was based on the perovskite oxide LSM ($La_{1-x}Sr_xMnO_{3-\delta}$). These innovations reduced the operating temperature below 1000 °C. Ceramic interconnects, specifically $LaCrO_3$, were also introduced, as metallic materials could not withstand such high temperatures over long operation. This generation of SOCs is commonly referred to as electrolyte-supported cells [35], [36]. Further reductions in electrolyte thickness to 10–20 μm (still primarily YSZ) lowered operating temperatures to the 800–900 °C range. Improved oxygen electrode materials, such as LSC ($La_{1-x}Sr_xCoO_{3-\delta}$) and LSCF ($La_{1-x}Sr_xCo_{1-y}Fe_yO_{3-\delta}$), were adopted, while a CGO ($Ce_{1-x}Gd_xO_{2-\delta}$) barrier layer was introduced to prevent the formation of $La_2Zr_2O_7$ and $SrZrO_3$ at the YSZ–perovskite interface—a phase that blocks ionic conduction. The reduced temperature also enabled the use of metallic interconnects, particularly high-chromium steels such as Crofer 22 APU. These developments increased the achievable power density per cm^2. At this stage, anode-supported cells became dominant, while cathode-supported designs were less common [37]. The next generation was characterized by further electrolyte thinning to below 10 μm. While YSZ remained the primary electrolyte,

the reduced operating temperature (650–800 °C) allowed for alternatives such as CGO and SDC (samaria doped ceria). Electrode materials remained largely unchanged [35], [38]. The next generation, still not implemented to the market, become interesting topic for explored replacing the anode support with porous stainless steel. Such supports provided both mechanical strength and effective gas distribution, enabling thinner electrodes while maintaining similar electrolyte thicknesses. These designs aimed to reduce the operating range to 650–750 °C, though challenges remain, including corrosion in both oxygen rich (oxygen side) and steam rich (fuel side) atmospheres and overall material degradation affecting long-term stability [39], [40]. The most recent concept involves micro-SOCs, where the total cell thickness does not exceed 1 μm. Initial designs employed YSZ electrolytes with platinum electrodes. Advances in thin-film deposition techniques have since enabled the fabrication of high-quality layers of more complex materials. It is anticipated that micro-SOFCs could operate even below 500 °C [41]. This goal is already feasible as is possible to find the reports already demonstrate power densities exceeding 1 $W \cdot cm^{-2}$ at temperatures around 500 °C and lower, highlighting their potential for next-generation low-temperature SOC technology [42]–[44]. Figure 4 shows the generations of fuel cells with emphasis on the support used and the assumed operating temperature range.

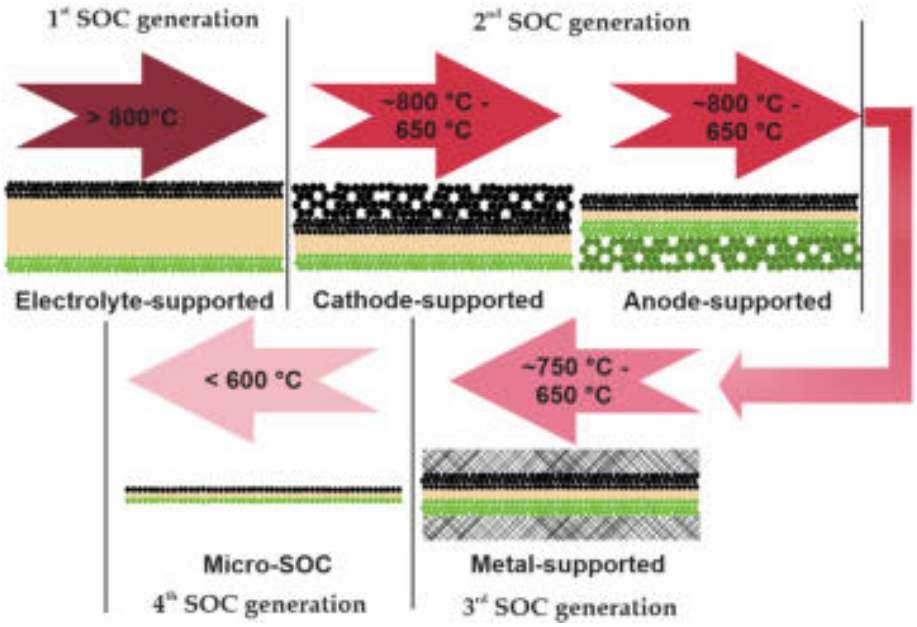


Figure 4. Generations of SOCs with support indication and operating temperature range (Figure created by the author).

4. Principles of SOCs operation

SOCs are electrochemical devices capable of operating in two modes: converting chemical energy into electricity (fuel mode) and converting electrical energy into chemical energy (electrolyser mode). The fuel, which may be hydrogen, methane and other hydrocarbons, alcohols such as methanol, ethanol or biogas, is subjected to an electrochemical and catalytic combustion reaction to obtain the energy stored in the bonds between the atoms of the fuel molecule. Depending on the type of fuel used, the side effects will either be water or carbon dioxide and water [45], [46]. The simplest construction of the SOC stack system as is shown in Figure 5. is based on four elements: electrolyte, fuel electrode, oxygen electrode and interconnects [45].

4.1. Electrolyte

The electrolyte is the central component of the cell, performing several critical functions. Primarily, it acts as an electronic barrier between the electrochemically active electrodes and enables the transport of oxygen ions from the oxygen electrode to the fuel electrode. In first SOC generation, it also provides mechanical support for the cell. Materials suitable for electrolytes in SOC technology must meet several criteria:

- High ionic conductivity
- Negligible electronic conductivity
- High chemical stability in both oxidizing and reducing environments
- Compatibility with electrode materials (no adverse reactions)
- Thermal expansion coefficient matched to other cell components
- Low fuel crossover (low porosity, gas-tight)
- Sufficient mechanical strength
- Resistance to long-term degradation
- Easy for fabrication
- Low cost

The most complex and, at the same time, crucial property for potential electrolyte materials is ionic conductivity - in this case, oxygen ion transport. The diffusion of ions between equilibrium positions is driven by concentration gradients across the electrolyte. This motion critically depends on the presence of point defects [47].

Three main diffusion mechanisms are typically distinguished in oxides, depending on the type of point defect: interstitial, interstitialcy, and vacancy mechanisms [48], [49]. The interstitial mechanism assumes that ions located in interstitial lattice sites migrate by hopping between adjacent interstitial positions. This mechanism does not require additional defects apart from the interstitial ions themselves [48]–[50]. In the interstitialcy mechanism, an interstitial oxygen atom displaces a lattice oxygen atom, which in turn moves to a new position in the sublattice. This process proceeds in two successive steps and can be affected by the presence of blocked sites or clusters [49], [51]–[53].

In the vacancy mechanism, a lattice oxygen ion migrates into a neighbouring vacancy. Oxygen vacancies are critical defects in transition metal oxides that are often created by either dopant substitution or a deviation from stoichiometry. Frenkel and Schottky defects are two key examples. The vacancy mechanism dominates oxygen self-diffusion in many stoichiometric systems, such as those with fluorite or perovskite structures. However, because of the typically high energy barriers associated with this process, these materials must operate at elevated temperatures. Consequently, at high temperatures (above ~900 K), materials such as YSZ are widely recognized as excellent oxygen-ion conductors [48], [54]–[59].

4.2. Fuel electrode

The fuel electrode in fuel mode is responsible for the oxidation of the gaseous fuel, such as hydrogen. The fuel electrode is typically composed of a composite material (cermet) consisting of a ceramic phase, which is usually the same material as the electrolyte and metallic phase – typically nickel. This ceramic phase is characterized by high ionic conductivity, low electrical conductivity, and high stability under highly reducing conditions. It is combined with a metallic

phase, which serves as an efficient electrical conductor and a catalyst for fuel oxidation. Active sites in these electrode are located at triple-phase boundaries where the nickel particles catalyse the breaking of the covalent bond between two hydrogen atoms. The ionically conductive ceramic phase transports oxygen anions to the point of contact with the metallic phase. At this interface, the oxygen anion reacts with the hydrogen cations, completing the electrochemical oxidation process. However, for the oxidation reaction to occur, several sequential steps must take place, each playing a significant role in the overall process. Understanding these steps is crucial for selecting optimal materials for fuel electrode fabrication. The first step is the mass transport of the fuel to the active sites within the electrode structure. The second step involves the adsorption of fuel molecules onto the electrode surface, where intermolecular interactions are formed. In the third step, two bonds are created between the catalyst and the dissociated hydrogen atoms. At this stage, the H_2 molecule is split into two individual hydrogen atoms, each bound to atoms on the electrode surface via specific interactions. Then, in step four, the hydrogen atoms combine with the oxygen anion provided by diffusion in the ionically conducting material to form a product molecule (water) and release it. Simultaneously in fifth step, the transfer of electrons from the chemisorbed hydrogen atoms to the electrode/interconnect [60]. Catalytic reaction of hydrogen diatom molecule creates two protons and two electrons. The result of the formation of H^+ ions according to the reaction [61]:

$$H_2 \leftrightharpoons 2H^+ + 2e^- \quad (1)$$

4.3. Oxygen electrode

The oxygen electrode is responsible for creating oxygen ions from atmospheric oxygen and transporting them to the electrolyte. Similar to the fuel electrode, the oxygen reduction process occurs in several stages. However, unlike the fuel electrode, the resulting oxygen–catalyst bond incorporates the oxygen atom into the crystal structure, from which it is then transported to the electrolyte. Because the electrochemical reaction requires both ionic and electronic conductivity, various material solutions have been developed. One approach is to use

a composite of a highly ionically conductive material with a highly electronically conductive material (e.g., CGO–LSM). The discovery of mixed ionic–electronic conductors (MIECs), which simultaneously meet both requirements, has greatly increased their use—although the associated processes are even more complex. The key advantage of MIEC materials is that, by conducting both ions and electrons, they extend the electrochemically active region from the triple phase boundary close to the electrolyte interface to the entire electrode volume. Oxygen electrode materials are often doped with cations of lower oxidation states to create vacancies in the crystal lattice and maintain charge neutrality. These vacancies enable the migration of oxygen anions by hopping between cations. In addition, MIEC materials can contain electronic defects, such as free electrons or holes. In one reaction, a single oxygen vacancy (Vö) is generated for every two atoms of dopant. In another, two holes ($h^{\cdot}$) are produced for every two cation substitutions. A reduction reaction of oxygen takes place with the use of four electrons according to the reaction [60], [62], [63]:

$$O_2 + 2V\ddot{o} + 4e^- \rightleftharpoons 2O_o^x \quad (2)$$

The electrons formed in the reaction diffuse towards the interconnects from the fuel electrode to ultimately participate in the reduction of oxygen.

4.4. Interconnects

Although interconnects are not directly involved in energy or fuel production, they are a critical component of the cell stack in commercial SOC applications. They represent a significant part of the stack's mass and can account for up to 50% of its total cost. Consequently, significant efforts are being made to lower interconnect costs as a means of reducing the cost per kilowatt of electricity produced. In solid oxide cell technology, interconnects perform two key functions. First, they ensure efficient access and optimal gas distribution to the electrode, thereby reducing concentration polarization. Second, they provide the shortest possible current path to minimize ohmic polarization by collecting electrons generated at the fuel electrode and delivering them to the oxygen electrode[64]. Because the interconnect is simultaneously exposed to both the

reductive and oxidizing environments, it must remain stable in both conditions. Materials used for interconnects must meet the following requirements:

- High electrical conductivity (area-specific resistance (ASR) ≤ 0.1 $\Omega \cdot cm^2$)
- Thermal expansion coefficient (TEC) compatible with electrodes and electrolyte in order to minimize thermal stresses
- Chemical stability and non-reactivity with fuel electrode, oxygen electrode, and electrolyte materials
- Low gas permeability for oxygen and hydrogen to prevent the direct mixing of the oxidant and fuel during operation
- Resistance to sulphur and carbon poisoning as well as oxidation resistance
- Easy for fabrication and low production cost. [65]

Early SOC designs used primarily ceramic interconnects (e.g. $LaCrO_3$) due to the high operating temperatures—close to 1000 °C. Advances in technology have since enabled operation at lower temperatures, making it possible to employ metallic interconnects [66]. Advances in lowering the operating temperature of SOCs, the temperature remains low enough to enable the use of high-chromium ferritic steels (e.g., Crofer 22 APU) to ensure long-term durability of up to 40,000 hours [67]. The presence of chromium is also linked to corrosion processes occurring under elevated temperatures and highly oxidizing conditions. Chromium oxide not only exhibits one of the highest electrical conductivities among transition metal oxides, but also has the ability to form a dense passivation layer and to react with other transition metals to produce spinels or perovskite oxides, which display higher conductivity than single oxides [68]–[73]. The formation of such a protective layer effectively slows further corrosion. However, it has been observed that volatile chromium species (e.g., CrO_3, $CrO_2(OH)_2$) generated at elevated temperatures can migrate and poison the oxygen electrode, leading to a significant reduction in electrochemical performance after only a few hundred hours. To mitigate this problem, protective coatings have been applied to metallic interconnects, both to slow down corrosion and to protect the oxygen electrode from chromium-related degradation [65], [74], [75].

Looking ahead, continued technological progress and further reductions in SOC operating temperatures may enable the use of less expensive austenitic alloys, which contain lower chromium levels but are unsuitable for today's higher-temperature conditions.

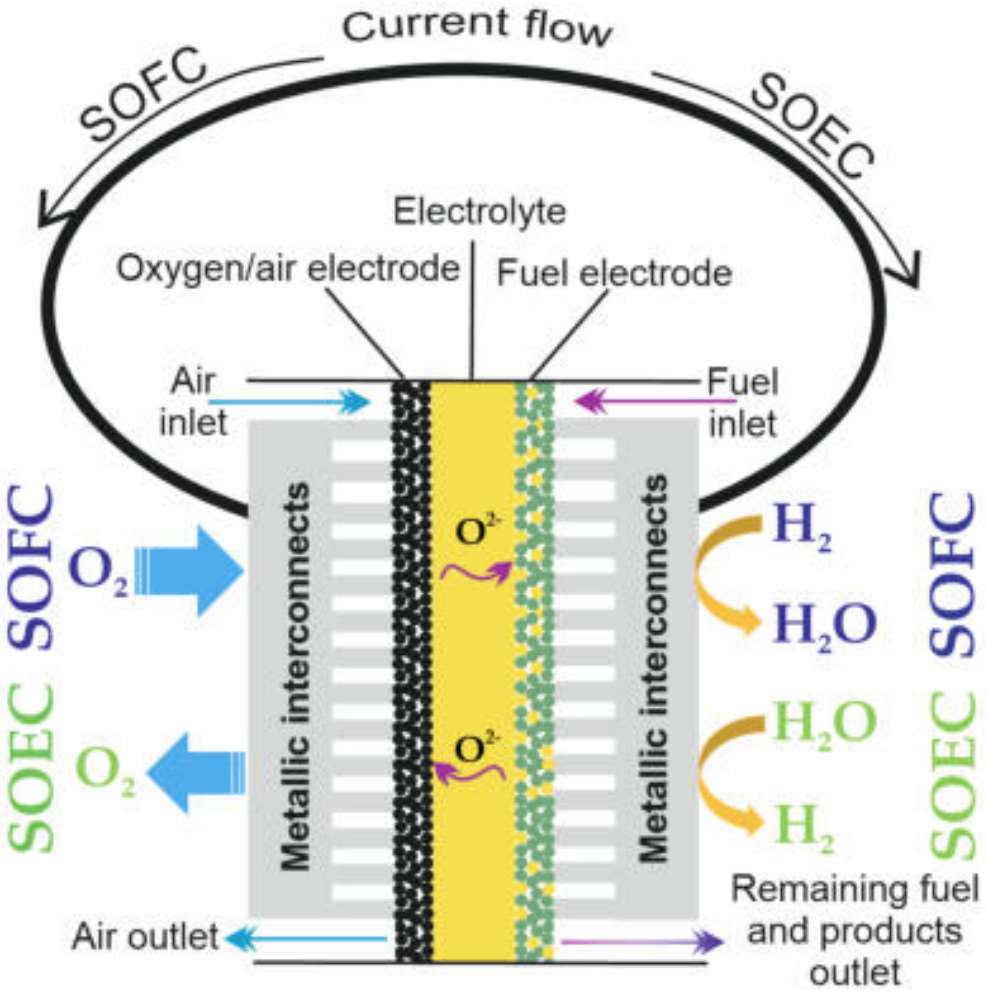


Figure 5. Construction and operation of basic SOC system (Figure created by the author).

5. Factors impacting SOCs performance

When analysing the parameters of the obtained electrodes, one cannot forget about the losses that affect the efficiency of the cell and take them away from the ideal model. In this section, the focus will be on the most important parameters that cause losses in SOCs cells. In the ideal model (Nernst equation), the potential between the fuel electrode and the oxygen electrode is +1.229V (this value is equivalent to the standard potential of electrode). The use of atmospheric air instead of pure oxygen causes the potential slightly decrease to +1.219V (therefore the use of air is a standard). Cell efficiency is also affected by activation polarization, ohmic losses from ion and electronic resistance, and concentration losses due to mass transport [76]. Figure 6. shows the effect of these losses on the I-V characteristics of the cell.

5.1. Activation polarisation

Electrochemical reactions are reactions on a completely different basis than the classical types of chemical reactions. This type involves the transfer of electrons between the electrode surface and a chemical compound related to intermolecular interactions with the electrode surface. Transferring an electron requires the use of a specific quantum of energy, and this energy is called activation energy. This potential can be defined as the internal energy of electrons. Thus, the energy used in the electron hopping process contributes to the decrease in the potential of the entire cell. It is clear, that materials with the lowest possible activation energy should be used [63], [77]–[79]. The activation loss is described by the Butler-Volmer equation:

$$i = i_o \left\{ \exp\left(\beta \frac{n_e F \eta_{Act}}{RT}\right) - \exp\left(-(1-\beta)\frac{n_e F \eta_{Act}}{RT}\right)\right\} \quad (3)$$

where i_0 is the exchange current density, β is the transfer coefficient, n_e is electrons transferred per reaction, F is Faraday constant (96 485 C·mol^{-1}), η_{Act} is activation polarization (V), R is universal gas constant (8.314 J·mol^{-1}·K^{-1}) and T is temperature (K) [79]. The electrode reaction rates at equilibrium are measured by the exchange current density. High exchange current density means a fast electrochemical reaction rate and high fuel cell performance. With high

activation polarization, the first part of the equation will have high values and the second part will be negligibly small, which will reduce the value of the potential between the electrodes (simplified to Tafel equation). In the case of low activation polarization, the value of the first term will be less than one, which will result in a smaller potential decrease - a favourable situation [63], [78]–[80].

5.2. Ohmic Voltage Loss

In the case of loss of potential due to cell resistance, the main factor is the resistance of the diffusion of oxygen ions in the electrolyte material and the flow of electrons in the oxygen electrode and fuel electrode materials. Depending on the material used, the loss of ohmic potential may be lower or higher. Temperature also has a significant influence on the loss of ohmic potential. In the case of lowering the cell operating temperature (what is the current trend), the resistance of the entire cell increases significantly. This phenomenon can be compensated by selecting materials with better conductive properties or thinner electrolytes. The internal resistance of a fuel cell dependent on the temperature change in the fuel cell is described by the equation [79]–[81]:

$$V_{ohmic} = \left\{\gamma \exp\left[\beta\left(\frac{1}{T_0} - \frac{1}{T}\right)\right]\right\} I_{fc} = rI_{fc} \tag{4}$$

where T is the fuel cell temperature; T_0 = 973 K, γ =0.2 Ω, and β = −2870 K are the constant coefficients of the fuel cell; and r is the internal resistance of the SOC [80].

5.3. Concentration Voltage Loss

Conventional diffusion occurs when the pore width of the material's mean path is larger than the gas molecules. Knudsen diffusion is defined as the molecular movement through pores that are small compared to the mean free path of the gas. In this regime, molecules collide with the pore walls more frequently than with other molecules. Upon collision, atoms are rapidly adsorbed onto the surface and subsequently desorbed in a diffusive manner. The repeated interactions with the pore walls slow down the overall molecular transport. The Knudsen diffusion coefficient can be estimated using kinetic theory by relating the pore diameter to the mean free path of the gas. In solid oxide cell electrodes,

gases must diffuse through the gas-filled pores to reach the electrochemical reaction sites. Under these conditions, concentration polarisation can become significant, as the partial pressure of the gas at the reaction sites is lower than in the bulk gas stream when current is generated. Consequently, a reduction in gas concentration within the pores may cause severe polarization and limit the current. However, under typical operating conditions, concentration polarization does not result in substantial voltage losses until the current density approaches the limiting current [79], [80], [82]. The voltage loss due to concentration may be calculated by the following equation:

$$V_{con} = \frac{RT}{nF} \ln\left(\frac{C_b}{C_\infty}\right) \tag{5}$$

where C_b is the concentration at the triple-phase boundary, where the gas, electrolyte, and electrode meet; C_∞ is the bulk concentration of reactant; and n is the number of moles of electrons participating in the reaction [80].

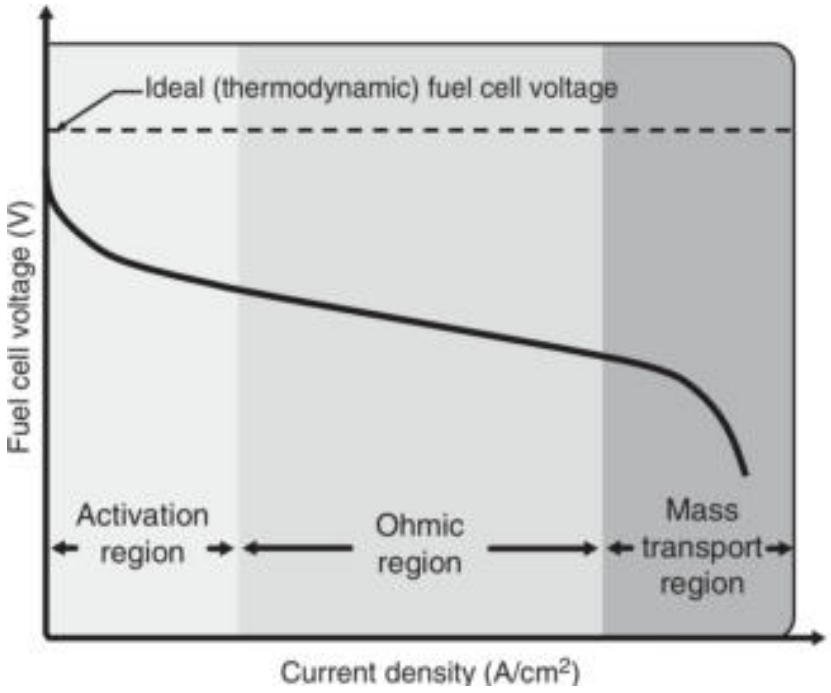


Figure 6. Activation, ohmic and mass losses plotted throughout the I–V curve [83].

Ultimately, considering all these factors, the actual cell potential is obtained from the thermodynamically determined potential, minus the

voltage losses described above. Accordingly, the resulting cell potential can be expressed by the following equation:

$$V = E_{thermo} - \eta_{act} - \eta_{ohmic} - \eta_{conc} \quad (6)$$

where: V – real output voltage of cell, E_{thermo} – thermodynamically predicted output voltage, η_{act} – activation losses, η_{ohmic} – ohmic losses, and η_{conc} – concentration losses [83].

6. Electrochemical impedance spectroscopy

Electrochemical impedance spectroscopy (EIS) is a research method used to investigate the electrical and electrochemical properties of various materials. This method is widely applied in both liquid and solid-state electrochemistry, including studies of batteries, fuel cells, sensors, and biosensors. The technique involves measuring the impedance of a system as a function of the frequency of an applied signal. EIS is considered a non-invasive method because only a small sinusoidal voltage or current perturbation is applied, and the system's response is subsequently analysed using a dedicated frequency response analyser.

Impedance consists of a real part (resistance) and an imaginary part (reactance). Differences between the input signal and the system's response arise from the intrinsic properties of the system that restrict electron flow. Analysis of changes in amplitude and phase shift allows determination of how electrons and charge carriers interact with the electrode. Measurements are typically performed over a wide frequency range (from mHz to MHz), enabling the investigation of processes occurring on different time scales. This technique has also found wide application in the field of solid oxide cells (SOC) and can be used in several measurement configurations. The most basic type of impedance measurement involves the analysis of a complete electrochemical cell. However, such analysis is complex due to the structural complexity (two different electrodes) of the cell and the multitude of electrochemical processes occurring at the electrodes. Therefore, symmetrical measurements are often performed, in which both electrodes are composed of the same electrochemically active material. These measurements provide information about the kinetics of electrochemical reactions, ion and electron transport, and the properties of both the electrodes and the electrolyte. They also enable analysis of the quality of interfaces between materials and allow monitoring of cell degradation processes during operation. Measurements of full cells can be conducted in *in situ* and *operando* modes. Such experiments are used to analyse the behaviour of the cell under operating conditions and to identify degradation

mechanisms. In contrast, symmetrical measurements are performed *in situ*, as they involve the analysis of a half-cell configuration. This approach provides detailed information about the electrode material without overlapping effects from the counter electrode.

EIS measurement results are most commonly presented as Bode or Nyquist plots. In a Nyquist plot, the impedance spectrum typically appears as a series of overlapping semicircles, each corresponding to a different electrochemical process occurring within a specific frequency range. An example of such a spectrum obtained from symmetrical measurements is shown in Figure 7. Depending on the temperature at which the system is measured, some processes may or may not be distinguishable. The example shown represents a complete set of processes that can be identified. Two semicircles are highlighted that correspond to the series resistance associated with the electrolyte. The first semicircle is related to ionic conduction within electrolyte grains, while the second corresponds to ionic transport across grain boundaries. The third semicircle represents the polarization resistance associated with the electrochemically active electrode. In practice, this semicircle often consists of several overlapping contributions that correspond to different electrochemical processes occurring at the electrode.

Analysis of impedance spectra is typically performed by fitting an appropriate equivalent circuit model. In such models, resistors represent resistance to ion and electron transport or charge transfer at the electrode, while capacitors describe polarization phenomena and processes occurring at the electrode surface. In practice, ideal capacitors are rarely used; instead, special elements such as the Constant Phase Element (CPE) are introduced to account for the non-ideal behaviour of the electrochemical double layer and structural heterogeneity of the electrode (e.g., porosity). Another commonly used element is the Warburg or Gerischer element, which represents impedance associated with mass transport; in the case of the Gerischer element, this transport is typically coupled with a chemical or distributed electrochemical reaction. From symmetric measurements, a

number of important parameters can be extracted, including the ohmic resistance (R_{ohm}) determined from the high-frequency intercept, the total polarization resistance (R_{pol}) calculated from the difference between the low- and high-frequency intercepts of the Nyquist plot, and characteristic processes located in different frequency ranges (e.g., charge transport, adsorption of analyte species on the electrode surface, or gas diffusion). Additional parameters such as activation energy from Arrhenius relationships, reaction orders with respect to partial pressures, partial resistances, and relaxation times can be obtained through equivalent circuit fitting or distribution of relaxation times (DRT) analysis [84]–[91].

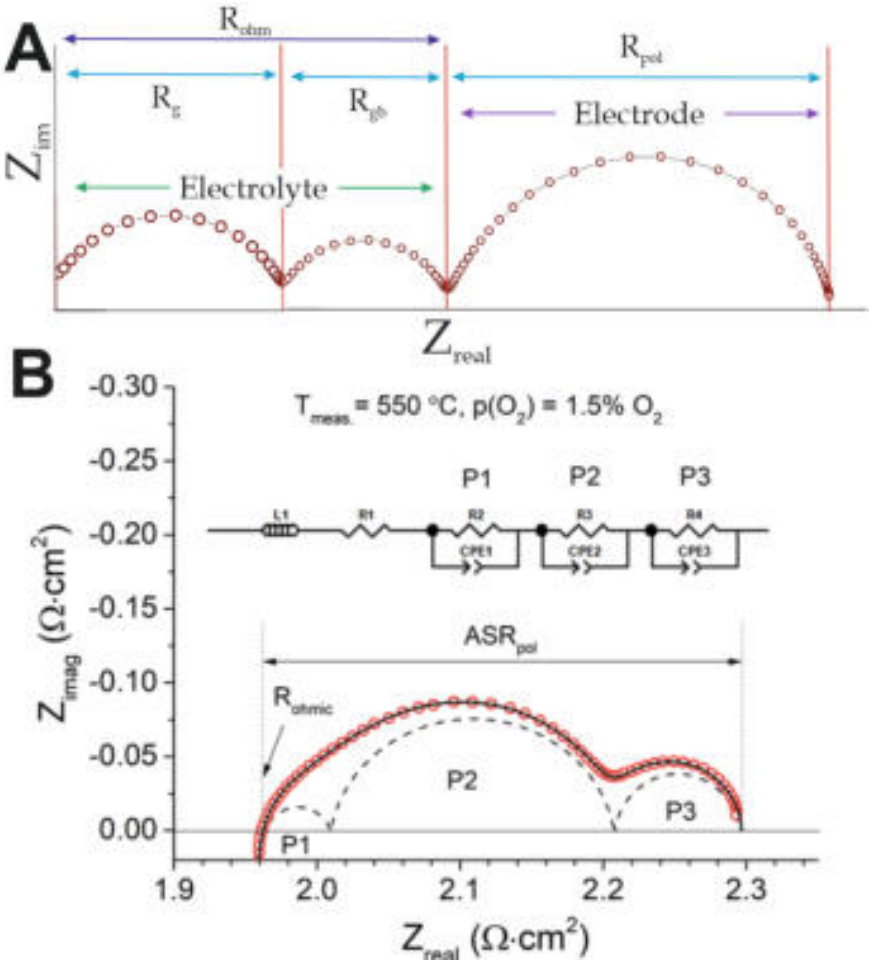


Figure 7. Example of an impedance spectrum with components listed (Figure created by the author) (A) and R_{pol} components related to processes at the oxygen electrode: P1—predominantly thermally activated interfacial process, P2—molecular oxygen adsorption, and P3—gas diffusion [85].

Identification of individual processes is often performed using measurements conducted at different oxygen partial pressures (pO_2) for oxygen electrodes and

hydrogen or steam partial pressures (pH_2, pH_2O) for fuel electrodes. For oxygen electrodes, changes in pO_2 are a key tool for identifying the mechanism of the oxygen reduction reaction (ORR). If R_{pol} decreases with increasing pO_2, this indicates that the rate-limiting step is related to oxygen reduction, adsorption, or dissociation processes. In such cases, power-law analysis is commonly applied:

$$R_p \propto pO_2^{-m} \tag{7}$$

The value of the exponent provides mechanistic insight. For example, m=1 may correspond to dissociative adsorption of O_2, m=3/8 to a subsequent electron-transfer step, and approximately m=1/8 to oxygen incorporation into the electrode material. Symmetric measurements can also be performed in the presence of electrochemical inhibitors. This approach provides information about the interaction between the electrode material and potentially poisoning species. The response of the material can generally be classified as no reaction, reversible reaction (the effect disappears once baseline conditions are restored), partially reversible reaction, or irreversible degradation [92], [93]. For oxygen electrodes, such studies are typically conducted at different pH_2O, pCO_2, and concentrations of other gas-phase species. Measurements performed at varying pCO_2 primarily indicate susceptibility to surface carbonation, changes in ORR activity, the reversibility of degradation processes, and whether degradation occurs mainly at the surface or involves deeper structural reconstruction of the electrode. Similar insights can be obtained from measurements performed in the presence of other inhibitors. For fuel electrodes, variations in pH_2, pH_2O, and sometimes the total gas flow are investigated. These experiments allow separation of the contributions of hydrogen oxidation reaction (HOR) kinetics, hydrogen and steam transport within electrode pores, gas conversion processes, TPB/DPB limitations, and local changes in gas composition in both functional and support layers. Furthermore, such measurements are typically performed at various temperatures, which enables identification of thermally activated processes as well as processes controlled by analyte concentration [86], [94], [95].

7. Materials for SOCs

7.1. Electrolyte materials

The basic and still most widely used electrolyte material in SOC technology is yttria-stabilized zirconia. Figure 8 shows the known phases for zirconium oxide. Pure zirconia exhibits a monoclinic structure (*$P2_1/c$; no. 14*) under standard conditions. Upon heating, it undergoes a phase transition to a tetragonal structure (*$P4_2/nmc$; no. 137)* at ~1000 °C, followed by a transition to a cubic fluorite structure (*Fm-3m; no. 225*) at around 2370 °C [96], [97]. The addition of Y_2O_3 stabilizes the cubic fluorite phase, maintaining its stability even at room temperature [98], [99]. Furthermore, the substitution of Zr^{4+} ions by Y^{3+} cations generates oxygen vacancies, which facilitate oxygen-ion diffusion, as discussed in Section 4.1. In the pioneering experiment by Baur and Preis, YSZ with 15 mol% Y_2O_3 was employed; however, such compositions are no longer relevant. Subsequent studies demonstrated that the dopant concentration critically influences ionic conductivity: above ~10 mol% Y_2O_3, conductivity decreases significantly [99]–[101]. Currently, the most widely applied compositions are 8 mol% YSZ (8YSZ) and 5 or 3 mol% YSZ (3YSZ). While 3YSZ and 5YSZ provides superior mechanical properties, 8YSZ is preferred in SOC applications due to its higher ionic conductivity [99], [102], [103]. YSZ exhibits high ionic conductivity, approximately 0.1 $S \cdot cm^{-1}$ at 1000 °C and between 10^{-2} and 10^{-3} $S \cdot cm^{-1}$ in the 600–800 °C range. It is also practically an electrical insulator. Its thermal expansion coefficient is approximately $10–11 \cdot 10^{-6} \cdot K^{-1}$, making it compatible with commonly used electrode materials [104]. This material is also characterized by excellent stability in both oxidizing and reducing atmospheres, which accounts for its continued widespread use in SOC technology. However, one of its major drawbacks is the tendency to chemically react with perovskite-type oxygen electrode materials based on La and Sr. At high temperatures, this leads to the formation of reaction products such as $La_2Zr_2O_7$ and $SrZrO_3$. Since these phases are non-ionically conductive, their presence at the electrode–electrolyte interface significantly reduces cell efficiency. YSZ performs particularly well at high operating temperatures (above 700 °C). Nevertheless, with the ongoing trend

toward lowering SOC operating temperatures into the intermediate-temperature range, the intrinsic properties of YSZ may become insufficient, motivating the search for alternative electrolytes with higher ionic conductivity at reduced temperatures. A different type of dopant can also be used, such as scandium instead of yttrium. Although scandium-doped ceria has higher ionic conductivity than YSZ, its use is limited due to the high cost of scandium [99].

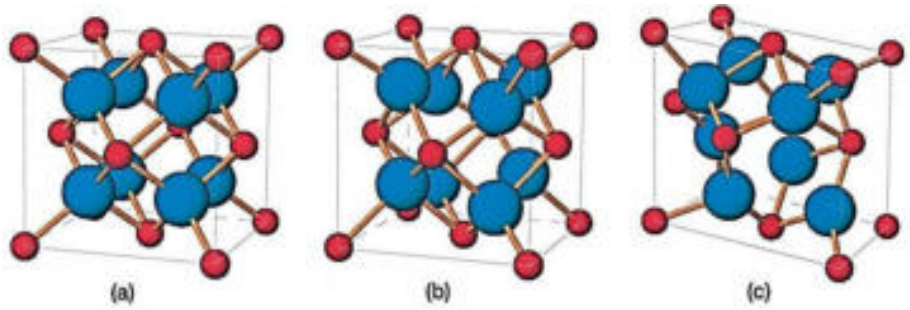


Figure 8. The crystal structure of all three zirconia phases: (a) cubic, (b) tetragonal, and (c) monoclinic [105], [106].

Another class of materials increasingly employed in SOC technology is cerium oxide doped with gadolinium or samarium (CGO – cerium gadolinium oxide; GDC – gadolinium-doped ceria; SDC – samarium doped ceria) [106]. Cerium oxide (CeO_2, Ce^{4+}) exhibits the cubic fluorite structure (*Fm-3m; no. 225*) stable from room temperature to melting point at around 2400 °C [106], [107]. Doping with lower-valence cations, such as Gd^{3+} or Sm^{3+}, does not change the crystal structure. However, the structural stability is enhanced across a broad temperature range and under varying oxygen partial pressures. Typical dopant concentrations reported in the literature and used commercially are 10 mol% or 20 mol%. Among them, CGO20 exhibits lower ionic conductivity compared to CGO10 [106], [108]. In general, CGO displays superior ionic conductivity relative to YSZ, making it a highly promising electrolyte material for intermediate- and low-temperature operation (500–750 °C) [108]. The ionic conductivity of CGO20 range from 10^{-1} to 10^{-2} $S \cdot cm^{-1}$ between 600 and 700 °C [108], [109]. Samarium-doped ceria (SDC) has slightly higher ionic conductivity than CGO[109]. However, unlike YSZ, CGO is less stable under reducing conditions. On the fuel electrode side, partial reduction of Ce^{4+} to Ce^{3+} occurs, introducing an electronic conduction pathway and rendering CGO a mixed ionic–electronic conductor

(MIEC). This electronic contribution lowers the open-circuit voltage (OCV) and increases power losses in the cell [110], [111]. The thermal expansion coefficient of CGO is in the range of 12–13·10^{-6}·K^{-1} (25–1000 °C)[112]. This value is higher than that of YSZ, but closer to the value of oxygen electrode materials (14–15·10^{-6}·K^{-1}). This facilitates better thermomechanical compatibility [113]. Furthermore, CGO does not chemically react with common oxygen electrode materials. For this reason, CGO is frequently employed as a barrier layer on YSZ electrolytes to prevent interfacial reactions between perovskite-type oxides and the electrolyte [114], [115].

Alternative electrolyte materials, though far less commonly employed, include doped perovskite oxides such as $LaGaO_3$ (*Pbnm/Pnma* up to 152 °C, and rhombohedral *R3c* above). This compound exhibits relatively low electrical conductivity but can be considered for use in the intermediate- and low-temperature range. Its major limitations are the complexity of synthesis and the tendency of reduced gallium to react with Ni. Other candidates of interest are doped bismuth oxides, including compositions such as ESB ($Er_xBi_{2-x}O_3$) and DWSB ($Dy_{0.08}W_{0.04}Bi_{0.88}O_{1.56}$). These materials display the highest ionic conductivities reported to date; however, they suffer from instability, readily transforming into phases with poor ionic conductivity. In addition, they require a barrier layer due to the relative ease of Bi reduction. Their low mechanical strength and challenges in densification further limit their practical application [32]. A comparison of the ionic conductivity for the more important electrolyte materials in SOC is shown in Figure 9.

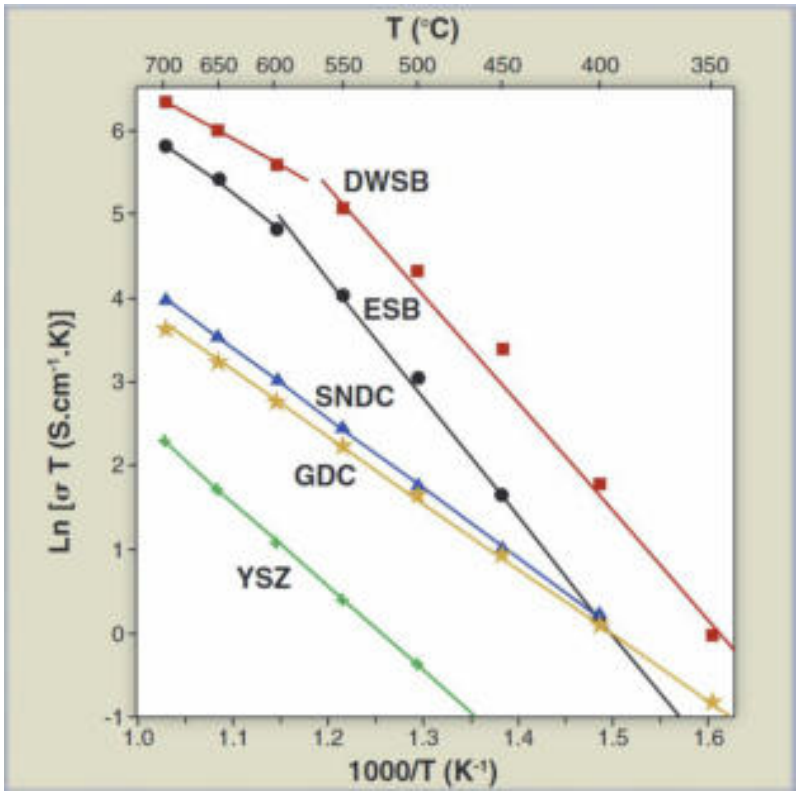


Figure 9. Comparison of the ionic conductivity of different types of solid oxide materials [32].

7.2. Fuel electrode materials

For fuel electrodes, the situation is relatively straightforward, with cermet-based compositions dominating over alternative solutions. The most common configuration is the Ni–YSZ composite. YSZ, employed as the ceramic component, provides sufficiently high ionic conductivity and stability in strongly reducing atmospheres. In addition, it ensures the best possible compatibility with the electrolyte (typically also YSZ), thereby avoiding thermal expansion mismatch issues. Nickel contributes both electrical conductivity and catalytic activity; however, electrochemical reactions occur only at the interfaces between the metallic and ceramic phases—within the so-called triple-phase boundaries. Effective electrode preparation is therefore essential: a continuous percolating network of the ceramic phase must connect to the electrolyte, while the metallic phase must form a continuous path to allow electron transport. These requirements substantially limit the effective active volume of the electrode. A major drawback of Ni–YSZ electrodes is their high susceptibility to sulphur poisoning, which can markedly reduce efficiency. Moreover, when operating with

fuels other than hydrogen (e.g., CO or methane), carbon deposition (coking) may occur, leading to catalyst deactivation. Long-term operation can also promote nickel agglomeration and the growth of large metallic clusters, thereby reducing the active surface area and overall cell performance [116]–[119]. At lower operating temperatures, Ni–CGO composites are considered as an alternative to Ni–YSZ. Their operation principle is analogous; however, as noted in Section 7.1, the partial reduction of cerium from Ce^{4+} to Ce^{3+} introduces mixed ionic–electronic conduction, effectively extending the length of the active reaction zone. While this effect can be beneficial, Ni–CGO systems are less stable under reducing conditions compared to YSZ-based electrodes. Nonetheless, the higher ionic conductivity of CGO relative to YSZ is advantageous, making such composites attractive for low-temperature SOCs [116], [117], [120], [121]. Beyond cermets, single-phase mixed conductors based on perovskites and double perovskites are also under investigation. Notable candidates include LSCM ($La_{0.75}Sr_{0.25}Cr_{0.5}Mn_{0.5}O_{3-\delta}$), LSCr ($La_{1-x}Sr_xCrO_3$), and double perovskites such as SFM ($Sr_2Fe_{1.5}Mo_{0.5}O_{6-\delta}$). These materials exhibit stability in reducing environments and are largely resistant to sulphur poisoning and carbon deposition. Moreover, the TEC values for these materials are comparable to those of YSZ and CGO (range: 9-13·10^{-6}·K^{-1}). However, their electrical conductivity and catalytic activity remain lower than those of conventional cermet composites. Despite these limitations, such materials may be promising for intermediate-temperature SOC applications [122]–[124].

7.3. Oxygen electrode materials

Oxygen electrode materials encompass the broadest spectrum of compounds employed in SOCs. At high operating temperatures, the most widely adopted material was initially LSM ($La_{1-x}Sr_xMnO_{3-\delta}$), a cubic close-packed perovskite structure (*Pm-3m*) [125]. LSM exhibits almost only electrical conductivity, making it effective primarily at temperatures above 800 °C, where its conductivity reaches 100 - 485 S·cm^{-1} in the 800–1000 °C range [125], [126]. Owing to the lack of significant ionic transport (10^{-7}-10^{-8} S·cm^{-1} at 800 °C), the oxygen reduction reaction is restricted to triple-phase boundaries, thereby limiting the active

electrode area [126]. While the material offers acceptable chemical stability, it may react with YSZ, as discussed previously. Its thermal expansion coefficient (TEC) of 11.3–12.4·10^{-6}·K^{-1} matches properly with the electrolyte [125], [127]. However, as SOC technology advanced and operating temperatures were reduced, the performance of LSM became insufficient. Subsequently, cobalt-based perovskites such as LSC ($La_{1-x}Sr_xCoO_{3-\delta}$) and LSCF ($La_{1-x}Sr_xCo_{1-y}Fe_yO_{3-\delta}$) emerged as leading alternatives (typically rhombohedral *R-3c* at room temperature, but commonly indexed as (pseudo)cubic *Pm-3m* at SOC operating temperatures). LSC exhibits mixed conductivity, combining high electronic conductivity (100–1000 S·cm^{-1} in the 600–800 °C range) with substantial ionic conductivity (0.01–0.22 S·cm^{-1} at 600–800 °C) [126], [128], [129]. This enables oxygen reduction to proceed over an extended electrode surface rather than being confined to triple-phase boundaries. However, LSC has a very high TEC (17-21·10^{-6}·K^{-1}), which reduces compatibility with electrolytes, and it relatively easily reacts with YSZ, necessitating the use of CGO barrier layers [128], [130]. Additional limitations include rapid performance degradation due to strontium segregation and sensitivity to moisture, leading to the formation of strontium hydroxide that block active sites. At present, LSCF is more commonly used than LSC. Like LSC, LSCF exhibits mixed conductivity, with electronic conductivity of ~200–300 S·cm^{-1} and ionic conductivity in the range of ~0.01–0.1 S·cm^{-1} in the same temperature range [131], [132]. Its TEC (15–17·10^{-6}·K^{-1}) is lower than that of LSC but still exceeds that of typical electrolyte and electrode materials [131], [133]. Other properties, including reactivity with YSZ and degradation mechanisms, largely mirror those of LSC. Figure 10 shows the electrical conductivity of some materials used as oxygen electrodes in SOCs.

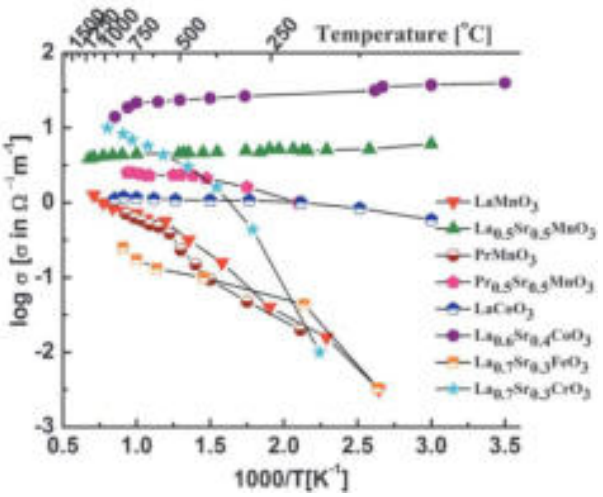


Figure 10. Arrhenius plots of electronic conductivity for various oxygen electrodes for SOCs [134].

A promising alternative to commonly used intermediate-temperature oxygen electrode materials is the cubic perovskite oxide STF ($SrTi_{1-x}Fe_xO_{3-\delta}$) (space group - *Pm-3m*), regarded as one of the best cobalt-free alternative [135]. Iron doping introduces oxygen vacancies, thereby enhancing the material's conductivity. While its electronic conductivity is moderate compared to LSC and LSCF, it still reaches between 0.6–100 $S \cdot cm^{-1}$ in the 600–800 °C range. Its ionic conductivity is comparatively high, reported at ~3.5 × 10^{-2} $S \cdot cm^{-1}$ at 900 °C [135], [136]. The thermal expansion coefficient (TEC), ranging from 11.7 to 16.5·$10^{-6} \cdot K^{-1}$ at 77-477 °C, and 16.6-31.1·$10^{-6} \cdot K^{-1}$ between 477 and 777 °C, is mismatched to typical electrolyte materials [136]. STF also exhibits greater chemical stability than LSC and LSCF, though its use is limited by the formation of a dense interfacial layer when the Sr-deficient in material structure at the electrode–electrolyte boundary, which reduces the effective active surface area [88].

Another material of growing interest for oxygen electrodes is praseodymium oxide (PrO_x). Praseodymium oxides are structurally complex, exhibiting multiple phases that complicate direct correlations between structure and electrochemical performance. The four main phases (shown in Figure 11) are PrO_2 (space group - *Pm-3m*), Pr_6O_{11} (space group - *Pm-3m*), Pr_7O_{12} (trigonal *R3*), and Pr_2O_3 (space groups – A -type - *P-3m1*, and C-type - *Ia-3*), but several other substoichiometric forms (e.g., Pr_5O_9 - monoclinic $P2_1/c$, $Pr_{11}O_{20}$ - triclinic *P-1*) are also known [137]–[141]. Literature reports identify the cubic β-phase (Pr_6O_{11}, or

$PrO_{1.833}$) as the most electrochemically active form, with total conductivity of 6.77 × 10^{-2} S·cm^{-1} at 400 °C and an activation energy of 0.52 eV per atom [142]. This phase is stable up to ~430 °C, after which successive phase transitions occur: to the δ-phase ($Pr_{11}O_{20}$) near 470 °C, to the ε-phase (Pr_5O_9) at ~490–520 °C, and to the rhombohedral ι-phase (Pr_7O_{12}) up to ~700 °C [142], [143]. The ι-phase is characterized by markedly lower total conductivity [143]. Despite these transformations, the phases remain structurally similar, reflecting a common underlying lattice framework. The pronounced phase variability, and the associated differences in physicochemical properties, necessitate careful optimization of parameters for the application of PrO_x in SOCs. Under reducing conditions, Pr^{4+} is readily reduced to Pr^{3+}, which alters the material's properties. Notably, PrO_x exhibits very high catalytic activity in the low-temperature range (<600 °C). However, its relatively low electrical conductivity—approximately 1 S·cm^{-1} at 800 °C [144], [145]—limits its use as a primary electrode material; instead, it is often employed as an infiltrated additive to enhance the electrocatalytic activity of composite electrodes [146]–[154]. The thermal expansion for PrO_x is strongly phase dependent: TEC increases from ~11·10^{-6}·K^{-1} (25–207 °C) to ~13·10^{-6}·K^{-1} at 527 °C, exceeding 16·10^{-6}·K^{-1} above 727 °C (1000 K). Above ~600 °C, TEC values surpass 14·10^{-6}·K^{-1}, leading to compatibility issues with other cell components [155]. In addition, PrO_x exhibits a reversible interaction with water, forming weak bonds with hydroxide groups. This behaviour contrasts with typical perovskite materials, where the reaction with hydroxide is only partially reversible and results in the irreversible loss of some active sites [86].

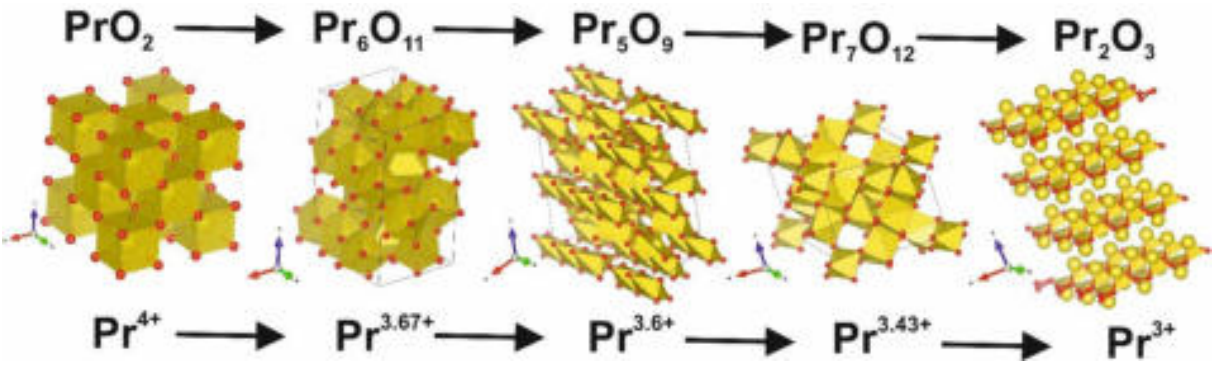


Figure 11. Variability of praseodymium oxides (Figure created by the author).

7.4. Interconnect coating materials

With the advancement of SOC technology, metallic interconnects have become widely adopted. The use of high-chromium ferritic steels, such as Crofer 22 APU, quickly revealed the need for protective coatings. These coatings serve to suppress chromium evaporation—which otherwise poisons the oxygen electrodes—and to reduce the corrosion rate. Without protection, the gradual increasing of chromium oxide thickness generates additional mechanical stresses that may ultimately lead to cell fracture and premature failure [156]. Several classes of materials have been investigated as protective coatings. The simplest are rare-earth oxides, including cerium oxide, yttrium oxide, gadolinium oxide, and lanthanum oxide. With the exception of CeO_2, these oxides effectively block oxygen diffusion to the steel surface, thereby slowing corrosion, while also impeding chromium diffusion. However, their relatively low electrical conductivity limits their use to thin layers (below 1µm), as thicker coatings would introduce excessive resistance [157]. The main differences among these oxides lie in their chemical stability and reactivity with chromium, often resulting in the formation of perovskite-type compounds with higher electrical conductivity than the initial protective oxide. For example, La_2O_3 reacts rapidly with chromium to form $LaCrO_3$ at 1000 °C. Gd_2O_3 forms $GdCrO_3$ after 144 h, while Y_2O_3 requires 288 h to form $YCrO_3$, and even then the reaction remains incomplete [157], [158]. Electrolytic deposition applied to create coatings of ~100 nm thickness significantly improved corrosion resistance, with La_2O_3 and Y_2O_3 yielding the lowest weight gain, followed by Gd_2O_3, whereas CeO_2 performed poorest [159].

Currently, the most widely applied coatings are spinel oxides, valued for their relatively high electronic conductivity and strong diffusion-blocking properties against both oxygen and chromium. Among these, $MnCo_2O_4$ (MCO) and $CuMn_2O_4$ are the most studied. MCO effectively inhibits chromium diffusion, forming dense, stable, high-quality layers. It also slows oxygen diffusion, which retards chromium oxide growth. Its electrical conductivity (10–100 $S \cdot cm^{-1}$) is sufficient for interconnect applications. The main limitation of MCO is its high cobalt content -an expensive and crucial element in many

areas such as batteries, and lower electrical conductivity in low temperature range. As a result, research has shifted toward alternatives such as $CuMn_2O_4$ and doped derivatives. These materials can reach higher conductivities—up to ~225 $S \cdot cm^{-1}$ at 750 °C—while being nearly pure electronic conductors, which makes them very effective oxygen diffusion barriers [160], [161]. However, their ability to block chromium diffusion is inferior to that of MCO. Their key advantages are the use of cheaper, more abundant elements and a thermal expansion coefficient (TEC) of 9.6–10.6 × 10^{-6} K^{-1} (50-600 °C), comparable to Crofer steel and other SOC components [161].

Perovskite oxides, such as $La_{1-x}Sr_xCrO_3$ [162]–[164] and LSC/LSCF [165]–[168], have also been explored as protective coatings. Their main advantages include high electronic conductivity—often exceeding that of spinels—together with acceptable chromium-blocking performance and good chemical compatibility with oxygen electrode materials [156]. Their mixed ionic–electronic conductivity can also facilitate faster formation of protective oxide layers, further mitigating corrosion. The main drawback, however, lies in difficulties associated with densification. Beyond these classes, additional alternatives such as CGO [169], composites [170], [171], and bilayer coatings [172], [173] have also been investigated.

7.5. Current status and gaps of developed research topics

7.5.1. Protective coatings for metal interconnects based on rare-earth oxides and spinel $CuMn_2O_4$ and its derivatives.

Replacing MCO with an alternative protective coating material for metallic interconnects requires the development of a solution of equivalent quality. Using rare-earth oxides is one possible solution, but the limitations described in Section 7.4 effectively restrict the potential application of these materials to thin coatings. Studies examining the use of these layers in SOC technology most often focus on operating temperatures of 750 °C and above. Studies analysing the impact on corrosion resistance at temperatures below 750 °C are relatively rare. A similar situation exists for the use of $CuMn_2O_4$ spinel and its derivatives. Given the decreasing effective operating temperature of cell

stacks, it is necessary to characterise corrosion processes at lower temperatures, and the reduced operating temperature and slower material degradation rate allow the use of materials with better properties than MCO. Table 1 provides an overview of studies investigating protective coatings based on rare-earth metals, $CuMn_2O_4$ spinel, and its derivatives.

Table 1. Review of works related to rare earth metals and spinel derivatives $CuMn_2O_4$.

Protective layer Composition	Oxidation time [hours]	Kp [$g^2\ cm^{-4}\ s^{-1}$]	Temperature [°C]	Reference
Y Y_2O_3	300	2.44×10^{-15} [5-300] 7.09×10^{-15} [8-300]	800	[174]
La_2O_3	1000	-	800	[175]
Gd_2O_3	2260	3.22×10^{-14} [260-2260]	800	[176]
MnCuFe0 MnCuFe01 MnCuFe03	3000	6.1×10^{-15} 4.92×10^{-15} 4.73×10^{-15}	750	[177]
$Mn_{1.9}CuFe_{0.1}O_4$	5000	8.05×10^{-15}	750	[178]
$Cu_{1.3}Mn_{1.7}O_4$	100	8.50×10^{-14}	750	[179]
$CuMn_{1.8}O_4$	1000	-	800	[180]
$CuMn_{1.8}O_4$	120	-	800	[181]
$Cu_xMn_{3-x}O_4$ ($1.0 \leq x \leq 1.3$)	1000	$5.16\text{-}8.33 \times 10^{-15}$	800	[182]

Studies addressing corrosion behaviour at 700 °C remain still rare. This gap is significant, as commercially available systems are already capable of efficient operation at such temperatures. Moreover, the proposed iron doping exhibits peak electrical conductivity within the 600–700 °C range, which to date has not been systematically investigated [161].

7.5.2. LSC- or PrO_x-based oxygen electrodes for low-temperature fuel cells

Based on the available literature, two promising materials were selected for research on oxygen electrodes in next-generation solid oxide cells operating at temperatures ≤600 °C: LSC and praseodymium oxide. While position of the crystalline form of LSC is relatively well-established, the knowledge of its partially amorphous or amorphous forms is very limited. Praseodymium oxide remains an intriguing and poorly understood material.

$La_{1-x}Sr_xCoO_{3-\delta}$ can exist in two crystalline forms - hexagonal (trigonal, rhombohedral) lattice structure between room temperature and 390 °C, and cubic perovskite form which remains stable above 611 °C [183]. Typically, the synthesis of LSC leads to multiphase products, not only the perovskite LSC phase but also $(La,Sr)_2Co_{4+\delta}$ and SrO [184]. Other studies additionally identified Co_3O_4[185]. At synthesis temperatures below 550 °C, LSC tends to form in semi-amorphous or amorphous states. LSC is a well-established oxygen electrode material, characterized by high ionic conductivity ranging from 0.56 to 1.2 S/m at 700 °C, which is around three times higher than LSCF exhibits a conductivity of 0.474 S/m at the same temperature [186], [187]. Most of the literature focuses on crystalline LSC, whereas reports on amorphous LSC are extremely rare. For crystalline LSC, the range of electrode polarization resistance values describing electrochemical performance is wide. The examples of works of LSC as an oxygen electrode at focused temperatures over the last dozen or so years is presented in Table 2.

Table 2.Overview of the results obtained so far for LSC as an oxygen electrode.

Composition	Deposition Technique	Polarisation resistance [Ω·cm^2]	Temperature [°C]	Reference
		Crystalline LSC		
CGO infiltrated with LSC	Infiltration	0.044	600	[188]
LSC 1 µm	hand-painted	0.97	600	[189]
LSC 200 nm	Metal organic deposition	0.023	600	[190]
LSC 113-214	Co-sputterring deposition	0.15	575	[191]
LSC 200 nm	pulsed laser deposition	0.1	600	[192]
LSC 300 nm	Metal organic deposition	0.13	600	[90]

LSC 200 nm	Metal organic deposition	0.007	600	[184]
LSC 400 nm	Spray pyrolysis	0.076	600	[85]
2D LSC nanosheets/LSCF	Immersion	0.316	600	[193]
Partially Amorphous / Amorphous LSC				
LSC8020 ~300 nm	Pulsed laser deposition	850	415	[194]
LSC 100 nm	Pulsed laser deposition	Lower than 0.3	400	[195]

There is limited research on partially amorphous or amorphous LSCs, but the few studies that exist indicate the potential application of such a solution. The trend of lowering the effective operating temperature of fuel cells enables the use of non-crystalline materials with very small grain sizes, which may be beneficial due to the high number of defects present in the material. The gap in detailed research on these materials is due to commercial cells still operating at excessively high temperatures, attempts to find alternative solutions, and the complexity of the structures and processes occurring in such systems. However, continuous progress in the field of solid oxide cells means that such a solution can be envisaged, and this is an area that requires further research.

The situation is different for praseodymium oxide. This relatively still unknown material is usually addition to the base material to improve the electrochemical performance of the entire electrode. A review of the available literature, presented in Table 3, indicates that the dominant technique is the infiltration of other materials. The few studies describing the material itself either treat these samples as reference samples for the infiltrated ones or report inferior electrode performance, in which case the material itself is not analysed in detail. As with LSC, a fairly wide range of polarization resistance results is observed for PrO_x at the same or similar temperatures.

Table 3. Overview of the results obtained so far for praseodymium as an part or functional oxygen electrode.

Composition	Deposition Technique	Polarisation resistance [$\Omega \cdot cm^2$]	Temperature [°C]	Reference
Pr_6O_{11}	Spray pyrolysis	0.245	600	[146]
PrO_x - CGO LSC:PrO_x – CGO	Immersion/ Infiltration	0.42 0.23	600	[147]
Pr_6O_{11} - CGO	Infiltration	0.028 0.14	600 500	[148]
Pr_6O_{11} with LSM as CC Pr_6O_{11} with LSCF as CC	Electrostatic spray deposition	0.02 0.022	600	[149]
LSM-YSZ – PrO_x LSM-YSZ – $(Pr,Ce)O_x$	Electro-chemical deposition	0.6 2	650	[150]
LSM - PrO_x LSC- PrO_x LSCF- PrO_x	Infiltration	0.284 ± 0.013 0.273 ± 0.011 0.482 ± 0.032	600	[151]
LSCF - PrO_x	Infiltration	0.991	500	[152]
LSCF – PrO_x STFC – PrO_x	Infiltration	0.556 0.067	650	[153]
PrO_x onto CGO PrO_x – CGO PrO_x LSM-CGO PrO_x -LSM	Spray pyrolysis /infiltration	0.125 0.03 0.06 0.1	650	[154]

Despite the growing interest in this material, and the clear improvements in its electrochemical performance demonstrated in the literature, detailed characterisation of praseodymium oxide remains incomplete. There is also a significant gap in understanding of the impact of potentially interfering factors, such as H_2O and CO_2, on electrode performance.

8. Objectives and hypothesis of the thesis

Fuel cell technology for electricity generation from hydrogen and hydrocarbons has been known and developed for more than a century. The trend toward lowering operating temperatures opens new opportunities and, as a consequence, may contribute to reducing energy production costs. It also highlights areas that remain insufficiently explored in the literature.

The objective of this work was to develop and characterize advanced electrochemically active materials suitable for next-generation solid oxide cells, with particular emphasis on their structural properties and suitability for lower-temperature operation. An additional consideration was the use of fabrication methods that are simple and cost-effective, requiring no specialized or expensive equipment, yet still ensuring adequate material quality.

A review of the literature indicates that the corrosion resistance of protective coatings is typically investigated at temperatures above 750 °C, corresponding to conventional commercial applications. However, cells operating in the intermediate range of 600–700 °C are becoming increasingly common. This temperature window remains relatively unexplored, and the slower reaction kinetics associated with reduced operating temperatures may, in fact, enable the long-term use of alternative protective materials. Similarly, oxygen electrode materials are rarely evaluated for operation at temperatures ≤600 °C, representing a notable gap in the knowledge base of fuel cell research. Lower-temperature operation also allows for the application of partially amorphous or nanocrystalline materials, where reduced crystalline and grain size increases the electrochemically active surface area. Drawing on existing literature, materials with promising protective or catalytic properties were identified and selected for implementation in solid oxide fuel cells operating below the temperatures typically used in current technologies. A complementary approach involved the proposal of novel materials with improved functional properties relative to established systems. Importantly, these properties can be tuned and optimized without altering the overall chemical composition. The presented direction of research and development

on advanced materials for next-generation solid oxide cells has enabled to formulate the following hypotheses:

1. **Effective chromium diffusion-blocking protective coatings for metallic interconnects in intermediate-temperature solid oxide cells can be developed by harnessing the synergistic effects of rare-earth oxides and the cobalt-free spinel $CuMn_{1.7}Fe_{0.3}O_4$ (CMFO).**

The effectiveness of the proposed synergistic approach stems from the properties of rare-earth oxides such as La_2O_3, CeO_2, Y_2O_3, and Gd_2O_3. These oxides limit oxygen diffusion to the steel surface, thereby improving corrosion resistance. However, they exhibit low electronic conductivity. In contrast, CMFO is characterized by high electronic conductivity, low ionic conductivity, and a good capacity to block chromium diffusion. The first hypothesis posits that a synergistic approach can be developed to combine the advantages of these materials while significantly mitigating their individual limitations. Articles 1 and 2 of this thesis address this hypothesis and demonstrate the feasibility of fabricating effective protective layers based on CMFO and rare-earth oxides that significantly reduce the oxidation rate and inhibit chromium diffusion.

2. **Electrochemical activity of oxygen reduction reaction in low-temperature solid oxide cells operating at ≤600 °C can be enhanced through optimization of the fabrication process of oxygen electrodes based on mixed ionic-electronic conductors such as LSC ($La_{0.6}Sr_{0.4}CoO_{3-\delta}$) and PrO_x.**

The application of thin-film techniques such as spin coating or infiltration enables more efficient use of materials, better control of microstructural parameters, including crystallite and grain size, and improved electrode-substrate contact. Articles 3–5 show that low-temperature fabrication of oxygen electrodes can enhance the electrochemical activity of LSC and PrO_x materials, especially at lower operating temperatures. Furthermore, despite

the low sintering temperature of the layers, no deterioration of the electrode-electrolyte interface was observed.

The research supporting these theses has been published in scientific journals listed in the Journal Citation Reports (JCR) and is presented in Chapter 10.

9. Materials preparation and measurement methods

9.1. Material synthesis and layer preparation

9.1.1. RE-oxide layer preparation

Deposition of La_2O_3, CeO_2, Y_2O_3, and Gd_2O_3 was carried out using an electrolytic technique. For this purpose, 2 mM ethanolic solutions of the respective metal nitrates were prepared. Crofer 22 APU samples, pretreated through a cleaning process, served as the working electrodes (cathodes) in a two-electrode deposition setup, with electrical connections made via crocodile clips. An oversized Crofer 22 APU steel sheet was used as the counter electrode (anode), positioned symmetrically on both sides of the working electrode, yielding an active geometric surface area of approximately 50 cm^2. The interelectrode spacing was maintained at ~1.5 cm. Deposition was performed by applying a constant DC voltage of 40 V for varying durations (10 seconds – 4 minutes). Following deposition, the specimens were carefully air-dried before undergoing an annealing treatment at 400 °C. Figure 12 presents the setup used for applying a ceramic coating by the electrolytic technique, together with example samples after coating deposition and during the annealing stage described above.

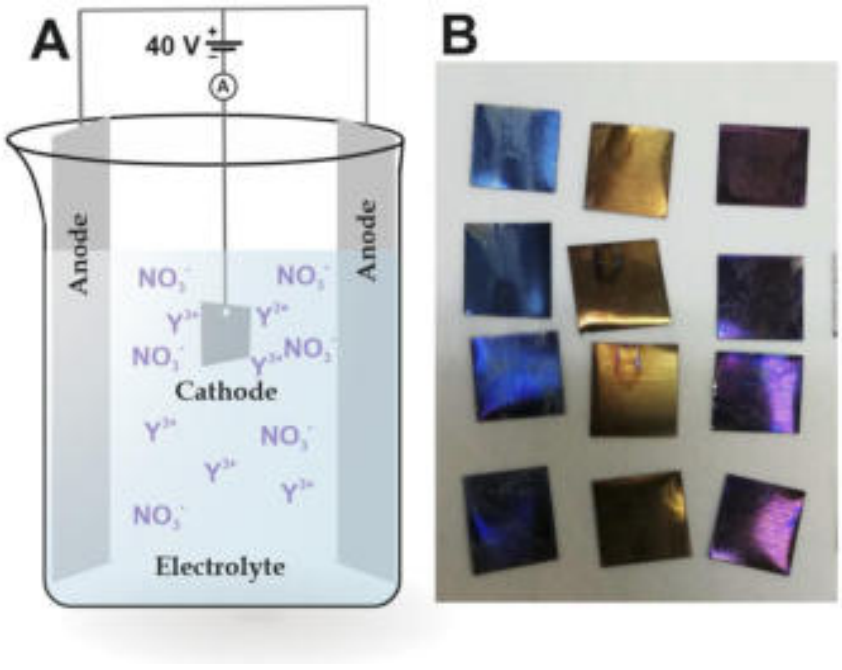


Figure 12. Sketch of deposition setup (A), and the example of samples after the deposition and annealing at 400 °C (B) (Figure created by the author).

9.1.2. Spinel synthesis and deposition

The spinel material $CuMn_{1.7}Fe_{0.3}O_4$ (CMFO) was synthesized via the sol–gel method. Metal ion precursors were introduced in the form of nitrate salts, while citric acid and ethylenediaminetetraacetic acid (EDTA) served as chelating agents. These components were dissolved in deionized water under magnetic stirring. During sol preparation, the pH of the solution was adjusted with aqueous ammonia to suppress precipitation of metal hydroxides. Ethylene glycol was added as a polyesterification agent to promote polymer network formation. The precursor solution was maintained at 80 °C until it formed a dense gel. The resulting gel was calcined in a muffle furnace at 400 °C for 2 h, followed by annealing of the obtained powder at 800 °C for 2 h. To minimize grain size, the powder was subsequently ball-milled in a planetary mill using zirconia balls (Ø = 3 mm) at 800 rpm for 4 h.

The spinel layer was prepared by electrophoretic deposition (EPD). A suspension was formulated by dispersing 1 g of CMFO powder in 100 cm^3 of an isopropanol:acetone mixture (4:1). Crystalline iodine (0.1 g per 100 cm^3) was added as a charging agent. The suspension was ultrasonicated for 15 min to ensure homogeneous dispersion of the spinel particles. Deposition was performed at a constant DC potential of 80 V for 4 min, yielding a layer thickness of approximately 10 μm. Finally, the coated samples underwent a two-step thermal treatment: reduction in hydrogen at 800 °C for 10 h, followed by oxidation at 900 °C for 2 h. Figure 13 presents the setup used for applying a spinel coating by the electrophoretic deposition, together with example sample after coating deposition.

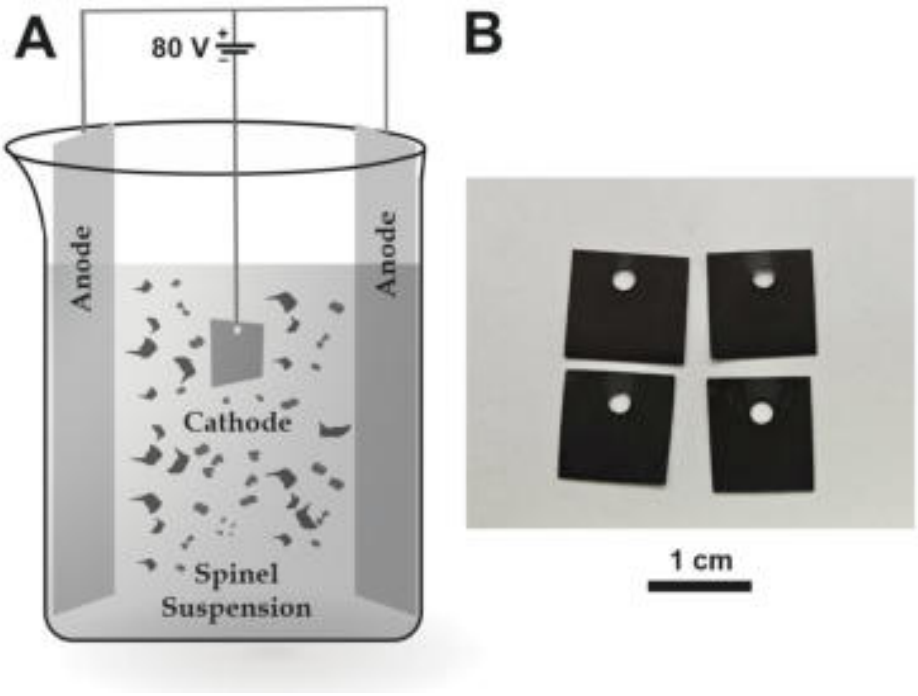


Figure 13. Sketch of deposition setup (A), and the example of Crofer 22 APU samples with deposited spinel layer (B) (Figure created by the author).

9.1.3. LSC oxygen electrode deposition

The $La_{0.6}Sr_{0.4}CoO_{3-\delta}$ precursor was synthesized via the ethylene glycol photopolymerization method. Metal nitrate salts were dissolved in distilled water with the addition of ethylene glycol, ethanol, and citric acid. To this solution, 0.05 wt% of the photoinitiator [2-hydroxy-4'-(2-hydroxyethoxy)]-2-m-ethylpropiophenone was introduced. The LSC oxygen electrode was subsequently deposited onto prepared CGO pellets using the spin-coating technique (Figure 14 and Figure 15). A droplet of the LSC precursor solution was applied to the substrate surface, and excess solution was removed by employing a three-step rotational speed program. After each coating step, thermal treatment was carried out on a hot plate at 400 °C to ensure layer stabilization. Finally, the coated pellets were annealed in a furnace at temperatures ranging from 400 to 1000 °C.

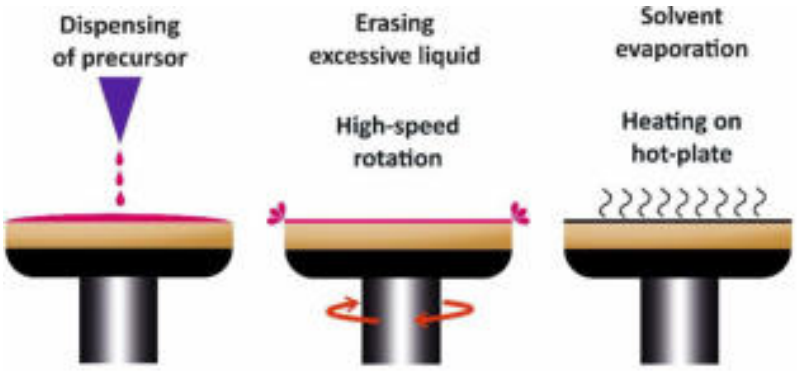


Figure 14. Graphic visualization of the process of deposition of ceramic layers by spin-coating technique (Figure created by the author).

9.1.4. PrO_x oxygen electrode deposition

Oxygen electrode layers based on PrO_x were fabricated analogously to LSC using the spin-coating method (as shown in Figure 14 and 15). The precursor solution was prepared from praseodymium nitrate dissolved in distilled water and 2-butoxyethanol (1:1 volume ratio), with citric acid added at a metal-to-ligand molar ratio of 1:2. Additionally, 5 wt.% ethanol was introduced into the mixture. The solution was heated on a hot plate at 100 °C under continuous stirring for ~15 min to evaporate most of the water and ethanol, thereby reducing the solution volume by half. To assess the influence of application cycles on the resulting layer thickness, samples were produced with 1–4 coating cycles. After deposition, the samples were annealed in a box furnace at 400–900 °C for 2 h.

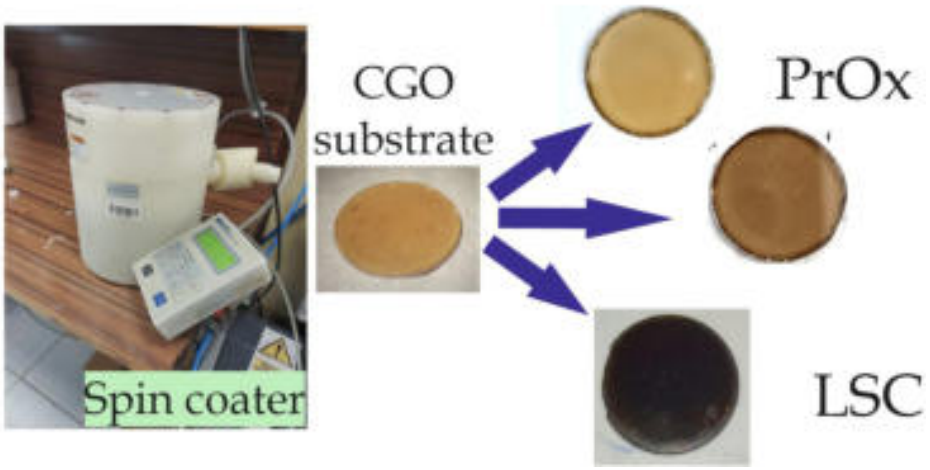


Figure 15. Spin coater used to deposit PrOx layers on YSZ, CGO, and LSC substrates, along with the sample before and after deposition (Figure created by the author).

9.1.5. Oxygen electrode prepared by infiltration CGO by LSC, PrOx and LSC:PrOx composite.

Polymeric precursors for infiltration were prepared using the Pechini method. Nitrates of the selected cations were dissolved in distilled water at a total molar concentration of 0.2 M and in the required stoichiometric ratio. Ethylene glycol was then added to initiate polymerization, and the solution was heated to 80 °C on a hot plate under continuous stirring until complete water evaporation. The end of this process was determined by monitoring the reduction in solution mass relative to the initial water content. A porous backbone with ~50% porosity was subsequently prepared. For this purpose, a slurry was formulated for wet-powder spraying, consisting of toluene and ethanol (toluene:ethanol ratio of 1:4), a binder (Heraeus), and CGO powder (3 wt.%). The slurry was applied to CGO pellets placed on a hot plate at 250 °C using an airbrush (Paasche VLS). The sprayed samples were sintered at 1150 °C for 2 h to ensure sufficient mechanical stability and strong adhesion between the dense electrolyte surface and the porous backbone. Infiltration was performed by immersing the pellets with the porous backbone into the prepared precursor solution (1 cm^3) and evacuating the trapped air in a vacuum chamber (0.08 Pa) for 10 min. The samples were pre-annealed on a hot plate at 400 °C, followed by final annealing in a muffle furnace at 600 °C for 2 h.

9.2. Measurement methods

9.2.1. Structural studies

9.2.1.1. X-ray diffractometry - XRD

One of the fundamental and most frequently employed structural characterization techniques in this doctoral dissertation was X-ray diffraction (XRD). The method is based on the interaction of X-ray photons (energy ~125 eV–125 keV; wavelength $\lambda \approx 0.01–10$ nm) with matter, where several interaction processes may occur. X-rays are scattered primarily by electrons, as scattering by the atomic nucleus is negligible. Two types of scattering can be distinguished:

- Elastic scattering (Thomson scattering) – the energy of the incident and scattered photons remains equal. This process is responsible for diffraction.
- Inelastic scattering (Compton scattering) – the scattered photon has lower energy than the incident photon.

The diffraction phenomenon is described by Bragg's law, which relates to constructive interference of X-ray beams reflected from crystallographic planes and reaching the detector. A schematic representation of Bragg's law is shown in Figure 16. and can be expressed as:

$$n\lambda = 2d \cdot sin\theta \tag{8}$$

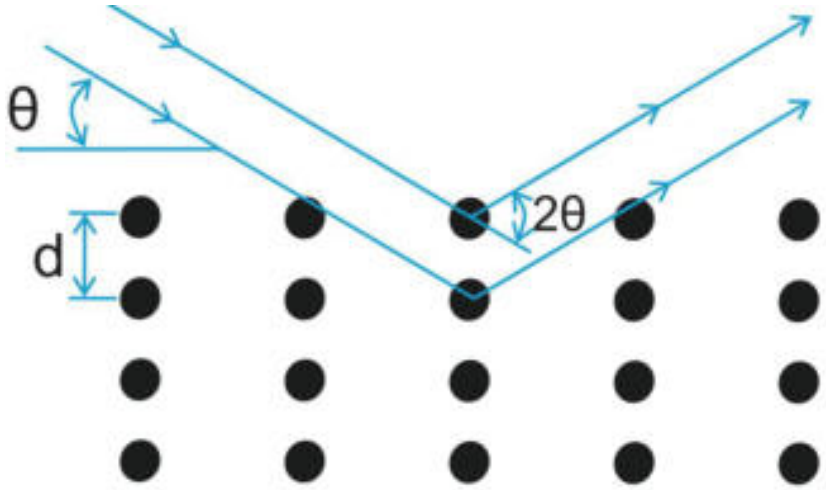


Figure 16. Bragg's Law (Figure created by the author).

where n is the order of reflection, λ is the X-ray wavelength, d is the interplanar spacing, and θ is the diffraction angle. As part of this research, samples were analysed using four different diffractometers and under various configurations:

- Parallel beam and GIXRD measurements were performed on a Bruker D2Phaser diffractometer equipped with a Lynxeye XE-T detector and Cu Kα radiation (λ = 0.15406 nm). Measurements performed at Gdańsk University of Technology and Warsaw University of Technology.
- High-temperature powder diffraction analyses were carried out on a Philips X'Pert Pro diffractometer equipped with an X'Celerator detector. Ni-filtered Cu

Kα radiation was employed, with λ_1 = 1.54056 Å and λ_2 = 1.54439 Å. Measurements at elevated temperatures were conducted using an Anton Paar HTK 1200 high-temperature chamber. A LaB_6 standard was used for calibration. Measurements performed at Warsaw University of Technology.

- High-temperature XRD measurements of oxygen electrode layers were performed on an X'Pert Pro MPD diffractometer (Malvern Panalytical) equipped with a Pixcel 1D detector. Cu Kα radiation was used as the source, with the setup including a Cu X-ray tube, β-filter, and a monochromator optimized for Cu radiation. Measurements performed at Tampere University, Finland.

9.2.1.2. X-ray photoelectron spectroscopy - XPS

X-ray photoelectron spectroscopy (XPS) is a versatile technique applicable to a vast range of materials. It enables semi-quantitative determination of the elemental composition, chemical states, and electronic structure of the sample surface, with a maximum information depth not exceeding ~10 nm. In XPS, atoms within the sample are excited by a beam of low-energy monochromatic X-ray radiation. The absorbed energy causes emission of electrons from inner shells (depending on the photon energy), and the kinetic energy of the emitted photoelectrons is measured by an analyser (Figure 17). Typically, the energy range analysed lies between 10 and 2000 eV. Each atom (with the exception of hydrogen) possesses core electrons that do not directly participate in chemical bonding. However, their binding energy is sensitive to the local chemical environment. Since the binding energy of a core electron is characteristic of a given element and orbital, knowledge of the incident photon energy allows conversion of the measured photoelectron kinetic energy into the corresponding binding energy. These binding energies are tabulated, which makes spectral interpretation straightforward once the sample composition is known. An XPS spectrum consists of distinct peaks corresponding to specific photoelectrons, superimposed on a background of inelastically scattered electrons. Shifts in binding energies provide valuable chemical-state information and can be explained, for example, by differences in

electronegativity between bonding atoms. When an atom of higher electronegativity is bonded to one of lower electronegativity, electron density shifts toward the more electronegative element, reducing valence electron screening. This effect manifests as a shift of the core-level peaks to higher binding energies. Furthermore, variations between single and multiple bonds can also be detected through such shifts.

In this study, XPS measurements were performed using a Thermo Fisher Scientific Escalab 250Xi spectrometer equipped with a monochromatic Al Kα X-ray source. Spectral deconvolution and peak fitting were conducted with the integrated Avantage software package (Thermo Fisher Scientific). Measurements performed at Gdańsk University of Technology.

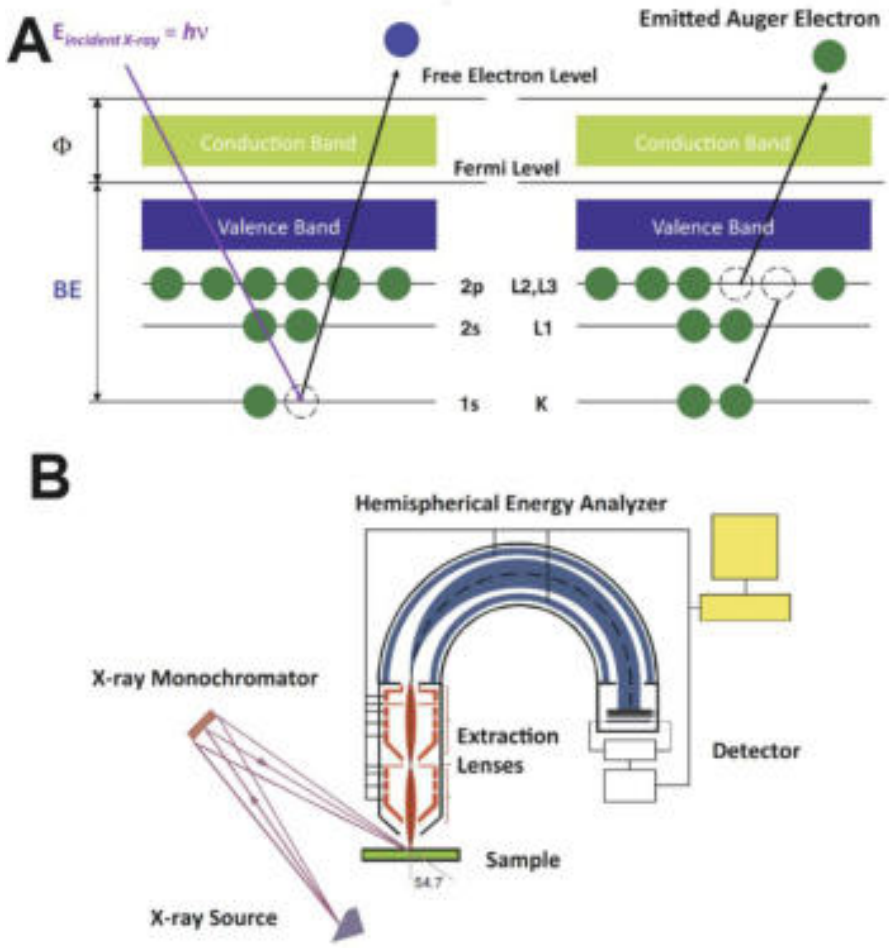


Figure 17. Scheme of photoelectron and Auger electron process (A) and the construction of modern XPS (B) [196].

9.2.1.3. X-ray Absorption Spectroscopy XAS

X-ray absorption spectroscopy (XAS) is based on the interaction of synchrotron radiation with matter. This technique enables the investigation of the local atomic and electronic structure of nearly all elements (with the exception of those lighter than Li). XAS provides insight into the energy distribution of unoccupied electronic states as well as the local chemical environment of the absorbing atom. Importantly, the method can be applied not only to crystalline but also to amorphous materials—a capability that only few other techniques offer. Key advantages of XAS include its high element selectivity, very high sensitivity (down to 10–100 molecules per mole), short acquisition times, and the small amount of sample required (typically on the order of tens of milligrams). In transmission mode, a sample is placed in the measurement chamber and analysed by recording the initial current intensity (I_0) and the current intensity after the beam go through the sample (I_x). The absorption coefficient μ(E) is then calculated as a function of energy according to the equation:

$$\mu(E) = -\ln\left(\frac{I_x}{I_o}\right) \tag{9}$$

Depending on the element of interest and the energy range, samples may be prepared in different forms: for soft XAS, material is typically deposited on a conductive substrate such as a carbon tape or Kapton tape, while for hard XAS, samples are commonly pressed into pellets with cellulose. Besides transmission, measurements can also be performed in fluorescence mode, which detects photons emitted during radiative recombination of the excited atom to its ground state. The X-ray Absorption Fine Structure (XAFS) comprises oscillations in the absorption coefficient observed above the absorption edge (1000–1500 eV beyond). The XAFS spectrum is divided into two regions:

- XANES (X-ray Absorption Near Edge Spectroscopy), extending from the absorption edge to ~50 eV above it,
- EXAFS (Extended X-ray Absorption Fine Structure), extending up to ~1000 eV above the edge.

XANES can be analysed experimentally, by comparison with reference spectra, or theoretically, through calculations of local densities of states and multiple scattering in real space. Experimentally, the shift of the absorption edge to higher energies allows estimation of the average oxidation state of the absorber. Moreover, linear combination fitting enables identification and quantification of the basic components of a material.

EXAFS provides complementary structural information, particularly valuable for amorphous systems, disordered phases, and low-dimensional impurities. Its greatest strength lies in its element selectivity, which allows reconstruction of the local atomic environment even at low concentrations. EXAFS oscillations originate from interference between the outgoing photoelectron wave and waves scattered by neighbouring atoms. When combined with crystallographic data, EXAFS modelling allows determination of interatomic distances, coordination numbers, and bond angles, enabling detailed comparison across materials. Furthermore, the application of wavelet transforms permits separation of contributions from atoms at similar distances (e.g., impurities) in two dimensions, offering refined insight into subtle structural differences, such as variations in bond lengths between impurity and host atoms.

For this PhD dissertation, XAS/XAFS experiments were conducted at the PIRX and ASTRA beamlines (Figure 18.) of the SOLARIS National Synchrotron Radiation Centre as part of the Jagiellonian University in Kraków. Spectral analysis was carried out using the Athena and Artemis software packages as well as PyMCA [197]. Crystallographic data employed for fitting Fourier-transformed (FT) spectra were obtained from the Crystallography Open Database (COD). FEFF input files for Artemis were prepared via the WebAtoms platform. Additionally, atomic distribution intensity maps were generated using wavelet transform analysis with Hama Fortran software [198].

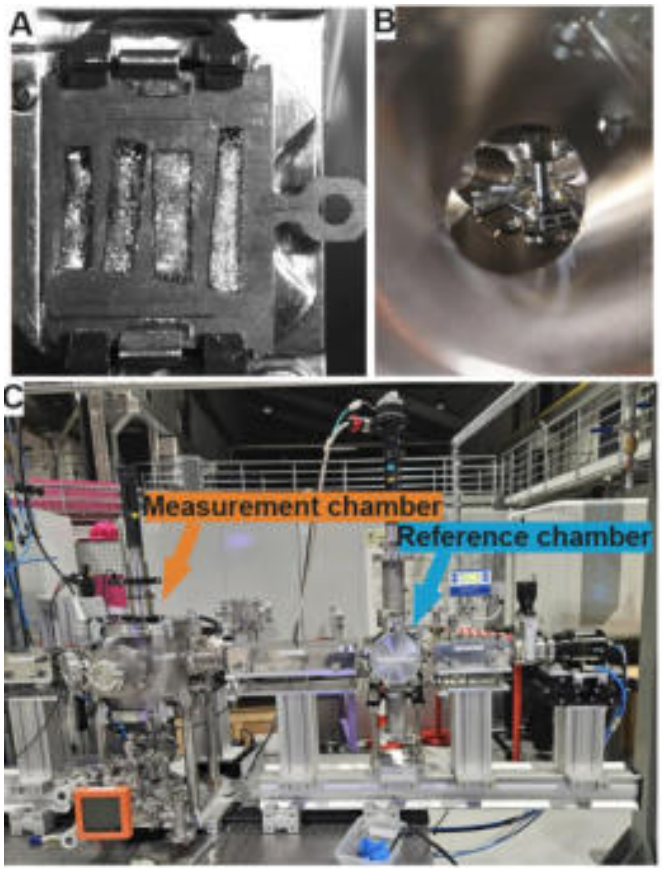


Figure 18. an Omicron plate with powders of the reference materials applied (A), a loading station with plates on the PIRX beamline (B) and the end part of the ASTRA beamline with the marking of the measurement and reference chamber (C) (Figure created by the author).

9.2.1.4. Raman Spectroscopy

Raman spectroscopy is based on the Raman effect, which arises from the inelastic scattering of electromagnetic wave. In this process, the energy of the scattered photons differs from that of the incident photons, with the difference corresponding to the energy absorbed or released through collective atomic vibrations—phonons in solids or normal vibrational modes in molecules, liquids, and gases. Since vibrational states are intrinsically linked to the atomic structure of a material, Raman spectroscopy serves as an effective tool for structural and chemical characterization, in a manner complementary to infrared (IR) spectroscopy. Raman scattering is typically very weak, with an intensity 9–20 orders of magnitude lower than incident beam intensity. It can be described as light emitted by oscillating electric dipoles induced in the material by the excitation source. When the scattered photons have lower energy than the incident photons, the effect is termed Stokes scattering; when

they have higher energy, it is called anti-Stokes scattering (Figure 19). In principle, photons with energies exceeding those of the vibrational modes can be inelastically scattered. If the excitation photon energy approaches that of an electronic transition, resonant Raman scattering may occur, greatly enhancing the intensity. The positions and intensities of Raman peaks are directly related to the symmetries of lattice vibrations and are characteristic for specific compounds. Major advantages of Raman spectroscopy include its (typically) non-destructive nature, high sensitivity to lattice symmetry and structural defects, and the ability to distinguish phases that may yield nearly identical XRD patterns.

As part of this PhD research, Raman spectra were recorded using an inVia spectrometer equipped with an optical microscope and motorized sample stage. A 532 nm diode laser was focused onto the sample through a 50x objective, yielding a spot size of ~1.5 μm, with a power of 3.2 mW at the surface. The Raman signal was dispersed with a diffraction grating of 2400 grooves·mm^{-1}, and spectra were collected using a Peltier-cooled CCD detector (1024 x 256 pixels). Measurement performed at Kaunas University of Technology.

In situ high-temperature measurements were performed using a Renishaw inVia Reflex spectrometer equipped with an 1800 lines·mm^{-1} grating. A 532 nm excitation laser was focused onto the sample through a 50x objective, with laser power limited to ~5 mW to minimize local heating. Measurements were conducted under a constant flow of dry synthetic air, while the sample was heated from 25 °C to 900 °C using a Linkam temperature-controlled stage. Measurement performed at Warsaw University of Technology.

Confocal Raman imaging was carried out using a WITec alpha 300 M+ spectrometer with a 488-nm laser line for Raman confocal imaging. Measurements were taken on pre-prepared cross sections using a ZEISS Epiplan-Neofluar 100× objective with an NA of 0.9 and a 600-grating spectrometer (spectral resolution of approximately 3 cm^{-1}). Areas of constant

width (5 μm) were scanned, and their height (from 8 to 13 μm) depended on the scale/coating thickness. Measurement performed at AGH University of Science and Technology.

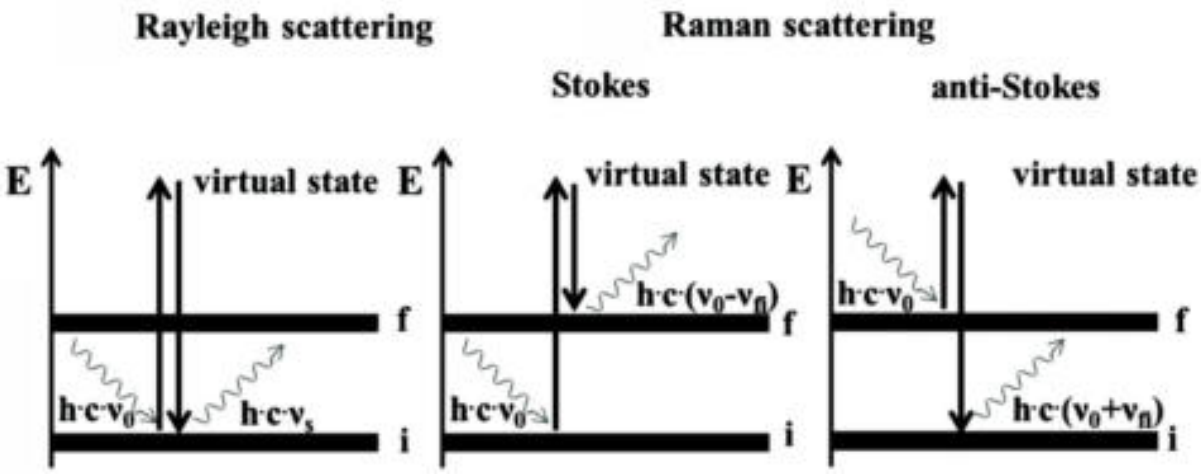


Figure 19. Energy level diagrams describing the physical phenomenon of Rayleigh scattering and Raman scattering [199].

9.2.1.5. Fourier Transform Infra-Red Spectroscopy – FTIR

FTIR is based on the analysis of the intensity of a radiation beam after it has passed through or been reflected from a sample. An example of the operating principle of an FTIR spectrometer is shown in Figure 20. The transmitted or reflected beam is compared with a reference beam that travels directly to the detector. Interaction of the sample-modified beam with the primary beam produces an interference pattern, which is subsequently processed by Fourier transform to obtain the relationship between radiation intensity and wavelength. The standard spectral range used in IR spectroscopy is 4000–400 cm^{-1} (corresponding to 2–16 μm). When molecules are excited to specific vibrational states, they absorb energy at characteristic frequencies, leading to a reduction in the intensity of the transmitted beam. Different functional groups absorb at distinct frequencies, reflecting the stretching or bending vibrations of their chemical bonds. This technique is most widely applied in the identification of functional groups and chemical bonds in organic compounds, in the structural characterization of inorganic materials, and in the monitoring of chemical processes.

In this study, Fourier transform infrared spectra were recorded at room temperature using a VERTEX 70 spectrometer. Measurements were performed in Kubelka–Munk mode at the Institute of Materials Science, Kaunas University of Technology.

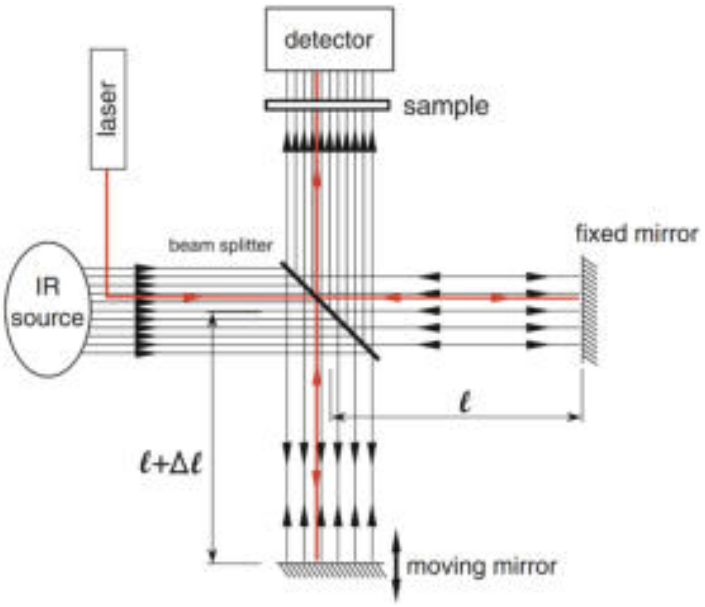


Figure 20. Schematic representation of the operating principle of an FTIR spectrometer using a Michelson interferometer [196].

9.2.1.6. Scanning Electron Microscopy with Energy Dispersive Spectroscopy - SEM-EDS

Scanning electron microscopy (SEM) is a high-resolution imaging technique that enables detailed observation of sample surfaces and topography, with magnifications reaching several hundred thousand times. Instead of visible light, SEM employs a focused beam of electrons with defined energy directed onto the sample surface. The interaction of the primary electron beam with the specimen excites the material, with a penetration depth that depends on the incident beam energy and may reach several micrometres. Imaging is achieved by detecting electrons emitted or reflected from the sample. Depending on the detection mode, different signals are collected. A backscattered electron detector (BSD) records elastically scattered, high-energy electrons, providing contrast sensitive to atomic number. A secondary electron detector (SED) captures low-energy inelastically scattered electrons, which typically originate from the near-surface region, making it particularly

useful for resolving fine surface details. The principle of SEM-EDS is shown in Figure 21.

Energy-dispersive spectroscopy (EDS) complements SEM by detecting the characteristic X-ray radiation emitted when excited atoms relax to lower energy states. The energy of the emitted X-rays is element-specific, enabling both qualitative and quantitative chemical analysis. EDS allows determination of elemental composition, concentration of specific elements, and their spatial distribution. Various acquisition modes are available, including point analysis, line scans, and two-dimensional elemental mapping, thus providing comprehensive microstructural and chemical information.

In this research, SEM–EDS analyses were carried out on multiple instruments. Measurements were performed at the Gdańsk University of Technology (ETI and FTIMS faculties) as well as at the AGH University of Science and Technology, Faculty of Metals Engineering and Industrial Computer Science.

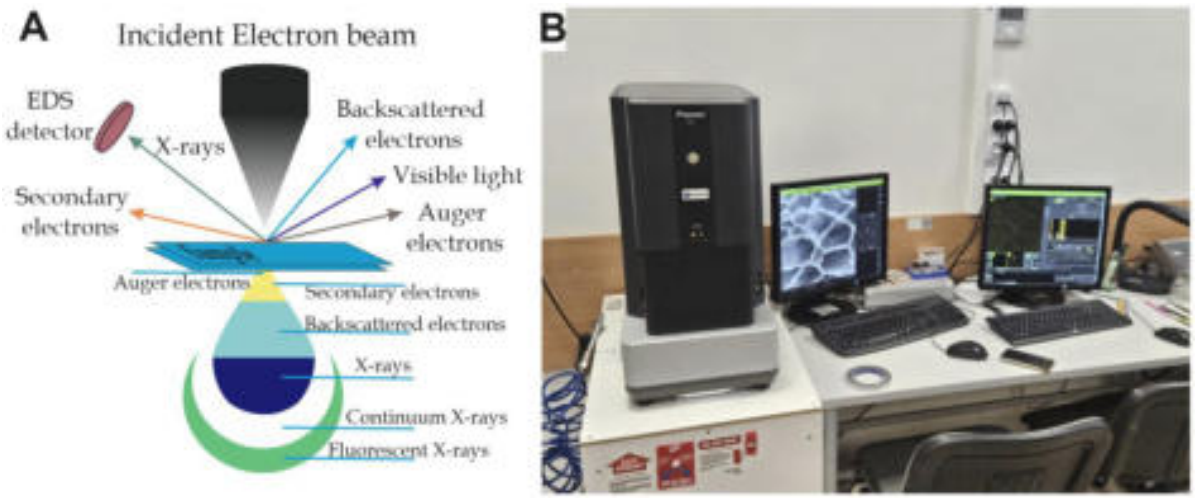


Figure 21. Principal function of the SEM-EDS analysis technique (A). Based on work [200]. *A stand with a Phenom XL microscope, which is part of the equipment of Gdańsk University of Technology, that where a significant part of the performed microscopic analyses (B) (Figure created by the author).*

9.2.2. Thermogravimetric measurements in high-temperature corrosion

High-temperature corrosion of metallic interconnects represents a critical challenge, as it directly affects the long-term durability of protective coatings. Verification of corrosion resistance is therefore essential. At elevated

temperatures, oxidation reactions proceed more rapidly due to enhanced reaction kinetics. In simplified form, the oxidation process may be expressed by the reaction:

$$Me + O_2 \rightarrow MeO_x \tag{10}$$

The kinetics of high-temperature oxidation are commonly studied by monitoring the change in sample mass, which corresponds to the uptake of oxygen relative to the total sample mass. Several kinetic models describe the growth behaviour of oxide scales. Linear law – assumes a linear increase in sample mass with time. This occurs when no protective oxide layer forms, and the chemical reaction proceeds unhindered. It may also indicate degradation or removal of the protective layer, exposing bare metal, or the formation of a porous oxide scale that allows easy access of oxygen to the metal surface. Parabolic law – typical of high-chromium steels such as Crofer alloys. It is based on the formation of a continuous and dense protective scale that separates the metal from the oxidizing environment. For further oxidation to occur, either oxygen must diffuse inward to the metal/oxide interface or metal cations must diffuse outward to the oxide/gas interface—or both. The parabolic rate law can be expressed as:

$$\left(\frac{\Delta m}{A}\right)^2 = k_p \cdot t + C \tag{11}$$

Where: Δm is the weight gain (g), A is the sample area (cm^2), k_p is the parabolic rate constant ($g^2 \cdot cm^{-4} \cdot s^{-1}$), t is the oxidation time (s), and C is the integration constant ($g^2 \cdot cm^{-4}$)

Cubic law – applied to more complex processes that deviate from the ideal parabolic assumption, often due to simultaneous competing mechanisms. Logarithmic law – usually observed at low temperatures, where oxide growth slows down considerably as the film thickens. In addition to kinetic modelling, determination of the activation energy (E_a) of oxidation is a key aspect of describing corrosion processes. Since oxidation is a thermally activated reaction, its rate constant follows the Arrhenius-type dependence:

$$ASR = A \cdot \exp\left(-\frac{E_a}{kT}\right) \quad (12)$$

Where: ASR – Area specific resistance, A is a pre-exponential factor ($\Omega \cdot cm^{-2} \cdot K^{-1}$), E_a is the activation energy ($kJ \cdot mol^{-1}$), k is Boltzmann's constant ($J \cdot K^{-1}$) and T is the temperature (K).

9.2.3. Electrical and electrochemical measurements

9.2.3.1. Electrical conductivity measurements

Electrical conductivity measurements, expressed in terms of area-specific resistance (ASR), provide insight into the electrical properties of samples, particularly with respect to oxide scale growth during high-temperature corrosion. For Crofer 22 APU steel, the relevant layer is chromium oxide, whose conductivity at 750 °C does not exceed 0.02 $S \cdot cm^{-1}$ [201]. As the oxide layer grows thicker—or becomes less conductive—the ASR value increases significantly. The ASR parameter can be calculated using the relation:

$$ASR = \frac{R \cdot A}{2} \quad (13)$$

where R is the measured resistance of the sample, and A is the active area, typically defined by the current collector (in this case, platinum). Because the bulk steel substrate and protective coatings are highly conductive, the main contribution to the measured resistance originates from the chromium oxide scale formed during corrosion.

In this work, ASR measurements were performed using a compression cell, in which platinum wires were connected to a gold mesh in direct contact with the sample as shown in Figure 22. Electrochemical impedance spectroscopy (EIS) was conducted in a four-electrode configuration at a fixed frequency of 1 Hz and an amplitude of 1 mA. At this frequency, the imaginary component of the spectrum was negligible (3–4 orders of magnitude lower than the real component). Measurements were performed across various temperature ranges, with the furnace temperature controlled by a PID regulator equipped with feedback from an internal thermocouple placed near the sample. The experiments were carried out using a Gamry Interface 1000 potentiostat and

a Vertex.5A potentiostat (Ivium Technologies). The measurements was performed at Gdańsk University of Technology.

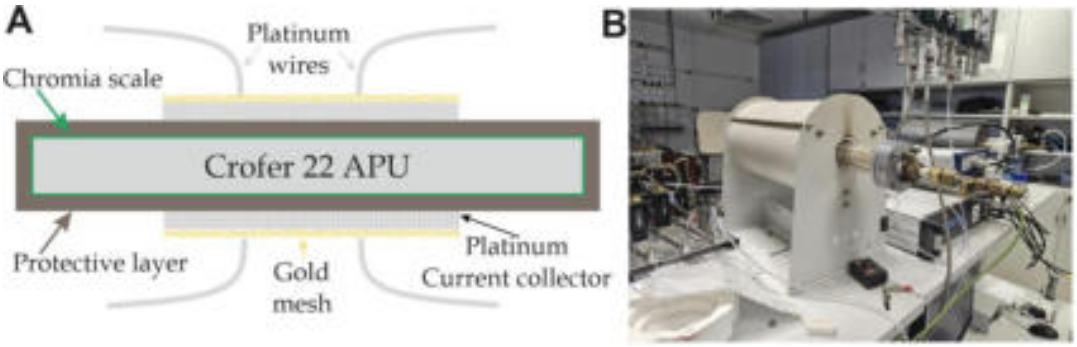


Figure 22. ASR measurement diagram for Crofer 22 APU steel samples after corrosion tests (A) and a measuring station for ASR measurements at the Gdańsk University of Technology (B) (Figure created by the author).

9.2.3.2. DC conductivity measurement using the Van der Pauw method

Van der Pauw (VdP) measurements are employed to determine the resistivity and Hall coefficient of a material. The resistivity measurement enables the calculation of the material's conductivity according to the Van der Pauw formalism. A major advantage of this method is its applicability to samples of arbitrary shape. The only requirement is that the sample be effectively two-dimensional—that is, its thickness must be much smaller than its lateral dimensions. The measurement setup (Figure 23) consisted of a ceramic measurement cell with a flat stage on which the sample was placed. The samples were positioned inside a tube furnace to allow temperature-dependent measurements. Electrical contacts were made at four peripheral points of the sample using platinum wires attached with silver paste. To ensure accuracy, the contact areas were kept as small as possible, as required by the VdP method. The four-point geometry allows for the determination of the average resistivity. The system enabled both current-controlled and voltage-controlled operation—either applying a potential and measuring the resulting current or vice versa. For the present work, potential control was selected, with an applied bias of 1 V. The measurement procedure involved applying a potential between two adjacent contacts (e.g., V_{34}) while measuring the

current through the opposite pair (e.g., I_{12}). The resistance was then calculated according to Ohm's law:

$$R_{12,34} = \frac{V_{34}}{I_{12}} \tag{14}$$

To obtain the material's conductivity, measurements were performed in four different contact configurations. From these, the characteristic resistances (R_1 and R_2) were determined and subsequently used in the Van der Pauw equation to calculate the sample conductivity:

$$f\left(\frac{R_1}{R_2}\right) = 1 - \left(\frac{R_1 - R_2}{R_1 + R_2}\right)^2 \cdot \frac{\ln 2}{2} - \left(\frac{R_1 - R_2}{R_1 + R_2}\right)^4 \cdot \left(\frac{(\ln 2)^2}{4} - \frac{(\ln 2)^3}{12}\right) \tag{15}$$

$$\sigma = \frac{2 \ln 2}{\pi d (R_1 + R_2) \cdot f\left(\frac{R_1}{R_2}\right)} \tag{16}$$

where: f is the correlation function, σ is the electrical conductivity ($S \cdot cm^{-1}$), and d is the thickness of the measured sample (cm). One important assumption is that the values of R_1 and R_2 should be as close to each other as possible. Ideally, they should be identical. The measurements was performed at Gdańsk University of Technology.

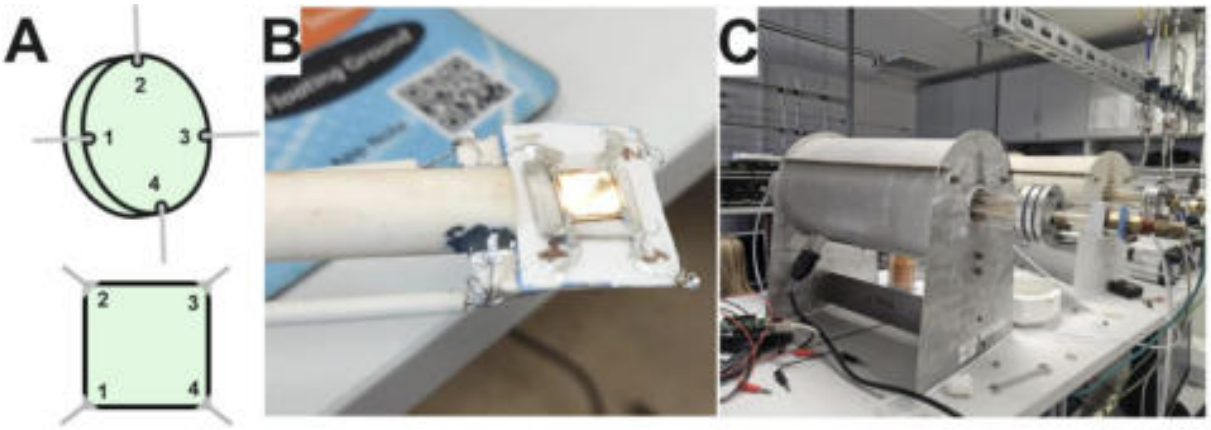


Figure 23. Schematic diagram of the sample and electrical connections on which conductivity was measured (A) and a photo of the measurement system with the sample - PrO_x layer deposited on fused silica (B), and a measuring station for Van der Pauw measurements at the Gdańsk University of Technology (C) (Figure created by the author).

9.2.3.3. Electrochemical impedance spectroscopy

Electrochemical impedance spectroscopy (EIS) is based on perturbing a electrochemical system with a sinusoidal excitation signal (either potential or alternating current) over a wide frequency range (in this work, typically from 3 MHz to 50 mHz). The technique provides kinetic and mechanistic insight into electrochemical systems and enables the identification of contributions from processes such as gas diffusion, charge transfer reactions, ion adsorption, mass transport, passive layer resistance, and ionic conductivity (particularly relevant in SOCs studies). It also allows determination of double-layer capacitance, among other parameters. The basic relations in EIS can be expressed as:

$$E(t) = E_0 \cdot \cos(\omega t) \tag{17}$$

$$I(t) = I_0 \cdot \cos(\omega t + \varphi) \tag{18}$$

$$Z = \frac{E(t)}{I(t)} = Z_0 \cdot \frac{\cos(\omega t)}{\cos(\omega t + \varphi)} \tag{19}$$

where: E(t) – excitation signal (V); E_0 – signal amplitude (V); ω – angular frequency (Hz); I(t) – current response (A); I_0 – response amplitude (A); ϕ – phase shift; Z – impedance (Ω); Z_0 – impedance modulus (Ω).

Measurement data are typically presented in two forms: Nyquist plots, which display impedance in the complex plane with the real part on the X-axis and the imaginary part on the Y-axis, plotted as a function of frequency and Bode plots, which show impedance modulus and phase shift versus frequency.

All experiments were performed in a four-electrode configuration. In symmetrical cell measurements, both electrodes consist of the same material, allowing elimination of contributions from other cell components (e.g., electrolyte) and enabling precise evaluation of electrode properties. This configuration minimizes asymmetry effects and simplifies interpretation, providing reliable insight into material behaviour. However, the drawback is that such measurements do not replicate the operation of a full cell. A typical impedance spectrum of a symmetrical cell (below ~500 °C) contains three polarization contributions and two ohmic component (Figure 24). The ohmic

resistance (series resistance) corresponds mainly to the electrolyte resistance and at high temperatures can be determined from the intercept of the spectrum with the X-axis. At lower temperatures, additional contributions from the electrolyte complicate the analysis. The polarization resistance represents the overall resistance of processes occurring at the electrode. The first semicircle, visible at high frequencies, corresponds to grain (bulk) resistance (R_g) within the electrolyte. The second semicircle, at intermediate frequencies, is associated with grain boundary resistance (R_{gb}). The third semicircle, observed at intermediate to low frequencies, reflects processes at the oxygen electrode, including gas exchange and ion transport. The spectra were fitted using the equivalent circuit model. To standardize the results, the measured resistances were normalized to the electrode surface area using the following relations:

$$R_{pol} = \frac{R_p \cdot A}{2} \tag{20}$$

$$R_{ohm} = R_s \cdot A \tag{21}$$

where: R_{pol} –calculated polarization resistance; R_p – measured polarization resistance; R_{ohm} – ohmic resistance; R_s – measured ohmic resistance; A – electrode surface area.

In this study, symmetrical measurements were carried out in the temperature range of 300–600 °C under standard conditions (pO_2 = 20%) using synthetic air. Additional experiments examined the effect of electrode thickness and annealing temperature, as well as the influence of varying pO_2, pCO_2, and pH_2O. The measurements was performed at Gdańsk University of Technology.

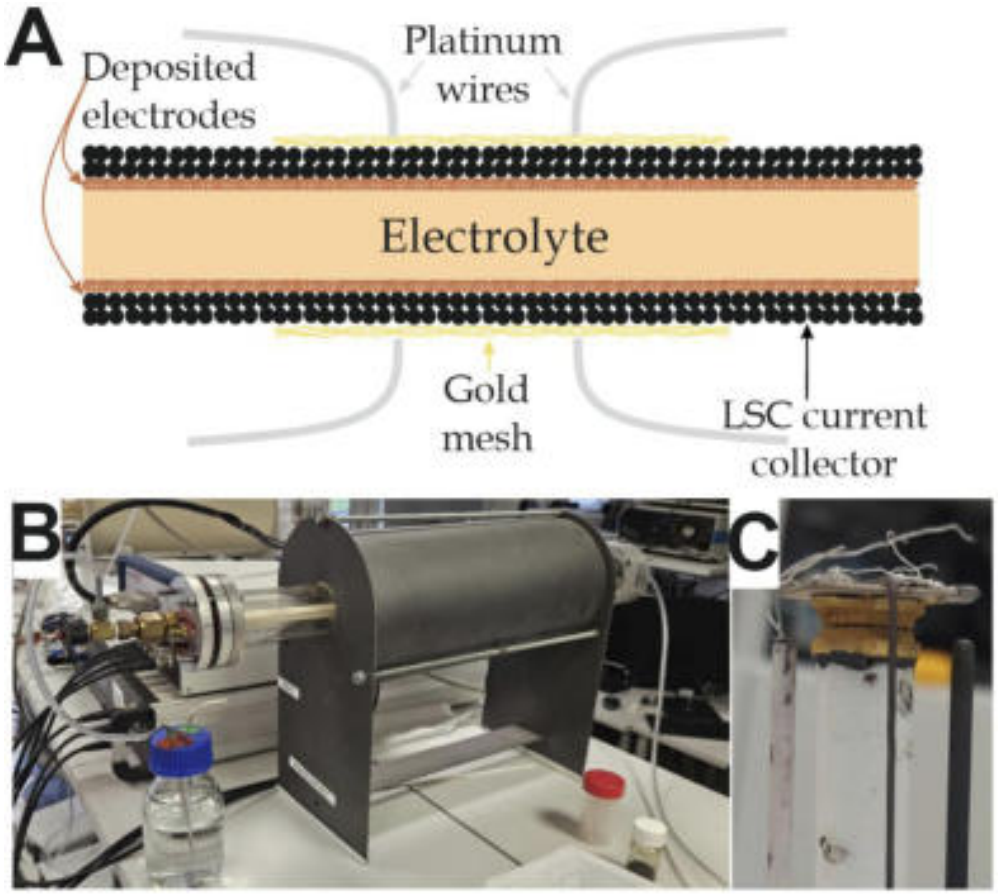


Figure 24. Graphic diagram of the sample for symmetrical measurements and the measurement system (A) and a measuring station for EIS measurements at the Gdańsk University of Technology (B) along with a photo of the compression cell where the measurement samples are placed (C) (Figure created by the author).

9.2.3.4. Distribution of relaxation times – DRT

Distribution of relaxation times (DRT) analysis assumes that the overall impedance response can be represented as an infinite series of resistive–capacitive relaxation processes, described by a time-domain distribution function γ(ln τ). The impedance corresponding to this distribution is expressed as:

$$Z_{DRT} = R_{\infty} + \int_{-\infty}^{\infty} \frac{\gamma(\ln \tau)}{1 + i2\pi f\tau} d(\ln \tau) \tag{22}$$

where: R_{∞} is the high-frequency intercept, f is the frequency, and τ is the relaxation time.

The DRT method enables separation of overlapping electrochemical processes that may not be clearly distinguishable in a classical Nyquist plot. Nevertheless, careful interpretation is required, since the number of peaks associated with distinct processes does not always match the expected

values, as peak overlap can occur—analogous to limitations encountered with equivalent circuit modelling. To facilitate the analysis, dedicated software packages such as DRTtools can be employed [202]. These tools offer substantial flexibility in parameter selection and preprocessing, though caution must be exercised to avoid artifacts. In this work, DRT analysis proved particularly valuable for interpreting impedance spectra obtained under varying pO_2 conditions, as it enabled identification of specific electrochemical processes occurring within the studied materials.

9.2.3.5. Fuel cell characterisation

To evaluate the proposed solutions, a series of solid oxide fuel cells was prepared using Elcogen half-cells. A CGO layer was deposited onto each half-cell by spray pyrolysis, followed by deposition of the oxygen electrode using the spin-coating technique. Electrochemical performance of the assembled fuel cells was assessed with the Open Flanges V5 test configuration (Figure 25). Power density was determined according to the relation:

$$P = U \cdot I \tag{23}$$

where P is the power density ($W \cdot cm^{-2}$), U is the measured cell voltage (V), and I is the current density ($A \cdot cm^{-2}$). The current density and the effective active area were calculated based on the measured surface area of the oxygen electrode. Electrical interconnection was achieved by placing a nickel mesh on the fuel electrode side and a gold mesh on the oxygen electrode side. The cell was mounted in a furnace equipped with a temperature controller with feedback regulation. All electrochemical measurements, including impedance spectroscopy and current–voltage (I–V) characterization, were performed using an Ivium Vertex.2A potentiostat. The measurements was performed at Gdańsk University of Technology.

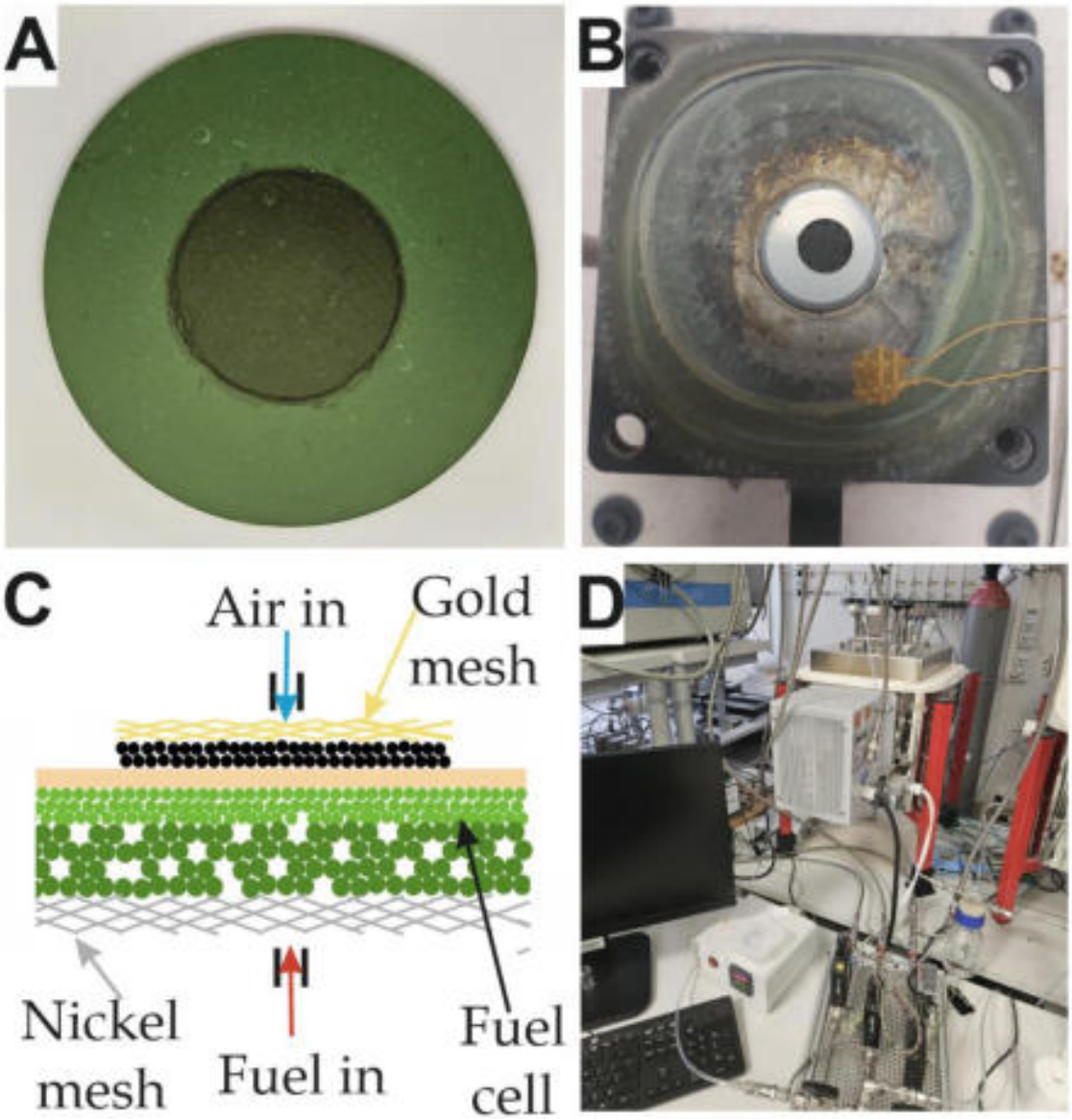


Figure 25. Prepared fuel cell with applied oxygen electrode (A), Fiaxell Open Flanges V5 test configuration with the cell after measurements (B) and cell connection diagram (C) and a measuring station for cell measurements at the Gdańsk University of Technology (D) (Figure created by the author).

10. List of publications included in the dissertation

This chapter contains scientific publications that were developed and published as part of PhD studies. Each publication is preceded by an abstract and author statements detailing their contributions to the work.

Articles 1 and 2 address hypothesis 1, which concerns the development of protective coatings that can effectively block chromium diffusion using cobalt-free compounds. The first article describes the formation of rare-earth oxide layers and their corrosion properties after 2,000 hours of oxidation at 700 °C. Based on this article's conclusions, two of the most promising materials were used to produce bilayers in combination with spinel oxide – $CuMn_{1.7}Fe_{0.3}O_4$. This solution combines the advantages of each material: good corrosion resistance due to the presence of rare-earth oxide layers and the blocking of chromium diffusion, as well as lower area-specific resistance after long-term corrosion exposure (4000 h) owing to the higher electrical conductivity of spinel compared with MCO.

Publications related to the second hypothesis are numbered 3 to 5, describing research on oxygen electrodes in low-temperature solid oxide cells at temperatures ≤600 °C. Article no. 3 describes the potential applications of, and the structural and electrochemical comparisons between, partially amorphous and crystalline LSC. Article 4. describes a process of infiltration of a porous CGO backbone with materials such as LSC or PrO_x, and a composite of these two materials. The infiltration process reduces the mass of the active electrode material required. Article 5. describes the use of thin oxygen electrodes in the form of praseodymium oxide, which was deposited by spin-coating technique. It provides a comprehensive description of the properties of the complex praseodymium oxide system, taking into account phase transitions and optimising the utilisation parameters of the material. It also identifies factors that hinder the efficient electrochemical reaction.

Publications related to the proof of hypothesis 1:

Effective chromium diffusion-blocking protective coatings for metallic interconnects in intermediate-temperature solid oxide cells can be

developed by harnessing the synergistic effects of rare-earth oxides and the cobalt-free spinel $CuMn_{1.7}Fe_{0.3}O_4$ (CMFO).

1. **Lemieszek B**, Ignaczak J, Kamecki B, et al. Electrolytic deposition of reactive element thin films on Crofer 22 APU and evaluation of the resulting high-temperature corrosion protection properties at 700 °C–900 °C. Int J Hydrogen Energy, IF = 7.2 (2022), MSHE (Ministry of Science and Higher Education) points 140, Citations: 13

2. **Lemieszek B**, Ignaczak J, Lankauf K, et al. CuMn1.7Fe0.3O4 – RE2O3 (RE = Y, Gd) bilayers as protective interconnect coatings for solid oxide cells. J Eur Ceram Soc. 2024;44(15), IF = 6.2 (2024), MSHE points 140, Citations: 10

Publications related to the proof of hypothesis 2:

Electrochemical activity of oxygen reduction reaction in low-temperature solid oxide cells operating at ≤600 °C can be enhanced through optimization of the fabrication process of oxygen electrodes based on mixed ionic-electronic conductors such as LSC ($La_{0.6}Sr_{0.4}CoO_{3-\delta}$) and PrO_x.

3. **Lemieszek B**, Ilickas M, Jamroz J, et al. Enhanced electrochemical performance of partially amorphous La0.6Sr0.4CoO3-δ oxygen electrode materials for low-temperature solid oxide cells operating at 400 °C. Appl Surf Sci. 2024;670. IF = 6.9 (2024), MSHE points 140, Citations: 8

4. Faruk Aksoy Ö, **Lemieszek B**, Murutoğlu M, Karczewski J, Jasiński P, Molin S. Developing high-performance oxygen electrodes for intermediate. Appl Phys A Mater Sci Process; IF = 2.8 (2024), MSHE points 70, Citations: 1

5. **Lemieszek B**, Alluhaibi L, Maximenko A, et al. Unveiling the Potential of Praseodymium Oxide as Efficient Oxygen Electrode for Low-Temperature Solid Oxide Cell Applications. *Chem Eng J*. 2026;531:173949. doi:10.1016/j.cej.2026.173949. IF = 13.2 (2024), MSHE points 200, Citations: 0

10.1. Electrolytic deposition of reactive element thin films on Crofer 22 APU and evaluation of the resulting high-temperature corrosion protection properties at 700 °C–900 °C

Authors: **Bartłomiej Lemieszek**, Justyna Ignaczak, Bartosz Kamecki, Jakub Karczewski, Mogens Bjerg Mogensen, Sebastian Molin, Piotr Jasiński

International Journal of Hydrogen Energy, vol. 47, issue 78, pages 33453-33465, 2022, https://doi.org/10.1016/j.ijhydene.2022.07.220

IF = 7.2 (2022), MSHE points 140, Citations: 13

In this study, thin rare-earth oxide ceramic layers – CeO_2, Gd_2O_3, La_2O_3, and Y_2O_3—were deposited on high-chromium Crofer 22 APU steel using electrolytic methods. The process was optimized to produce coatings about 100 nm thick. Even very short deposition times, 1 minute (and 10 seconds for La_2O_3), significantly improved high-temperature corrosion resistance, as shown by reduced weight gain after 250 hours of oxidation at 900 °C. Short-term tests at 700 °C and 800 °C, supported by ASR measurements, confirmed these results and showed a clear decrease in ASR, especially at the lower temperatures. At 900 °C, however, no clear ASR improvement was observed, likely due to the formation of thick oxide scales regardless of coating type.

After 2,000 hours of oxidation, the lowest weight gains were recorded for La_2O_3- and Y_2O_3-coated samples, followed by Gd_2O_3, while CeO_2 was the least effective, although still better than the uncoated reference. In terms of electrical performance, Gd_2O_3, La_2O_3, and Y_2O_3 showed the most promising results, whereas CeO_2 performed the worst, even below the reference sample. Post-corrosion crystallographic analysis revealed the formation of $GdMnO_3$ and $LaCrO_3$ for Gd_2O_3- and La_2O_3-coated samples, respectively, while no secondary phases were detected for CeO_2 and Y_2O_3 beyond their primary oxides.

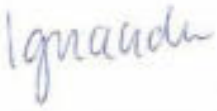
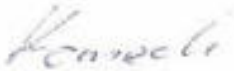
A key outcome of this work was the nearly 40% reduction in weight gain for Y_2O_3- and La_2O_3-coated samples, despite the coatings being only ~100 nm

thick. Moreover, the ASR values decreased by up to a factor of four compared with the uncoated reference sample.

The novelty of this work lies in investigating the corrosion properties of single metal oxide protective layers deposited onto Crofer 22 APU steel at 700 °C, a temperature range that remains insufficiently explored despite the availability of commercial cell solutions operating under such conditions.

My contributions to this study included preparing precursor solutions for the target coatings, performing layer deposition onto Crofer 22 APU steel, and calibrating the deposition process. I carried out both short- and long-term corrosion experiments at 700 °C, 800 °C, and 900 °C, and independently conducted weight-gain analyses. In addition, I performed significant part of SEM-EDS and ASR measurements. I was also responsible for analysing the obtained results, preparing figures, and writing the manuscript. As the corresponding author, I was responsible for article submission and for preparing responses to reviewer comments.

Declaration of co-authors on their contribution to the publication: "Electrolytic deposition of reactive element thin films on Crofer 22 APU and evaluation of the resulting high-temperature corrosion protection properties at 700 °C–900 °C".

Name and Surname	Contribution	Signature
Bartłomiej Lemieszek	Investigation: corrosion study, ASR, SEM, Methodology, Writing – original draft, Writing – review & editing,	
Justyna Ignaczak	Investigation - Corrosion study, Methodology, Writing – review & editing,	
Bartosz Kamecki	Investigation (XRD), Methodology, Writing – review & editing,	
Jakub Karczewski	Investigation (SEM), Methodology, Writing - review and editing	
Mogens Bjerg Mogensen	Methodology, Writing – original draft, Writing – review & editing,	
Sebastian Molin	Conceptualization, Methodology, Writing – review & editing, Writing – original draft, Supervision	
Piotr Jasiński	Conceptualization, Funding acquisition, Methodology, Writing – review & editing, Supervision.	

INTERNATIONAL JOURNAL OF HYDROGEN ENERGY 47 (2022) 33453–33465

Available online at www.sciencedirect.com

ScienceDirect

journal homepage: www.elsevier.com/locate/he

Electrolytic deposition of reactive element thin films on Crofer 22 APU and evaluation of the resulting high-temperature corrosion protection properties at 700 °C–900 °C

Bartłomiej Lemieszek [a,*], *Justyna Ignaczak* [a], *Bartosz Kamecki* [a], *Jakub Karczewski* [b], *Mogens Bjerg Mogensen* [c], *Sebastian Molin* [a], *Piotr Jasiński* [a]

[a] Advanced Materials Centre, Faculty of Electronics, Telecommunications and Informatics, Gdańsk University of Technology, Ul. G. Narutowicza 11/12, 80-233 Gdańsk, Poland

[b] Advanced Materials Centre, Faculty of Applied Physics and Mathematics, Gdańsk University of Technology, Ul. G. Narutowicza 11/12, 80-233 Gdańsk, Poland

[c] Department of Energy Conversion and Storage Electrochemistry, Technical University of Denmark, Fysikvej, Building 310, 2800 Kgs. Lyngby, Denmark

HIGHLIGHTS

- New technique of obtaining thin ceramic layers - electrolytic technique.
- Electrolytic deposition of cerium, gadolinium, lanthanum and yttrium oxide layers.
- Thin ceramic layers, on the order of tens of nanometers.
- Reduction of the thermogravimetric weight gain of samples covered with a ceramic layer.
- Electrical measurements showed that the surface-modified samples had lower resistance than the uncoated sample.

ARTICLE INFO

Article history:
Received 14 March 2022
Received in revised form
14 June 2022
Accepted 26 July 2022
Available online 20 August 2022

Keywords:
Ceramic layers
Electrolytic technique
Rare earth elements
Corrosion

ABSTRACT

This article presents electrolytic deposition of thin Rare Earth (RE) coatings on Crofer 22 APU stainless steel substrates for high temperature applications, such as interconnects in solid oxide cell stacks. The deposition of coatings based on yttrium-, gadolinium-, lanthanum-, and cerium nitrates is discussed. The high temperature corrosion properties of surface-modified steels were examined using thermogravimetry and electrical resistivity measurements. Coatings and oxide microstructures were examined by XRD and SEM of surfaces and cross-sections. The results showed that the use of the RE element oxide layers reduced the growth of oxide scale, as evidenced by lower weight gain. The layers based on Y- and Gd-oxides showed the best corrosion protection properties. The electrical measurements showed that the surface-modified samples had lower resistance than the uncoated sample.

© 2022 The Author(s). Published by Elsevier Ltd on behalf of Hydrogen Energy Publications LLC. This is an open access article under the CC BY license (http://creativecommons.org/licenses/by/4.0/).

* Corresponding author.
E-mail address: bartlomiej.lemieszek@pg.edu.pl (B. Lemieszek).

https://doi.org/10.1016/j.ijhydene.2022.07.220

0360-3199/© 2022 The Author(s). Published by Elsevier Ltd on behalf of Hydrogen Energy Publications LLC. This is an open access article under the CC BY license (http://creativecommons.org/licenses/by/4.0/).

Introduction

High-temperature corrosion of stainless steel interconnects is one of the main undesirable phenomena of solid oxide cells, limiting their long-term operation [1–3]. Current generation anode-supported Solid Oxide Cells (SOCs) operate at the 600–900 °C temperature range and therefore, surface oxide scale growth is inevitable during exposure of iron-chromium alloys at these temperatures. Due to the low electrical conductivity of the oxide, its growth results in an increase in the electrical resistance across the interconnects, leading to a decrease in the power output of the stack. The increase in resistance and deterioration of physical properties due to corrosion spurred the development of protective layers [4–6]. One type of protective coatings is thick and dense spinel layers that block chromium evaporation. These are mostly based on cobalt or cobalt-manganese oxides [7–10]. Our group has so far extensively studied thick Mn–Co oxide spinel-based coatings for the reduction of Cr-evaporation [11,12]. Another type of coating is very thin Rare Earth elements-based (RE) oxide coatings applied to decrease the rate of corrosion, e.g., cerium-, gadolinium-, lanthanum-, and yttrium oxide [13–17]. These two types of coatings can be combined to obtain synergistic effects [18,19]. The use of even very low RE oxide thickness (~10 nm) coatings is very beneficial in decreasing scale thickness [20,21].

Among the many ceramic deposition methods, the electrolytic technique seems well suited for the deposition of RE oxide thin layers on steel interconnects [22]. In comparison to the electrophoretic deposition process, where solid particles are deposited, the electrolytic method utilises metal salts (e.g. nitrates, chlorides) and solvents (ethanol or water) which, by electrochemical reaction, form deposits on the working electrode [23]. The thickness of the deposits can be controlled by the deposition voltage, time, and concentration of the solution. This method and similar cost-effective techniques have been previously used for the deposition of ceramic coatings in order to improve corrosion protection of steel at high temperature. Some works refer to coating process only, while some include also corrosion tests. Molin et al. presented results of the electrolytic deposition of a Y-based layer from a 0.05 M ethanol solution of yttrium nitrate together with the results of corrosion investigation. The corrosion rate of the yttria–coated Crofer 22 APU sheets at 750 °C was 20 times lower than that of uncoated samples [22]. Zhitomirsky et al. showed the results of coating nickel with the layer of yttrium oxide using precursor consisting of 0.02 M aqueous yttrium nitrate solution mixed with poly (diallyldimethylammonium chloride). During the process of cathodic electrodeposition at the current density of 10 mA cm-2, the layer of about 0.2 μm was obtained [24]. In another work, Zhitomirsky et al. proposed the deposition of the cerium oxide layer by electrolytic technique from 0.01 M cerium chloride solution dissolved in a 19:1 ethanol: water mixture. The deposition at the current density of 10 mA cm^{-2} resulted in the cerium oxide layer thickness of ~0.2–0.3 μm [25]. Yang et al. deposited 0.1–0.3 μm thick layer of cerium oxide using a solution consisting of 5 mM cerium chloride [26]. Mazur et al. proposed coating ferritic steel intended for interconnectors with gadolinium oxide nanoparticles using the electrolytic and immersion techniques. The obtained results indicate a reduction of oxidation rate of about 10 times at 700 °C [27]. Yoon et al. coated steel using the dip-coating technique, which allowed depositing 200–210 nm thick layers of lanthanum oxide. After the 500-h oxidation process at 700 °C, the presence of lanthanum-chromium and manganese-chromium spinels on the sample surface was proven [28]. Saeidpour et al. coated Crofer 22 APU steel with a composite of metallic cobalt and yttrium oxide using the electroplating method. After 500 h at 800 °C, weight gain was much higher for the coated samples than for uncoated one. However, the oxidation rate was greatly reduced, and the coated samples would perform much better in time. The initial greater weight gain was due to the rapid oxidation of cobalt [29]. As presented, RE oxides may be deposited by the cost-effective techniques and usually these layers lower the oxidation rate of the steel, however thorough corrosion protection studies of RE oxides still should be carried out.

This work is an investigation of promising thin RE oxide layers fabricated by electrodeposition. The results of the fabrication of thin ceramic films based on cerium-, yttrium-, gadolinium-, and lanthanum oxides and their effects on the resulting high temperature corrosion properties relevant for solid oxide cells are presented. The surface-modified samples were studied by thermogravimetry, electrical conductivity measurements, and post-mortem analyses (microscopy, diffractometry).

Experimental procedures

Commercial hydrated metal salts: $Gd(NO_3)_3 \cdot 6H_2O$ (Sigma Aldrich 99.9% purity, Saint Louis, United States of America), $Y(NO_3)_3 \cdot 6H_2O$ (Sigma Aldrich 99% pure, Saint Louis, United States of America), $Ce(NO_3)_3 \cdot 6H_2O$ (Honeywell Fluka, North Carolina, United States of America), and $La(NO_3)_3 \cdot 6H_2O$ (Sigma Aldrich 99.99%, Saint Louis United States of America) were used for the preparation of solutions in ethyl alcohol (Sigma Aldrich 99.8%, Saint Louis, United States of America) with a cation concentration of 2 mM. The solution was semi-transparent without visible precipitation even after several months of shelf life. The specific conductivity of electrolytic solutions was determined from impedance spectra obtained by 2-probe measurement with 100 mV amplitude in the range from 100 kHz to 1 Hz. For conductivity calculations, 1 mM and 0.1 M KCl were used as reference solutions.

A 0.3 mm thick sheet of Crofer 22 APU steel (VDM Metals, Verdohl, Germany) was cut into 1.5 × 1.5 cm plates to be used as the substrates for RE electrodeposition. A small hole (3 mm in diameter) was punched in the top part of the samples so they could be suspended on an alumina rod for corrosion exposure. The edges of plates were smoothed out in order to remove visible flexures using a polishing machine with wet 1200 grit paper. Before applying the RE coatings, the plates were thoroughly cleaned in acetone (POCH, Gliwice, Poland) in an ultrasonic bath. The cleaned and dried plates were crocodile clips connected as the working electrode (cathode) in a two-electrode electrolytic deposition system. The counter electrode (anode) was an oversized Crofer 22 APU steel sheet and was placed symmetrically on both sides of the working

electrode (active geometrical surface area of about 50 cm^2). The distance between the working electrode and the counter electrodes was ~1.5 cm 3 samples were made for each RE-oxide, and each sample was weighed three times. Each sample was gently air dried before being annealed at 400 °C. Each operation was performed with extreme care to ensure that the layers were undamaged. A sketch of the deposition setup is presented in Fig. 1.

A voltage of 40 V was applied between the electrodes as in Ref. [19] using a programmable power supply (Delta Elektronika Power Supply SM 300–5, Zierikzee, The Netherlands). Current measurements were recorded using the ammeter (Sanwa PC500A, Sanwa Electric Instrument Co., Ibaraki, Japan). The optimised deposition time for each of the solutions was deduced from the preliminary tests (not reported here). After application of the RE layer, each of the samples was air-dried and heated to a temperature of about 400 °C for complete conversion of the deposited layers to oxides and the decomposition of residual nitrates. This process has been studied and described in the literature [30–32].

To determine corrosion kinetics, the thermogravimetry (weight changes) method was used. Oxidation tests were performed in a chamber furnace (Kittec SQ11, Vranovice-Kelčice, Czech Republic) in stagnant air. The oxidation tests were carried out in a cyclic manner in two stages. The first "pre-evaluation" was based on a relatively short time (250 h with weight measurements every 50 h) at three different temperatures (700 °C, 800 °C, and 900 °C). The second step, "long-term" corrosion study, was carried out for a total of 2000 h at 700 °C with weight gain measurements every 250 h. The weight gain measurements were performed on a balance with an accuracy of 10^{-6} g (Radwag XA 6/21.4Y.M.A.B PLUS, Radom, Poland).

The microstructure of the Crofer 22 APU steel samples was analysed by X-ray diffraction (XRD) using a Bruker D2Phaser (Bruker AXS, Mannheim, Germany) diffractometer with a Lynxeye XE-T detector with CuKα radiation (k = 0.15406 nm). Post-mortem studies in the form of surface and cross-section analyses were performed using a scanning electron microscope with an integrated energy dispersive X-ray (EDS) analyser (Thermo Fischer Phenom XL, Waltham, United States of America).

Electrical resistance measurements were performed in a cross-scale configuration (across Pt/oxide/steel/oxide/Pt). The platinum electrodes (with an area of 0.5 cm^2) were brush-painted on the two sides of the steel, dried and heated to 700 °C for 2 h. The electrical resistance measurement was carried out in a four-electrode system using an impedance analyser (Gamry Interface 1000E, Warminster, PA, United States). The measurement was performed at a frequency of 1 Hz (the imaginary part of the impedance was negligible) with an amplitude of 5 mV. The sample was heated to 700 °C and then cooled to 300 °C while the resistance was measured. The maximum current flowing through the sample was limited to 5 mA cm^{-2}.

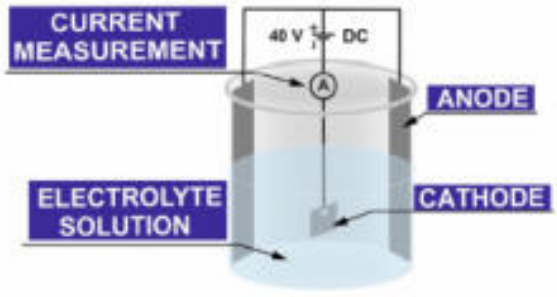


Fig. 1 – Sketch of the deposition setup.

Results and discussion

The results section is organised as follows: first, the results related to the deposition process of the RE coatings with different thicknesses are presented. Then an accelerated oxidation screening test of the differently coated samples is shown. Based on the accelerated test, the most promising RE coating thickness was selected. Short-term (250 h at 700/800/900 °C) and long-term oxidation studies are conducted on the selected samples. Finally, post-mortem analyses are performed to describe the microstructures of the samples.

Preparation of the layers

The preparation of the layers was started by analysing the solution conductivity and electrical charge density measurements during the electrodeposition process. Measurements on the solutions of Ce-, La-, Gd-, and Y-nitrates showed specific conductivity of 24.6 μS cm^{-1}, 23.1 μS cm^{-1}, 32.1 μS cm^{-1} and 41.0 μS cm^{-1}, respectively. The obtained conductivities show similar values, which may suggest that this parameter should not have a crucial influence on the deposition process of the RE-layer on the steel surface. During the deposition, the electric current was recorded in order to estimate the effectiveness of the deposition process. Based on this measurement, the electric charge per cm^2 was calculated and shown in Fig. 2A. The calculated value of deposited RE-oxide according to charge (for the deposition time of 1 min) is 3,28, 59,6; 22,9 and 19,9 μmol × C^{-1} for Ce-, Gd-, La-, and Y-oxide, respectively. According to Faraday's first law, the deposition efficiency of the proposed method was calculated for each RE-oxide. The determined efficiencies are 60%, 79%, 79%, and 80% for the deposition of Ce-, Gd-, La-, and Y-oxide, respectively. In the initial stage of the study, the dependence of the deposition time on the deposit weight was studied, and Fig. 2B shows the results. For this purpose, a series of Crofer 22 APU steel samples with different deposition times (of up to 4 min) were prepared.

The deposition of the La-coating showed the highest weight gain, thus deposition times within 10–60 s were also studied. The deposition of the La-oxide layer seems more intense than the other coatings. It was estimated, assuming formation of a continuous and dense layer, that 10 s of La-oxide deposition results in ~24 nm layer thickness (16 μg cm^{-2}), while in the case of Y-oxide deposition, 1 min of deposition results in ~37 nm layer thickness (44 μg cm^{-2}). Calculated layer thicknesses can be compared with those obtained by theoretical calculations. Namely, ~30 nm for La-oxide and ~46 nm for Y-oxide were obtained, which is

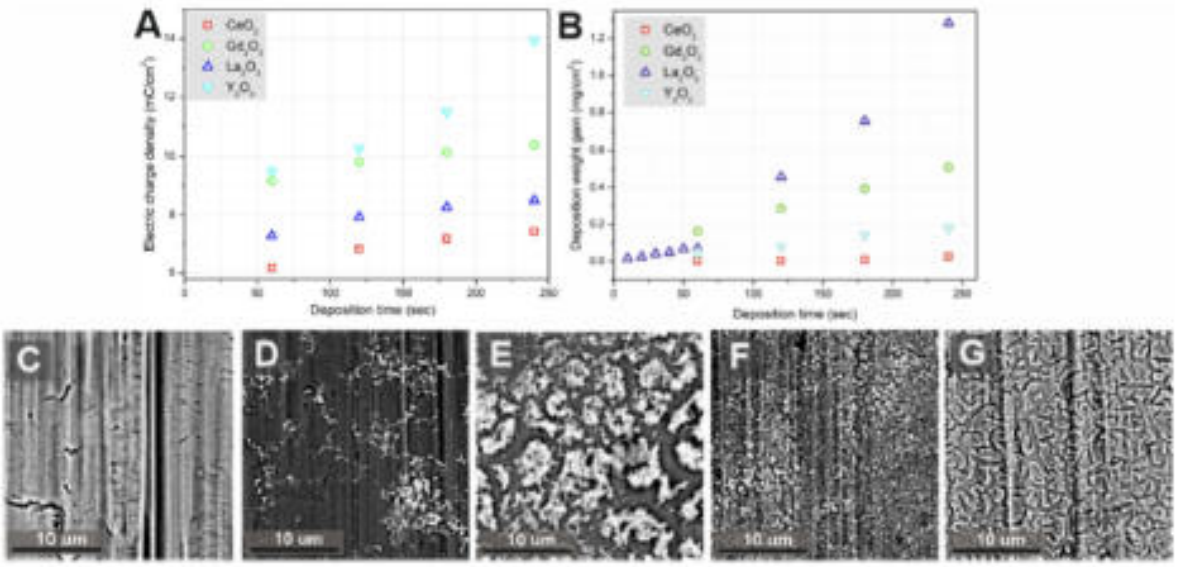


Fig. 2 – Electric charge density vs. the deposition time (A) weight of the coating materials vs. the deposition time (B), SEM surface images of the reference, uncoated steel (C), Ce- (D), Gd- (E), La- (F), Y- (G) coated for 1 min.

reasonably close to the experimentally calculated layer thicknesses and at the same time to the mass change values given in Fig. 2B. Since 10 s is a relatively short time, the weight obtained during the electrodeposition process was compared with the dip coating technique. In the case of the La-oxide layer, ten times greater weight gain was obtained during 10 s of La-nitrate deposition in comparison with the dipped sample in the La-nitrate solution for the same period of time.

Electron microscopy images of the 60 s deposits are presented in Fig. 2 C–G. In nearly all cases, the deposits are visible as discontinuous layers. The presence of the respective RE was further confirmed by EDS analysis, where the RE content (based on low magnification surface analysis) was estimated to be ~1 at.% for the prepared coatings. The weight gain results show that the Ce-oxide layer is less effectively formed in comparison with the other layers. The SEM observations showed that Ce-oxide is formed as randomly distributed deposits. Local agglomerates of deposited RE-oxides are visible. However, according to the EDS analysis on the surface of steel samples (where the RE-oxide layer is not visible), the concentration of the analysed rare earth elements is in the range of 0.6–0.7% by area. In the case of the areas where these agglomerates occur, the obtained result of atomic concentration increases to 1.2%. The mapping of elements in combination with the determined deposition efficiency indicates the efficiency of the process. Formed oxide agglomerates may be caused by local imperfections of the steel surface (formed in the process of rolling steel, which can be seen in the reference sample). Despite this observation, the EDS tests clearly show the presence of deposited Ce oxides in significant amounts, though it is impossible from these measurements to judge the layer thickness or its continuity. Nevertheless, all tested RE layers were further investigated since the RE layer quality on corrosion protection effectiveness is unknown.

Short-term corrosion evaluation

Initial corrosion screening at 900 °C

After the fabrication of samples with different weights of the RE-oxide layer, the samples were subjected to high temperature oxidation to assess the influence of the oxide layer thickness on the corrosion rate. This helps the selection of samples for extended measurements.

The effect of the coating deposition time (~thickness) on the weight gain of the samples was determined by cyclic oxidation at a temperature of 900 °C for 250 h (5 cycles of 50h). An initial test at a relatively high temperature of 900 °C was carried out to highlight the differences resulting from the physicochemical properties of the oxides in a short time frame – it acts as an accelerated test procedure.

For the Ce-, Gd-, and Y-oxide layers, samples with deposition times varying between 1 min and 4 min were studied. The time was also varied between 10 and 60 s due to the formation of thick deposits.

The oxidation weight gain values for samples exposed at 900 °C are shown in Fig. 3. In all cases, the uncoated steel was used as a reference. The weight gain of the uncoated Crofer 22 APU steel after 250 h at 900 °C is ~0.6 mg cm^{-2}, which is consistent with the literature data. Talic et al. reported virtually the same value for a Crofer 22 APU sheet with a similar thickness (1 mm) [33].

The deposition of all coatings resulted in visibly reduced weight gains caused by oxidation. The obtained weight gain data indicates that there was no significant effect of the deposition time on the weight gain. The average weight gain of the coated steel sheets was similar in all cases (~0.37 mg cm^{-2}). The weight gain difference between the uncoated and coated alloys was ~40%, which is a marked improvement in corrosion resistance. Similar thermogravimetric results at high temperatures for the oxides analysed

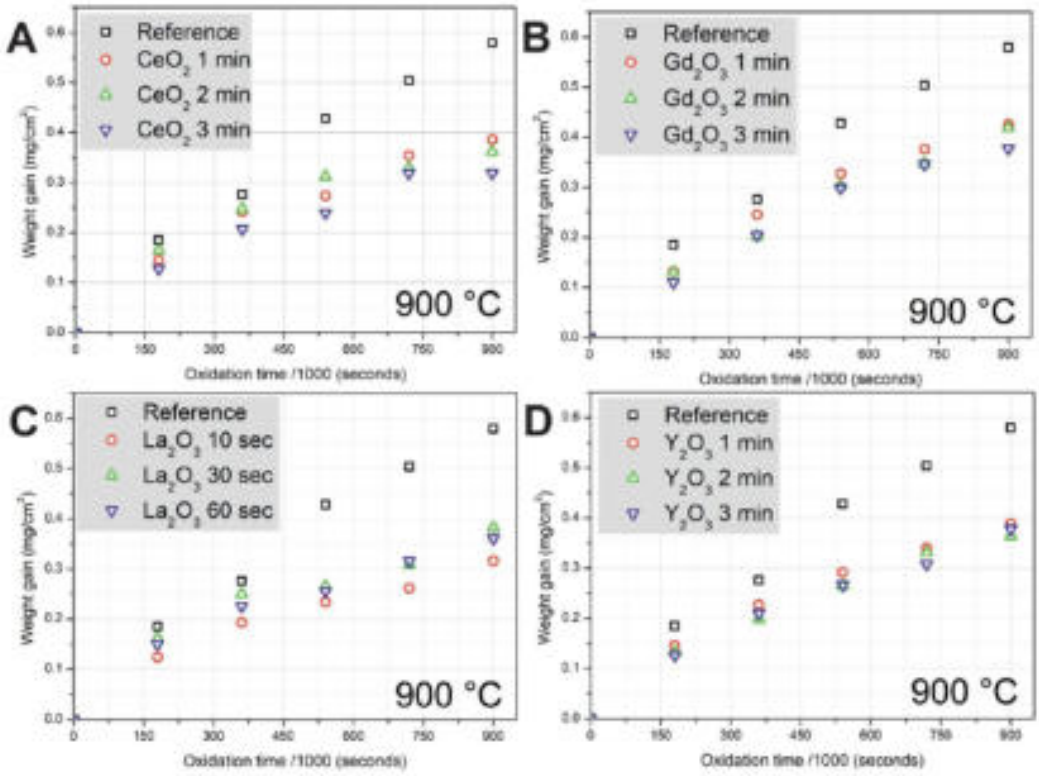


Fig. 3 – Weight gain curves for samples oxidised at 900 °C deposited with a layer of: Ce- (A), Gd- (B), La- (C), Y- (D).

may have a different basis. The fact is that even a thin layer of rare earth oxides reduces weight gain. High corrosion temperature (900 °C) affects the corrosion rate and the influence of RE-oxides is visible. Therefore, despite the lower efficiency in the deposition of cerium oxide compared to other analysed ceramics, the result is ultimately similar. The initial stage of oxidation of the cerium oxide coated sample shows the least reduction of weight gain compared to the other RE-oxide layers. This information may indicate the behaviour of cerium oxide at lower temperatures. Another observation is the flattening of the weight gain for lanthanum oxide, which initially showed similar values to the reference sample, then to slow down the oxidation process and get the most promising result. Each of the described results indicates that each of the rare earths has its own physical–chemical process behind the reduction of weight gain under the influence of oxidation.

Based on these results, the samples prepared with the shortest deposition times (10 s for La-oxide and 1 min for Ce-, Gd-, and Y-oxides) were selected for further research. These samples showed (Fig. 2 B) the deposited weights in the range of 0.01–0.05 mg cm^{-2} (60 s deposition for Ce-, Gd-, and Y-oxides, and 10 s for the La-oxide coating). Based on layer weight, one can predict the layer thickness. The theoretical average equivalent thickness of the coating is 50 nm when the density of the RE oxides (5–7 g cm^{-3}) and the specified deposit weight are considered.

Short-term corrosion exposure at 900/800/700 °C

The selected samples were tested for their corrosion properties at lower temperatures for 800 °C and 700 °C. Typically, the temperature range between 900 °C and 700 °C is most often studied for the determination of corrosion properties of alloys used in solid oxide cell stacks [34].

The weight gain results for 800 °C and 700 °C are shown in Fig. 4. At all temperatures, the uncoated samples have the largest weight gain, also confirming the protective properties of the coating materials used at lower temperatures. At 800 °C, the lowest weight gain was obtained for the Y-oxide coated sample (~0.089 mg cm^{-2}), followed closely by the Gd-oxide coated sample (~0.093 mg cm^{-2}). The La-oxide coated samples showed intermediate weight gain values, with the weight gain of the Ce-oxide samples closest to the uncoated alloy.

At 700 °C, the weight gain behaviour is similar to that observed at 800 °C. The lowest weight gain is noted for the Gd-oxide coated sample (~0.028 mg cm^{-2}), whereas the Y-oxide and La-oxide coated samples are slightly worse, but still present a lower weight gain than the uncoated sample. Again, the Ce-oxide coated alloy has a weight gain quite similar to the uncoated alloy.

Analysing the results of oxidation at 700, 800, and 900 °C, it seems that the sample with ceria layer coating is effective only at the highest temperature, whereas the Gd-oxide, La-oxide, and Y-oxide are effective in the whole temperature range. The Gd-oxide coating seems the most effective at

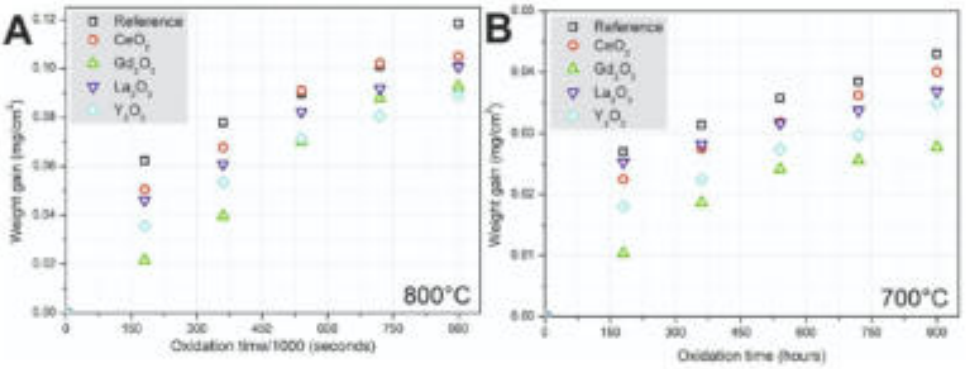


Fig. 4 – Weight gain and parabolic plots for samples oxidised (for 250 h) at 800 °C (A) and 700 °C (B).

reducing the oxide growth, especially in lower temperatures (700 °C). That confirmed the first ~100 h at 800 °C, during which the Gd_2O_3 -based layer showed less weight gain than the other ceramic layers, but in the subsequent phase of the experiment, the samples with the gadolinium oxide layer showed growing weight gain, and finally, after 150 h, they showed a higher weight gain than the sample coated with yttria. RE-oxide coatings are able to provide a marked reduction of the oxide growth rate even at a moderate temperature of 700 °C, which seems especially important since, e.g., the Mn–Co oxide spinels do not provide an oxide growth rate reduction at this temperature [30]. Thus, by potentially combining these two coating materials (RE + spinel), a synergistic low-temperature effective coating can be designed.

Electrical resistivity measurements. The weight gain measurements showed a protective effect of the applied thin coatings in terms of the lowered weight gain. The influence of the coatings can also be studied by electrical resistivity measurements. The thicker the oxide scales formed on the alloys due to oxidation, the higher the cross-scale electrical resistance of the alloys. The deposited ceramic coatings can also influence the electrical resistivity of the samples since the oxide form of the coated elements (CeO_2, Gd_2O_3, La_2O_3 and Y_2O_3) are electrical insulators. Thus, their applicability to solid oxide cell stacks should not negatively influence the electrical properties, which must be studied.

The Area Specific Resistance (ASR) was studied on samples after the 250-h oxidation test at 700, 800 and 900 °C. Graphs showing the temperature dependence of the ASR, including the comparison of the ASR values obtained at 700 °C, are shown in Fig. 5. The ASR results show that in almost all cases, the samples with the applied coatings have a lower electrical resistance than the uncoated samples (with the exception of the Ce-coated alloy oxidised at 800 °C). As indicated in Fig. 5 A–C and summarised in D, there is a strong effect of the exposure temperature on the resulting ASR level: the higher the exposure temperature, the higher the resistance. For example, for the uncoated samples, the ASR values after 250 h of exposure at 900, 800, and 700 °C were ~140 mΩ cm^2, ~70 mΩ cm^2 and ~35 mΩ cm^2 (values measured at 700 °C, Fig. 5 D). For the surface-modified samples, the lowest ASR values were obtained for the yttria-coated series. The ASR values were ~95 mΩ cm^2, ~15 mΩ cm^2 and ~7 mΩ cm^2 after 250 h exposures at 900/800 and 700 °C. The difference in the ASR between the uncoated and the Y-oxide coated sample is pronounced at lower oxidation temperatures, where as high as a 5-fold decrease in the ASR value was obtained. For the Ce-oxide, Gd-oxide, and La-oxide modified samples, the ASR values were also lower than for the reference sample (except for the ceria coated sample measured at 800 °C), with the Gd-oxide and La-oxide coatings being slightly inferior to the Y-oxide coating. The slopes of the ASR curves were also similar for all samples, indicating a similar overall conductivity mechanism of the uncoated and coated samples, most probably dominated by chromia scale in all cases.

The RE coating procedure, especially in the case of Y-oxide and La-oxide, has a very positive effect on the resulting ASR value, which is very important for efficient and low-degradation SOC stacks.

After short-term weight gain and ASR measurements, the samples were analysed by scanning electron microscopy (SEM). Micrographs of the sample cross-sections were taken to assess the differences in the surface structure after short-term corrosion at 700 °C, 800 °C and 900 °C. Selected images of the lanthanum coated samples are shown in Fig. 6.

At 700 °C, where the weight gain was very low (~0.035 mg cm^{-2}), only a very thin, rough corrosion layer is visible. No sign of the La-oxide coating is noticeable. At 800 °C, due to the higher weight gain (~0.1 mg cm^{-2}), the oxide layer becomes more apparent. The formed oxide uniformly covers the sample surface. Within the oxide (in the middle), a very thin bright layer is visible, which is the deposited La-oxide material. The sample at 900 °C has the highest weight gain (~0.35 mg cm^{-2}) and traces of the La-oxide coating are noticeable on the surface of the oxide.

Long-term oxidation at 700 °C

A temperature of 700 °C was selected for performing the longer-term study, as it is of interest for intermediate temperature SOFC technology [35]. As discussed, the RE-oxide coatings seem to provide an important reduction in oxide scale growth at this temperature. The exposures were

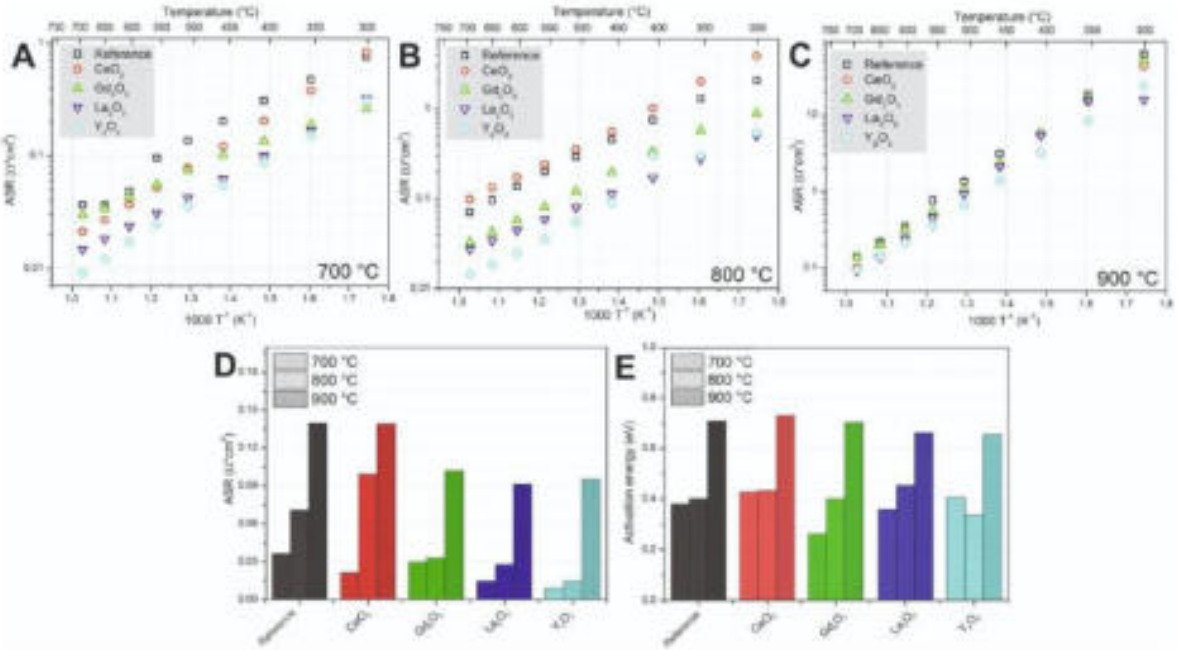


Fig. 5 – Arrhenius plots of Area Specific Resistance of samples oxidised at 700 °C (A), 800 °C (B) and 900 °C (C) for 250 h, and a comparison of ASR values measured at 700 °C (D) and comparison of the activation energies (E).

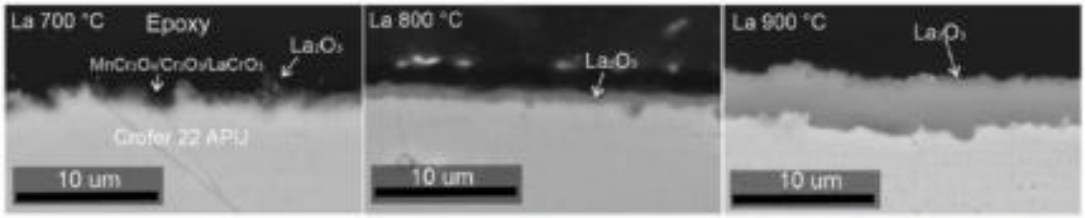


Fig. 6 – SEM pictures of the cross-section for La-coated samples. From the left for 700 °C, 800 °C and 900 °C.

performed up to 2000 h (8 cycles of 250 h) and the obtained weight gain results are presented in Fig. 7 A together with a parabolic plot (Fig. 7 B).

Typically, the weight gain values determined at 700 °C are very low due to slow corrosion kinetics [15]. The weight gain was again the highest for the uncoated alloy; after 2000 h it reached ~0.09 mg cm^{-2}. The coated samples showed lower weight gain values, with the yttria- and La-oxide coated alloys resulting in a weight gain of ~0.055 mg cm^{-2}, so a decrease of ~40% was achieved.

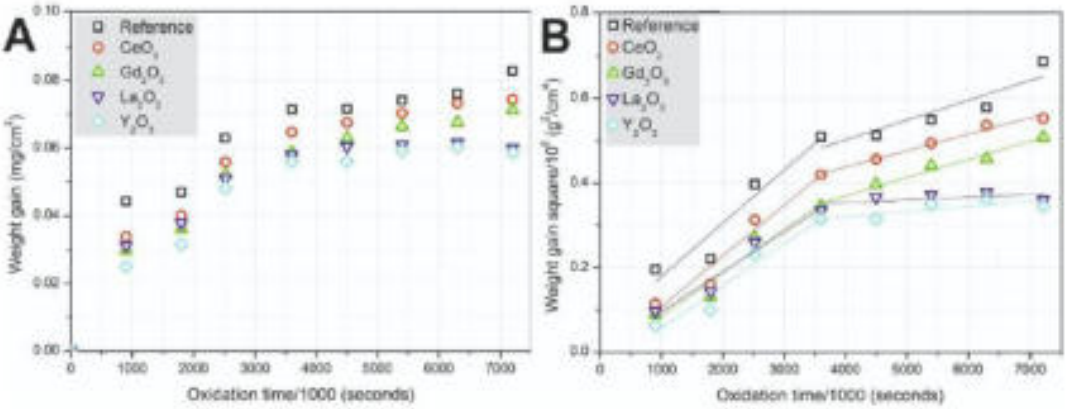


Fig. 7 – Weight gain (A) and parabolic plot (B) for the long-term oxidation of differently coated samples at 700 °C (A, B).

When considering the kinetics of high-temperature oxidation, usually a square (parabolic) dependence of the weight increase vs. time is used:

$$\left(\frac{\Delta m}{A}\right)^2 = k_p t + C$$

where: Δm is the weight gain [g], A is the sample area [cm^2], k_p is the corrosion rate parameter [$g^2\ cm^{-4}\ s^{-1}$], t is the oxidation time [s], and C is the integration constant [$g^2\ cm^{-4}$].

A parabolic plot of the weight gain values is presented in Fig. 7B. Due to its nonlinear behaviour, the fitting of the k_p was performed separately for the periods of 250–1000 and 1000–2000 h. The calculated k_p values are summarised in Table 1. The constant C is usually assigned to the initial corrosion phenomena. For the uncoated samples, the C value is visibly larger than for the coated alloys, meaning that the initial stage of corrosion was modified by the addition of the reactive element.

The initial oxidation of the alloys follows a similar kinetics, where the k_p values range from 1.26×10^{-15} $g^2\ cm^{-4}\ s^{-1}$ to 0.94×10^{-15} $g^2\ cm^{-4}\ s^{-1}$ for the uncoated and La-oxide coated alloys, respectively. A more pronounced difference is visible for the 2nd analysis period (1000–2000 h), where the corrosion kinetics slows down. The difference between the uncoated and the La-oxide coated sample is one order of magnitude. Also, the Y-oxide coated sample shows a marked corrosion rate decrease. The samples coated with Gd-oxide and Ce-oxide show little improvement.

The possible change of slopes of the weight gain is often reported in the literature. One of the reasons might be changes in the chemistry of the layers, including phase stabilisation/grain growth (e.g., Cr_2O_3 and/or $(Mn,Cr)_3O_4$), or depletion of oxide scale-forming elements (Mn) from the substrate. Additionally, differences in the formation of spinel $(Mn,Cr)_3O_4$ and chromium oxide may be caused by the formation of protective phases during the conversion of deposited Ce-/Gd-/La-/Y-oxide coating precursors [36].

Overall, the deposited reactive element coatings, especially in the case of the Y_2O_3 and La_2O_3 coatings, resulted in a marked improvement in corrosion resistance.

After the long-term exposure test, the samples were also subjected to electrical resistivity measurements. The results are shown in Fig. 8. The samples coated with La-, Gd-, and Y-oxide show a visible decrease of the ASR, whereas Ce-oxide has a minor effect. The highest ASR values at 700 °C were found for the uncoated samples (~85 mΩ cm^2 at 700 °C). Slightly lower values were found for the Ce-, Y- and La-oxide coated samples (~45 mΩ cm^2 for Ce-oxide, ~35 mΩ cm^2 for yttria and La-oxide). The lowest ASR value was obtained for the Gd-oxide modified sample (~20 mΩ cm^2). At a temperature of <600 °C, the highest resistance was obtained for the ceria-coated sample, which showed an activation energy of ~0.55 eV.

The ceria-coated sample showed the highest ASR, possibly due to the combination of several effects. The first is the ceria layer itself, which is an electrical insulator, and the weight gain of the Ce-oxide coated sample was comparable to that of the reference, uncoated sample (especially at lower temperatures). This contributes to the formation of a fairly thick corrosion layer on top of which the cerium oxide layer is deposited. Ultimately, this increases the ASR value even compared to the reference sample. Also, the slope of the obtained curve clearly indicates the highest activation energy. The La-oxide and Y-oxide coated samples showed improvement compared to the reference sample. Despite the thicker layers, the ASR values were lower due to the formation of a much thinner corrosion layer for the La-oxide-based layer. In the case of the Y-oxide based layer, this value was slightly worse because the layer itself was the most continuous of all. This was also confirmed by the activation energy values. The best ASR properties were obtained for samples coated with Gd-oxide. The thickest layer of the Gd_2O_3-based sample did not cause the thinnest corrosion layer, but even this did not prevent the greatest decrease in the ASR value. The application of Gd-oxide-based coating led to a 4-fold decrease in the ASR, which is an important achievement regarding potential long-term stack operation.

In Fig. 9 A X-ray diffractometry analysis was performed on the samples oxidised at 700 °C for 2000 h. Due to the small thickness of the oxide coating layer, the intensity of the coatings-related peaks is low but still allows qualitative identification.

For the uncoated sample, the peaks from the steel substrate could be detected together with the peaks from the formed oxide phases. The most intensive peak came from the cubic $MnCr_2O_4$ (ICDD card #75–1614) followed by Cr_2O_3 (#38–1479). The measured peaks were shifted in comparison to the database inputs, but qualitatively they very well describe the oxides. The shift might be caused by sample misalignment or a slight difference in the chemical composition of the oxides. The two found oxide phases are typical for Crofer 22 APU oxidised in the conditions used [36,37].

The analysis of the coated samples revealed some differences in the oxide scale formation on different substrates. The sample coated with cerium showed the formation of $(MnCr)_3O_4$, Cr_2O_3 and the CeO_2 phase (#34–394), which seems

Table 1 – Determined values of the k_p coefficient corresponding to the kinetics of the oxidation reaction. Corrosion was divided into two stages (1st from 250 to 1000 h, 2nd from 1000 h to 2000 h) due to the visible difference in the reaction rate.

Temperature	$k_{p\ (250h-1000h)}$ [$\times 10^{-15}$ $g^2\ cm^{-4}\ s^{-1}$]	C [$\times 10^{-10}$ $g^2\ cm^{-4}$]	$k_{p\ (1000h-2000h)}$ [$\times 10^{-15}$ $g^2\ cm^{-4}\ s^{-1}$]	C [$\times 10^{-9}$ $g^2\ cm^{-4}$]
Reference	1.26	5.35	0.47	3.41
CeO_2	1.20	1.25	0.39	2.82
Gd_2O_3	1.01	1.15	0.43	1.97
La_2O_3	0.94	0.21	0.07	3.27
Y_2O_3	1.00	4.26	0.12	2.71

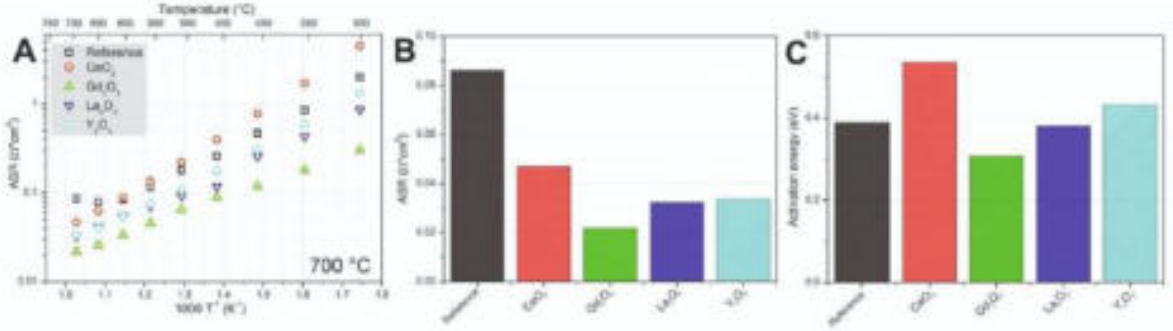


Fig. 8 – Arrhenius plots of Area Specific Resistance of samples oxidised at 700 °C for 2000 h (A), comparison of ASR values measured at 700 °C (B) and comparison of the activation energies (C).

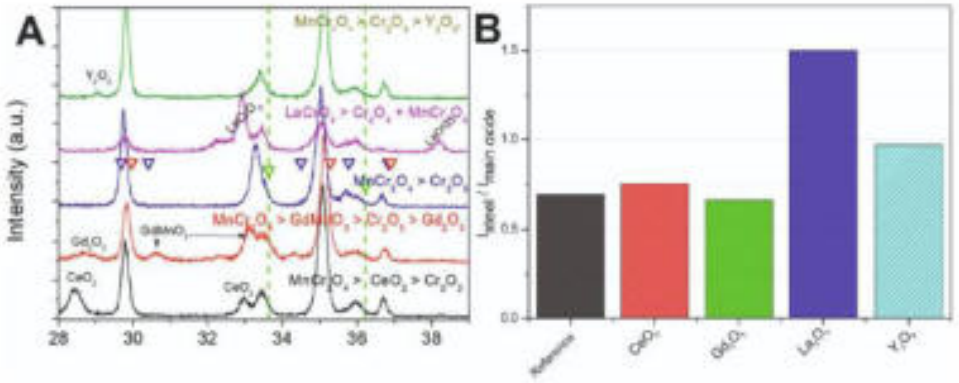


Fig. 9 – XRD spectra of coated alloys after 2000 h of oxidation (A), relative ratio of the intensities of the steel peak to the main peak of the oxide phase (B).

to retain its fluorite structure. In the case of the gadolinium-coated sample, the most intensive peaks came from the $MnCr_2O_4$ spinel, followed by $GdMnO_3$ (#25–337), Cr_2O_3 and Gd_2O_3 (#12–797) phases. Gadolinium oxide reacts with manganese oxide, forming a new phase. Some gadolinium remained in the pure oxide form. The La-oxide coated sample showed the formation of a $LaCrO_3$ perovskite phase (#24–1016), which was the most intense peak. In addition, Cr_2O_3 could be detected. For this sample, the formation of the $MnCr_2O_4$ seemed suppressed – it had the lowest relative intensity among the studied samples. In the case of the samples with a Y_2O_3 layer, the most intense peak corresponded to cubic $MnCr_2O_4$. The less intense peak corresponded to Cr_2O_3 and the least intense, but still characteristic peak, to Y_2O_3 (# 41–1105) [38–41].

To qualitatively compare the oxide scale thickness formed on different samples, the relative intensity ratio of the main steel substrate peak and the most intensive oxide phase peaks is plotted in Fig. 9 B.

For the long-term samples, the sample with the La-based layer had the highest value of the intensity ratio coefficient. This was mainly due to the formation of the chromium-lanthanum spinel. This spinel is the most intense peak in the diffraction pattern. There is no visible spinel in the Y_2O_3 layer, only the oxide itself. These two layers also showed the lowest weight gain. In the case of the sample with a layer of cerium oxide and gadolinium oxide, both the presence of the oxide and the spinel were identified. At the same time, these samples showed a little better weight gain properties than the reference sample.

The results obtained are supported by studies conducted by Chevalier et al. [40]. In his work, he investigated the formation of perovskites from Gd-oxide, Y-oxide and La-oxide. The tests were performed at a temperature of 1000 °C. Chevalier showed that La_2O_3 converts to perovskites very quickly. Gd_2O_3 transforms much slower (more than 100 h at this high temperature). In the case of Y_2O_3, this time was even longer, nearly 300 h. In our case, the described tests were carried out at a lower temperature (700 °C) but the phase formation after 2000 h of exposure was similar [42]. Gil et al. undertook the task of explaining the effect of the grain structure on the oxidation product in the case of the application of protective layers on steel. Studies have shown that thin yttria layers do not form a continuous layer at temperatures close to 1000 °C. At lower temperatures, the oxide forms a continuous layer. However, attention should be paid to the short measurement time of 100 h. When using longer times, a tendency towards oxide discontinuity may be observed. The formation of perovskite in the form of $YCrO_3$ facilitates the slow diffusion of oxygen to the inside, which at the same time significantly slows down the diffusion of chromium to the outside [37]. The cited studies show that the temperature of

700 °C is too low for the formation of the perovskite form of $YCrO_3$. More time and a higher temperature are needed to produce such a phase that could inhibit the diffusion of chromium to the outside. This problem does not occur in the case of lanthanum, which is produced in a significant amount in the form of $LaCrO_3$, and even the shorter deposition time and the thinner layer did not significantly deteriorate the thermogravimetric results obtained. The samples with Gd2O3 and CeO2 partially form a perovskite phase, so the protective effect is more complex. It seems that several "protective" mechanisms are plausible, and these have been studied for many years, as pointed out in a recent summary of Chevalier

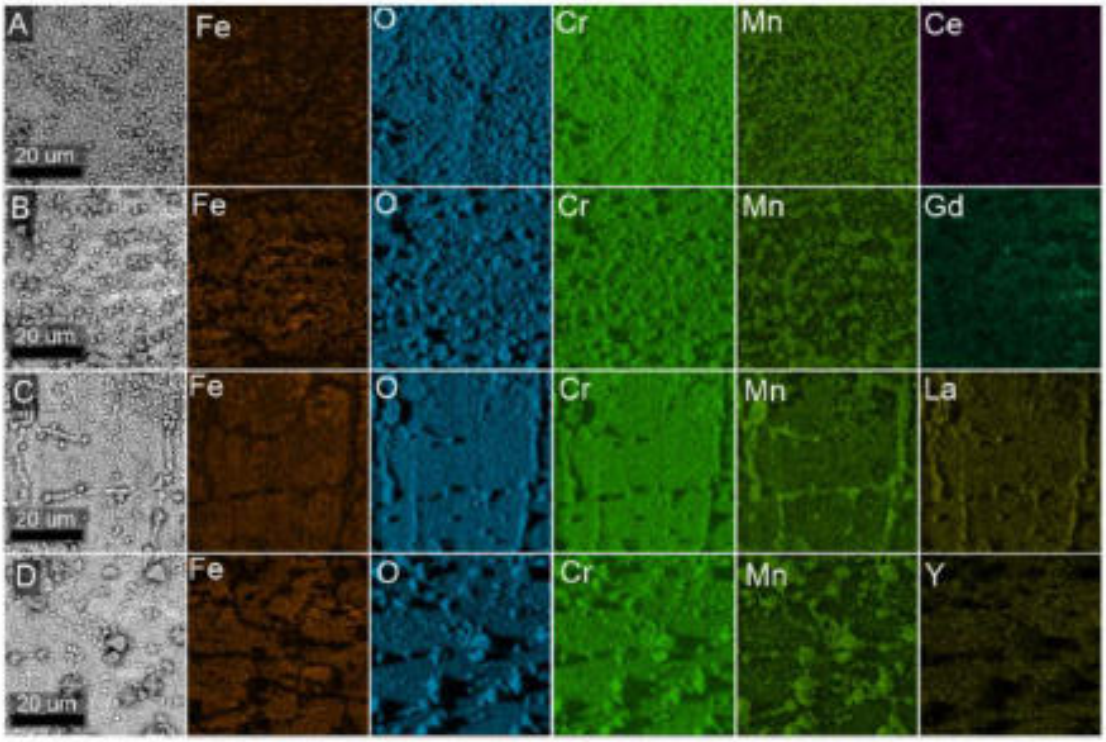


Fig. 10 – SEM and EDS elemental maps of surfaces of CeO_2 (A), Gd_2O_3 (B), La_2O_3 (C) and Y_2O_3 coated (D) samples after 2000 h of oxidation at 700 °C.

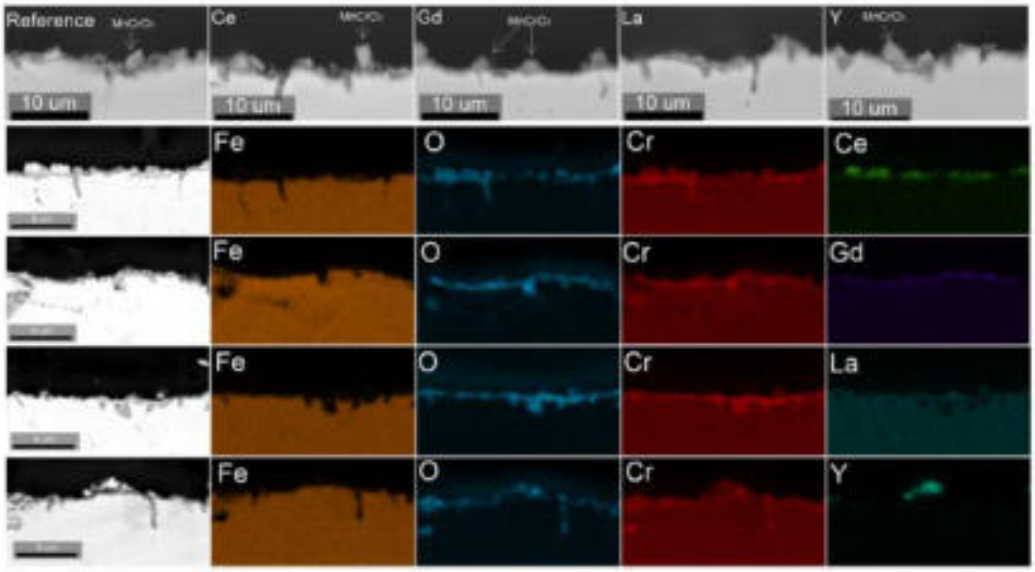


Fig. 11 – SEM photos and the EDS analysis taken for sections of samples after long-term corrosion at 700 °C for the discussed layers and the reference sample.

[43]. Nevertheless, both thermogravimetric, electrical and XRD measurements show the importance and effectiveness of rare earths in corrosion protection.

A post-mortem examination was performed by SEM/EDS to analyse the surfaces and cross-sections of the samples. This analysis was performed after 2000 h at 700 °C. The results are shown in Fig. 10 and Fig. 11.

On the Ce-oxide and Gd-oxide coated samples' surfaces, small (1–2 μm) manganese-chromium spinel crystals are visible. The Y-oxide coated sample shows the largest surface crystallites, which are composed of Cr and Mn. In these cases, the active elements seem to be distributed uniformly on the surface of the alloy and are not present in the large crystallites.

The samples based on a layer of La_2O_3 show a different surface morphology. In this case, it seems that the formation of the $LaCrO_3$ perovskite phase occurred uniformly over the sample surface. According to the XRD, this indicates a significantly reduced formation of $MnCr_2O_4$, which seems to grow along the alloy grain boundaries. The surface of the La-oxide coated sample is the smoothest, with no large crystallites.

The results of the SEM/EDS cross-section analyses are presented in Fig. 11. The oxidation at 700 °C resulted in a very thin oxide scale. The corrosion products seem similar in all cases. The chemical composition of the outer oxide determined by EDS shows the presence of reactive elements at some spots. The coatings are not continuous as they are quite thin and they react with the Mn/Cr oxide scale. Some internal oxidation is visible on all samples, which is connected to the growth of the oxide scale in the grain boundaries of the alloy.

Conclusions

This article presents the results of the electrodeposition of Ce-, Gd-, La-, and Y-oxide coatings based on ethanol solutions of dissolved reactive element nitrates. In terms of reducing the kinetics of oxide scale growth, all of the coatings performed similarly. This was confirmed by both thermogravimetric and electrical resistivity measurements. The lowest weight gain was obtained for the Y-oxide and La-oxide based coatings, where the corrosion rate parameter was decreased by ~40%. The electrical resistivity of the oxide scale was reduced by a factor of 4-7-fold depending on the particular coating. X-ray diffractometry allowed for the qualitative identification of the oxides on the surface of the Crofer 22 APU plates. The reactive elements showed different reactivity with the Mn/Cr from the alloy. In the case of the yttria coated sample, no reaction with Cr/Mn was detected, whereas for the La-oxide coated samples, transformation of the La-oxide coating to $LaCrO_3$ perovskite was apparent. SEM microscopy confirmed the dissimilar behaviour of the different coatings. In the case of the La-oxide coating, its distribution was also uniform on the sample surface and no large Mn–Cr oxide spinel particles were formed, whereas in the case of the Y-oxide coating, its distribution was also uniform but large Mn–Cr oxide crystallites grew. Overall, the most promising layers seem to be either La-/Y-/Gd-oxide based, offering quite similar performance and benefits.

Declaration of competing interest

The authors declare that they have no known competing financial interests or personal relationships that could have appeared to influence the work reported in this paper.

Acknowledgement

This research has been supported by National Science Centre (NCN) Harmonia 9 project number UMO-2017/26/M/ST8/00438: "Quest for novel materials for solid oxide cell interconnect coatings".

REFERENCES

[1] Niewolak L, Wessel E, Singheiser L, Quadakkers WJ. Potential suitability of ferritic and austenitic steels as interconnect materials for solid oxide fuel cells operating at 600 °C. J Power Sources 2010;195:7600–8. https://doi.org/10.1016/J.JPOWSOUR.2010.06.007.

[2] Reisert, M.; Aphale, A.; Singh, P. Materials solid oxide electrochemical systems: Material degradation processes and novel Mitigation Approaches., doi:10.3390/ma11112169.

[3] Ghiara, G.; Piccardo, P.; Bongiorno, V.; Geipel, C.; Spotorno, R. Characterization of metallic interconnects extracted from solid oxide fuel cell stacks operated up to 20,000 h in real life conditions: The Air Side., doi:10.3390/en13246487.

[4] Mah JCW, Muchtar A, Somalu MR, Ghazali MJ. Metallic interconnects for solid oxide fuel cell: a review on protective coating and deposition techniques. Int J Hydrogen Energy 2017;42:9219–29. https://doi.org/10.1016/J.IJHYDENE.2016.03.195.

[5] Zhu WZ, Deevi SC. Development of interconnect materials for solid oxide fuel cells. Mater Sci Eng, A 2003;348:227–43. https://doi.org/10.1016/S0921-5093(02)00736-0.

[6] Fontana S, Chevalier • S, Caboche • G, Lamour J, Chevalier S, Caboche AG, Caboche G. Metallic interconnects for solid oxide fuel cell: performance of reactive element oxide coating during 10, 20 and 30 Months exposure made of La 2 O 3 or Y 2 O 3 resulted in an important improvement in the high. Oxid Met 2012;78:307–28. https://doi.org/10.1007/s11085-012-9308-4.

[7] Brylewski T, Kucza W, Adamczyk A, Kruk A, Stygar M, Bobruk M, Dabrowa J. Microstructure and electrical properties of Mn1+xCo2−xO4 (0≤x≤1.5) spinels synthesized using EDTA-gel processes. Ceram Int 2014;40:13873–82. https://doi.org/10.1016/J.CERAMINT.2014.05.106.

[8] Brylewski T, Kruk A, Bobruk M, Adamczyk A, Partyka J, Rutkowski P. Structure and electrical properties of Cu-doped Mn-Co-O spinel prepared via soft chemistry and its application in intermediate-temperature solid oxide fuel cell interconnects. J Power Sources 2016;333:145–55. https://doi.org/10.1016/J.JPOWSOUR.2016.09.136.

[9] Bobruk M, Brylewska K, Durczak K, Wojciechowski K, Adamczyk A, Brylewski T. Synthesis of manganese-cobalt spinel via wet chemistry methods and its properties. Ceram Int 2017;43:15597–609. https://doi.org/10.1016/J.CERAMINT.2017.08.116.

[10] Kruk A, Stygar M, Brylewski T. Mn-Co spinel protective-conductive coating on AL453 ferritic stainless steel for IT-SOFC interconnect applications. J Solid State Electrochem 2013;17:993–1003. https://doi.org/10.1007/s10008-012-1952-8.

[11] Szymczewska D, Molin S, Chen M, Ski PJ, Hendriksen PV. Corrosion study of ceria protective layer deposited by spray pyrolysis on steel interconnects. Ceram Eng Sci Proc 2017;37:79–86. https://doi.org/10.1002/9781119320197.ch7.
[12] Szymczewska D, Molin S, Vang Hendriksen P, Jasi Ński P. Microstructure and electrical properties of Fe,Cu substituted (Co,Mn) 3 O 4 thin films. 2017. https://doi.org/10.3390/cryst7070185.
[13] Cabouro G, Caboche G, Chevalier S, Piccardo P. Opportunity of metallic interconnects for ITSOFC: reactivity and electrical property. J Power Sources 2006;156:39–44. https://doi.org/10.1016/J.JPOWSOUR.2005.08.039.
[14] Piccardo P, Gannon P, Chevalier S, Viviani M, Barbucci A, Caboche G, Amendola R, Fontana S. ASR evaluation of different kinds of coatings on a ferritic stainless steel as SOFC interconnects. Surf Coating Technol 2007;202:1221–5. https://doi.org/10.1016/J.SURFCOAT.2007.07.096.
[15] Grolig JG, Froitzheim J, Svensson JE. Effect of cerium on the electrical properties of a cobalt conversion coating for solid oxide fuel cell interconnects – a study using impedance spectroscopy. Electrochim Acta 2015;184:301–7. https://doi.org/10.1016/J.ELECTACTA.2015.10.111.
[16] Molin S, Kusz B, Gazda M, Jasinski P. Evaluation of porous 430L stainless steel for SOFC operation at intermediate temperatures. J Power Sources 2008;181:31–7. https://doi.org/10.1016/J.JPOWSOUR.2007.10.009.
[17] Ebrahimifar, H.; Zandrahimi, M. Oxidation and electrical behavior of a ferritic stainless steel with a Mn-Co-based coating for SOFC interconnect applications., doi:10.1007/s11085-015-9557-0.
[18] Gannon PE, Tripp CT, Knospe AK, Ramana CV, Deibert M, Smith RJ, Gorokhovsky VI, Shutthanandan V, Gelles D. High-temperature oxidation resistance and surface electrical conductivity of stainless steels with filtered arc Cr–Al–N multilayer and/or superlattice coatings. Surf Coating Technol 2004;188–189:55–61. https://doi.org/10.1016/J.SURFCOAT.2004.08.067.
[19] Canovic S, Froitzheim J, Sachitanand R, Nikumaa M, Halvarsson M, Johansson LG, Svensson JE. Oxidation of Co- and Ce-nanocoated FeCr steels: a microstructural investigation. Surf Coating Technol 2013;215:62–74. https://doi.org/10.1016/J.SURFCOAT.2012.08.096.
[20] Falk-Windisch H, Claquesin J, Sattari M, Svensson JE, Froitzheim J. Co- and Ce/Co-coated ferritic stainless steel as interconnect material for intermediate temperature solid oxide fuel cells. J Power Sources 2017;343:1–10. https://doi.org/10.1016/J.JPOWSOUR.2017.01.045.
[21] Magrasó A, Falk-Windisch H, Froitzheim J, Svensson JE, Haugsrud R. Reduced long term electrical resistance in Ce/Co-coated ferritic stainless steel for solid oxide fuel cell metallic interconnects. Int J Hydrogen Energy 2015;40:8579–85. https://doi.org/10.1016/J.IJHYDENE.2015.04.147.
[22] Molin S, Persson H, Skafte TL, Smitshuysen AL, Jensen SH, Andersen KB, Xu H, Chen M, Hendriksen PV. Effective yttrium based coating for steel interconnects of solid oxide cells: corrosion evaluation in steam-hydrogen atmosphere. J Power Sources 2019;440. https://doi.org/10.1016/j.jpowsour.2019.226814.
[23] Boccaccini AR, Zhitomirsky I. Application of electrophoretic and electrolytic deposition techniques in ceramics processing. Curr Opin Solid State Mater Sci 2002;6:251–60. https://doi.org/10.1016/S1359-0286(02)00080-3.
[24] Zhitomirsky I, Petric A. Electrochemical deposition of yttrium oxide. J Mater Chem 2000;10:1215–8. https://doi.org/10.1039/b000311p.
[25] Zhitomirsky I, Petric A. Electrolytic and electrophoretic deposition of CeO2 films. Mater Lett 1999;40:263–8. https://doi.org/10.1016/S0167-577X(99)00087-7.
[26] Yang L, Pang X, Fox-Rabinovich G, Veldhuis S, Zhitomirsky I. Electrodeposition of cerium oxide films and composites. Surf Coating Technol 2011;206:1–7. https://doi.org/10.1016/j.surfcoat.2011.06.029.
[27] Mazur Ł, Pleśniak J, Dąbek J, Gil A, Brylewski T. High-temperature oxidation of ferritic steel surface-modified with gadolinium oxide nanoparticles. Ceramic Materials 2019;71:179–92.
[28] Yoon JS, Lee J, Hwang HJ, Whang CM, Moon JW, Kim DH. Lanthanum oxide-coated stainless steel for bipolar plates in solid oxide fuel cells (SOFCs). J Power Sources 2008;181:281–6. https://doi.org/10.1016/J.JPOWSOUR.2007.12.053.
[29] Saeidpour F, Zandrahimi M, Ebrahimifar H. Evaluation of pulse electroplated cobalt/yttrium oxide composite coating on the crofer 22 APU stainless steel interconnect. Int J Hydrogen Energy 2019;44:3157–69. https://doi.org/10.1016/J.IJHYDENE.2018.12.062.
[30] Hamlaoui Y, Pedraza F, Remazeilles C, Cohendoz S, Rébéré C, Tifouti L, Creus J. Cathodic electrodeposition of cerium-based oxides on carbon steel from concentrated cerium nitrate solutions: Part I. Electrochemical and analytical characterisation. Mater Chem Phys 2009;113:650–7. https://doi.org/10.1016/J.MATCHEMPHYS.2008.08.027.
[31] Strydom CA, Van Vuuren CPJ. The thermal decomposition of lanthanum(III), praseodymium(III) and europium(III) nitrates. Thermochim Acta 1988;124:277–83. https://doi.org/10.1016/0040-6031(88)87030-8.
[32] Strydom CA, Vuuren CPJ, Van THE. Thermal decomposition of cerium (ill) nitrate 1987;32:157–60.
[33] Talic B, Molin S, Wiik K, Hendriksen PV, Lein HL. Comparison of iron and copper doped manganese cobalt spinel oxides as protective coatings for solid oxide fuel cell interconnects. J Power Sources 2017;372:145–56. https://doi.org/10.1016/J.JPOWSOUR.2017.10.060.
[34] Fergus JW. Synergism in the design of interconnect alloy–coating combinations solid for oxide fuel cells. Scripta Mater 2011;65:73–7. https://doi.org/10.1016/J.SCRIPTAMAT.2010.09.020.
[35] Jacobson AJ. Materials for solid oxide fuel cells. Chem Mater 2010;22:660–74. https://doi.org/10.1021/cm902640j.
[36] Molin S, Chen M, Hendriksen PV. Oxidation study of coated crofer 22 APU steel in dry oxygen. J Power Sources 2014;251:488–95. https://doi.org/10.1016/J.JPOWSOUR.2013.09.100.
[37] Gil A, Kryshtal O, Brylewski T, Czyrska-Filemonowicz A. Characterization of a Cr2O3 scale formed on chromium with implanted yttrium ions by advanced electron microscopy. Surf Coating Technol 2019;368:232–42. https://doi.org/10.1016/j.surfcoat.2019.03.081.
[38] Faisal M, Khasim S. Electrical conductivity, dielectric behavior and emi shielding effectiveness of polyaniline-yttrium oxide composites. Bull Kor Chem Soc 2013;34:99–106. https://doi.org/10.5012/bkcs.2013.34.1.99.
[39] Ma R, Jahurul Islam M, Amaranatha Reddy D, Kim TK. Transformation of CeO2 into a mixed phase CeO2/Ce2O3 nanohybrid by liquid phase pulsed laser ablation for enhanced photocatalytic activity through Z-scheme pattern. Ceram Int 2016;42:18495–502. https://doi.org/10.1016/j.ceramint.2016.08.186.
[40] Kabir H, Nandyala SH, Rahman MM, Kabir MA, Stamboulis A. Influence of calcination on the sol–gel synthesis of lanthanum oxide nanoparticles. Appl Phys Mater Sci Process 2018;124:0. https://doi.org/10.1007/s00339-018-2246-5.
[41] Tóthová E, Tarasenko R, Tkáč V, Orendáč M, Hegedüs M, Danková Z, Holub M, Baláž M, Matik M. Microcrystalline Gd 2 MoO 6 prepared by combined mechanochemical/thermal

process and its magnetic properties. J Mater Sci 2019;54:6111–21. https://doi.org/10.1007/s10853-019-03331-z.
[42] Chevalier S, Larpin JP. formation of perovskite type phases during the high temperature oxidation of stainless steels coated with reactive element oxides. Acta Mater 2002;50:3107–16. https://doi.org/10.1016/s1359-6454(02)00106-4.
[43] Chevalier S. What did we learn on the reactive element effect in chromia scale since pfeil 's patent? Mater Corros 2014;65:109–15. https://doi.org/10.1002/maco.201307310.

10.2. $CuMn_{1.7}Fe_{0.3}O_4 – RE_2O_3$ (RE = Y, Gd) bilayers as protective interconnect coatings for solid oxide cells

Authors: **Bartłomiej Lemieszek**, Justyna Ignaczak, Krystian Lankauf, Patryk Błaszczak, Maciej Bik, Marcin Zając, Maciej Sitarz, Piotr Jasiński, Sebastian Molin

Jornal of European Ceramic Society, vol. 44, issue 15, pages 116743, 2024, https://doi.org/10.1016/j.jeurceramsoc.2024.116743

IF = 6.2 (2024), MSHE points 140, Citations: 10

This work, a continuation of Article 1, focused on two selected rare-earth oxides, Gd_2O_3 and Y_2O_3, combined with $CuMn_{1.7}Fe_{0.3}O_4$ (CMFO) spinel to form protective bilayers. While the role of rare-earth oxide layers was described previously, here CMFO was electrodeposited as an alternative to the commonly used $MnCo_2O_4$ spinel in order to achieve higher electrical conductivity. The bilayer design was intended to compensate for the low electrical conductivity of rare-earth oxides through the use of CMFO, while maintaining effective chromium diffusion-blocking properties.

Structural analysis of sol–gel synthesized CMFO by XRD and TPR showed that it decomposes and reduces at lower temperatures than MCO. Three coating systems were prepared: CMFO, CMFO–Gd_2O_3, and CMFO–Y_2O_3. After 4,000 hours of oxidation at 700 °C, the lowest weight gain was observed for CMFO–Y_2O_3, followed by CMFO and CMFO–Gd_2O_3. ASR measurements also indicated the best performance for the CMFO–Y_2O_3 bilayer, while CMFO–Gd_2O_3 showed similarly low values. In contrast, CMFO alone exhibited higher ASR than the reference samples.

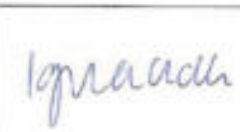
SEM–EDS analysis confirmed that the rare-earth oxide layers effectively inhibit the formation of a thick chromia layer, which causes stronger chromium migration, as observed in samples without these layers. Confocal Raman imaging supported this result by showing markedly higher MnO_2 content in CMFO-only coatings, which was absent in the bilayers. XAS analysis further revealed changes in the manganese oxidation state, suggesting possible degradation processes in the material.

The novelty of this work lies in the application of double layers with CMFO spinel and in evaluating the effect of the protective layer on corrosion resistance at 700 °C. The additional layer significantly enhanced the blocking of chromium diffusion. Furthermore, the material's reduction and oxidation mechanisms were investigated using the TPR (Temperature Programmed Reduction) and TPO (Temperature Programmed Oxidation) techniques.

The main achievements of this work include demonstrating the feasibility of obtaining a protective coating for Crofer 22 APU steel using cobalt-free materials, while simultaneously eliminating the problem associated with such materials. Notably, after 4,000 hours of oxidation at 700 °C, the ASR value was below 10 $m\Omega \cdot cm^2$ - well below the commonly accepted limit of 100 $m\Omega \cdot cm^2$.

My contributions to this study included material synthesis, coating deposition, corrosion testing, ASR measurements, SEM–EDS and XAS analyses, as well as evaluation of corrosion, ASR, XRD, and XAS data. As in Article 1, I was also responsible for interpreting results, preparing figures, and writing the manuscript. As the corresponding author, I handled article submission and prepared revisions in response to reviewer comments.

Declaration of co-authors on their contribution to the publication: "$CuMn_{1.7}Fe_{0.3}O_4$ – RE_2O_3 (RE = Y, Gd) bilayers as protective interconnect coatings for solid oxide cells".

Name and Surname	Contribution	Signature
Bartłomiej Lemieszek	Investigation (Corrosion study, ASR, SEM-EDS, XAS), Methodology, Writing – review & editing, Writing – original draft, Visualization.	
Justyna Ignaczak	Investigation - Corrosion study, Methodology, Writing – review & editing.	
Krystian Lankauf	Investigation (XAS), Methodology, Writing – review & editing,	
Patryk Błaszczak	Investigation (XRD, TPR), Methodology, Writing – review & editing.	
Maciej Bik	Investigation (Confocal Raman imaging), Methodology, Writing – original draft, Writing – review & editing.	
Marcin Zając	Methodology, Writing – review & editing,	
Maciej Sitarz	Investigation, Methodology, Writing – review & editing.	
Sebastian Molin	Conceptualization, Methodology, Writing – original draft, Writing – review & editing, Supervision.	
Piotr Jasiński	Methodology,	

	Conceptualization, Funding acquisition, Writing – review & editing, Supervision.	

Journal of the European Ceramic Society 44 (2024) 116743



Contents lists available at ScienceDirect

Journal of the European Ceramic Society

journal homepage: www.elsevier.com/locate/jeurceramsoc





$CuMn_{1.7}Fe_{0.3}O_4$ – RE_2O_3 (RE = Y, Gd) bilayers as protective interconnect coatings for solid oxide cells

Bartłomiej Lemieszek [a,*], Justyna Ignaczak [a], Krystian Lankauf [a], Patryk Błaszczak [b], Maciej Bik [c], Marcin Zając [d], Maciej Sitarz [c], Piotr Jasiński [a], Sebastian Molin [a]

[a] Advanced Materials Center, Faculty of Electronics, Telecommunications and Informatics, Gdańsk University of Technology, ul. G. Narutowicza 11/12, Gdańsk 80-233, Poland
[b] Advanced Materials Center, Faculty of Applied Physics and Mathematics, Gdańsk University of Technology, ul. G. Narutowicza 11/12, Gdańsk 80-233, Poland
[c] AGH University of Science and Technology, Faculty of Materials Science and Ceramics, Al. Mickiewicza 30, Kraków 30-059, Poland
[d] National Synchrotron Radiation Centre SOLARIS, Jagiellonian University, Czerwone Maki 98, Kraków 30-392, Poland

ARTICLE INFO

Keywords:
High temperature corrosion
Solid oxide cell (SOC)
Bilayers
Protective coating
Reactive element effect

ABSTRACT

Efficient replacement of materials based on critical elements such as cobalt is one of the greatest challenges facing the field of solid oxide cells. New generation materials, free of cobalt show potential to replace conventional materials. However, these materials are characterised by poor ability to block chromium diffusion. This article described the study of $CuMn_{1.7}Fe_{0.3}O_4$ (CMFO) spinel combined with single metal oxide (Y_2O_3 or Gd_2O_3) thin films as protective coatings for steel interconnects. CMFO was examined using XRD and TPR. Coated steel samples were oxidised in an air atmosphere at 700 °C for 4000 h. The coatings and oxide scale microstructures and cross-sections were examined by CRI, XRD, and SEM-EDX. The electrical properties of the steel-coating system were evaluated using Area Specific Resistance measurements. Based on the results obtained, it can be concluded that the use of thin layers of rare earth oxides allowed for better blocking of chromium diffusion.

1. Introduction

High-temperature corrosion of steel interconnects is one of the main degradation problems in solid oxide cell stacks. At high temperatures, ferritic steels develop a chromium oxide scale, which further protects the steel substrate from uncontrolled oxidation [1,2]. The thickness of the chromium oxide layer increases with time according to parabolic oxidation kinetics [3]. Oxide growth causes two important factors: an increase in the electrical resistance (area specific resistance – ASR) and the evaporation of chromium (at air side), reducing the efficiency of the fuel cells [1,2,4]. One of the mitigation strategies is to coat the interconnects with dedicated protective coatings. Various materials have been considered for coating ferritic steels, including metallic coatings [5–8], reactive element oxides [9–18], perovskite oxides [1,19–26], and spinels [27–34]. Among these materials, reactive-element oxides and spinels are particularly often used.

Reactive-element oxides in the form of La_2O_3, CeO_2, Gd_2O_3, and Y_2O_3 are used commonly as coatings or additives for high temperature alloys and also were successfully used to coat interconnects. These materials are characterised by a high affinity for oxygen, blocking the diffusion of chromium to the surface of the layer, and increasing the adhesion of the layer to the metallic substrate [1]. The main disadvantage of this group of ceramics is limited electronic conductivity, therefore the coating thicknesses are usually low, below ~ 1 µm [9]. Yoon et al. described the application of La_2O_3 as a coating of STS444 interconnects (stainless steel). The study examined the surface morphology and cross-sections after 500 h at 700 °C. The presence of phases such as Cr_2O_3, $LaCrO_3$, and $(Mn,Cr)_3O_4$ was demonstrated [14]. Molin et al. used thin Y_2O_3 coatings of a thickness below 100 nm on Crofer 22 APU and tested the protective properties of the layer on the steam-hydrogen side at 750 °C for 2000 h. The described thin-layer coating resulted in a reduction in the thickness of the oxide layer and a high and stable ASR value over time [10]. Lemieszek et al. demonstrated the influence of thin layers (CeO_2, Gd_2O_3, La_2O_3, Y_2O_3—thickness below 100 nm) on Crofer 22 APU steel in an air atmosphere at 700 °C for 2000 h. It has been shown that the use of coatings reduces significant weight gain, especially in the case of La_2O_3 and Y_2O_3 coatings. The best ASR values were demonstrated by samples with a Gd_2O_3 or Y_2O_3 coating [18]. These coatings, even though they reduce oxide scale growth kinetics, they do not prevent Cr-diffusion and

* Corresponding author.
E-mail address: bartlomiej.lemieszek@pg.edu.pl (B. Lemieszek).

https://doi.org/10.1016/j.jeurceramsoc.2024.116743
Received 10 May 2024; Received in revised form 22 June 2024; Accepted 10 July 2024
Available online 11 July 2024
0955-2219/© 2024 The Authors. Published by Elsevier Ltd. This is an open access article under the CC BY license (http://creativecommons.org/licenses/by/4.0/).

evaporation, as the external surface remains as Cr_2O_3, just with a lowered thickness.

As $MnCo_2O_4$ (MCO) spinel is the current state-of-the-art protective layer for SOC metallic interconnects. This material was found to be highly effective at preventing oxidation and reducing chromium diffusion and evaporation in metallic interconnects [35]. The focus is now aimed towards finding alternative materials than MCO. The cost and difficult working conditions of mining cobalt, as well as its carcinogenicity, cannot be overlooked [36,37]. That is why materials substituting cobalt with, e.g., copper have been developed, with various dopants [32–34]. For example, Ignaczak et al. synthesised a new spinel material, $Mn_{1.7}Cu_{1.3-x}Fe_xO_4$ (x = 0, 0.1, 0.3, 0.5) [38] and $Mn_{2.4}CuFe_xO_4$ (x = 0.0, 0.1, 0.3) [39], using a modified Pechini method.

The structure of the $Mn_{1.7}CuFe_{0.3}O_4$ after synthesis and calcination at 400 °C reveals the presence of the main phase being $CuMn_{1.7}Fe_{0.3}O_4$ with a mixed cubic (*Rd-3m*) and a tetragonal (*I41/amd:2*) spinel structure. Following the increase in Fe doping, the size of the unit cell was reduced. Additional CuO phases were not detected when annealing spinel at temperatures higher than 400 °C. [38]. Mazur et al. denoted a conductivity of 106 S cm^{-1} for $Cu_{1.15}Mn_{1.55}Fe_{0.3}O_4$ at 800 °C when the material was synthesised by the EDTA-gel peocess [40]. Hosseini et al. described the coating of AISI 430 steel with a layer of $Cu_{1.3}Mn_{1.7}O_4$ spinel, and the corrosion properties were examined at 750 °C for 500 h. A 70 % reduction in the ASR value was observed from 63.5 to 19.3 mΩ cm^2 at 750 °C. It was also observed that the oxide layer formed after the oxidation process was ~ 4 μm [41]. Study by Ignaczak et al. showed several beneficial features of the Mn-Cu based oxide spinels over the Mn-Co based oxide spinels: higher electrical conductivity, especially ≤ 700 °C, well matched thermal expansion coefficient. The drawback has been lower intrinsic oxidation protection, i.e. the steels coated with MCO showed lower weight gain in comparison to the Mn-Cu based oxide spinels coated steels [39].

A new trend is the coating of interconnects with double layers, most often in the form of a thin layer of a reactive element oxide and a thicker layer of spinel, but also double layers based of perovskite oxides [42,43]. The concept of coating interconnects with two materials is to use the advantages of each type of material. The use of a RE-oxide in combination with spinels makes use of the advantages of each material. Balland et al. presented the results of an investigation on the coating of interconnects with lanthanum oxide and $(Co,Mn)_3O_4$ on Crofer APU steel for a maximum of 1000 h at 800 °C. Coating involved applying lanthanum oxide and annealing for 100 h then depositing metallic (Co, Mn). This ultimately resulted in the formation of $La(Cr_{1-x}Mn_x)O_3$ and $(Co,Mn)_3O_4$ layers [17]. Brylewski et al. examined the influence of a double layer composed of Gd_2O_3 and $MnCo_2O_4$. The RE-oxide layer was applied by spin coating and the spinel layer by electrophoretic deposition. The samples were fired at 800 °C for 2260 h in an airtight atmosphere. An effective reduction in the formation of volatile chromium compounds and a significant reduction in weight gain and area-specific resistance were found [44]. Mazur et al. presented the results of coating Crofer 22 APU steel with a double layer composed of Gd_2O_3 and $MnCo_2O_4$. Thermogravimetric tests were performed at 800 °C for 7000 h. A significant reduction in weight gain and a very low ASR value of 0.019 Ω cm^2 after the final stage of oxidation were demonstrated. Tests were also carried out using a fuel cell to check the ability of the protective layers to block the formation of active chromium species that could poison the cell's cathode. This study clearly indicated the effective blocking of this element by the combination of materials used as protective layers [45]. To the best of our knowledge, there is no mention in the literature of the use of bi-layer coating in the form of reactive element oxide and spinel $(CuMnFe)_3O_4$.

This research work presents the results of coating Crofer 22 APU steel with bi-layers of RE-oxide (yttrium oxide or gadolinium oxide) and a top layer of $CuMn_{1.7}Fe_{0.3}O_4$ spinel. The selection of these two RE-oxides is based on conclusions from previous studies due to the reduction in weight gain and lower ASR values [18]. The samples were tested via thermogravimetric measurements in isothermal conditions for a 4000 h. Post-mortem analysis was used to study and compare the structural properties of the materials using methods such as XRD, SEM-EDS, XAS spectra, and Confocal Raman imaging. Additionally, the electrical properties of the samples were tested.

2. Materials and methods

2.1. RE-oxide layer deposition

The base solution used to obtain the RE-oxide layers was 2 mM Gd $(NO_3)_3$•$6H_2O$ (Sigma Aldrich 99.9 % purity, USA) or $Y(NO_3)_3 \bullet 6H_2O$ (Sigma Aldrich 99 % purity, USA) dissolved in ethanol (Sigma Aldrich 99.8 %, USA). For rare earth oxide electrolytic deposition, substrates of 1.5 × 1.5 cm^2, 0.3 mm thick plates were cut from Crofer 22 APU steel (VDM Metals, Germany). A small hole (3 mm in diameter) was punched in the upper part of the samples. Noticeable flexures were removed from the edges of the plates using a polishing machine with wet 1200 grit paper. Before applying the rare earth yttrium or gadolinium oxide coatings (attributed as RE further in the text), the plates were meticulously cleaned in an ultrasonic bath containing a solution of distilled water, then in acetone (POCH, Poland). Crofer 22 APU steel plate was used as the working electrode (cathode) in a two-electrode electrolytic deposition system. Crocodile clips were used to connect to the cleaned and dried plates. The counter electrode (anode) was a large Crofer 22 APU steel sheet positioned symmetrically on either side of the working electrode (active geometric surface area of about 50 cm^2). The distance between the working and counter electrodes was less than 15 mm.

A programmable power supply was used to apply 40 V between the electrodes (Delta Elektronika Power supply SM 300-5, The Netherlands). Based on a previous study, the deposition time was selected as 1 min (thickness ~ 100 nm) [18]. After applying the RE layer, each sample was air-dried and heated to 400 °C to ensure the complete conversion of the deposited layers to oxides and the breakdown of residual nitrates.

2.2. Spinel synthesis and deposition

$Cu(NO_3)_2 \bullet 2.5H_2O$ (Sigma Aldrich, 99.999 % purity, USA), $Mn(NO_3)_2 \bullet 4H_2O$ (Sigma Aldrich, 97 % purity, USA), and $Fe(NO_3)_3 \bullet 9H_2O$ (Sigma Aldrich, 99.999 % purity, USA) were dissolved in distilled water and used as the starting solutions. According to the intended nominal composition of the spinel powders, those were mixed in proper molar ratio. The solutions were heated to 80 °C with constant stirring on a heating plate equipped with a magnetic stirrer. Citric acid ($C_6H_8O_7$, Sigma Aldrich, 99 % purity, USA) and EDTA ($[CH_2N(CH_2COOH)_2]_2$, Sigma Aldrich, 99 % purity, USA) were added to the stirred solution in a molar ratio of 2:1:1-TMI as chelating agents (TMI – total number of molar ions). Diluted ammonia (25 w/w% H_2O) was added dropwise to adjust the pH to 9. To initiate the transesterification process, ethylene glycol ($C_2H_6O_2$, 98 % purity, Saint Louis, USA) was added while stirring constantly in an amount sufficient to obtain a ratio of 1 mol polyalcohol to 1 mol metal cations. The liquid precursor was maintained at 80 °C until a dense gel-like structure was achieved. The resultant gel was placed in a muffle furnace and heated to 400 °C for two hours. After this, the obtained powder was fired at 800 °C for 2 h. To achieve the lowest possible grain size, the powder was ball milled using the roll mill method with zirconia milling balls (Ø – 3 mm) and a rotational speed of 800 rpm for 4 h using a planetary mill.

The $CuMn_{1.7}Fe_{0.3}O_4$ (CMFO) spinel layer was applied by the electrophoretic deposition technique using Crofer 22 APU steel as the cathode (identical to the RE-oxide layer) with the same dimensions. The anode was Crofer 22 APU steel with a larger surface area (50 cm^2). The base solution contained 1 g of CMFO powder dispersed in isopropanol: acetone (4:1 ratio, 100 ml). Crystalline iodine (0.1 g per 100 ml of solution) was added to the solution. The resulting mixture was sonicated in an ultrasonic bath for 15 min to disperse the spinel particles in the

liquid. Three types of samples were prepared. The first type was Crofer 22 APU steel samples with only the spinel layer (labelled as 'CMFO'). The second type consisted of samples with a thin layer of gadolinium oxide and, on top of that, a spinel layer (labelled as 'CMFO-Gd_2O_3'). The last type was samples with an yttrium oxide layer (same thickness) and the spinel layer (labelled as 'CMFO-Y_2O_3'). Uncoated Crofer 22 APU steel plates were used as reference samples (labelled as 'reference'). The summary of the prepared samples is presented in Table 1. A programmable power supply (Delta Elektronika Power Supply SM 300-5, The Netherlands) was used to apply 80 V between the electrodes. The duration of the electrophoresis was 4 minutes to obtain a spinel layer of ~ 10 μm thickness. After coating the steel, a heat treatment process was applied under a reducing and oxidising atmosphere. The reduction step was carried out in tube furnace (Carbolite STF 16/450, Germany) at 800 °C for 10 h under a hydrogen atmosphere with a flow 175 ml min^{-1}, and an oxidation step at 900 °C for 2 h under air in a box furnace (Linn High Therm LM412.05, Germany). The selection of these conditions was based on preliminary tests determining the optimal conditions, and the choice of a lower temperature was associated with the result of smaller metallic particles of copper and iron. The use of a lower temperature for the reduction stage also reduces the thickness of the chromium oxide layer after the oxidation stage.

2.3. Measurements methods

Temperature-programmed reduction (TPR) test was performed for $CuMn_{1.7}Fe_{0.3}O_4$ using an in-house-built TPx unit including a TCD (Buck Scientific, USA), heated transfer line, and specially designed quartz reactor. For the reduction test, 75 mg of spinel powder was placed in the reactor. Quartz wool was used to create a homogeneous reactive bed and limit the elution of the powder. The TPR test was performed under the standard 5 vol% H_2 in Ar and flow rate of 40 ml min^{-1}. The sample was heated up from room temperature to ~ 900 °C at a rate of 10 °C min^{-1} with the data collection frequency set to 1 Hz. The sample of $CuMn_{1.7}Fe_{0.3}O_4$ underwent two following cycles of reduction interspersed with the collection of the oxidation profile under the same experimental conditions, although under a stream of 5 % O_2/He reactive gas. For comparison, a sample of commercial $MnCo_2O_4$ powder (Marion Technologies, France) was measured while under reduction.

X-ray diffraction (XRD) was used to examine the microstructure of the coated Crofer 22 APU steel samples using a Bruker D2Phaser (Bruker AXS, Germany) diffractometer with a Lynxeye XE-T detector and CuKα radiation (λ = 0.15406 nm). XRD measurements of the synthesised powder were made for the powder after treatment at 800 °C under atmospheric air and for prepared samples after 1000 h, 2000 h and 4000 h of oxidation.

To determine the oxidation kinetics, the samples were subjected to a temperature of 700 °C under an air atmosphere in a box furnace (Nabertherm L9/11/B180, Germany). The weight gain was measured using a balance with a precision of 10^{-6} grammes (Radwag XA 6/21Y.M. A.B PLUS, Poland). The 'long-term' corrosion study was carried out for 4000 h in 250-hour cycles (16 cycles), followed by mass measurement and calculation of the mass increase. For each of the sample types, 16 specimens were assigned for long-term testing, of which 3 samples were taken out after 1000 h, 4 after 2000 h, and the remaining 9 were removed after the final period of 4000 h. Uncoated Crofer 22 APU steel was used as a reference sample (5 samples). As for the coated samples, one reference sample was taken out after 1000 h, two after 2000 h and two after 4000 h.

Electrical resistance measurements were performed ex-situ for samples after oxidation times equal to zero, 1000, 2000, and 4000 h. As a reference, uncoated samples that had undergone the same oxidation times were used. In a cross-scale setup, electrical resistance tests were conducted (Pt/layers/steel/layers/Pt). On both sides of the steel, platinum electrodes (with a surface area of 0.5 cm^2) were painted with a brush, dried, and heated at 700 °C for two hours. The electrical resistance was measured using an impedance analyser in a four-electrode setup (Vertex.5A, Ivium Technologies, The Netherlands). The test was performed at a frequency of 1 Hz with an amplitude of 1 mA (the imaginary component of the impedance was negligible). The samples were heated to 700 °C, and the resistance was measured in a cooling cycle every 50 °C down to 300 °C. The maximum current density through the specimen was restricted to 10 mA cm^{-2}.

Cross-sections and the steel surface with a protective layer were examined using scanning electron microscopy (SEM) on a stationary SEM Phenom XL (Thermo Fisher Scientific, USA) at an accelerating voltage of 15 kV and a pressure of 0.1 Pa. A SED (secondary electron detector) and integrated energy dispersive X-ray microanalyser (EDX) were used. The samples were imbedded in epoxy resin (EpoFix, Struers) and then polished to a 1 μm finish using a semi-automatic Struers Tegramin-20 machine. Prior to the imaging step, the samples were sputtered with a thin carbon layer for better charge transfer and higher resolution of the SEM images.

Raman spectroscopy (Raman Confocal Imaging) was carried out using a WITec alpha 300 M+ spectrometer (488 nm laser line). Measurements were carried out on pre-prepared cross sections, using a 100 × ZEISS Epiplan-Neofluar objective with NA = 0.9 and 600 grating (spectral resolution of ca. 3 cm^{-1}). The areas of a constant width (5 μm) were scanned and their height (from 8 to 13 μm) was dependent on scale/coating thickness. The integration time for a single spectrum was equal to 15 s. The WITec Control FIVE software was used to record Raman spectra, whereas WITec Project FIVE 5.3 PLUS, as well as the OPUS 7.2 software were used to post-process and analyse the results. Prior to analysis, preliminary mathematical processing – extracting the desired range (115–1000 cm^{-1}), baseline correction and cosmic spikes removal (the CRR filter) – was executed. Subsequently, an integration filter (with both specific position and width on the spectrum) was applied to the characteristic spectral regions (e.g. the Cr_2O_3 band at ca. 555 cm^{-1}). As a result, chemical distribution maps were generated, a set of distribution images was revealed, and the most representative spectra for each phase were extracted manually, which determined the presence of dominating phases.

X-ray Absorption Spectroscopy (XAS) was performed using the PIRX beamline at the SOLARIS National Synchrotron Radiation Centre, Kraków, Poland. The spectra were collected for various compositions of the prepared protective coating as well as the samples subjected to different oxidation times. Measurements were made for all three elements included in the analysed material by measuring the absorption spectra at the L_3 and L_2 edges of Cu, Mn, and Fe. In the case of copper, pure, and high-grade oxides of Cu_2O and CuO were used as the reference. For manganese, MnO oxide, Mn_2O_3, and MnO_2 oxides were taken as nominal materials. Fe_3O_4 oxide was used to determine the iron oxidation state in the prepared samples.

3. Results

3.1. Powder preparation and characterisation

The phase composition of the powders was determined by XRD measurements. The obtained diffraction pattern for the $CuMn_{1.7}Fe_{0.3}O_4$

Table 1
Nomenclature division of samples with different types of protective layers.

Sample name	Reference	CMFO	CMFO-Gd_2O_3	CMFO-Y_2O_3
Sample composition	Bare Crofer 22 APU	$CuMn_{1.7}Fe_{0.3}O_4$	$CuMn_{1.7}Fe_{0.3}O_4$ – Gd_2O_3	$CuMn_{1.7}Fe_{0.3}O_4$– Y_2O_3

powder is presented in Fig. 1A. Peaks were observed for the cubic phase (space group: *Fd-3m*) at 17°, 31°, 36°, 37.5°, 43°, 52°, 54°, 58°, 64°, and 75°, and for the tetragonal phase (space group: *I41/amd:2*) at 32°, 45°, and 65°. Impurities in the form of MnO_2 and Mn_3O_4 oxide were also observed. Peaks corresponding to MnO_2 were found at 29°, 37°, 57°, 59°, 61°, and 65° and for Mn_3O_4 at 18°, 31°, 44°, and 65°. Ignaczak et al. also observed a mixed cubic and tetragonal phase occurring for $Mn_{1.7}CuFe_{0.3}O_4$ [38]. Bobruk et al. observed $Cu_{1.3}Mn_{1.7}O_4$ impurities in the form of Mn_2O_3 [46].

Due to the requirement of sintering of the spinel-based coatings in reducing-oxidising conditions (redox sintering), understanding the spinel reduction process can be valuable [47]. TPR profiles can indicate the reducing reactivity of metal oxides. In general, a decrease in the reduction temperature indicates an increase in the reduction activity. The composition, particle size and surface area of the metal oxide influence its reducing capacity. The resulting reduction profiles of the spinel are presented in Fig. 1B. Two reduction cycles were performed to better understand the processes happening during the coating preparation step. Two main reduction regions (peaks) were observed, which describe the processes taking place in a complex way. At a temperature close to ~ 250 °C, the start of the reduction of the Cu^{2+} is visible (α), which is quite common in the field of Cu-based spinels. The Cu ions are being easily reduced to Cu^{+} and further into metallic form, which is quite a fast process with no clear distinction between the two steps [48]. The reduction process of Cu ions, depending on the degree of doping, can take place up to a temperature of 400 °C. In this case, it seems to overlap with the manganese ions reduction signal when reducing Mn^{4+} to Mn^{3+} at around 306 °C (β) [49].

Lower temperatures of the reduction into purely metallic species are characteristic for CuO deposited onto carriers such as YSZ or ZrO_2, as well as for highly dispersed copper oxide and Cu^{2+} cations in the octahedral structure of the materials [50–55]. The β peak is a superposition of the single-step bulk Cu^{2+} reduction and the first Mn reduction step. The manganese reduction process from Mn^{4+} to Mn^{2+} revealed a first maximum at ~ 306 °C and continues as a two-step process up to 365 °C (γ) when most of the Mn ions are being converted into a Mn^{2+} state, forming a precipitate of MnO. The lowering of the Mn reduction temperature can be attributed to the Cu-induced spillover effect [56]. Metallic Cu particles are increasing the kinetics of the reduction process of the bulk spinel and the coating preparation temperature can be lowered. The aforementioned processes are also overlapping with the reduction of $Fe^{4+/3+}$ ions into $Fe^{3+/2+}$ species, also indicated as the γ peak. After that step, the sample still contains the Fe_3O_4-FeO phase, which upon further heating above 600 °C under H_2, is slowly converted into metallic iron [55,57–59]. The reduction of iron above 600 °C does not have such a large impact due to the low content of this element in the material. Following the reduction of the spinel structure, it is decomposed into the corresponding mixture of separated oxides/metals. The formation of metallic manganese is not possible within the analysed temperature/pO_2 range and the sample is composed of MnO mixed with metallic Cu and FeO/Fe. The oxidation profile is shown in Fig. S1 A and indicates that full reoxidation was finished up to 800 °C with visible maxima coming from each of the substituents found in the reduced sample. The secondary reduction profile visible in Fig. 1B shows that after the reduction and oxidation process, the spinel structure seems to become more homogenous and most likely tends to recrystallise into micrometric grains, that due to the overwhelming amount of Cu is being reduced in one step with no clear distinction between the undergoing processes. One should take that into account when performing the reduction process, as too-rapid structural changes might induce huge internal stresses and may lead to lower integrity of the layer. Fig. S1 B shows the reduction profile of $MnCo_2O_4$ (MCO) spinel. Compared to the MCO spinel, most of the reduction process of $CuMn_{1.7}Fe_{0.3}O_4$ takes place at temperatures lower than for MCO. For MCO, the main peaks corresponding to the reduction of Co and Mn species to metallic Co and MnO were located at 500 and 685 °C. The result is in line with previous reports on the MCO reduction behaviour [60]. Disregarding the sluggish reduction of the FeO down to metallic Fe, the $CuMn_{1.7}Fe_{0.3}O_4$ is more easily reducible. The reason for such recognition of peaks in TPR is to take into account the value of the redox potential of each cation and to take into account literature data. The redox potentials are respectively for the conversion from $\varphi MnO_2/Mn^{2+}$, $\varphi Mn^{3+}/Mn^{2+}$: + 1.224 eV and + 1.51 eV, respectively, ($\varphi Mn^{2+}/Mn^{0}$) is − 1.186 eV; $\varphi Fe^{3+}/Fe^{2+}$, $\varphi Fe^{2+}/Fe^{0}$ are + 0.771 eV and − 0.44 eV, respectively. The redox potential for copper reduction Cu^{2+}/Cu^{0} is + 0.342 eV.

3.2. Oxidation test

The influence of the spinel layer on steel corrosion behaviour and the influence of a thin ceramic layer of gadolinium oxide and yttrium oxide were investigated by subjecting the samples to corrosion tests at 700 °C. Those conditions were chosen based on the current temperature trend in the SOC [61].

The results of the cyclic thermogravimetry measurements are shown in Fig. 2A in a linear scale, in 2B in a parabolic scale, and in 2 C, the variation of the instantaneous corrosion rate over the course of the experiment. In the case of long-term corrosion, the highest weight gain was observed for the reference sample, equal to 0.158 ± 0.009 mg cm^{-2} after 4000 h. However, a slowdown in the increase in weight gain is visible after 3000 h, where the weight change is small, and after 3500 h, the mass is being maintained practically constant. For the CMFO samples, the total weight gain after 4000 h was 0.042 ± 0.005 mg cm^{-2},

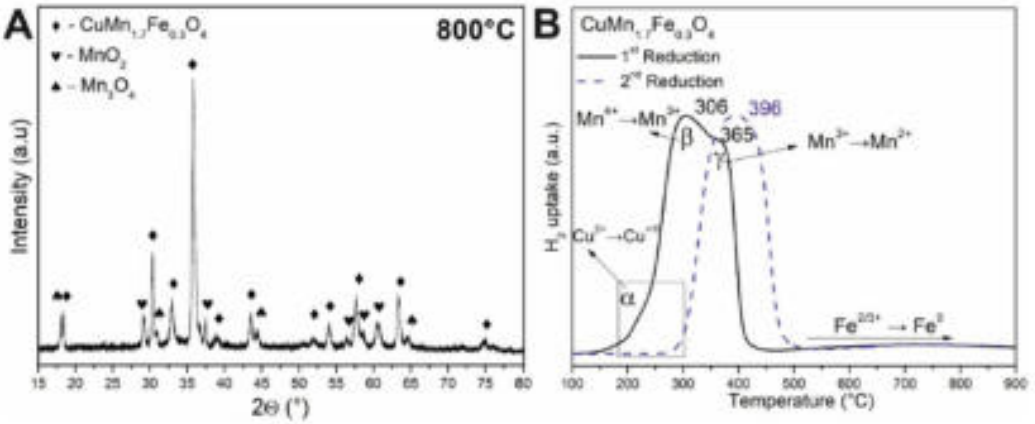


Fig. 1. XRD of the $CuMn_{1.7}Fe_{0.3}O_4$ spinel after calcination at 800 °C (A) and the TRP plot for the reduction of the $CuMn_{1.7}Fe_{0.3}O_4$ (B).

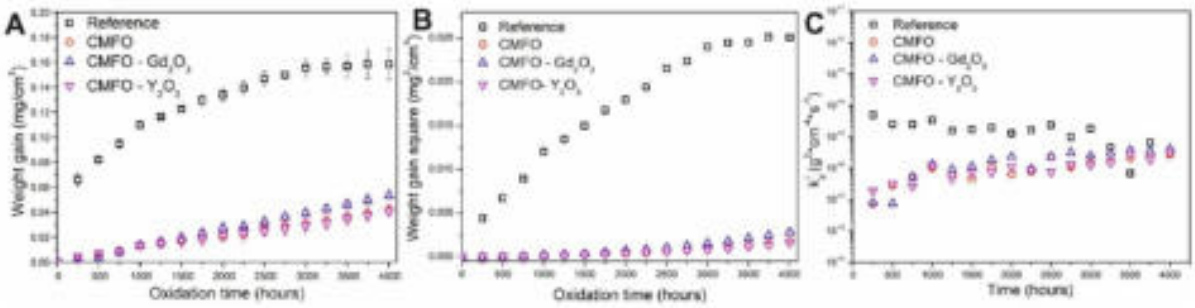


Fig. 2. Weight gain plots for long-term corrosion tests (a), parabolic plot (b), and calculated instantaneous k_p values (c).

which was more than a threefold decrease in this value compared to the reference sample. The same was observed with the CMFO-Gd_2O_3 samples, where after 4000 h, an increase in mass was equal to 0.053 ± 0.004 mg cm^{-2} was seen. The lowest weight gain was obtained for the CMFO-Y_2O_3 samples. Samples with a yttria layer and spinel showed a weight gain after 4000 h equal to 0.041 ± 0.004 mg cm^{-2}, i.e., nearly four times less weight gain than the reference sample.

For clarity, Fig. S2 A and B shows weight gains of coated samples excluding the reference sample. Values presented in Figs. 2 and S2 are based on the average weight gain of the samples. Fig. S3 shows the individual weight gains of the tested specimens of CMFO (S3 A), CMFO-Gd_2O_3 (S3 B) and CMFO-Y_2O_3 (Fig. S3 C). All samples showed a similar variation in weight gain values. However, for the CMFO samples, a smaller number of samples was included in the average due to the occurrence of the layer detaching during the oxidation. This may be influenced by a slightly different TEC (thermal expansion coefficient) which for MCO is 13.1 10^{-6} K^{-1} and for spinel $Cu_{1.4}Mn_{1.6}O_4$ it was set at 13.9 10^{-6} K^{-1} [62,63]. For Crofer 22 APU steel, this value was defined as ~ 12 10^{-6} K^{-1} [63].

The obtained results were compared with other results for similar materials obtained by other groups. Talic et al. showed that Crofer 22 APU steel coated with an MCO protective layer showed a weight gain after 4000 h of a little over 0.08 mg cm^{-2}. Higher weight gains were observed for MCO doped with iron and copper, with ~0.10 mg cm^{-2} and ~ 0.12 mg cm^{-2} in that study [29]. Mazur et al. described a weight gain close to 0.1 mg cm^{-2} [40] for samples of Nirosta 4016/1.4016 steel coated with spinel $Cu_{1.25}Mn_{1.65}Ni_{0.1}O_4$ and oxidised at 800 °C for 2000 h. In their work, Ignaczak et al. compared the weight gains of Crofer 22APU steel samples coated with iron-doped Mn_2CuO_4, $Mn_{1.9}CuFe_{0.1}O_4$, $Mn_{1.7}CuFe_{0.3}O_4$, and MCO, a reference sample (steel sample), and a reference sample of pre-oxidised steel. The smallest mass increase was found in samples with an MCO layer, then pre-oxidised, and subsequently $Mn_{1.7}CuFe_{0.3}O_4$, $Mn_{1.9}CuFe_{0.1}O_4$, and Mn_2CuO_4. The oxidation was carried out at 750 °C for 3000 h [39]. Talic et al. tested the MCO coating of Crofer 22H, 441, and 430 steel, and the corrosion properties were analysed at 700 °C. The corrosion time was 2000 h. The obtained weight gain values at the final stage of the experiment were approximately 0.081 mg cm^{-2}, 0.003 mg cm^{-2}, and ~ 0.031 mg cm^{-2} for steel 441, 430, and Crofer 22H, respectively. The weight gain measurements were subject to considerable error, as indicated by the error bars. A weight loss was observed for Crofer 22H steel coated with MCO. In the case of 430 steel, a reduction in weight gain was initially observed. Then, an increase in mass was observed, and at the final stage of the experiment, the mass increase was higher than the initial value. This problem did not occur in the case of steel 441; however, the weight gain values were very close to the values for steel without a protective layer [64]. The cited literature data indicate good anti-corrosion properties. All the quoted weight gain values are higher than those obtained in this work. The only lower mass increases were observed in the work where it was difficult to analyse mass increases at such low temperatures. In this work, this effect was also improved by using a thin layer of RE-oxide.

The kinetics of the oxidation reaction at high temperatures is described by the square dependence of the weight change during oxidation. The parabolic law is described by the equation:

$$\left(\frac{\Delta m}{A}\right)^2 = k_p t + C \quad (1)$$

where: Δm is the weight gain (g), A is the sample area (cm^2), k_p is the parabolic rate constant (g^2 cm^{-4} s^{-1}), t is the oxidation time (s), and C is the integration constant (g^2 cm^{-4}) [65]. The calculated values of the k_p coefficient are shown in Table 2. The analysed oxidation time was divided into 3 stages (0–1000 h, 1000–3000 h, and 3000–4000 h), taking into account the visible change in mass with the progress of oxidation. For the reference sample, in the first stage, the k_p value was determined to be 3.18 × 10^{-15}, and in subsequent stages, it decreased to 1.68 × 10^{-15} and 3.04 × 10^{-16}, respectively. In the case of coated samples, the initial values were 4.55 × 10^{-17}, 4.61 × 10^{-17}, and 4.57 × 10^{-17} for CMFO, CMFO-Gd_2O_3, and CMFO-Y_2O_3, respectively. An increase in this parameter was observed for all the samples in the period 1000–3000 h. The determined values of the k_p coefficient for coated steels indicate the beneficial effect of using a thin additional layer. This is especially visible for samples with an additional layer of yttrium oxide.

The values of the k_p coefficient indicate the general corrosion properties of the material. As noticed in this study, k_p values vary with time, so an additional analysis of corrosion kinetics vs. time has been added: the instantaneous parabolic oxidation rate constant. The values of k'_p are independent of their duration and assume a constant value for a process consistent with the parabolic law. The net oxidation rate constant k'_p can be calculated by summing the instantaneous values across the measurement range employed in the experiments, according to the formula [66]:

$$k'_p = \sum_{i=1}^{N} \left(\frac{k_p^i + k_p^{i+1}}{2}\right)\left(\frac{t_{i+1} - t_i}{t_N - t_{i+1}}\right) \quad (2)$$

where k'_p is the instantaneous parabolic oxidation rate constant (g^2 cm^{-4} s^{-1}), t is the oxidation time [s], and N represents the number of measurement points.

When the increase in the scale follows the parabolic oxidation rule

Table 2
Calculated k_p values for corrosion experiments.

k_p coefficient × 10^{-15} g^2 cm^{-4} s^{-1}				
Time interval (h)	Reference	CMFO	CMFO-Gd_2O_3	CMFO-Y_2O_3
0–1000	3.18	0.0455	0.0461	0.0457
1000–3000	1.68	0.105	0.199	0.0907
3000–4000	0.304	0.226	0.361	0.236

across all temperatures, the ratio of k_p to k'_p is close to 1. The determined net oxidation rate constants (k_p') are presented in Table 3. The k'_p/k_p ratio, which is used to determine the departure from parabolic oxidation kinetics, is presented in Table 4. The determined values of the instantaneous parabolic oxidation rate do not differ significantly from the parabolic law for each type of presented samples. This indicates that the use of additional thin layers does not significantly affect the corrosion mechanisms. For samples covered with protective layers at the last stage of oxidation, these values are closest to 1, which is well described by the parabolic rate law.

The determined corrosion coefficients showed compliance of the oxidation process with the parabolic law, and the obtained values for Crofer 22 APU steel should be compared with the available literature data. Previous work for the same steel showed a k_p coefficient of 1.26×10^{-15} in the range of 250–1000 h and 0.47×10^{-15} in the range of 1000–2000 h [18]. Talic et al. determined this parameter for Crofer 22H steel as 3.2×10^{-15} at 750 °C for 2000 h [67]. Koszelow et al. showed a value of 4.5×10^{-15} for porous Fe22Cr steel after an oxidation time of 100 h [68]. Shahbaznejad et al. received a value of 2.54×10^{-13} for Crofer 22 APU steel oxidised for 200 h isothermally at 700 °C [69]. Ignaczak et al. obtained values of this coefficient equal to 3.76×10^{-15} and 2.28×10^{-14} for oxidation times of 0–500 h and 500–3000 h at 750 °C [39]. In the case of Crofer 22H steel coated with MCO, Talic et al. reported that the parabolic oxidation coefficient was 9×10^{-16} after 2000 h at 750 °C [64]. In another work, where the coated material was spinel MCO, $MnCo_{1.7}Fe_{0.3}O_4$, and $MnCo_{1.7}Cu_{0.3}O_4$, the k_p coefficient at 700 °C was 5.5×10^{-16}, 6.9×10^{-16} and 1.1×10^{-15} at 700 °C, respectively, for an oxidation time of 4000 h [29]. Ignaczak et al. reported k_p values for Crofer 22 APU steels coated with MnCuFe0, MnCuFe01, and MnCuFe03 spinel of 6.1×10^{-15}, 4.92×10^{-15}, and 4.73×10^{-15}, respectively, at 750 °C for isothermal oxidation for 3000 h [39]. The obtained values of the k_p coefficient are comparable to those reported in the literature. No significant differences are observed for both uncoated steel and the proposed protective layer.

3.3. Electrical resistivity measurement

The interconnects should have a working life of close to 40,000 h and should not exceed the ASR value of 0.1 Ω cm^2 [70]. Fulfilling these two conditions is necessary to obtain adequate efficiency. The results obtained for cross-scale electrical resistance measurements are shown in Fig. 3A–C. In addition, Supplementary Figs. S4A and S4B show the calculated ASR values after the 1000- and 2000-h stages, and Figs. S4 C and S4 D show the activation energy values calculated based on the measurements divided into two stages: high-temperature (700–550 °C) and low-temperature (500–300 °C).

For samples with an oxidation time of zero hours (i.e., for samples with layers and after the heat treatment process and the bare Crofer steel as reference), the ASR values were 7.62 mΩ cm^2, 14.92 mΩ cm^2, 11.47 mΩ cm^2, and 8.07 mΩ cm^2 for the reference sample, CMFO, CMFO-Gd_2O_3, and CMFO-Y_2O_3 samples, respectively. After the final oxidation stage (4000 h), the ASR values were as follows: 12.89 mΩ cm^2, 14.69 mΩ cm^2, 8.76 mΩ cm^2, 7.37 mΩ cm^2 for the reference sample, CMFO, CMFO-Gd_2O_3 and CMFO-Y_2O_3 samples, respectively. It is also worth noting the changes in the ASR values at lower temperatures. In this case, a significant difference was observed in the slope of the curve for the reference sample at the initial stage and after 4000 h, and there was no visible difference in the electrical properties of the reference and coated samples. However, the ASR values for samples coated with a protective layer for each of the analysed types indicate a similar character, and the ASR values at 300 °C were between 1 and 2 Ω cm^2. Together with the ongoing oxidation process, we also observe the convergence of ASR values for individual types. These values also match the trend observed in weight gain measurements. After 1000 h of oxidation, we observe that the lowest ASR value can be observed for samples with an additional layer of Gd_2O_3. Also, the lowest weight gain value was observed for the CMFO-Gd_2O_3 samples. In the next oxidation stage, it was observed that the lowest ASR values were measured for the CMFO-Y_2O_3 samples. This result is equivalent to the lowest weight gain. The sample with an additional layer of gadolinium oxide, despite the worst weight gain among the protective layers used, showed a lower ASR value than the sample with spinel only. Mazur et al. determined the ASR values for the $Mn_{1.5}Co_{1.5}O_4$ and $Mn_{1.45}Co_{1.45}Cu_{0.1}O_4$ layers as 21.4 mΩ cm^2 and 29.3 mΩ cm^2 at 750 °C after oxidation for 1200 h at the same temperature[71]. In another work describing the effect of coating Crofer 22 APU steel with double layers of gadolinium oxide and $MnCo_2O_4$ spinel at 800 °C for 7000 h, an ASR of 19 mΩ cm^2 was obtained [45]. Ignaczak et al. determined the ASR values for the same steel coated with MnCuFe0, MnCuFe01, and MnCuFe03 spinel and oxidised at 750 °C for 3000 h as values between 3 and 5 mΩ cm^2 at 750 °C, which were lower values than for samples with an MCO layer and peroxided samples [39]. Sun et al. reported the coating of Crofer 22 APU steel with $Cu_{1.3}Mn_{1.7}O_4$ spinel and oxidation at 800 °C for 185 h. The ASR value obtained for these combinations was 6.13 mΩ cm^2 at 800 °C [34]. Huang et al. indicated an ASR value of 4.6 mΩ cm^2 for the applied layer of coating the same steel with $CuMn_{1.8}O_4$ spinel and oxidisation for 100 h at 800 °C [72].

The activation energy was determined using the slope obtained during the ASR measurements and according to the Arrhenius law:

$$ASR = A \bullet \exp\left(\frac{E_a}{kT}\right) \quad (3)$$

where: A is a pre-exponential factor (Ω cm^{-2} K^{-1}), Ea is the activation energy (kJ mol^{-1}), k is Boltzmann's constant (J K^{-1}) and T is the temperature (K). The initial activation energies were 11.41 kJ mol^{-1}, 36.53 kJ mol^{-1}, 55.06 kJ mol^{-1}, and 44.58 kJ mol^{-1}, for the reference sample, with a $CuMn_{1.7}Fe_{0.3}O_4$ layer, $CuMn_{1.7}Fe_{0.3}O_4$ with Gd_2O_3 layer, and $CuMn_{1.7}Fe_{0.3}O_4$ with Y_2O_3, respectively (in the range 700–550 °C). A very low value is noticeable for the reference sample, which is not surprising since the initial stage of corrosion of uncoated steel is very fast. The highest value of the activation energy was observed for the $CuMn_{1.7}Fe_{0.3}O_4$-Gd_2O_3 samples. After the final stage of oxidation, the value of Ea was 42.98 kJ mol^{-1}, 54.88 kJ mol^{-1}, 39.48 kJ mol^{-1} and 49.96 kJ mol^{-1} for the reference sample, with a $CuMn_{1.7}Fe_{0.3}O_4$ layer, $CuMn_{1.7}Fe_{0.3}O_4$ with Gd_2O_3 layer, and $CuMn_{1.7}Fe_{0.3}O_4$-Y_2O_3, respectively. These values refer to the analysed range in the higher temperature region. Talic et al. obtained activation energy values for $MnCo_{1.7}Fe_{0.3}O_4$ and $MnCo_{1.7}Cu_{0.3}O_4$ protective coatings in the range of 77–78 kJ mol^{-1} for samples aged at 800 °C for 4370 h and 65 kJ mol^{-1} for clean Crofer 22 APU steel [29]. Bednarz et al. determined the activation energies for $Mn_{1.5}Co_{1.5}O_4$ and $Mn_{1.45}Co_{1.45}Fe_{0.1}O_4$ materials oxidised at 800 °C for 1200 h as 52.40 kJ mol^{-1} and 48.44 kJ mol^{-1}, respectively [73]. The obtained data are comparable with the literature

Table 3
Determined values of the instantaneous oxidation coefficient.

	k'_p coefficient × 10^{-15} g^2 cm^{-4} s^{-1}			
Time interval (h)	Reference	CMFO	CMFO-Gd_2O_3	CMFO-Y_2O_3
0–1000	13.4	0.182	0.200	0.199
1000–3000	16.8	0.930	1.64	0.843
3000–4000	2.98	1.04	1.69	1.06

Table 4
Determined values of the k'_p/k_p ratio for the coatings used, taking into account the oxidation stages.

	k'_p / k_p			
Time interval (h)	Reference	CMFO	CMFO-Gd_2O_3	CMFO-Y_2O_3
0–1000	4.23	4.11	4.34	4.36
1000–3000	9.99	8.86	8.69	9.30
3000–4000	9.81	4.59	4.69	9.30

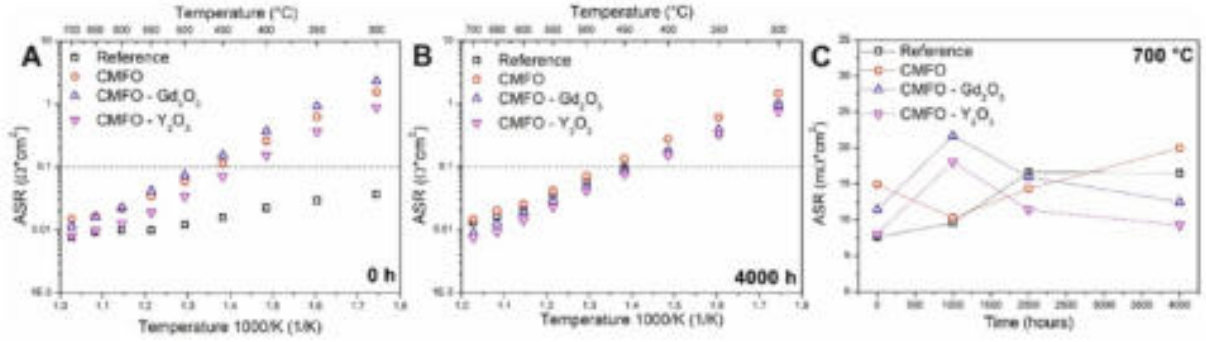


Fig. 3. Arrhenius plots of the surface resistance of samples oxidised at 700 °C for 0 h (A) and 4000 h (B) and comparison of the ASR value at 700 °C over time.

data. Comparisons are mainly at higher temperatures, as corrosion analysis at low temperatures (700 °C) is still largely unknown. However, these values are rational and do not differ from the literature trend.

3.4. XRD and SEM analysis

XRD measurements and SEM analysis of post-mortem samples were also performed. Fig. S5 shows the XRD measurement after 4000 h stages to check the stability of the material over time. The obtained diffraction spectrum makes it possible to identify the main phase in the form of a cubic structure (space group: *Fd*-3*m*) of the $CuMn_{1.7}Fe_{0.3}O_4$ spinel. For samples where the only protective layer is CMFO, small peaks at 29° and 57° were also identified, indicating the presence of MnO_2 in the coating. However, there are no observations of peaks corresponding to Cr_2O_3 and $MnCr_2O_4$ formed during oxidation. For layers with an additional RE oxide protective layer in the case of CMFO-Gd_2O_3, an additional peak is observed at 32.5°, which identified the tetragonal phase (space group: *I*41/*amd*:2). As in the case of CMFO, no peaks corresponding to Cr_2O_3/$MnCr_2O_4$ corrosion were observed and there was no signal from RE oxide in the form of Y_2O_3 or Gd_2O_3. There were also no peaks responsible for $YMnO_3$ or $GdCrO_3$ formed during the oxidation, the existence of which was confirmed in previous work [18].

Fig. 4 presents cross-section images for the sample with the $CuMn_{1.7}Fe_{0.3}O_4$ spinel (Fig. 4A), for the sample with an additional layer of gadolinium oxide (4B), and for the sample with an additional layer of yttrium oxide (4 C) obtained for samples subjected to corrosion for 4000 h at 700 °C. The darker layer visible near the surface of the steel indicates that a very thin layer of Cr_2O_3/$MnCr_2O_4$ had formed. SEM images show a thin layer of chromium oxide (thickest for the sample with CMFO layer). A layer of dense spinel is also observed close to the steel surface. A thin gadolinium oxide-based layer was observed on the Gd_2O_3-modified sample. On the Y_2O_3-modified sample, a discontinuous Y_2O_3 thin layer was observed. Despite these microstructural differences, as shown in Section 3.2, it revealed good corrosion protection properties. Fig. S6 show SEM images showing a larger area of the analysed samples.

Fig. S7 depicts an SEM-EDS analysis illustrating the elemental distribution within the layer. It was demonstrated that there exists a chromium-rich layer in direct contact with the steel. Moreover, noticeable in samples with a CMFO layer are regions of heightened intensity closer to the layer's surface, indicating chromium diffusion through the layer. In samples CMFO-Gd_2O_3 and CMFO-Y_2O_3, a distinct border of chromium oxide occurrence is observed, coinciding with the presence of an additional layer. The discontinuous nature of the Y_2O_3 layer was observed in previous work [18]. Line scans were conducted on the discussed sample types to further understand and illustrate the blocking of chromium diffusion. The obtained line scans are shown in Fig. S8. For the CMFO sample, after 4000 h, a region corresponding to the chromium oxide layer is visible at the peak chromium concentration. The chromium content gradually decreases until reaching the surface area. In samples with an additional layer of gadolinium oxide or yttrium oxide, a distinct flattening of the chromium line after the layer is observed, indicating blocking of chromium diffusion. The inherent blocking capacity of the CMFO layer alone is limited, as demonstrated in prior studies on similar materials. The inclusion of a thin additional layer of yttrium or gadolinium oxide results in a slight reduction in chromium diffusion, possibly influenced by the discontinuous nature and small thickness (~ 100 nm) of the yttrium oxide layer. Reddy et al. described the coating of Crofer 22 APU steel with various protective materials, including $CuMn_{1.8}O_4$ compared to MCO, and compared, among others, chromium evaporation. EDS analysis after 3000 h of oxidation at 800 °C showed that the layer composed of $CuMn_{1.8}O_4$ had the worst parameters

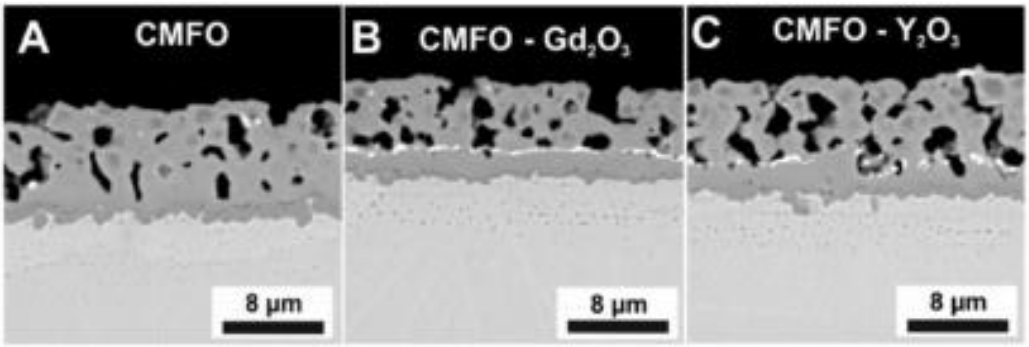


Fig. 4. SEM pictures taken for samples after oxidation for 4000 h at 700 °C. Cross-sections obtained for a sample with a layer of spinel $CuMn_{1.7}Fe_{0.3}O_4$ (A), spinel and gadolinium oxide (B), and spinel and yttrium oxide (C).

for blocking chromium diffusion. In this case, a gradual decrease in the amount of chromium is visible. In the case of MCO, much smaller diffusion is observed, and the chromium map indicates a very small content of chromium diffused into the layer itself [74]. The reason for this may be the greater solubility of chromium in the Cu and Mn-based spinel layers. It has been shown that $CuMn_2O_4$ spinel is an excellent getter of chromium (or chromium oxide) [75]. A similar relationship in EDS maps, like for $CuMn_{1.8}O_4$, is observed for the CMFO layer. A clear change in the slope of the curve in line scans observed for samples with an additional layer indicates an increase in the degree of chromium blocking, but not completely preventing it. Spot measurements were also conducted to precisely determine the chromium content in individual layer parts. The data presented in Fig. S9B were gathered from four points distributed along the layer (Fig. S9A). Chromium content is comparable across all samples at the point nearest to the steel surface. However, a notable reduction in chromium content is observed at the second point for CMFO-Gd_2O_3 and CMFO-Y_2O_3 samples. Chromium concentrations for points closer to the surface have the lowest chromium concentration and comparable across all types. It is also worth noting that the chromium content near the surface is low and a large error is possible at this point with EDS spot analysis. In the case of the comparison of the coefficient between the atomic content of manganese and copper (presented in Fig. S8C), it was shown that the area rich in chromium oxide and the reactive layer have a significantly different coefficient from the basic one. This indicates the potential decomposition of spinel by chromium diffusing into the layer. For the two analysed points further away from the steel surface, it is visible that this coefficient has values close to the target value. This also indicates the lack of degradation of the material itself and the decomposition of spinel into various oxides.

The SEM-EDS analyses presented in the form of element identification mapping, line scans, and point analysis of the layer demonstrated an enhancement in blocking chromium diffusion compared to samples with only a CMFO spinel layer. This enhancement is associated with the presence of a thin layer of Gd_2O_3 or Y_2O_3. However, the extent of improvement is constrained by the low thickness of the additional layer and its discontinuous nature.

3.5. Confocal Raman imaging

In order to describe and understand the reactions between Crofer 22 APU steel, protective layers, and oxygen, measurements were made using Raman Confocal Imaging. For this purpose, samples that had undergone 4000 h of oxidation were selected from among the CMFO, CMFO-Gd_2O_3, and CMFO-Y_2O_3 specimens and were cross-sectioned and polished. Similarly to literature reports [45,76], the formation of two very typical phases for Crofer 22APU below the protective coating was confirmed with Raman Confocal imaging (Fig. 5) – Cr_2O_3 based on bands at ca. 296, 352, 555 (the most characteristic ones) and 616 cm^{-1} [77], as well as $(Mn,Cr)_3O_4$ spinel based on Raman modes at around 509 and 691 cm^{-1} [78]. Moreover, bands at ca. 430 and 541 cm^{-1} were observed for the thickest, top layer, which is composed of CuMnFe spinel [79,80]. As can be seen, two spectra of a very similar shape, especially within the 350–700 cm^{-1} spectral range, were determined – the only, but easily noticeable difference concerns the opposite intensity relation of characteristic bands coming from CuMnFe spinel (541 cm^{-1}) and MnO_2 (622 cm^{-1} [81]) located mainly in the upper part of the protective coating. For specimens with additional protection in the form of Y_2O_3 (Fig. 4B) and Gd_2O_3 (Fig. 4C), results similar to first sample, which were also alike, were obtained – in both cases, Cr_2O_3, Mn-Cr spinel and protective $CuMn_{1.7}Fe_{0.3}O_4$ spinel mixed with MnO_2 were found. In this case, it was impossible to differentiate the location of protective spinel and MnO_2, which suggests the scattering of the latter within the whole coating. As far as Y- and Gd-based phases are concerned, two intriguing observations were made. Firstly, no bands typical for Y_2O_3 and Gd_2O_3 were noticed. Secondly, different type of perovskite-like non-continuous phases were formed, just above the Mn-Cr spinel, depending on the applied oxide – for yttria, $YMnO_3$ was formed (bands at ca. 224, 418, 448, 637, and 691 cm^{-1} [82]) and for gadolinium, it is probable that $GdCrO_3$ or $GdMn_{1-x}Cr_xO_3$ (with x close to 1) was nucleated (modes at around 222, 330, 634, 690 cm^{-1} [83]). Mazur et al. described the formation of a similar Gd-based perovskite–like structure, but for a different protective spinel ($MnCo_2O_4$) [45]. In a previous study that only focused on protective ceramic layers, similar results were also noticed. In that study, the formation of perovskite compounds based on Y and Gd, as well as phases of chromium oxide and manganese-chromium spinel, standard for Crofer 22 APU steel, was observed [18]. The identification of the $YMnO_3$ layer as the reaction product of yttrium during oxidation is an interesting observation. Linescans performed for CMFO-Gd_2O_3 and CMFO-Y_2O_3 samples indicate an increased concentration of manganese near the RE-oxide layer. This may also indicate the reason for the occurrence of $YMnO_3$. In the literature, most often, $YCrO_3$ is identified as a result of the reaction of yttrium oxide and chromium oxide formed during oxidation [18,84,85]. The only work found in which $YMnO_3$ was present described the coating of AISI 430 steel with a layer of Y_2O_3. However, in the cited work, the XRD peaks identified as $YMnO_3$ were small, and the remaining peaks obscured them [86,87]. The influence of the transformation of yttrium oxide and gadolinium oxide on perovskite compounds is also visible in those described in Section 3.3 by observing lower ASR values for the CMFO-Y_2O_3 and CMFO-Gd_2O_3 samples, even despite the greater weight gain for the second type. The reason for this is that perovskite oxides are characterised by much higher electronic conductivity than reactive element oxides. Additionally, the highest ASR value was observed for the sample with only spinel, which is probably related to the significant amount of manganese oxide observed in this study.

3.6. XAS spectroscopy

To supplement the discussion on the characteristics of the $CuMn_{1.7}Fe_{0.3}O_4$ spinel material and the impact of interactions with other materials, such as the applied ceramic layers and the Crofer 22 APU steel itself, a series of X-ray absorption spectroscopy (XAS) measurements was taken. The obtained Cu L_3-edge spectra for copper are presented in Fig. 6A. Analogous measurements for manganese and iron electronic surrounding are shown in Fig. 6B and Fig. 6C, respectively. The absorption edges of the Cu reference powders were observed at 938.85 eV for CuO and 931.55 eV for Cu_2O. This is in line with the standardised data recorded previously for Cu oxides. In case of the copper-manganese-iron spinel analysis, a sharp band at ~ 938.85 eV was observed in all cases, which indicates the presence of copper in the Cu^{2+} oxidation state. The observed peaks indicate the excitation of the Cu 2p electron, which under the influence of the energy quantum, goes to a higher energy level, in this case 3d, occupying the unoccupied band and resulting in the $2p^5\ 3d^{10}$ configuration [87]. The obtained spectra correspond to the presence of copper as a divalent cation within the A-site in the spinel structure [88]. A more complex situation is observed in the case of manganese. For the MnO, the absorption edge white line was observed at 640.2 eV, for the Mn_2O_3 at 642.2 eV, and for the MnO_2 at 642.9 eV, respectively. For manganese in the Mn^{2+} oxidation state, the observed binding energy value of the edge can stand for high-spin manganese ions in the $3d^5$ configuration. Respectively, for the Mn^{3+} oxidation state, the electronic configuration of $3d^4$ was recorded, and the $3d^3$ configuration for the Mn^{4+} ions [89]. The manganese ions in the $CuMn_{1.7}Fe_{0.3}O_4$ spinel were found to be in mixed valence, occupying all three oxidation states. A change in the valence after the exposure to an oxidising environment was also observed. With the CMFO and CMFO-Gd_2O_3 samples, a decrease in the oxidation state of the Mn oxidation state was observed in relation to the initial data, while the Mn^{3+} and Mn^{2+} bands became more pronounced at 640.2 eV and 642.2 eV, respectively. In contrast, for the samples with an additional layer of yttrium oxide, the transition of manganese to higher oxidation

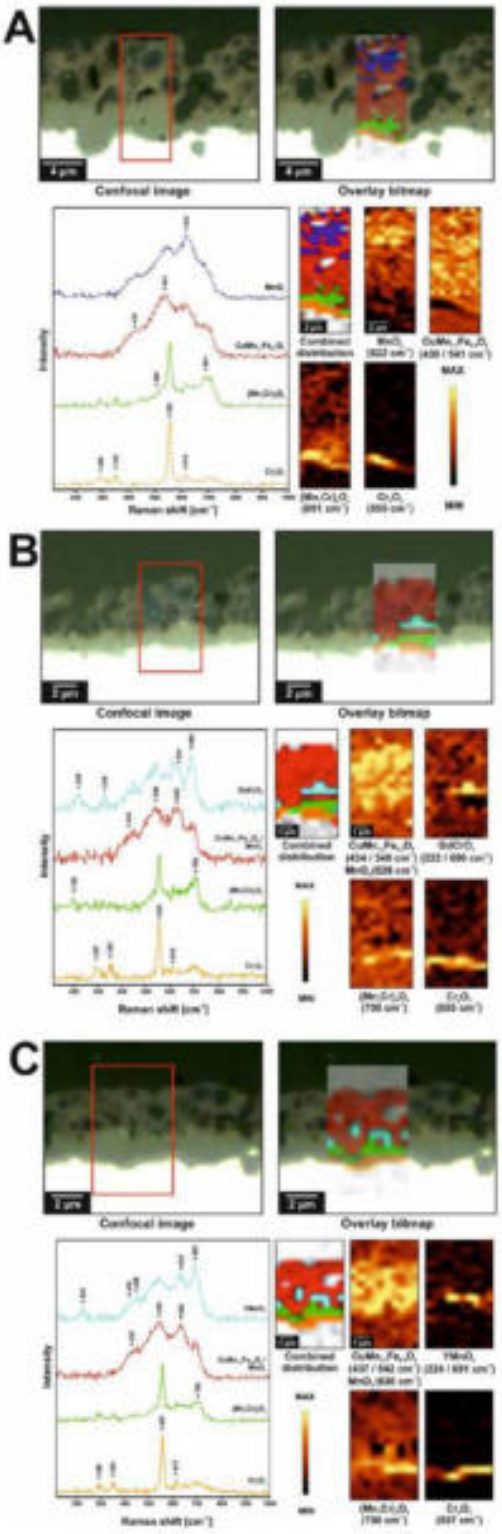


Fig. 5. Raman Confocal imaging for Crofer 22 APU steel samples with a protective layer of $CuMn_{1.7}Fe_{0.3}O_4$ (A), $CuMn_{1.7}Fe_{0.3}O_4$-Gd_2O_3 (B) and $CuMn_{1.7}Fe_{0.3}O_4$-Y_2O_3(C) after 4000 h of oxidation at 700 °C. For all Raman data: red square in confocal image corresponds to area investigated with Raman laser. Raman distribution images (obtained via the integration of the most characteristic band for the specific phase along with value of its Raman shift given in the brackets) are illustrated with the Raman spectra. Each spectrum was also marked with bands that can be unequivocally attributed to corresponding phase(s).

(caption on next column)

states was observed. For the Fe reference powder, the absorption edges were observed at 708.3 eV (corresponding to Fe^{2+}) and at 709.7 eV (the characteristic maximum for Fe^{3+}). The Fe L_3-edge of the spinel-only-covered sample was located at 709.7 eV, which implies that most of the iron ions had undergone Fe^{3+} oxidation. This indicates a successful occupancy of the octahedral position of the $3d^5$ trivalent iron in the spinel B-site structure [89]. No significant differences after the corrosion tests were observed for both copper and iron. Copper occupies the spinel's tetrahedral A-site, and trivalent iron resides in the B-site of the spinel. Only minor changes were observed for the manganese valence. XAS measurements indicate differences that occur in the material during oxidation (specifically in the case of Mn). For the CMFO samples, the MnO_2 that was seen in the CRI and XRD measurements could not be found in the XAS, probably due to the possibility because only the sample's surface could be analysed.

4. Conclusions

This work demonstrated the potential of using $CuMn_{1.7}Fe_{0.3}O_4$ spinel with thin additional protective layers (Gd_2O_3, Y_2O_3) to protect interconnectors at 700 °C. The material was characterised using TPR, which showed that reduction begins at approximately 250 °C with Cu reducing to metallic copper. The spinel exhibited a lower reduction temperature compared to MCO, influenced by the presence of metallic Cu.

Electrophoretic deposition technique allowed for adequate application of protective layers on Crofer 22 APU steel. Three coating types were tested: spinel only (CMFO), spinel with gadolinium oxide (CMFO-Gd_2O_3), and spinel with yttrium oxide (CMFO-Y_2O_3). These were oxidised at 700 °C for 4000 h. The CMFO-Y_2O_3 coating demonstrated the lowest weight gain, while the other samples showed slightly higher values. Electrical resistivity measurements revealed low Area Specific Resistance (ASR) values for all coated samples, with no significant increase in ASR or activation energy observed throughout the analysis period.

Comprehensive material analysis after oxidation was conducted using SEM-EDS, Confocal Raman imaging (CRI), X-ray Absorption Spectroscopy (XAS), and X-ray Diffraction (XRD). These techniques indicated the presence of standard phases in Crofer 22 APU steel, including chromium oxide and manganese-chromium spinel. The additional yttria and gadolinium oxide coatings resulted in the formation of $YMnO_3$ and $GdCrO_3$ perovskite phases, respectively. These analyses also confirmed the presence of a low content of the MnO_2 phase.

Spot and linescan microscopic analyses confirmed enhanced chromium diffusion blocking in samples with additional RE-oxide layers. This is particularly significant due to the nature of copper manganese spinels, which typically show weaker chromium diffusion blocking compared to state-of-the-art $(Mn,Co)_3O_4$.

XAS measurements carried out on samples with different oxidation times detected changes occurring in the structure of the protective layer after subsequent stages of oxidation. No changes in the oxidation state of copper and iron were observed. During the oxidation process, the significant changes were observed with the manganese, where shifts towards a higher oxidation state (CMFO-Y_2O_3) or towards a lower one (for other types of samples) were observed. A graphical summary of the impact of the additional reactive element layer is presented in the Fig. 7.

The proposed new combination of coating represents a viable

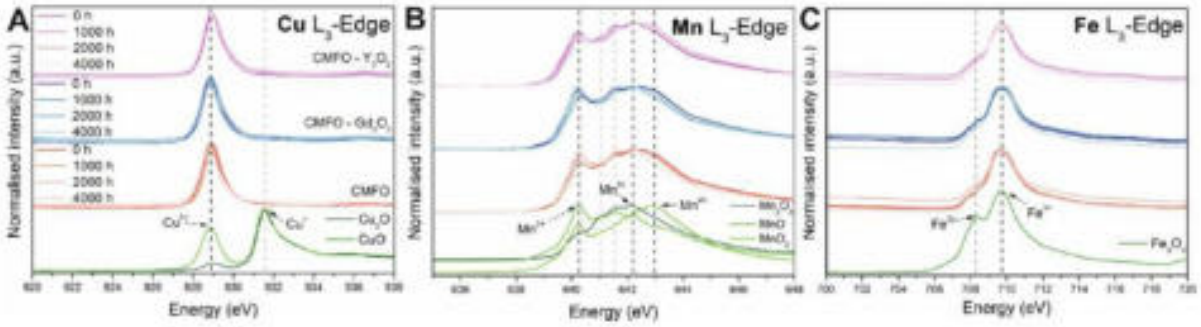


Fig. 6. XAS spectra collected for samples after different oxidation times for the L3 edge of copper (A), manganese (B), and iron (C).

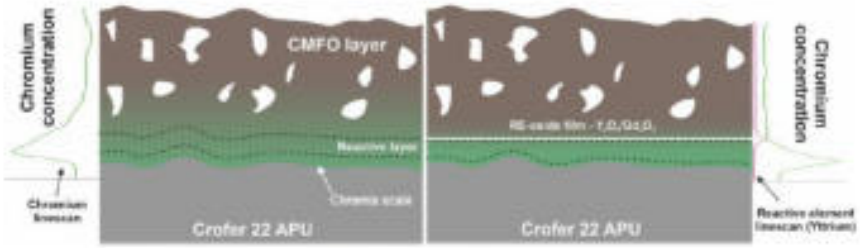


Fig. 7. Sketch explaining the effect of an additional layer in blocking chromium diffusion.

alternative to the state-of-the-art $(Mn,Co)_3O_4$ spinels. The tested materials are free of cobalt, while maintaining its protective and even improving the electrical properties. The effective reduction of cobalt in SOC materials opens the door to an effective reduction in production costs and dispels doubts in the context of possible health and environmental issues.

CRediT authorship contribution statement

Maciej Bik: Writing – review & editing, Writing – original draft, Methodology, Investigation. **Piotr Jasiński:** Writing – review & editing, Supervision, Methodology, Funding acquisition, Conceptualization. **Sebastian Molin:** Writing – review & editing, Writing – original draft, Supervision, Methodology, Conceptualization. **Marcin Zając:** Writing – review & editing, Methodology, Investigation. **Maciej Sitarz:** Writing – review & editing, Methodology. **Bartłomiej Lemieszek:** Writing – review & editing, Writing – original draft, Methodology, Investigation. **Justyna Ignaczak:** Writing – review & editing, Methodology, Investigation. **Krystian Lankauf:** Writing – review & editing, Methodology, Investigation. **Patryk Błaszczak:** Writing – review & editing, Methodology, Investigation.

Declaration of Competing Interest

The authors declare the following financial interests/personal relationships which may be considered as potential competing interests: Piotr Jasinski reports financial support was provided by National Science Centre Poland. If there are other authors, they declare that they have no known competing financial interests or personal relationships that could have appeared to influence the work reported in this paper.

Data availability

The raw/processed data required to reproduce these findings cannot be shared at this time as the data also forms part of an ongoing study.

Acknowledgement

This research has been supported by National Science Centre (NCN) Harmonia 9 Project no. UMO-2017/26/M/ST8/00438: 'Quest for novel materials for solid oxide cell interconnect coatings'. This publication was partially developed under the provision of the Polish Ministry and Higher Education project 'Support for research and development with the use of research infra-structure of the National Synchrotron Radiation Centre SOLARIS' under Contract nr. 1/SOL/2021/2. The authors would like to acknowledge MSc Patryk Zając from AGH UST for his help during the execution of the Raman Confocal Imaging.

Declaration of Competing Interest

The authors declare that they have no known competing financial interests or personal relationships that could have appeared to influence the work reported in this paper.

Appendix A. Supporting information

Supplementary data associated with this article can be found in the online version at doi:10.1016/j.jeurceramsoc.2024.116743.

References

[1] N. Shaigan, W. Qu, D.G. Ivey, W. Chen, A review of recent progress in coatings, surface modifications and alloy developments for solid oxide fuel cell ferritic stainless steel interconnects, J. Power Sources 195 (2010) 1529–1542, https://doi.org/10.1016/J.JPOWSOUR.2009.09.069.

[2] N. Mahato, A. Banerjee, A. Gupta, S. Omar, K. Balani, Progress in material selection for solid oxide fuel cell technology: a review, Prog. Mater. Sci. 72 (2015) 141–337, https://doi.org/10.1016/j.pmatsci.2015.01.001.

[3] S. Chevalier, L. Combemale, I. Popa, S. Chandra-Ambhorn, W. Chandra-Ambhorn, P. Promdirek, P. Wongpromrat, Development of sofc interconnect stainless steels, Solid State Phenom. 300 (2020) 135–156, https://doi.org/10.4028/www.scientific.net/SSP.300.135.

[4] Z. Yang, J.E. Soc, Z. Yang, K.S. Weil, D.M. Paxton, J.W. Stevenson, Selection and Evaluation of Heat-Resistant Alloys for SOFC Interconnect Applications Selection and Evaluation of Heat-Resistant Alloys for SOFC Interconnect Applications, 2003. (https://doi.org/10.1149/1.1595659).

[5] S. Canovic, J. Froitzheim, R. Sachitanand, M. Nikumaa, M. Halvarsson, L. G. Johansson, J.E. Svensson, Oxidation of Co- and Ce-nanocoated FeCr steels: a microstructural investigation, Surf. Coat. Technol. 215 (2013) 62–74, https://doi.org/10.1016/J.SURFCOAT.2012.08.096.
[6] A. Magrasó, H. Falk-Windisch, J. Froitzheim, J.E. Svensson, R. Haugsrud, Reduced long term electrical resistance in Ce/Co-coated ferritic stainless steel for solid oxide fuel cell metallic interconnects, Int. J. Hydrog. Energy 40 (2015) 8579–8585, https://doi.org/10.1016/J.IJHYDENE.2015.04.147.
[7] F. Soeidpour, M. Zandrahimi, H. Ebrahimifar, Evaluation of pulse electroplated cobalt/yttrium oxide composite coating on the Crofer 22 APU stainless steel interconnect, Int. J. Hydrog. Energy 44 (2019) 3157–3169, https://doi.org/10.1016/J.IJHYDENE.2018.12.062.
[8] X. Deng, P. Wei, M.R. Bateni, A. Petric, Cobalt plating of high temperature stainless steel interconnects, J. Power Sources 160 (2006) 1225–1229, https://doi.org/10.1016/J.JPOWSOUR.2006.03.024.
[9] K. Huang, P.Y. Hou, J.B. Goodenough, Reduced area specific resistance for iron-based metallic interconnects by surface oxide coatings, Mater. Res. Bull. 36 (2001) 81–95, https://doi.org/10.1016/S0025-5408(01)00506-2.
[10] S. Molin, H. Persson, T.L. Skafte, A.L. Smitshuysen, S.H. Jensen, K.B. Andersen, H. Xu, M. Chen, P.V. Hendriksen, Effective yttrium based coating for steel interconnects of solid oxide cells: corrosion evaluation in steam-hydrogen atmosphere, J. Power Sources 440 (2019), https://doi.org/10.1016/j.jpowsour.2019.226814.
[11] L. Yang, X. Pang, G. Fox-Rabinovich, S. Veldhuis, I. Zhitomirsky, Electrodeposition of cerium oxide films and composites, Surf. Coat. Technol. 206 (2011) 1–7, https://doi.org/10.1016/j.surfcoat.2011.06.029.
[12] I. Zhitomirsky, A. Petric, Electrolytic and electrophoretic deposition of CeO2 films, Mater. Lett. 40 (1999) 263–268, https://doi.org/10.1016/S0167-577X(99)00087-7.
[13] I. Zhitomirsky, A. Petric, Electrochemical deposition of yttrium oxide, J. Mater. Chem. 10 (2000) 1215–1218, https://doi.org/10.1039/b000311p.
[14] J.S. Yoon, J. Lee, H.J. Hwang, C.M. Whang, J.W. Moon, D.H. Kim, Lanthanum oxide-coated stainless steel for bipolar plates in solid oxide fuel cells (SOFCs), J. Power Sources 181 (2008) 281–286, https://doi.org/10.1016/J.JPOWSOUR.2007.12.053.
[15] L. Mazur, J. Pleniński, J. Dąbek, A. Gil, T. Brylewski, High-temperature oxidation of ferritic steel surface-modified with gadolinium oxide nanoparticles, Ceram. Mater. 71 (2019) 179–192.
[16] L. Venkataraman, R. Ae, M.F. Pillis, A.E. Stela, M.C. Fernandes, Role of rare earth oxide coatings on oxidation resistance of chromia-forming alloys, J. Mater. Sci. 43 (2008) 530–535, https://doi.org/10.1007/s10853-007-1855-8.
[17] A. Ballard, P. Gannon, M. Deibert, S. Chevalier, G. Caboche, S. Fontana, Investigation of La_2O_3 and/or $(Co,Mn)_3O_4$ deposits on Crofer22APU for the SOFC interconnect application, Surf. Coat. Technol. 203 (2009) 3291–3296, https://doi.org/10.1016/J.SURFCOAT.2009.04.017.
[18] B. Lemieszek, J. Ignaczak, B. Kanecki, J. Karczewski, M.B. Mogensen, S. Molin, P. Jasiński, Electrolytic deposition of reactive element thin films on Crofer 22 APU and evaluation of the resulting high-temperature corrosion protection properties at 700–900 °C, Int. J. Hydrog. Energy 47 (2022) 33453–33465, https://doi.org/10.1016/J.IJHYDENE.2022.07.220.
[19] N. Orlovskaya, A. Coratolo, C. Johnson, R. Gemmen, Structural characterization of lanthanum chromite perovskite coating deposited by magnetron sputtering on an iron-based chromium-containing alloy as a promising interconnect material for SOFCs, J. Am. Ceram. Soc. 87 (2005), https://doi.org/10.1111/j.1151-2916.2004.tb06350.x.
[20] N. Shaigan, D.G. Ivey, W. Chen, Oxidation and electrical behavior of nickel/lanthanum chromite-coated stainless steel interconnects, J. Power Sources 183 (2008) 651–659, https://doi.org/10.1016/j.jpowsour.2008.05.024.
[21] X. Montero, N. Jordán, J. Pirón-Abellán, F. Tietz, D. Stöver, M. Cassir, I. Villarreal, Spinel and perovskite protection layers between Crofer22APU and $La_{0.8}Sr_{0.2}FeO_3$ cathode materials for SOFC interconnects, J. Electrochem. Soc. 156 (2009) B188, https://doi.org/10.1149/1.3029914.
[22] Z. Yang, G.-G. Xia, G.D. Maupin, J.W. Stevenson, Evaluation of perovskite overlay coatings on ferritic stainless steels for SOFC interconnect applications, J. Electrochem. Soc. 153 (2006) A1852, https://doi.org/10.1149/1.2219371.
[23] N.S. Waluyo, R.-H. Song, S.-B. Lee, T.-H. Lim, S.-J. Park, J.-W. Lee, Electrophoretically deposited $LaNi_{0.6}Fe_{0.4}O_3$ perovskite coatings on metallic interconnects for solid oxide fuel cells, J. Electrochem. Soc. 163 (2016) F1245–F1250, https://doi.org/10.1149/2.1171610jes.
[24] R. Lacey, A. Poursaeidesfahani, J.C. Lee, J.I. Jung, B. Jiang, D.D. Edwards, R. Nasim, S. T. Misture, Evaluation of Co and perovskite Cr-blocking thin films on SOFC interconnects, Solid State Ion. 181 (2010) 1294–1302, https://doi.org/10.1016/J.SSI.2010.07.007.
[25] B.-K. Park, R.-H. Song, S.-B. Lee, T.-H. Lim, S.-J. Park, C.-O. Park, J.-W. Lee, A perovskite-type lanthanum cobaltite thin film synthesized via an electrochemical route and its application in SOFC interconnects, J. Electrochem. Soc. 162 (2015) F1549–F1554, https://doi.org/10.1149/2.0901514jes.
[26] A. Masi, S. Frangini, D. Pumiglia, L. Della Seta, A. Masci, S.J. Mcphail, M. Carlini, $LaFeO_3$ perovskite conversion coatings grown on a 13Cr ferritic stainless steel: a corrosion degradation study in simulated solid oxide fuel cell (SOFC) interconnect conditions, at 700 (2016) RC.
[27] R.J. HE, J.R. Craig, G.V. Gibbs, PHYSICS I] CHEMISTRY MIHERALS Systematics of the Spinel Structure Type, 1979.
[28] J. Xiao, W. Zhang, C. Xiong, B. Chi, J. Pu, L. Jian, Oxidation of $MnCo_{1.5}O_{1.5}O_4$ spinel coated SUS430 alloy interconnect in anode and cathode atmospheres for intermediate temperature solid oxide fuel cell, Int. J. Hydrog. Energy 40 (2015) 1868–1876, https://doi.org/10.1016/J.IJHYDENE.2014.11.124.
[29] B. Talic, S. Molin, K. Wiik, P.V. Hendriksen, H.L. Lein, Comparison of iron and copper doped manganese cobalt spinel oxides as protective coatings for solid oxide fuel cell interconnects, J. Power Sources 372 (2017) 145–156, https://doi.org/10.1016/J.JPOWSOUR.2017.10.060.
[30] D. Szymczewska, S. Molin, P. Vang Hendriksen, P. Jasi Nski, Microstructure and Electrical Properties of Fe,Cu Substituted $(Co,Mn)_3O_4$ Thin Films (2017).
[31] A. Masi, M. Bellusci, S.J. McPhail, F. Padella, P. Reale, J.E. Hong, R. Steinberger-Wilckens, M. Carlini, The effect of chemical composition on high temperature behaviour of Fe and Cu doped Mn-Co spinels, Ceram. Int. 43 (2017) 2829–2835, https://doi.org/10.1016/J.CERAMINT.2016.11.135.
[32] S. Joshi, A. Petric, Nickel substituted $CuMn_2O_4$ spinel coatings for solid oxide fuel cell interconnects, Int. J. Hydrog. Energy 42 (2017) 5584–5589, https://doi.org/10.1016/J.IJHYDENE.2016.08.075.
[33] Z. Sun, R. Wang, A.Y. Nikiforov, S. Gopalan, U.B. Pal, S.N. Basu, $CuMn_{1.8}O_4$ protective coatings on metallic interconnects for prevention of Cr-poisoning in solid oxide fuel cells, J. Power Sources 378 (2018) 125–133, https://doi.org/10.1016/J.JPOWSOUR.2017.12.031.
[34] Z. Sun, S. Gopalan, U.B. Pal, S.N. Basu, $Cu_{1.3}Mn_{1.7}O_4$ spinel coatings deposited by electrophoretic deposition on Crofer 22 APU substrates for solid oxide fuel cell applications, Surf. Coat. Technol. 323 (2017) 49–57, https://doi.org/10.1016/J.SURFCOAT.2016.09.028.
[35] S.R. Akanda, N.J. Kidner, M.E. Walter, Spinel coatings on metallic interconnects: effect of reduction heat treatment on performance, Surf. Coat. Technol. 253 (2014) 255–260, https://doi.org/10.1016/J.SURFCOAT.2014.05.049.
[36] B.K. Sovacool, The precarious political economy of cobalt: balancing prosperity, poverty, and brutality in artisanal and industrial mining in the Democratic Republic of the Congo, Extr. Ind. Soc. 6 (2019) 915–939, https://doi.org/10.1016/J.EXIS.2019.05.018.
[37] D. Lison, S. Van Den Brule, G. Van Maele-Fabry, Critical Reviews in Toxicology Cobalt and its compounds: update on genotoxic and carcinogenic activities Cobalt and its compounds: update on genotoxic and carcinogenic activities, 2018. (https://doi.org/10.1080/10408444.2018.1491025).
[38] J. Ignaczak, Y. Naumovich, K. Górnicka, J. Janrus, W. Wróbel, J. Karczewski, M. Chen, P. Jasi, S. Molin, Preparation and characterisation of iron substituted $Mn_{1.5}Cu_{1.5-x}Fe_xO_4$ spinel oxides (x = 0, 0.1, 0.3, 0.5), J. Eur. Ceram. Soc. (2020) 1–10, https://doi.org/10.1016/j.jeurceramsoc.2020.07.001.
[39] J. Ignaczak, L. Zeng, D.F. Sanchez, M. Makowska, K. Górnicka, K. Lankauf, J. Karczewski, P. Jasiński, S. Molin, Fe-modified Mn_2CuO_4 spinel oxides: coatings based on abundant elements for solid oxide cell interconnects, Int. J. Hydrog. Energy (2023), https://doi.org/10.1016/J.IJHYDENE.2023.06.041.
[40] L. Mazur, D. Kosmelow, M. Zając, M. Łapiński, M. Bik, P. Zając, A. Adamczyk, P. Rutkowski, S. Molin, T. Brylewski, Comparison of $Cu_{1.3}Mn_{1.7}O_4$ spinels doped with Ni or Fe and synthesized via wet chemistry and solid-state reaction methods, designed as potential coating materials for metallic interconnects, J. Eur. Ceram. Soc. 43 (2023) 5557–5574, https://doi.org/10.1016/J.JEURCERAMSOC.2023.05.015.
[41] N. Hosseini, M.H. Abbasi, F. Karimzadeh, G.M. Choi, Development of $Cu_{1.3}Mn_{1.7}O_4$ spinel coating on ferritic stainless steel for solid oxide fuel cell interconnects, J. Power Sources 273 (2015) 1073–1083, https://doi.org/10.1016/j.jpowsour.2014.10.017.
[42] B.K. Park, D.W. Kim, R.H. Song, S.B. Lee, T.H. Lim, S.J. Park, C.O. Park, J.W. Lee, Design of a dual-layer ceramic interconnect based on perovskite oxides for segmented-in-series solid oxide fuel cells, J. Power Sources 300 (2015) 318–324, https://doi.org/10.1016/J.JPOWSOUR.2015.09.082.
[43] X. Yang, H. Tu, Q. Yu, Fabrication of Co_3O_4 and $La_{0.6}Sr_{0.4}CoO_{3-\delta}$-$Ce_{0.8}Gd_{0.2}O_{2-\delta}$ dual layer coatings on SUS430 steel by in-situ phase formation for solid oxide fuel cell interconnects, Int. J. Hydrog. Energy 40 (2015) 607–614, https://doi.org/10.1016/J.IJHYDENE.2014.11.021.
[44] T. Brylewski, S. Molin, M. Marczyński, Mazur, K. Domaradzki, O. Krystiał, A. Gil, Influence of Gd deposition on the oxidation behavior and electrical properties of a layered system consisting of Crofer 22 APU and $MnCo_2O_4$ spinel, Int. J. Hydrog. Energy 46 (2021) 6775–6791, https://doi.org/10.1016/J.IJHYDENE.2020.11.169.
[45] L. Mazur, J. Ignaczak, M. Bik, S. Molin, M. Sitarz, T. Aleksander Gil, Brylewski, Effectiveness of a dual surface modification of metallic interconnects for application in energy conversion devices, Int. J. Hydrog. Energy 47 (2022) 6295–6311, https://doi.org/10.1016/J.IJhydene.2021.11.256.
[46] M. Bobruk, K. Durczak, J. Dąbek, T. Brylewski, Structure and electrical properties of Mn-Co-O spinels, J. Mater. Eng. Perform. 26 (2017) 1598–1604, https://doi.org/10.1007/s11665-017-2588-8.
[47] M. Bobruk, S. Molin, M. Chen, T. Brylewski, P.V. Hendriksen, Sintering of $MnCo_2O_4$ coatings prepared by electrophoretic deposition, Mater. Lett. 213 (2018) 394–398, https://doi.org/10.1016/j.matlet.2017.12.046.
[48] X. Wan, N. Tang, Q. Xie, S. Zhao, C. Zhou, Y. Dai, Y. Yang, A $CuMn_2O_4$ spinel oxide as a superior catalyst for the aerobic oxidation of 5-hydroxymethylfurfural toward 2,5-furandicarboxylic acid in aqueous solvent, Catal. Sci. Technol. 11 (2021) 1497–1509, https://doi.org/10.1039/d0cy01649g.
[49] Y.T. Ting Zhou, Qing Wang Aijuan Xie, Zerui Zhu Xiang Li, Wanqi Zhang, A novel high-performance CeO_2-$CuMn_2O_4$ catalyst for toluene degradation, Environ. Sci. Pollut. Res. Ifqp. 306 (2020) 22008316.
[50] R. xian Zhou, T. ming Yu, X. yuan Jiang, F. Chen, X. ming Zheng, Temperature-programmed reduction and temperature-programmed desorption studies of CuO/ZrO_2 catalysts, Appl. Surf. Sci. 148 (1999) 263–270, https://doi.org/10.1016/S0169-4332(99)00269-9.

[51] S.D. Robertson, B.D. McNicol, J.H. De Baas, S.C. Kloet, J.W. Jenkins, Determination of reducibility and identification of alloying in copper-nickel-on-silica catalysts by temperature-programmed reduction, J. Catal. 37 (1975) 424–431, https://doi.org/10.1016/0021-9517(75)90179-7.
[52] C.J.G. Van Der Grift, A. Mulder, J.W. Geus, Characterization of silica-supported copper catalysts by means of temperature-programmed reduction, Appl. Catal. 60 (1990) 181–192, https://doi.org/10.1016/S0166-9834(00)82181-8.
[53] M. Shimokawabe, H. Asakawa, N. Takezawa, Characterization of copper/zirconia catalysts prepared by an impregnation method, Appl. Catal. 59 (1990) 45–58, https://doi.org/10.1016/S0166-9834(00)82186-7.
[54] W.P. Dow, Y.P. Wang, T.J. Huang, Yttria-stabilized zirconia supported copper oxide catalyst: I. Effect of oxygen vacancy of support on copper oxide reduction, J. Catal. 160 (1996) 155–170, https://doi.org/10.1006/JCAT.1996.0135.
[55] L. Dong, Z. Liu, Y. Hu, Y. Chen, Dispersion and reduction behavior of systems CuO/α-Fe_2O_3 systems, J. Chem. Soc., Faraday Trans. 94 (1998) 3033–3038, https://doi.org/10.1039/A803630F.
[56] F.C. Buciuman, F. Patcas, T. Hahn, A spillover approach to oxidation catalysis over copper and manganese mixed oxides, Chem. Eng. Process. Process. Intensif. 38 (1999) 563–569, https://doi.org/10.1016/S0255-2701(99)00053-7.
[57] Z. Zhang, Y. Wang, Q. Tan, Z. Zhong, F. Su, Facile solvothermal synthesis of mesoporous manganese ferrite ($MnFe_2O_4$) microspheres as anode materials for lithium-ion batteries, J. Colloid Interface Sci. 398 (2013) 185–192, https://doi.org/10.1016/J.JCIS.2013.01.067.
[58] G. Munteanu, L. Ilieva, D. Andreeva, Kinetic parameters obtained from TPR data for α-Fe_2O_3 and Au/α-Fe_2O_3 systems, Thermochim. Acta 291 (1997) 171–177, https://doi.org/10.1016/S0040-6031(96)03097-3.
[59] H. Qin, Y. Yang, W. Shi, Y. She, S. Wu, Heterogeneous Fenton degradation of azithromycin antibiotic in water catalyzed by amino/thiol-functionalized $MnFe_2O_4$ magnetic nanocatalysts, J. Environ. Chem. Eng. 9 (2021) 106184, https://doi.org/10.1016/j.jece.2021.106184.
[60] M. Ghiasee, M. Rezaei, F. Meshkani, S. Mobini, Preparation of the Mn/Co mixed oxide catalysts for low-temperature CO oxidation reaction, Environ. Sci. Pollut. Res. 28 (2021) 379–388, https://doi.org/10.1007/s11356-020-10484-x.
[61] L. Chen, Z. Yang, B. Jha, G. Xia, J.W. Stevenson, Clad metals, roll bonding and their applications for SOFC interconnects, J. Power Sources 152 (2005) 40–45, https://doi.org/10.1016/J.JPOWSOUR.2005.01.055.
[62] A. Petric, H. Ling, Electrical conductivity and thermal expansion of spinels at elevated temperatures, J. Am. Ceram. Soc. 90 (2007) 1515–1520, https://doi.org/10.1111/j.1551-2916.2007.01522.x.
[63] A. Das Sharma, J. Mukhopadhyay, R.N. Basu, Synthesis and characterization of nanocrystalline $MnCo_2O_{4.4}$ spinel for protective coating application in SOFC, ECS Trans. 35 (2011) 2509–2517, https://doi.org/10.1149/1.3570249.
[64] B. Talic, V. Venkatachalam, P.V. Hendriksen, R. Kiebach, Comparison of $MnCo_2O_4$ coated Crofer 22H, 441, 430 as interconnects for intermediate-temperature solid oxide fuel cell stacks, J. Alloy. Compd. 821 (2020) 153229, https://doi.org/10.1016/j.jallcom.2019.153229.
[65] B. Pieraggi, Calculations of parabolic reaction rate constants, Oxid Met. 27 (1987) 177–185, https://doi.org/10.1007/BF00667057.
[66] J. Karczewski, T. Brylewski, T. Miruszewski, K.B. Andersen, P.Z. Jasiński, S. Molin, High-temperature kinetics study of 430L steel powder oxidized in air at 600–850 °C, Corros. Sci. 149 (2019) 100–107, https://doi.org/10.1016/J.CORSCI.2019.01.005.
[67] B. Talic, V. Venkatachalam, P.V. Hendriksen, R. Kiebach, Comparison of $MnCo_2O_4$ coated Crofer 22H, 441, 430 as interconnects for intermediate-temperature solid oxide fuel cell stacks, J. Alloy. Compd. 821 (2020) 153229, https://doi.org/10.1016/J.JALLCOM.2019.153229.
[68] D. Kosacow, M. Makowska, F. Marmo, J. Karczewski, P. Jasiński, S. Molin, High temperature corrosion evaluation and lifetime prediction of porous Fe22Cr stainless steel in air in temperature range 700–900 °C, Corros. Sci. 189 (2021) 109589, https://doi.org/10.1016/J.CORSCI.2021.109589.
[69] H. Shahbazmojad, H. Ebrahimifar, A study on the oxidation and electrical behavior of crofer 22 APU solid oxide fuel cell interconnects with Ni-Co-CeO_2 composite coating, J. Mater. Sci. Mater. Electron. 32 (2021) 7550–7566, https://doi.org/10.1007/s10854-021-05470-z.
[70] A. Weber, E. Ivers-Tiffée, Materials and concepts for solid oxide fuel cells (SOFCs) in stationary and mobile applications, J. Power Sources 127 (2004) 273–283, https://doi.org/10.1016/J.JPOWSOUR.2003.09.024.
[71] L. Mazur, S. Molin, J. Dąbek, K. Durczak, M. Pyzalski, T. Brylewski, Physicochemical properties of $Mn_{1.45}Co_{1.45}Cu_{0.1}O_4$ spinel coating deposited on the Crofer 22H ferritic steel and exposed to high-temperature oxidation under thermal cycling conditions, J. Therm. Anal. Calor. 147 (2022) 5649–5666, https://doi.org/10.1007/s10973-021-10884-2.
[72] W. Huang, J.E. Soc, Evaluation of Electrophoretically Deposited $CuMn_{1.8}O_4$ Spinel Coatings on Crofer 22 APU for Solid Oxide Fuel Cell Interconnects Coatings on Crofer 22 APU for Solid Oxide Fuel, Cell (2008).
[73] M. Bednarz, S. Molin, M. Bobruk, M. Stygar, E. Długoń, M. Sitarz, T. Brylewski, High-temperature oxidation of the Crofer 22 H ferritic steel with $Mn_{1.45}Co_{1.45}Fe_{0.1}O_4$ and $Mn_{1.5}Co_{1.5}O_4$ spinel coatings under thermal cycling conditions and its properties, Mater. Chem. Phys. 225 (2019) 227–238, https://doi.org/10.1016/J.MATCHEMPHYS.2018.12.090.
[74] M.J. Reddy, B. Kamecki, B. Talic, E. Zanchi, F. Smeacetto, J.S. Hardy, J.P. Choi, L. Mazur, R. Valles, S.N. Basu, T. Brylewski, J.-E. Svensson, J. Froitzheim, Experimental review of the performances of protective coatings for interconnects in solid oxide fuel cells, J. Power Sources 568 (2023) 232831, https://doi.org/10.1016/J.JPOWSOUR.2023.232831.
[75] Z. Zhu, C. Darl-Uzu, U. Pal, S. Gopalan, A.M. Hussain, N. Dale, Y. Fukuyama, Y. Mizuno, Y. Miyoshi, S. Basu, Comparison of Cu-Mn and Mn-Co spinel coatings for solid oxide fuel cell interconnects, Int. J. Hydrog. Energy 47 (2022) 36953–36963, https://doi.org/10.1016/J.IJHYDENE.2022.08.239.
[76] M. Bik, M. Galetz, J. Dąbrowa, K. Mroczka, P. Zając, A. Gil, P. Jeleń, M. Gawęda, M. Owsiaka, M. Stygar, M. Zając, J. Wyrwa, M. Sitarz, Polymer derived ceramics based on SiAlOC glasses as novel protective coatings for ferritic steel, Appl. Surf. Sci. 576 (2022) 151826, https://doi.org/10.1016/j.apsusc.2021.151826.
[77] J. Mougin, T. Le Bihan, G. Lucazeau, High-pressure study of Cr_2O_3 obtained by high-temperature oxidation by X-ray diffraction and Raman spectroscopy, J. Phys. Chem. Solids 62 (2001) 553–563, https://doi.org/10.1016/S0022-3697(00)00215-8.
[78] R.L. Farrow, P.L. Mattern, A.S. Nagelberg, Characterization of surface oxides by Raman spectroscopy, Appl. Phys. Lett. 36 (1980) 1529–1542, https://doi.org/10.1063/1.91429.
[79] H.D. Lutz, B. Müller, H.J. Steiner, Lattice vibration spectra. LIX. Single crystal infrared and Raman studies of spinel type oxides, J. Solid State Chem. 90 (1991) 54–60, https://doi.org/10.1016/0022-4596(91)90171-D.
[80] T.Van Everbroeck, B.G. Ciocarlan, W.Van Hoey, M. Mertens, P. Cool, Copper-containing mixed metal oxides (Al, Fe, Mn) for application in three-way catalysis, Catalysts 10 (2020) 1–20, https://doi.org/10.3390/catal10111344.
[81] C.M. Julien, M. Massot, C. Poinsignon, Lattice vibrations of manganese oxides: Part I. Periodic structures, Spectrochim. Acta - Part A Mol. Biomol. Spectrosc. 60 (2004) 689–700, https://doi.org/10.1016/S1386-1425(03)00279-8.
[82] G. Zhou, X. Gu, W. Xie, T. Gao, J. Peng, X.S. Wu, Polarized Raman scattering studies of hexagonal $YMnO_3$ single crystal, IEEE Trans. Magn. 51 (2015), https://doi.org/10.1109/TMAG.2015.2438154.
[83] S. Mahana, S.K. Pandey, B. Rakshit, P. Nandi, R. Basu, S. Dhara, S. Turchini, N. Zema, U. Manju, S.D. Mahanti, D. Topwal, Site substitution in $GdMnO_3$: effects on structural, electronic, and magnetic properties, Phys. Rev. B 102 (2020), https://doi.org/10.1103/PhysRevB.102.245126.
[84] S. Chevalier, J.P. Larpin, Formation of perovskite type phases during the high temperature oxidation of stainless steels coated with reactive element oxides, Acta Mater. 50 (2002) 3107–3116, https://doi.org/10.1016/S1359-6454(02)00106-4.
[85] S. Molin, H. Persson, T.L. Skafte, A.L. Smitshuysen, S.H. Jensen, K.B. Andersen, H. Xu, M. Chen, P.V. Hendriksen, Effective yttrium based coating for steel interconnects of solid oxide cells: corrosion evaluation in steam-hydrogen atmosphere, J. Power Sources 440 (2019), https://doi.org/10.1016/j.jpowsour.2019.226814.
[86] E. Toodo, M. Boniardi, D. Cannoletta, M.P. De Riccardis, B. Bozzini, Electrodeposition of yttria/cobalt oxide and yttria/gold coatings onto ferritic stainless steel for SOFC interconnects, J. Power Sources 195 (2010) 4772–4778, https://doi.org/10.1016/j.jpowsour.2010.02.005.
[87] M. Grioni, J.B. Goedkoop, R. Schoorl, F.M.F. de Groot, J.C. Fuggle, F. Schäfers, E. E. Koch, G. Rossi, J.-M. Esteva, R.C. Karnatak, Studies of copper valence states with Cu L 3 x-ray-absorption spectroscopy, Phys. Rev. B 39 (1989) 1541–1545. (https://link.aps.org/doi/10.1103/PhysRevB.39.1541).
[88] S. Gautam, S. Muthurani, M. Balaji, P. Thakur, D.P. Padiyan, K.H. Chae, S.S. Kim, K. Asokan, Electronic structure studies of nanoferrite $Cu_xCo_{1-x}Fe_2O_4$ by X-ray absorption spectroscopy, J. Nanosci. Nanotechnol. (2011), https://doi.org/10.1166/jnn.2011.3249.
[89] J. Kang, G. Kim, H.J. Lee, D.H. Kim, H.S. Kim, J.H. Shim, S. Lee, H. Lee, J. Kim, B. H. Kim, B.I. Min, Soft x-ray absorption spectroscopy and magnetic circular dichroism study of the valence and spin states in spinel $MnFe_2O_4$, Phys. Rev. B (2008) 1–7, https://doi.org/10.1103/PhysRevB.77.035121.

Supporting information

$CuMn_{1.7}Fe_{0.3}O_4$ – RE_2O_3 (RE=Y, Gd) ceramic bilayers as a protective interconnect coatings for Solid Oxide Cells

Bartłomiej Lemieszek[a], Justyna Ignaczak[a], Krystian Lankauf[a], Patryk Błaszczak[b], Maciej Bik[c], Marcin Zając[d], Sebastian Molin[a], Piotr Jasiński[a]

[a] Advanced Materials Centre, Faculty of Electronics, Telecommunications and Informatics, Gdańsk University of Technology, ul. G. Narutowicza 11/12, 80-233 Gdańsk, Poland

[b] Advanced Materials Center, Faculty of Applied Physics and Mathematics, Gdańsk University of Technology, ul. G. Narutowicza 11/12, 80-233 Gdańsk, Poland

[c] AGH University of Science and Technology, Faculty of Materials Science and Ceramics, Al. Mickiewicza 30, 30-059 Kraków, Poland

[d] National Synchrotron Radiation Centre SOLARIS, Jagiellonian University, Czerwone Maki 98, 30-392, Kraków, Poland

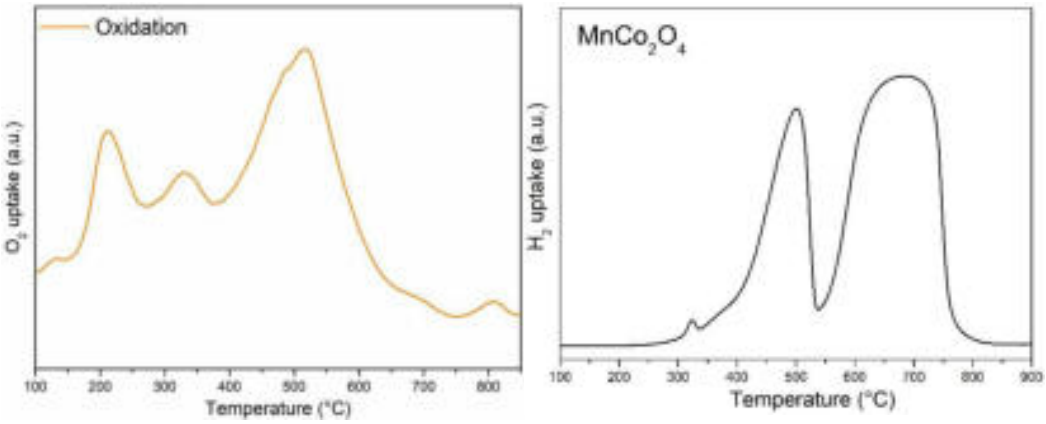


Figure S1. Oxidation profile obtained for $CuMn_{1.7}Fe_{0.3}O_4$ powder after prior reduction (A), and the reduction

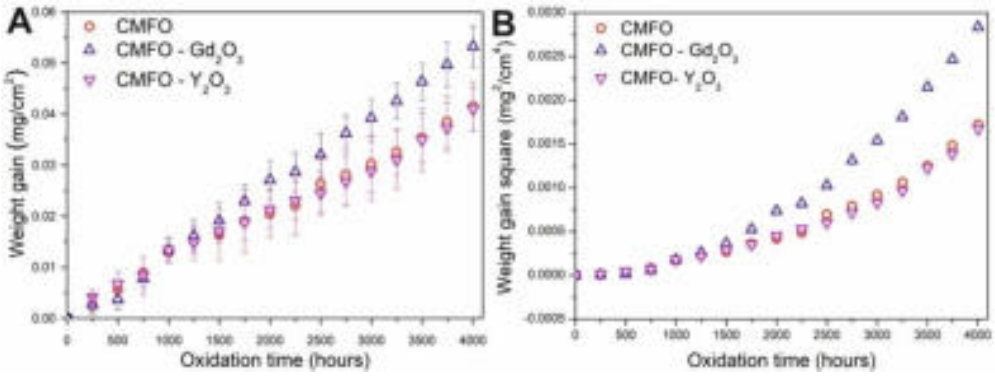


Figure S2. Weight gain plots of corrosion study of three types of coated samples (A) and parabolic plots showing the kinetic of the reaction (B).

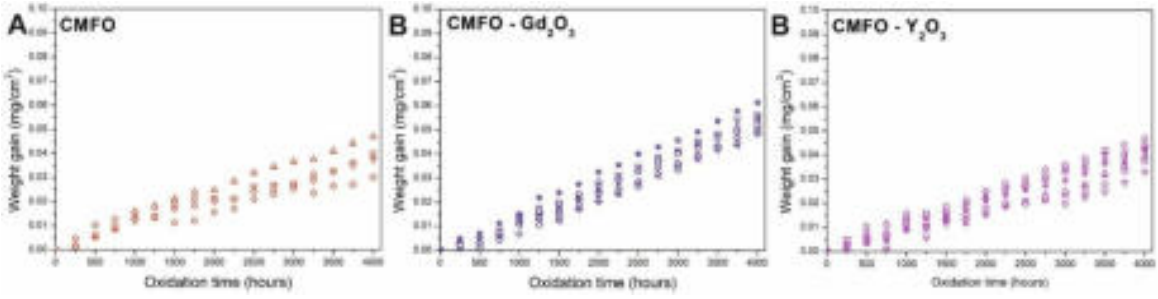


Figure S3. Weight gain plots for each sample separately present the repeatability of tested samples and show the anticorrosion behaviour of $CuMn_{1.7}Fe_{0.3}O_4$ spinel and the influence of additional ceramic layers.

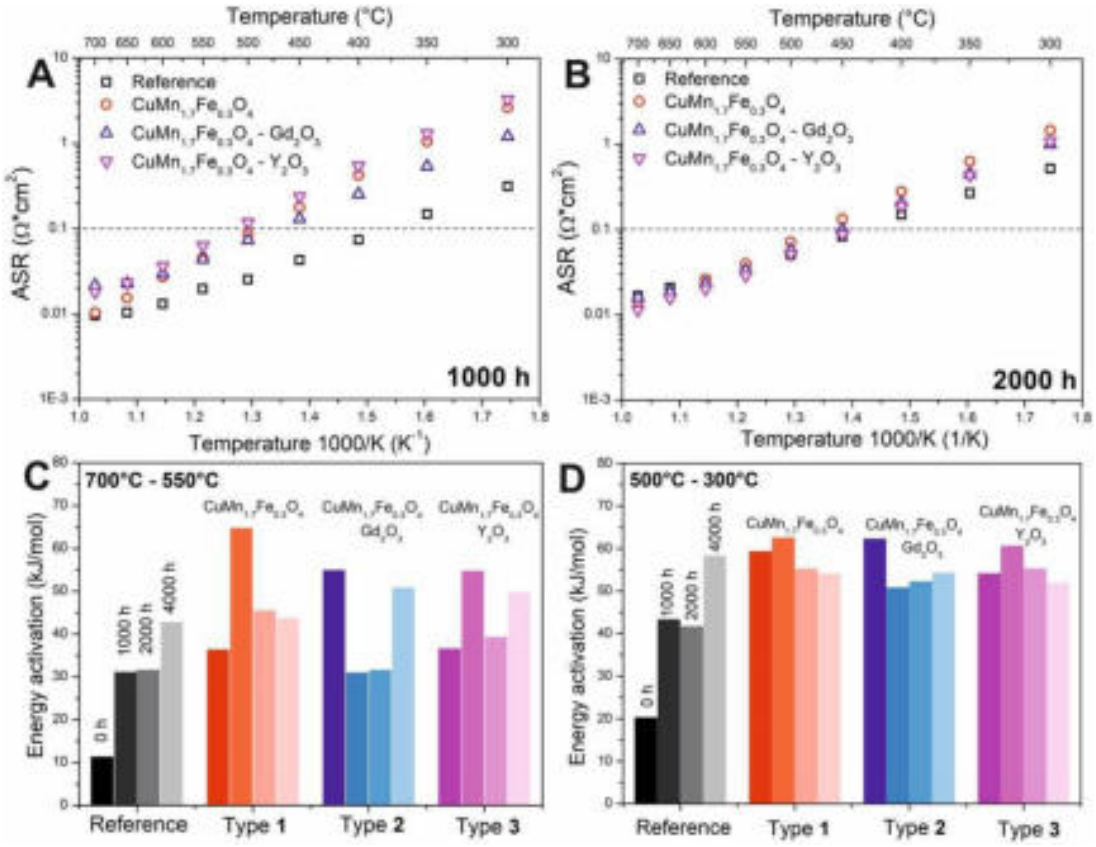
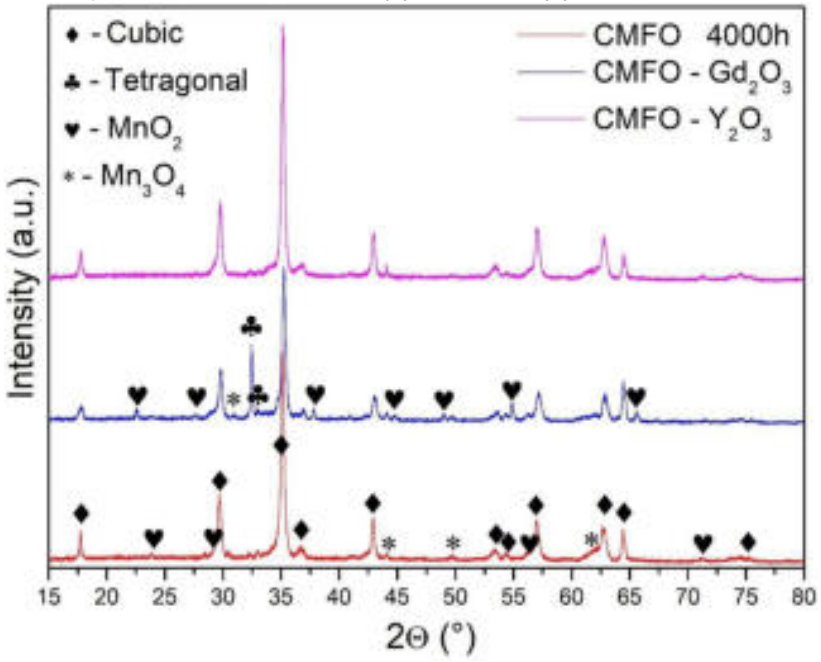


Figure S5. XRD plots made for Crofer 22 APU steel with CMFO, CMFO-Gd_2O_3, and CMFO-Y_2O_3 protective layers after corrosion time of 4000 h

Figure S4. Arrhenius plots for samples oxidised for 1000 hours (A), 2000 hours (B) and calculated activation energies divided into



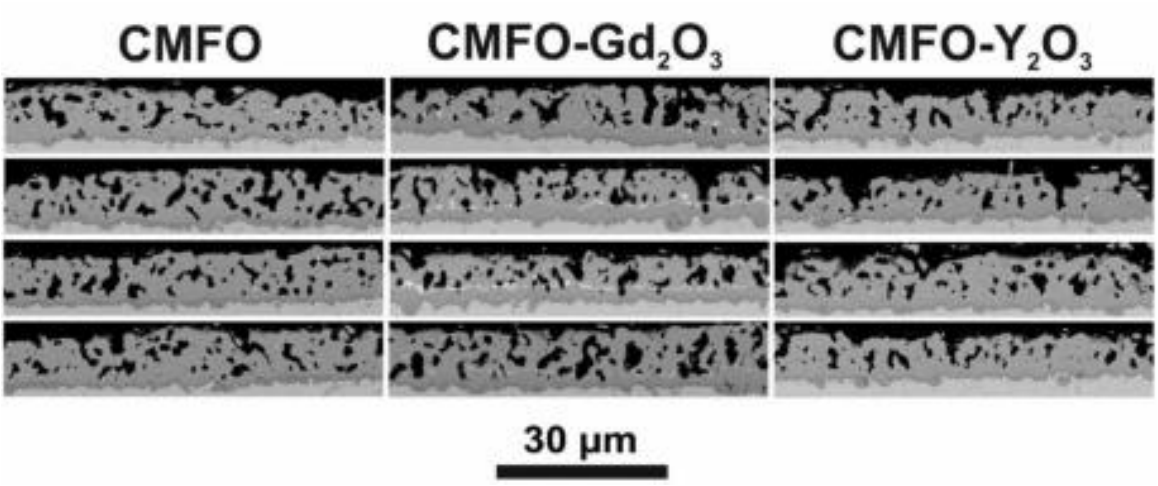


Figure S6. SEM images of cross-sections of protective layers after 4000 hours for a larger area.

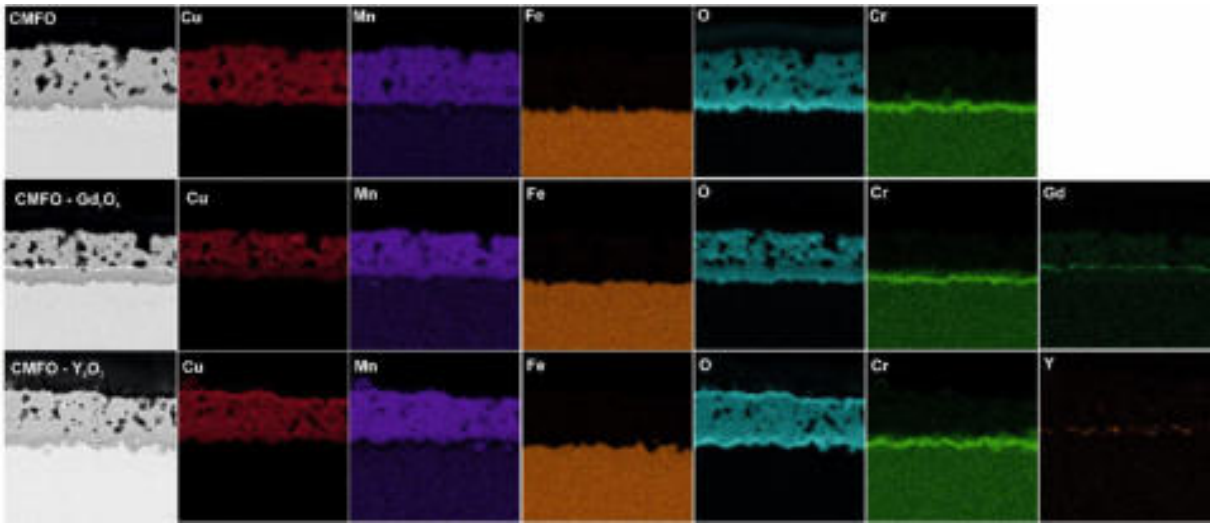


Figure S7. EDS analysis of prepared sample cross-sections after 4000 hours of oxidation at 700°C.

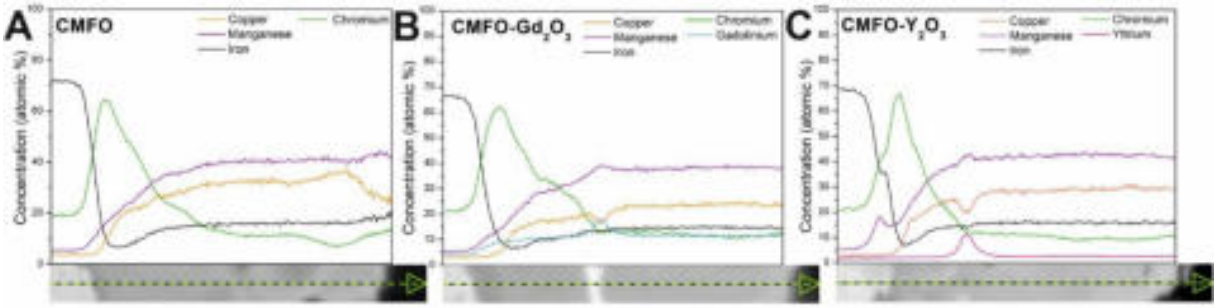


Figure S8. EDS linescans for CMFO (A), CMFO – Gd_2O_3(B) and CMFO – Y_2O_3(C).

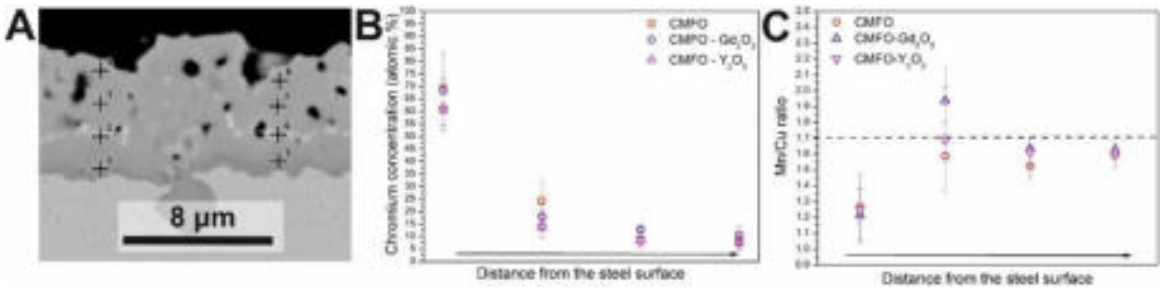


Figure S9. SEM image show the distribution of point analysis (A), and a changes in the chromium concentration in the cross-section of the layer (B).

10.3. Enhanced electrochemical performance of partially amorphous $La_{0.6}Sr_{0.4}CoO_{3-\delta}$ oxygen electrode materials for low-temperature solid oxide cells operating at 400 °C

Authors: **Bartłomiej Lemieszek**, Mindaugas Ilickas, Jan Jamroz, Asta Tamulevičienė, Jakub Karczewski, Patryk Błaszczak, Alexey Maximenko, Brigita Abakevičienė, Marcin Małys, Sigitas Tamulevičius, Piotr Jasiński, Sebastian Molin

Applied Surface Science, vol. 670, pages 160620, 2024, https://doi.org/10.1016/j.apsusc.2024.160620

IF = 6.9 (2024), MSHE points 140, Citations: 8

Article 3 addresses the second thesis by examining the feasibility of using partially amorphous LSC ($La_{0.6}Sr_{0.4}CoO_{3-\delta}$) as an oxygen electrode in low-temperature fuel cells. Thin electrode layers were deposited on CGO electrolytes by spin coating and characterized using XRD, HT-XRD, Raman spectroscopy, FTIR, and XAFS. Among these methods, XAFS was particularly useful for describing the partially amorphous phase. It showed that cobalt in partially amorphous LSC has an average oxidation state 0.5 lower than in the crystalline form, along with significant changes in the distance to its nearest cation neighbours.

Electrochemical properties were investigated in symmetrical half-cells using EIS. The study optimized electrode thickness and annealing temperature to improve the oxygen reduction reaction under atmospheric conditions. The optimal thickness was 500 nm, corresponding to 20 deposition cycles, while the lowest polarization resistance was obtained after annealing at 400 °C. This behaviour was linked to grain size and the resulting active surface area. Measurements under different oxygen partial pressures helped identify the rate-limiting step, showing that the P2 process, related to surface oxygen exchange and oxygen ion diffusion, was critical. Stability tests over 100 hours confirmed good material stability, although resistance gradually increased with time.

The novelty of this work lies in employing partially amorphous LSC as an effective oxygen electrode material for low-temperature SOCs (400 °C). The

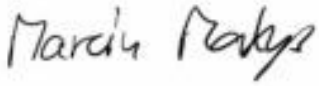
material was comprehensively characterized by means of XANES, EXAFS, and Wavelet Transform analyses, an approach that has not previously been reported for partially amorphous or amorphous LSC. Moreover, investigating the reaction kinetics of LSC at temperatures as low as 400 °C represents another novel aspect of this study.

The main achievement of this work was the detailed characterization of LSC in its partially amorphous form, with XAFS providing unique insights. This analysis demonstrated a reduction in the average oxidation state of cobalt, the electrochemically active element, which explain enhancement for performance. The study thus showed that partially amorphous, and potentially fully amorphous, materials may represent promising alternatives to conventional crystalline electrodes.

My contributions included developing a new type of precursor for oxygen electrode fabrication, depositing the electrode layers, and conducting symmetric-cell and XAFS measurements. I also analysed XRD, Raman, HT-XRD, XAFS, and FTIR data, interpreted the results, prepared figures, and wrote the manuscript. As the corresponding author, I was responsible for article submission and for preparing responses to reviewer comments.

Declaration of co-authors on their contribution to the publication: "Enhanced electrochemical performance of partially amorphous $La_{0.6}Sr_{0.4}CoO_{3-\delta}$ oxygen electrode materials for low-temperature solid oxide cells operating at 400 °C".

Name and Surname	Contribution	Signature
Bartłomiej Lemieszek	Writing – review & editing, Writing – original draft, Validation, Methodology, Investigation (EIS, XAFS, Formal analysis, Data curation, Conceptualization Visualization.	
Mindaugas Ilickas	Writing – review & editing, Methodology, Investigation (FTIR, Contact angle, Raman spectroscopy)	
Jan Jamroz	Writing – review & editing, Methodology, Investigation (XRD, HT-XRD)	
Asta Tamulevičienė	Writing – review & editing, Methodology, Investigation (FTIR).	
Jakub Karczewski	Writing – review & editing, Methodology, Investigation (SEM).	
Patryk Błaszczak	Writing – review & editing, Methodology, Investigation	
Alexey Maximenko	Writing – review & editing, Supervision, Methodology, Investigation (XAFS), Data curation	

Brigita Abakevičienė	Writing – review & editing, Supervision, Methodology, Investigation (Raman spectroscopy)	
Marcin Małys	Writing – review & editing, Methodology, Investigation (XRD, HT-XRD)	
Sigitas Tamulevičius	Writing – review & editing, Supervision, Resources, Methodology	
Piotr Jasiński	Writing – review & editing, Supervision	
Sebastian Molin	Writing – review & editing, Supervision, Resources, Methodology, Data curation, Conceptualization	

Applied Surface Science 670 (2024) 160620

Contents lists available at ScienceDirect

Applied Surface Science

journal homepage: www.elsevier.com/locate/apsusc

Full Length Article

Enhanced electrochemical performance of partially amorphous $La_{0.6}Sr_{0.4}CoO_{3-\delta}$ oxygen electrode materials for low-temperature solid oxide cells operating at 400 °C

Bartłomiej Lemieszek [a,*], Mindaugas Ilickas [b], Jan Jamroz [c], Asta Tamulevičienė [b], Jakub Karczewski [d], Patryk Błaszczak [d], Alexey Maximenko [e], Brigita Abakevičienė [b], Marcin Małys [c], Sigitas Tamulevičius [b], Piotr Jasiński [a], Sebastian Molin [a]

[a] Advanced Materials Centre, Faculty of Electronics, Telecommunications and Informatics, Gdańsk University of Technology, ul. G. Narutowicza 11/12, 80-233 Gdańsk, Poland
[b] Institute of Materials Science of Kaunas University of Technology, K. Baršausko str. 59, Kaunas LT-51423, Lithuania
[c] Warsaw University of Technology, Faculty of Physics, Koszykowa 75, 00-662 Warsaw, Poland
[d] Advanced Materials Centre, Faculty of Applied Physics and Mathematics, Gdańsk University of Technology, ul. G. Narutowicza 11/12, 80-233 Gdańsk, Poland
[e] National Synchrotron Radiation Centre SOLARIS, Jagiellonian University, Czerwone Maki 98, 30-392, Kraków, Poland

ARTICLE INFO

Keywords:
Solid oxide cells
Oxygen electrode
LSC
Partially amorphous
XAFS
EIS

ABSTRACT

This work evaluates partially amorphous $La_{0.6}Sr_{0.4}CoO_{3-\delta}$ (LSC) as a potential oxygen electrode for low-temperature solid oxide cells. LSC was deposited using the spin-coating technique onto $Ce_{0.9}Gd_{0.2}O_{2-\delta}$ (CGO) substrates. The optimal oxygen electrode thickness was determined as 500 nm. The electrochemical impedance spectroscopy (EIS) study showed a significant improvement in oxygen reduction/oxidation reaction kinetics when annealing temperatures below 600 °C. The lowest value of the polarisation resistance was observed for the sample annealed at 400 °C, followed by a temperature of 500 °C. EIS measurements at different pO_2 content were performed at levels between 0.5 % and 20 %. A comprehensive equivalent circuit analysis was carried out for an explanation of the limiting factors of the catalytic reaction. X-ray absorption fine structure analysis allowed for the identification of differences between crystalline LSC and its partially amorphous form. X-ray absorption near-edge spectroscopy analysis indicated that cobalt adopts a lower oxidation state for the partially amorphous form. Moreover, extended X-ray absorption fine structure analysis indicated the decreased of cobalt oxidation state in partially amorphous LSC. It can be assumed that the increased activity of LSC at temperatures below the crystallization may be due to increased defects and oxygen vacancies in the material.

1. Introduction

Solid oxide cells (SOCs) technology has been continuously developing for decades [1]. This potentially zero-emission technology to obtain energy from hydrogen may be crucial in the process of energy transformation [2]. Initially, the operating temperature of the fuel cells was 1000 °C and above, and it immediately became clear to commercialise the technology, it was necessary to reduce the working temperature and the high operating costs associated with it. Over the last 20 years, it has been provided to reduce the operating temperature of cells to the operating range of 600 °C to 800 °C, and the temperature of 500 °C is increasingly being studied. Reducing the optimal operating temperature for SOCs and increasing the efficiency requires solving many problems. In such a situation, it became necessary to find appropriate materials that allow for a reaction to happen at lower temperatures with high efficiency [1,3].

Recently, much attention has been devoted to the development of high-performance oxygen electrodes for intermediate and low-temperature SOCs applications. Pristine material used as a oxygen electrode was a perovskite material that conducts both electronically and ionically, $La_{1-x}Sr_xMnO_3$ (LSM). However, lowering the operating temperature creates a need for new materials with properties better than LSM. The search for alternatives led to materials such as LSC ($La_xSr_{1-x}CoO_{3-\delta}$) or LSCF ($La_xSr_{1-x}Co_yFe_{1-y}O_{3-\delta}$). Among the materials used as

* Corresponding author.
E-mail address: bartlomiej.lemieszek@pg.edu.pl (B. Lemieszek).

https://doi.org/10.1016/j.apsusc.2024.160620
Received 17 May 2024; Received in revised form 22 June 2024; Accepted 27 June 2024
Available online 30 June 2024
0169-4332/© 2024 The Authors. Published by Elsevier B.V. This is an open access article under the CC BY license (http://creativecommons.org/licenses/by/4.0/).

oxygen electrodes in low-temperature SOCs, one should include $Ce_{0.8}Gd_{0.2}O_{2-\delta}$ (CGO) infiltrated by LSC and LSCF [4]. Other potentially promising materials include praseodymium oxide [5,6], $Pr_2NiO_{4+\delta}$ [6], and strontium-cobalt oxide doped with antimony [7].

Of the materials mentioned, LSC and LSCF currently seem to be the most promising. LSC can exhibits two crystalline forms. Chen et al. examined the crystallographic structure of the LSC and showed the presence of the hexagonal (trigonal, rhombohedral) lattice form in the temperature range from room temperature up to 390 °C. Between 390 °C and 611 °C, there is a phase transition to the cubic perovskite phase, which is stable above 611 °C. In that study, LSC powders were synthesised by a solid-state reaction [8]. The synthesis of LSC usually ends with obtaining a product consisting of several phases, as demonstrated by Hayd et al. The crystallographic analysis of LSC layers deposited on CGO showed, in addition to the perovskite $La_{0.6}Sr_{0.4}CoO_{3-\delta}$ phase, the $(La,Sr)_2Co_{4+\delta}$ and SrO phases [9]. Moreover, Co_3O_4 phase was also detected in other works [10]. The synthesis temperature below 550 °C results in obtaining the material in semi-amorphous or amorphous form [11,12]. LSC is known as a oxygen electrode material with a high ionic conductivity between 0.56 S/m and 1.2 S/m at 700 °C [13,14]. For LSCF, this value is 0.474 S/m at the same temperature [14]. So far, the electrochemical properties of LSC have been mainly studied at temperatures >400 °C, whereas its performance at lower temperatures remains unexplored [15]. Such a low operating temperature also allows the possibility of using amorphous and partially amorphous materials.

In the literature, the vast majority of works refer to crystalline LSC. Limited number of papers undertake research on amorphous LSC. At low temperatures, the best results when it comes to the performance of crystalline electrodes, so far, has been achieved by Kim et al., who obtained polarisation resistance (R_{pol}) value ~1.51 Ω·cm^2 at 400 °C for the oxygen electrode in the form of LSC-LSCF composite, where the LSC was added in the process of infiltration in the form of nanosheets [16]. The infiltration of CGO with LSC was also used by Samson et al. and the research team obtained at the same temperature value of R_{pol} equal to 2.57 Ω·cm^2 [17]. Hayd et al. investigated the use of LSC as a oxygen electrode in their work. The 200 nm-thick oxygen electrode layer was screen-printed. The area specific resistance (ASR) value for the symmetrical half-cell was ~3.2 Ω·cm^2 at 400 °C [9]. Samat et al. presented a oxygen electrode in the form of LSC prepared by the polymeric complexation method. The oxygen electrode thickness used was around 1 μm. At a temperature of 400 °C, the polarisation resistance was approximately 32 Ω·cm^2 [18]. Januschewsky et al. reported the use of LSC as a oxygen electrode deposited on yttria-stabilised zirconia (YSZ) using pulsed laser deposition (PLD), and the selected layer thickness was set at 200 nm. For the layer deposited at a temperature of 420 °C and kept for 3 days at 600 °C, the polarisation resistance was determined in the temperature range of 600–400 °C. At 400 °C, the value of the polarisation resistance was approximately 180 Ω·cm^2 [19].

For amorphous or partially amorphous electrode materials, the number of valuable scientific publications is quite limited. Cavallaro et al. investigated the potential use of an amorphous LSC as a oxygen electrode in low-temperature SOCs. A layer with a thickness of around 300 nm was deposited by the PLD technique and subjected to thermal treatment in the temperature range from room temperature through 200 °C and up to 750 °C. The R_{pol} value at the temperature of 415 °C was as high as 850 Ω·cm^2 [20]. Evans et al., used partially amorphous LSC as a oxygen electrode for micro-solid oxide fuel cells. Oxygen electrode thicknesses were set as 100 nm and 200 nm, and for the latter value at 400 °C, the ASR value for the oxygen electrode was determined to be no more than 0.3 Ω·cm^2 as deconvoluted from fuel cell measurements [12]. Due to limited number of studies, and a wide range of R_{pol} values, the electrochemical performance of amorphous or partially amorphous electrode materials remains interesting for further exploration. In this article, we present and discuss the influence of the LSC structure on the electrocatalytic properties of oxygen reduction/oxidation at low-temperatures.

2. Experimental

The base on which the oxygen electrode layer was deposited was pellets prepared from $Ce_{0.8}Gd_{0.2}O_{2-\delta}$ powder (GDC-20 K or CGO, Daiichi Kigenso Kagaku Kogyo, Japan). 0.8 g of CGO powder was placed in a mould with a diameter of 16 mm and pressed at 98 MPa for 1 min. The prepared pellets were sintered at 1450 °C for 10 h in the box furnace. After sintering, the pellets shrank to an average diameter of 13 mm. The samples were polished on both sides on a semi-automatic polisher (Struers Tergamin-20) and annealed again at 1200 °C for 2 h.

The $La_{0.6}Sr_{0.4}CoO_{3-\delta}$ precursor was prepared in the ethylene glycol photopolymerization process. $La(NO_3)_3{\cdot}6H_2O$ (99.9 % purity, Alfa Aesar), $Sr(NO_3)_2$ (99 % purity, Sigma Aldrich), and $Co(NO_3)_3{\cdot}6H_2O$ (99 % purity, Sigma Aldrich) were dissolved in proper stoichiometry in distilled water to obtain a concentration of 0.25 mol·dm^{-3}. Ethylene glycol (99 % purity, Sigma Aldrich) and citric acid (99 % purity, Chempar) were added to the solution in a mass ratio of 1:1. Additionally,10 wt% of ethanol (99,8% POCH) was added, along with 0.05 wt% of the photoinitiator [2-hydroxy-4'-(2-hydroxyethoxy)]-2-m-ethyl-propiophenone (98 % purity, Sigma Aldrich). When all substrates were mixed, the solution was exposed to UV light for 13 min (a time selected from preliminary studies to determine optimal conditions). UV light was provided by the laboratory ultraviolet lamp EMITA VP-60, rated power 180 W, at a supply voltage of 220–240 V AC. A wood glass filter was used that transmits UV radiation in the range of 320 to 400 nm, with a maximum at 365 nm.

To determine the crystalline or partially amorphous structure at low temperatures, a series of LSC powders synthesised from the described precursor, was prepared and sintered in a furnace for two hours at a temperature ranging from 400 °C to 1000 °C in increments of 100 °C. The product of sintering obtained in this way was ground in a mortar to obtain a homogeneous powder. These samples were analysed by X-ray diffraction (XRD), high-temperature X-ray diffraction (HT-XRD), and XAFS (X-ray absorption fine structure) in XANES (X-ray absorption near-edge spectroscopy) and EXAFS (extended X-ray absorption fine structure) regions.

The LSC oxygen electrode was deposited onto the prepared pellets using the spin-coating technique (Laurell spin coater, model WS-400B-6NPP/LITE). 20 μl of LSC precursor was dropped onto the surface of CGO, and using a three-stage rotational speed, excess solution was removed at 500 rpm for 20 s, 1000 rpm for 20 s, and 3000 rpm for 30 s. After each application of a new layer, the heat treatment process was applied using a hot plate, and the pellets were heated to 400 °C for 15 min. A series of samples with a different number of application cycles, from 1 to 20, were made to determine the relationship between the number of cycles and the thickness of the final layer. It was determined that 10 cycles gave a oxygen electrode thickness of around 300 nm, and 20 cycles resulted in a thickness of around 500 nm. After the predetermined oxygen electrode thickness was reached, the edges of the half-cells were polished to remove the remaining LSC at the edges. Then, they were annealed in the furnace (Carbolyte RHF 16/8 box furnace) in the temperature range of 400–1000 °C for 2 h. The method of sample preparation (multiple heating and cooling cycles) did not cause delamination of the layer from the substrate. After determining the proper thickness layer, still good adhesion with the substrate was achieved. Moreover, further measurements at higher temperatures did not show significant differences in ohmic resistance values over a wide temperature range. A current collector layer in the form of LSC paste (Fiaxell) was applied to each of the pellets and annealed at 400 °C for 2 h. The symmetrical half cells prepared in this way, with the LSC oxygen electrode on both sides, were used for further tests.

The viscosity of the prepared precursor was measured using a FUNGILAB ALPHA series rotational viscometer with an adapter for measuring small samples. 10 ml of the precursor before and after the photopolymerization process was used to perform the measurement. The rotation speed was selected for each sample to ensure the highest

accuracy of the measurement indicated by the viscometer.

Wetting properties were probed with drop shape analyser DSA25 (Krüss) under the sessile drop mode. The contour of the 2 µl drop was imaged using dedicated software Advance and fitted with the Young Laplace method.

XRD was used to examine the microstructure of LSC powder samples using a Bruker D2Phaser (Bruker AXS, Mannheim, Germany) diffractometer with a Lynxeye XE-T detector and CuKα radiation (α = 0.15406 nm).

Data for high-temperature X-ray powder diffraction was gathered on a Philips X'Pert Pro diffractometer, equipped with an X'Celerator detector. Ni-filtered Cu-Kα radiation was used to generate the data, and the values for λ_1 and λ_2 were 1.54056 Å and 1.54439 Å, respectively. Measurements at the elevated temperatures were carried out with the assistance of an Anton-Paar HTK 1200 high temperature camera. The LaB_6 standard was used for the calibration process. Diffraction patterns were obtained in air at room temperature as well as at intervals of 50 °C ranging from 50 °C to 850 °C.

Raman spectra were acquired using an inVia spectrometer (Renishaw, United Kingdom) outfitted with an optical microscope (Leica, Wetzlar, Germany) and a motorised sample platform. Using a 50x objective, the excitation beam from a diode laser emitting at 532 nm was focused on the sample. At the surface of the sample, the laser power was 3.2 mW. The Raman Stokes signal was scattered using a diffraction grating with 2400 grooves per millimetre, and the data were captured using a Peltier-cooled charge-coupled device (CCD) detector with 1024 × 256 pixels. This system has a spectral resolution of around 1 cm^{-1}. Silicon was used to calibrate both the Raman wavenumber and the spectral intensity of the Raman apparatus.

Fourier transform infrared (FTIR) spectra were acquired at room temperature using a VERTEX 70 (Bruker, Ettlingen, Germany) spectrometer. Scans were performed in Kubelka-Munk mode in the range of 4000 to 400 cm^{-1}.

The X-ray absorption spectroscopy measurements at the Co K-edge were made at the ASTRA beamline at the SOLARIS National Synchrotron Radiation Centre in Cracow, Poland. The white beam from the 1.3 bending magnet was monochromatized by modified Lemonnier type double crystal monochromator equipped with Ge(220) crystal pair. At the sample position the size of the monochromatized beam was 7x1 mm. The XAFS spectra in XANES and EXAFS regions were collected in transmission mode, where sample chamber and ionisation chambers were filled with N_2 gas at atmospheric pressure. The monochromator at the Co K-edge was calibrated using Co foil from Exafs Company. During the measurements of the samples of interest the Co foil was also measured as a reference sample in order to control alignment of the collected spectra. For the measurements the homogeneous powder of samples of interest were mixed with cellulose and uniform pellets of diameter 1.3 cm were made. To get a good edge step the mass of the powders before mixing with cellulose were evaluated using XAFSmass program. A further analysis of the spectra was performed using Athena and Arthemis softwares. The crystallography data used to fit the calculated Fourier transform (FT) spectra was taken from the Crystallography Open Database (COD). FEFF files for fitting into the Artemis software have been prepared on the WebAtoms website. A map of the intensities of the atom distribution was made using wavelet transforms (WT) with Hama Fortran software [21,22].

Electrochemical impedance spectroscopy (EIS) was used to measure the ohmic and polarisation resistance (R_{ohm} and R_{pol}) of the prepared symmetrical cells (LSC|CGO|LSC) with an excitation amplitude of 25 mV and a frequency range of 3 MHz-50 mHz. The samples were placed in a compression cell where on each side of the sample was a gold mesh electrically connected to platinum wires leading outside the furnace. EIS studies aimed to determine the influence of the material structure (partly amorphous and crystallised) on the catalytic properties. Measurements were performed in an atmosphere of synthetic air with a flow rate of 50 ml·min^{-1}. The tested temperature range varied depending on the annealing temperature. For lower annealing temperatures, more frequent measurements were used to more precisely analyse the low-temperature range.

Measurements at various partial contents occurred at pO_2 values of 0.5 %, 1 %, 3 %, 5 %, 10 %, and 20 % at a flow rate of 50 ml·min^{-1}. Before the measurement, stabilisation in an atmosphere of selected pO_2 for 4 h was done. EIS measurements were performed in the range of 400 °C–300 °C every 25 °C. The Distribution of Relaxation Times (DRT) method was used for detailed analysis. For this purpose, the DRTtool Matlab GUI was used [23]. The DRT analysis was performed by choosing the C4 Matern method of discretization utilizing the 2nd order of the regularization derivative and a regularization parameter (λ) of 10^{-4}.

The samples were aged in an atmosphere of synthetic air, where pO_2 is 20 %, and in isothermal conditions at a temperature of 400 °C. Measurements were carried out for 100 h, with collecting spectra every 5 h.

3. Results and discussion

3.1. Layer preparation and structural analysis

The preparation of the oxygen electrode layer began with the preparation of the precursor. In this case, instead of the standard precursor prepared by the Pechini patent [24], the photopolymerization process was used. The increase in viscosity from 50.6 mPa·s to 88.88 mPa·s indicates that the use of a photoinitiator and UV light accelerated the polymerization process of ethylene glycol (EG) to polyethylene glycol. Contact angle analysis was used to see how the wettability changed and to compare it with the EG-based solution that was made as described above (S1 and S2 in the supplementary). In the case of distilled water, the initial contact angle was around 60° and gradually decreased to reach the minimum measured angle of approximately 7° after appeoximately 12 min. In the case of the EG-based reference solution, the initial value of the contact angle was around 20°, and after 6 min, it dropped to approximately 5°. As expected, the prepared precursor had an initial contact angle lower than before photopolimerisation and the value was about 20°. However, the CGO surface was much more wettable, so after two to three minutes, the contact angle became too small to measure. Contact angle measurements indicate that the new precursor preparation method accelerates the wettability of the CGO surface.

Fig. S3 shows the SEM images of the LSC layers deposited on the CGO surface using the spin-coating technique with a varying number of deposition cycles. The average LSC layer thicknesses from the SEM images were ~50 nm, ~100 nm, ~190 nm, ~230 nm, ~290 nm, and ~500 nm for 2, 4, 6, 8, 10, and 20 cycles respectively. Fig. S4 presents the calibration curve for oxygen electrode layer deposition depending on the number of cycles.

Fig. 1A shows the XRD results of the LSC powders sintered at different temperatures. It shows that the diffractograms have characteristic peaks that correspond to both R3c rhombohedral phases. These are the main peaks at 33° (110, 104), 47.5° (113), and 58° (024). However, there were also peaks indicating the $Pm\bar{3}m$ phase at 23.25° (012) and 40,75° (202). At 600 °C, in addition to the main peaks, characteristic of strontium carbonate became visible at 25.5° and 36° as well as faint peaks at 45° and 50°. The presence of strontium carbonate as an impurity is typical for LSC materials [25]. Below the temperature of 600 °C, the diffraction pattern indicates a partially amorphous form of the analysed material. LSC-specific peaks are noticeable and recognisable. In addition, peaks at 31.3° and 65.2°, not present at higher temperatures, were observed, indicating the presence of Co_3O_4.

Fig. 1B shows the Co K-edge XANES spectra for the LSC material as a function of annealing temperature. At around 7709 eV in each of the LSC samples, the pre-edge feature is observed, regardless of the annealing temperature. For 3d metals, the pre-edge feature depends on the contribution of the 1 s electric dipole transition to the 4p component in 3d – 4p hybridized orbitals and the tiny quadrupole transition to 3d

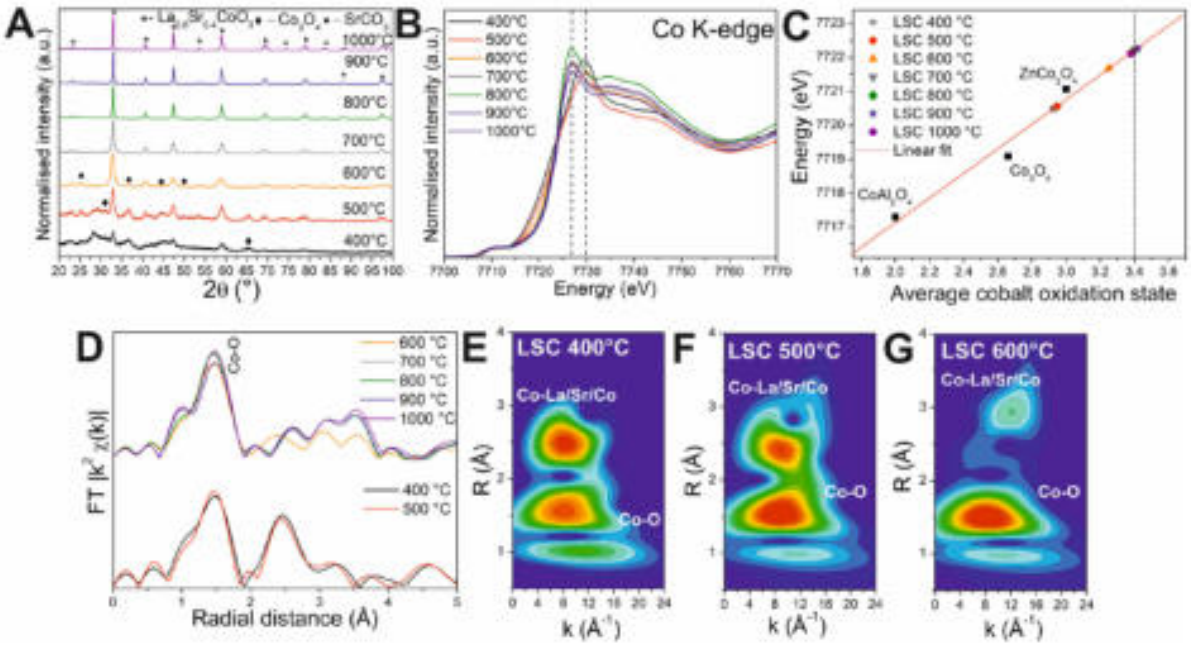


Fig. 1. X-ray diffraction of LSC powders annealed at different temperatures (A); XANES spectra (B); Average cobalt oxidation state calculated from mid-energy (C) R-space FT Fourier transform (k2χ(k)) Co-K-edge EXAFS for LSC as a function of annealing temperature (D); and Wavelet Transform calculated from EXAFS for LSC annealed at range 400 °C-600 °C (E-G).

component. The p-d hybridization could not occur for a regular octahedral symmetry, and the pre-edge peak is weak because the transition momentum of the electric quadrupole process is small. When the center of inversion symmetry is broken due to progressive distortion from octahedral to tetrahedral geometry, the pre-edge feature gains additional intensity due to the 1 s transition to the 4p component in the 3d–4p hybridized orbital, where the mixing of 4p and 3d depends strongly on the coordination symmetry [26]. In this case, the pronounced pre-edge peak for LSC could be explained by distortions of the octahedral structure due to the occurrence of defects and oxygen vacancies. Additional distortions introduced by the lack of a fully crystalline structure only increase the level of distortion, resulting in a distinct pre-edge peak [27,28].

Fig. 1C presents a linear relationship between the cobalt oxidation state and the mid-edge energy. It should be noted that the choice of the edge position is rather arbitrary, therefore the value of mid-egde energy was chosen to verify the spectral shift. In order to determine the curve determining this relationship, standard compounds with known and established oxidation states were used. The XANES spectra indicate the presence of cobalt is close to the theoretical value of 3.4^{+}, so therefore, cobalt occurs in both 3^{+} and 4^{+} oxidation states in LSC annealed above 600 °C. The situation was different for LSC annealed below 600 °C. The lower the annealing temperature, the more a more a gradual decrease in the average oxidation state of cobalt is observed. At a temperature of 600 °C, this value is already -3.3^{+}; at annealing temperatures of 500 °C and 400 °C, it is 2.9^{+}. The decrease in the average oxidation state of the cobalt in the LSC structure significantly affects the properties of the material itself. Fig. 1D shows k-space oscillation plots and Fourier transform (FT) (k2 χ(k)) plots of EXAFS for LSC annealed at different temperatures (no phase correction were applied). In the obtained spectrum, the first peak reaches its maximum at a radial distance of approximately 1.5 Å. This peak occurs for both partially amorphous and crystalline structures. In non-crystalline LSC, a peak at approximately 1.1 Å is also visible, the intensity of which in the crystal structure is much lower. In the case of partially amorphous structures, the next peak is observed at a radial distance of ~2.5 Å. This is a significant difference from the crystal structure, where the three broad peaks indicate Co-Sr/La/Co is in the range of 2.7–3.8 Å. Figs. S6A and S6B present the LSC spectra and the results of fitting the vibrational spectra $|X(R)|$ (Å^{-4}) in k-space and k^3 X(k)(Å^{-3}) in q-space. The parameters obtained during fitting are presented in Table S1. The EXAFS analysis indicates a significant decrease of number of oxygen atoms around the central atom for partially amorphous LSC. For annealing temperatures below 600 °C, the value of the coordination number is close to 4, and for crystalline samples it oscillates between 4.6 and 5.0. The decrease in this value for annealing temperatures of 900 °C and 1000 °C may be related to the formation of additional phases. They may not be visible in the diffractogram, as shown in work Zhang et al., where the formation of the CoO_x phase was not detected using XRD and its occurrence was observed using SEM-EDS. They also determined the stability phase diagrams for $(La_{0.6}Sr_{0.4})_{0.99}Co_yO_{3-\delta}$ and for temperatures above 800 °C in air, the occurrence of LSC with spinel (La,Sr)CoO_4 is possible, and above 900 °C, LSC with halite CoO is observed [29]. To better understand the differences between crystalline and partially amorphous material, a wavelet transform (WT) based on Morlet wavelets ($\kappa = 15$, $\sigma = 1$), was also performed for each analysed sample as a function of the annealing temperature. The WT determines the centres of the backscatter wave functions in energy (or wave vector) space. This method is particularly helpful when their waves cannot be separated by the Fourier transform/backtransform approach due to the presence of several elements in one shell, or the irregular nature of the material. Moreover, this method is particularly useful in determining minor changes in the centres of wave functions depending on various factors. Fig. 1 E–G present the obtained maps for annealing temperatures from 400 °C to 600 °C, and Fig. S6 C–F presents the obtained maps for annealing temperatures in the range of 700–1000 °C. For crystalline LSC, there are two areas with maximum intensities at R around 1.5 Å and 3 Å. The first of them corresponds to the Co–O bond and has a quite wide range. The second area originates from the Co-La/Sr/Co. Similar results were observed for all temperatures above 600 °C. In the case of the annealing temperatures of 900 °C

and 1000 °C, changes was observed in oxygen occupancy. It may be related to a new phase formation in the LSC at a high temperature [29]. For partially amorphous LSC a clear leftward shift is observed for Co-La/Sr/Co scattering path, where maximum intensities are observed at 2.5 Å, compared to 3 Å for the crystalline LSC. At an annealing temperature below 600 °C, two distinct areas with comparable intensities are observed, which distributions are broader, than for crystalline LSC. Based on the determined values of coordination numbers for Co-O bonds, it can be assumed that the number of oxygen atoms near the central atom has decreased, and may be comparable to the number of cations. This suggests that it can contribute to the occurrence of many more defects in the material itself. The appearance of defects in the structure of the material is related to its activity. Wang et al. analysed the LSC-Co_3O_4 composite in the context of oxygen activation in the material structure. The presence of an interface composed of LSC-Co_3O_4 increases the conversion of inactive oxygen species O^{2-} to active O^{2-x}. This is done by increasing the number of electrons transferred from the perovskite LSC to the Co_3O_4 lattice [30]. The occurrence of such defects may have a beneficial effect on the electrochemical reaction.

Fig. S5A shows high-temperature XRD analysis (HT-XRD) for the powder annealed at 400 °C (amorphous form). The characteristic first peaks of $La_{0.6}Sr_{0.4}CoO_3$ appear at a temperature of 550 °C, which indicates that the minimum temperature for the formation of the LSC perovskite crystal form is between 500 °C and 550 °C. In the temperature range of 550–600 °C, the characteristic $SrCO_3$ peaks are visible. Above 611 °C, a stable perovskite structure is observed, as shown in the literature [8]. The measurements reveal that LSC annealed at temperatures below 550 °C is partially amorphous and will be taken for future examination. To further improve the understanding of the structural properties, the examination with additional is required to offer more accurate details.

Raman spectroscopy was performed on oxygen electrode layers deposited on CGO pellets, and the results are shown in Fig. S5B. Measurements were made for a pure CGO pellet and an LSC layer with a thickness of 500 nm in the range of annealing temperatures from 400 °C to 1000 °C. For the pure CGO pellet, a broad and intensive band was observed with a Raman shift of 470 cm^{-1}. This is the only band observed in the analysed range of the measurement. Raman shift bands for the LSC are visible at 480 cm^{-1}, 520 cm^{-1} and 678 cm^{-1}. At the annealing temperatures of 400 °C and 500 °C, no band at 520 cm^{-1} was observed. In the case of perovskites, the presence of bands in Raman spectroscopy corresponds to Jahn-Teller distortions. In contrast to the perovskite's ideal structure, these distortions cause structural disturbances in the oxygen sublattice structure. Specifically, they cause the differences in the lengths of the Co-O bonds in the octahedral CoO_6, which leads to the formation of a monoclinic structure. In the case of a material such as LSC, strontium doping causes a decrease in the intensity of the bands and their broadening. These bands may be related to the Co^{3+} intermediate spin state [31]. There is a limited number of articles in the literature that even partially deal with the study of Raman scattering of perovskites such as $LaCoO_3$, and in the case of LSC, finding such studies is even more difficult. In the case of the $LaCoO_3$ perovskite, Ishikawa et al. observed Raman bands at 425 cm^{-1}, 536 cm^{-1} and 653 cm^{-1} (relative to the measurement range presented here), but only 425 cm^{-1} for $La_{0.7}Sr_{0.3}CoO_3$ [32]. In the case of $La_{1-x}Sr_xCoO_3$, the Raman shifts were different depending on the grain size and the stoichiometry of the material. Orlovskaya et al. for $La_{0.8}Sr_{0.2}CoO_3$ distinguished shifts of 448 cm^{-1}, 557 cm^{-1} and 673 cm^{-1} [33] and Li et al. for $La_{0.8}Sr_{0.2}CoO_3$ (grain size 11.5 nm) observed shifts at 500 cm^{-1} and 630 cm^{-1} [34]. Celikbilek et al. for $La_{0.6}Sr_{0.4}CoO_3$ he observed bands at 420 cm^{-1} and 678 cm^{-1} [31].

The lack of agreement in the literature regarding the specific bands responsible for LSC makes the analysis of the results even more complex. In this case, $La_{0.6}Sr_{0.4}CoO_3$ overlaps the band at 678 cm^{-1} with the Celikbilek work, and it is also seen that the band at 420 cm^{-1} cannot be determined due to CGO. The band at 500 cm^{-1} was observed in $La_{0.8}Sr_{0.2}CoO_3$ and in $LaCoO_3$ at 536 cm^{-1}, 557 cm^{-1} or 570 cm^{-1} [7]. Aakib et al. showed the presence of Raman bands at 470 cm^{-1}, 510 cm^{-1}, 610 cm^{-1} and 670 cm^{-1} for Co_3O_4 [35].

Fig. S5C shows the FTIR spectra of LSC deposited on CGO pellets and sintered at different temperatures. Bands at wavenumbers 400 cm^{-1}, 562 cm^{-1} and 660 cm^{-1} are recognised. The observed bands at about 400 cm^{-1} and 660 cm^{-1} are attributed to the modes of deformation and stretching vibrations in the plane of the O–Co–O bonds. In addition, the band width at 400 cm^{-1} may indicate the overlapping of the La–O and Sr–O bond stretching vibrations. The vibrations occurring at 562 cm^{-1} can be attributed to the stretching vibrations of the La/Sr–O–Co bonds. At low annealing temperatures, the bands are hardly visible, probably due to irregularities in the surroundings of the analysed bonds, which also affect the shift of the absorption maximum (local minimum of transmittance). The most sharp and visible bands are for LSC annealed at 1000 °C. The values of the wavenumbers that have been matched to the appropriate vibrations correspond to the data from the literature. The FTIR spectra obtained by Ghorbani-Moghadam et al. showed the bands and types of vibrations for the spinel material $La_{0.7}Sr_{1.3}CoO_4$ and the Cu/Fe dopants. They identified three distinct bands at the wavenumbers of 400 cm^{-1}, 520 cm^{-1} and 600 cm^{-1}, respectively. They attributed the first and last bands to stretching vibrations in the plane of the Co(Fe/Cu)-O bonds, and the band between 450–550 cm^{-1} to stretching vibrations of the apical La/Sr-O(II)–Co–(Fe/Cu) bond [36]. In another study, they studied a series of spinels with the $La_{2-x}Sr_xCoO_4$ structure. In the case of $La_{1.3}Sr_{0.7}CoO_4$, bands at wavelengths of 421 cm^{-1}, 486 cm^{-1}, 616 cm^{-1} and 672 cm^{-1} were determined. It was also shown that this band shifted to lower wavenumber values with the change of the La:Sr ratio, and at the La:Sr ratios of 0.9:1.1 and 0.7:1.3, this shift reached the minimum value of 468 cm^{-1} (from 512 cm^{-1}) [37]. In this study, the content of lanthanum and strontium in the perovskite structure is much lower, so it is possible that stretching of the octahedral CoO_6 is present, but it is invisible, or it consists of a wide band from 400 cm^{-1} to as much as 480 cm^{-1}. Sivakumar et al. identified bands at 446 cm^{-1}, 476 cm^{-1} and 620 cm^{-1} for the $LaCoO_3$ perovskite. They determined that at 446 cm^{-1}, can be attributed to the La-O stretching, and at 620 cm^{-1} for O-Co-O stretching vibrations. Mishra et al. analysed the $LaCoO_3$ material and identified the band at 586 cm^{-1} as stretch vibration between Co-O-Fe/Ni-O, as well as vibrations in the octahedral perovskite structure [38]. Garces et al. performed the FTIR spectroscopy measurement for the $LaSrCoO_3$ perovskite. In the spectrum, they identified bands at wavenumbers of 686 cm^{-1} and 523 cm^{-1}. The band at 686 cm^{-1} was related to the O-Co-O bond stretching vibrations, and the band at 523 cm^{-1} is related to the La-O and Sr-O bond stretching vibrations [39]. The occurrence of the described bands for each annealing temperature indicates the similar nature of the crystalline and partially amorphous material. The decrease in band intensity with decreasing annealing temperature is also noticeable and indicates the presence of a more disordered structure.

SEM images in Fig. 2A–G depict the surface morphology of the oxygen electrode. At an annealing temperature of 400 °C, the grains are too small (<10 nm) to distinguished. The grain size was ~23 nm at the annealing temperature of 500 °C. The average grain sizes for crystalline LSC were around 40 nm, 68 nm, 82 nm, 147 nm, and 112 nm at annealing temperatures of 600 °C, 700 °C, 800 °C, 900 °C, and 1000 °C, respectively. There is also a considerable increase in the pore size. The pore size of a partially amorphous LSC is nanometric and grows as the annealing temperature increases. During high annealing temperatures, the pores expand to a size larger than the grains.

3.2. Electrochemical impedance spectroscopy

Structural analysis indicated differences between crystalline and amorphous LSC. These differences may affect the catalytic properties of the material. To determine the efficiency of the electrochemical oxygen electrochemical reaction, various types of measurements were carried

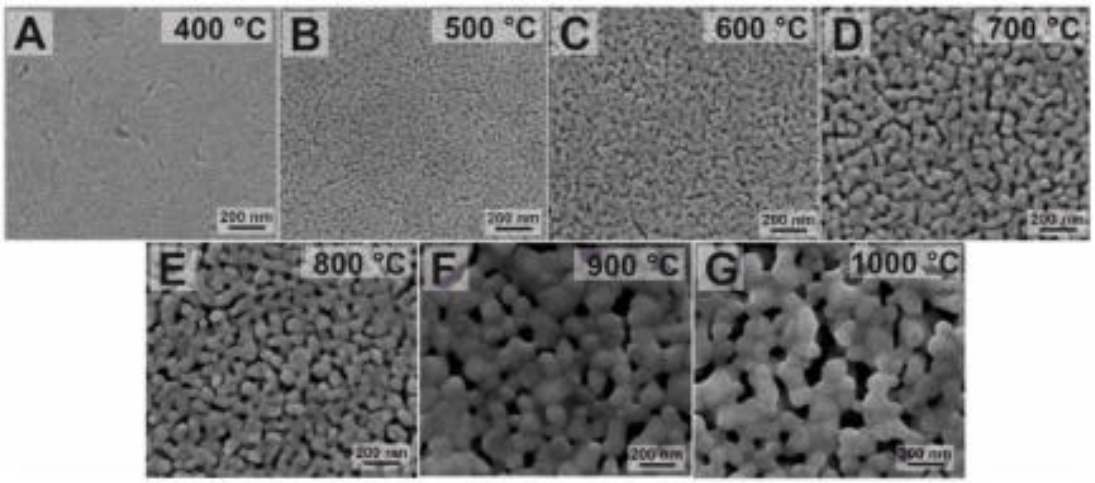


Fig. 2. SEM images of the LSC-based oxygen electrode surface depending on different annealing temperatures: from 400 °C to 1000 °C (A-G).

out using electrochemical impedance spectrometry. The value of polarisation resistance (R_p or R_{pol}) was taken into account as a key parameter for assessing the efficiency of this process. A series of symmetrical samples was prepared for the tests.

3.2.1. Optimal thickness determinations

The first stage of the research using EIS was to determine the optimal thickness of the LSC layer, starting at 200 nm and ending at 1000 nm. The electrochemical performance, depending on the thickness, was determined in the temperature range of 400 °C-300 °C by performing three impedance measurements every 25 °C. Fig. 3A and 3B show the ohmic and polarisation resistances, and Fig. 3C shows the obtained impedance spectra for various oxygen electrode thicknesses. At 400 °C, values of polarisation resistance of 59.3 Ω·cm^2, 38.8 Ω·cm^2, 35.9 Ω·cm^2, and 51.6 Ω·cm^2 were obtained, respectively, for layer thicknesses of 200 nm, 300 nm, 500 nm, and 1000 nm. For the sample without LSC layer (reference sample), this value is 527 Ω·cm^2. The nanoporous LSC oxygen electrode causes a significant increase in the oxygen electrode-air

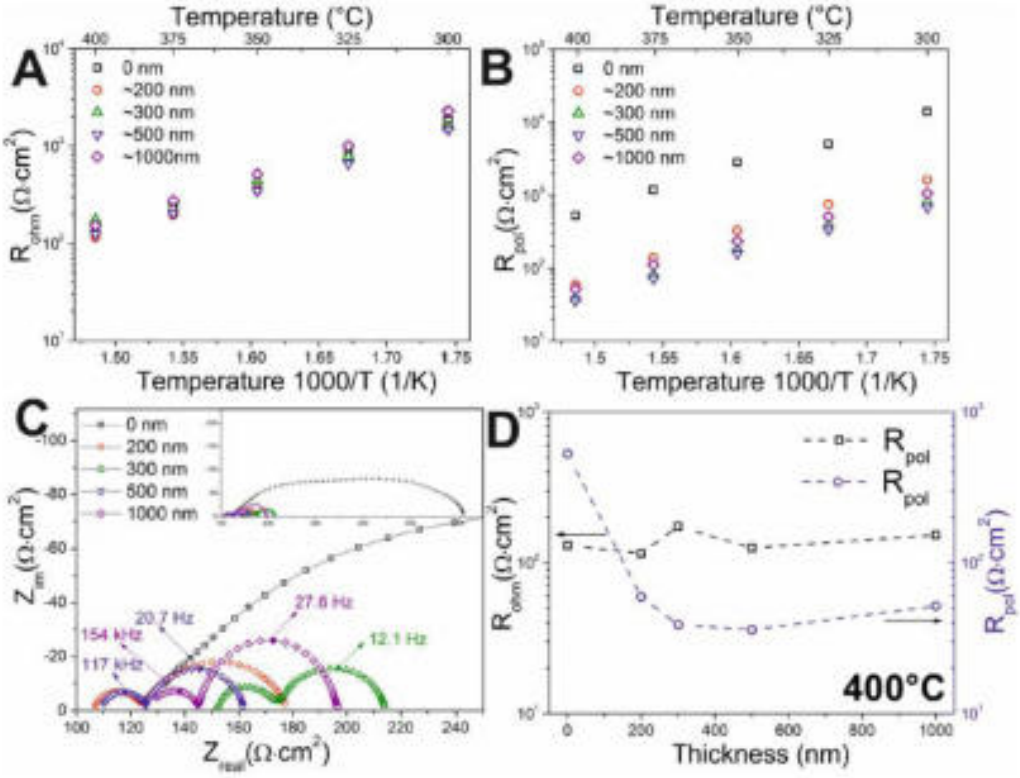


Fig. 3. Influence of $La_{0.6}Sr_{0.4}CoO_{3-\delta}$ oxygen electrode thickness on ohmic (A), polarisation resistance (B), obtained impedance spectra (C), and the relationship between annealing temperature and ohmic and polarisation resistance (D).

contact area, which is reflected in the value of the polarisation resistance of the cell. The initial decrease in the polarisation resistance value is related to the increase in the area of the active oxygen electrode layer and more efficient electrochemical reaction. The R_p values for the thickness of 300 nm are close to the sample thickness of 500 nm, and the positive effect of the increase in the active surface is inhibited. At a thickness of 1000 nm, an increase in the R_{pol} value was observed. This might be because the limiting charge transfer through the electrolyte layer. It may become more significant as the thickness of the oxygen electrode increases. Moreover, it can be assumed that the optimal range of oxygen electrode thickness is from 200 nm to 1000 nm. Fig. 3D shows the changes in the values of ohmic resistance and polarisation resistance as a function of electrode thickness. The visible decrease in the R_{pol} value with an increase in electrode thickness is noticeable. This trend is stopped when the thickness is higher than 300 nm, and the lowest value is achieved for a thickness of 500 nm. For the R_{ohm} the values are similar, and no significant effect is noticed. Therefore, a thickness of 500 nm was selected for further research.

3.2.2. *Effect of annealing temperature*

The next stage of the analysis was to assess of the effect of the annealing temperature on the efficiency of the catalytic reaction. This parameter has been proven to have a significant impact of electrode perfoemance [40]. This is due to, among others, the formation of a crystal structure as well as changing the grain size, which directly affects the active surface area.

Fig. 4A shows the ohmic resistance values, Fig. 4B shows the polarisation resistances, Fig. 4C shows the impedance spectra, and Fig. 4D shows the influence of the annealing temperature on the ohmic and polarisation resistance values. The sample annealed at 1000 °C and 800 °C revealed the smallest R_{ohm} values, 78.3 Ω·cm^2 and 82.2 Ω·cm^2 respectively. For other samples, the difference in R_{ohm} value was negligible. Such values for the R_{ohm} parameter indicate that a good bond with the CGO substrate has been achieved. The highest R_{ohm} value at 400 °C was observed of 125 Ω·cm^2 for the sample annealed at 400 °C, followed by the sample annealed at 900 °C with R_{ohm} equal to 117 Ω·cm^2 at the same temperature. Polarisation resistance gives information on the efficiency and activity of the reaction between $La_{0.6}Sr_{0.4}CoO_{3-\delta}$ and O_2. The lowest value was observed for the sample annealed at 400 °C and the highest at 900 °C. These values are respectively 35.9 Ω·cm^2 and 2370 Ω·cm^2 at 400 °C. A significant decrease in polarisation resistance is the result of the nanoporous structure of a partially amorphous $La_{0.6}Sr_{0.4}CoO_{3-\delta}$. A promising result was also obtained for the sample annealed at 500 °C, where the R_{pol} value at 400 °C was 112 Ω·cm^2. The advantage of using partially amorphous LSC is revealed here. The results for fully crystallised LSC are similar, and the best results with crystalline LSC were observed at an annealing temperature of 600 °C. This is influenced by the small grain size of the crystalline LSC, whose active surface is larger compared to LSC annealed at higher temperatures. This effect has been described in previous works [40–42]. The use of a sintering temperature below the formation temperature of a crystalline structure contributes to a significant decrease in the R_{pol} value. This means that the oxygen electrode's activity got enhanced.

Fig. 4D shows the influence of annealing temperature on the ohmic resistance and the polarisation resistance. The results shows the differences in the parameters describing the oxygen electrode, and indicates the optimal parameters. There is a visible downward polarisation resistance with lowering the annealing temperature. For the ohmic resistance, there is a clear indication of a decrease of this parameter with the increase in the annealing temperature. Moreover, activation energy

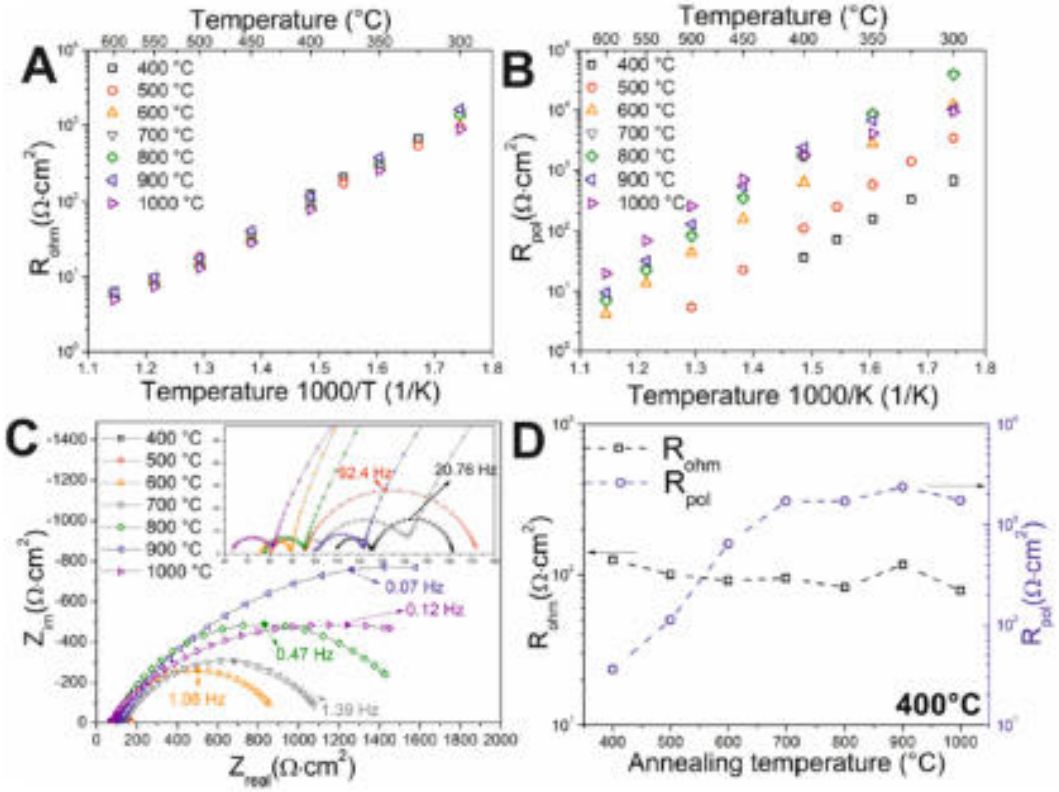


Fig. 4. Ohmic (A) and polarisation (B) values of symmetrical half-cells as a function of annealing temperature; obtained impedance spectra (C), and ohmic resistance and polarisation resistance changes in a function of annealing temperature (D).

for the annealing temperature of 400 °C is lower than that calculated for crystalline form (in this case compared to the annealing temperature of 600 °C), and it takes a value of 0.99 eV compared to 1.15 eV. This phenomenon was also described by Cavallaro et al. with amorphous LSC [20].

Additionally, analysing the Bode plots for partially amorphous and crystalline LSC presented in Fig. S7, they show significant differences. A significant reduction in the middle frequencies was observed for the partially amorphous material, as well as a small change in the frequency characteristic of R_{pol} towards higher frequencies. It follows that the reaction mechanism does not differ much in relation to the crystal structure. Obtaining a low R_{pol} value compared to other works describing amorphous materials indicates that the problem of electron migration resistance from the current collector to the active reaction site is avoided. Additionally, the relationship obtained during EIS measurements at different pO_2 resembles the relationship obtained in work on crystalline form of the LSC [40].

Obtaining the best result for the annealing temperature of 400 °C indicates that the presence of an irregular structure with a significant number of defects has a positive effect on the catalytic activity. According to XANES and EXAFS analyses using WT, there may be variations in the arrangement of atoms in the material that could have an impact on the electrochemical efficiency of the material. The possible occurrence of a mixture of LSC with Co_3O_4, as indicated by XRD and Raman spectroscopy and supported by the literature, indicates the superior properties of an partially-amorphous material [30].

3.3. Detailed electrochemical impedance spectroscopy investigation of electrode processes

The measurements performed using EIS gave only a partial answer to the question of the effectiveness of the oxygen electrode material. In order to better understand the phenomena that occur in the partially amorphous LSC, a series of measurements were performed at different pO_2 in the temperature range of 400 °C–300 °C. Fig. 5A show obtained impedance spectra, and 5B-C show the ohmic and polarisation resistance values obtained for the measurements at different partial pressures of oxygen. Fig. 5D and 5E show the DRT analysis performed for these

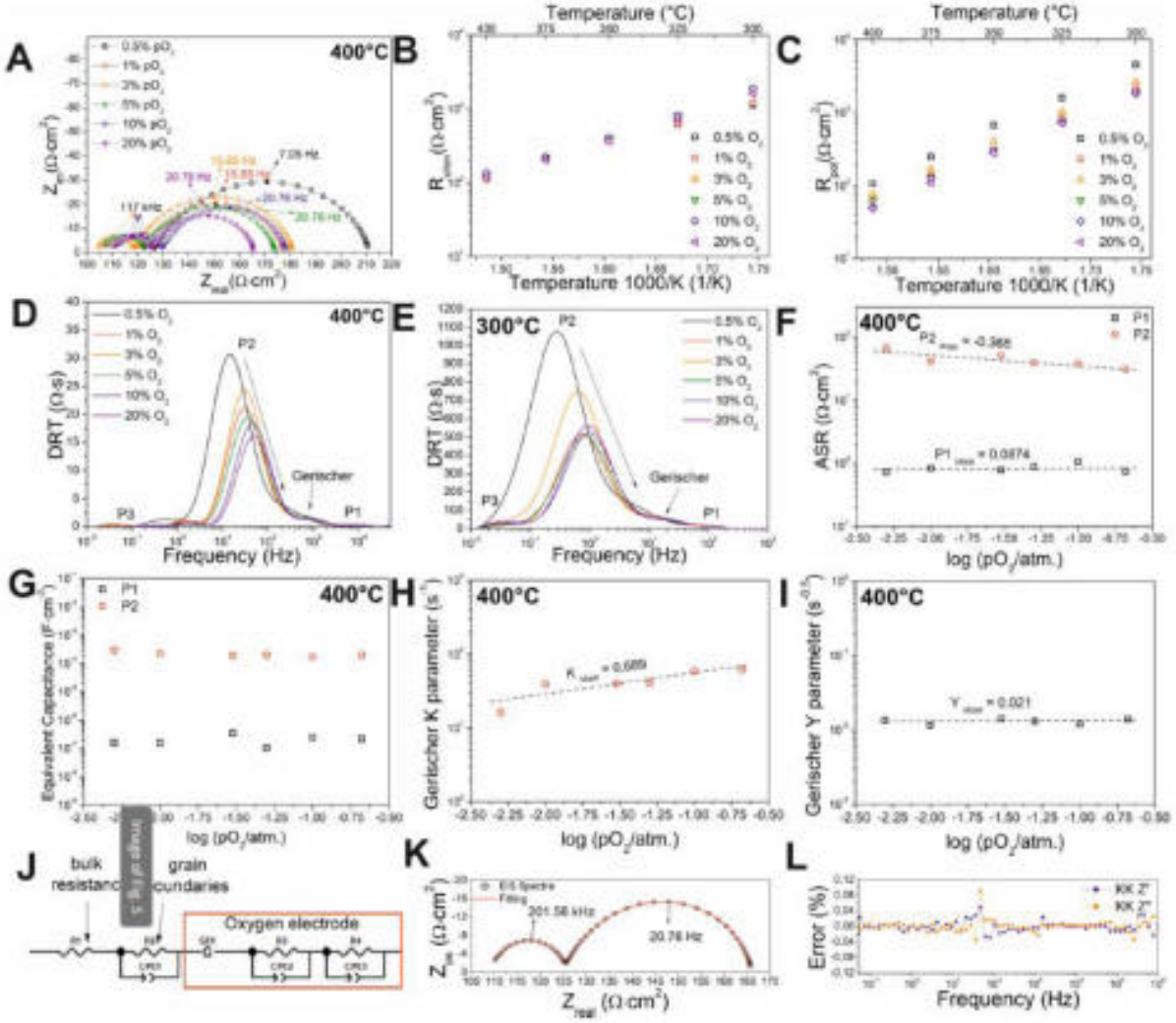


Fig. 5. Impedance spectra obtained during a measurements (A); Arrhenius plots for ohmic (B) and polarisation (C) resistance for measurements at different partial pressures of oxygen and DRT analysis for measurements made at 400 °C (D) and 300 °C (E); determined ASR values for processes P1 and P2 (F), equivalent capacitance values for (G) measured at 400 °C; determined 'K' (H) and 'Y' (I) parameters value for Gerischer element; determined equivalent circuit (J) representative example of fitting for impedance spectra collected in synthetic air (K) and Kronig-Kramers analysis result comparison (L).

measurements. According to the available literature analysing DRT at higher temperatures, three processes can be distinguished [40,43]. The decrease in the pO_2 leads to a modest increase in P1 peak area. Furthermore, the area of the P1 process peak grows as the temperature decreases. In comparison to the high frequency range, this behaviour can be attributed to charge transfer at the electrode/electrolyte contact. The P2 process, which occurs in the medium frequency range, is highly dependent on pO_2 and temperature. P2 can be linked to a variety of electrode processes known as surface oxygen exchange kinetics and oxygen ion diffusion, including adsorption of oxygen gas O_2, dissociation of O_2, and charge transfer diffusion (O_2) [44,45]. The final subprocess, P3, occurs at low frequencies and is strongly dependent primarily on pO_2, with peak area increasing as pO_2 decreases. This mechanism is similar to gas diffusion in the porous oxygen electrode and is only marginally temperature-dependent but substantially dependent on microstructural characteristics [46]. Therefore, it is clear that these phenomena are purely thermally activated.

DRT analysis revealed three peaks typical of oxygen electrodes, denoted as subprocesses P1, P2, and P3. Moreover, at higher frequencies, a characteristic is observed indicating the presence of the Gerischer element, which determines mass transport in the electrode. The impedance of the Gerisher element results from the relation:

$$Z(\omega) = \frac{1}{Y(k + j\omega)^{0.5}} \quad (1)$$

where 'k' is the effective transfer rate of the chemical reaction and 'Y' is the initial coefficient, i.e. the inverse of Z_0 [47]. Variations of the ASRs of the identified electrode subprocesses with pO_2 are shown in Fig. 5F–G. The slope of the curves helps to deduce the likely mechanism of the reaction occurring in the electrodes [48]. The dependency can be attributed to adsorption and surface exchange for slopes 0.5 to 0.25, but a slope of 1 involves the contribution of molecular oxygen and is attributed to gaseous diffusion [49]. For different oxygen concentrations at 400 °C, we observed a slope of 0.087 for process P1 and −0.368 for process P2. It was impossible to analyse the value for the P3 process with the indicated gas diffusion. The reason for that is the low temperature of the experiment, when part of the impedance spectra describing this process is negligible, and it was impossible to achieve proper and valid results. Processes P2 and P1 have different slopes, which may indicate oxygen surface exchange kinetics and oxygen ion diffusion, respectively. In the case of the P1 process, we are talking rather about the charge-transfer reaction at the interface, which has a higher resistance compared to other subprocesses.

The observed capacitance values do not change significantly with increasing oxygen content in the analysed samples. Values observed for the P2 process indicate that it could be the adsorption process [40,45]. In this case, there is no dependence or very small dependence of the capacitance on the oxygen concentration. Capacitance values decrease with increasing oxygen concentration, which correlates with literature data [40,49]. For the P1 process, the capacitance values were $\sim 10^{-7}$ F·cm^{-2}. This is likely because of the charge transfer that occurs at the interface between the electrode and the electrolyte layer. Fig. 5H–I present the determined values of the parameters 'k' and 'Y' for the Gericher element. Examining the impact of oxygen partial pressure on the Gerischer element parameters, a pronounced reliance on the rate constant parameter k (with a slope of 0.689) becomes apparent. Conversely, the Y parameter associated with admittance appears unaffected by changes in pO_2, displaying a nearly constant value with a very small slope. Notably, the resistance of the Gerischer element at 400 °C and pO_2 of 20 % measures 9.3 Ω·cm^2 and exhibits dependency on pO_2. Fig. 5J shows the equivalent circuit obtained by DRT analysis. Fig. 5K shows a representative example of the fit obtained for the equivalent circuit used. Additionally, a Kronig–Kramers (KK) analysis was performed [50,51]. Representative analysis results are presented in Fig. 5L. For most of the spectrum, the relative error of both the real and imaginary data was under 0.04 %.

3.4. Stability tests

The use of a low annealing temperature and the use of partially amorphous $La_{0.6}Sr_{0.4}CoO_{3-\delta}$ can affect the stability of the oxygen electrode over time. The active surface of the electrode may also change. Nyquist plots show the changes over time and are presented in Fig. 6A. Fig. 6B and C show the change of R_{ohm} and R_{pol} parameters over time. In the case of R_{ohm}, an initial value of 92.8 Ω·cm^2 was observed, and the value fluctuated around this value. The final value was 92.3 Ω·cm^2, which means a reduction of 0.5 Ω·cm^2. In the case of the polarisation resistance, an increase in the value from the initial value of 35.7 Ω·cm^2 to the value of 43.2·Ω cm^2 was observed, which means a change in degradation rate of 21 % in 100 h. The observed increase in polarisation resistance is also different from that observed for the crystalline form of LSC at higher temperatures [40,52]. This may be related to various processes, mainly chemical and not necessarily related to degradation, occurring in the partially amorphous material.

Fig. S8 shows the XRD spectra taken on the samples after EIS measurements. Along with the LSC-matched peaks, which were the same as for the powders in the first part of this article, CGO peaks at 29° and 57° and overlapping LSC peaks at 33° and 48° were also found. Moreover, starting from an annealing temperature higher than 600 °C, the occurrence of additional peaks was identified, which indicate the formation of an additional phase adapted to the presence of cobalt spinel at 32°, 37°, 54°, and 66°. At lower temperatures, crystallisation occurs slowly, and the SRN (signal-to-noise ratio) at 400 °C is lower than that observed at 500 °C. Peaks corresponding to the appearance of Co_3O_4 are also not observed. The results obtained for higher temperatures are consistent with those available in the literature. The lack of identification of $SrCO_3$ should also be noted. At the same time, the use of an amorphous material causes its high variability because the diffractogram made after the tests for temperatures below 600 °C differs significantly from the one made before the tests. It seems that the material crystallises slowly, which may cause an initial large variability in the parameters describing the electrode. This may also explain the increase in polarisation resistance obtained during ageing measurements, and the observed increase in this parameter is due to changes occurring in the material and not to its degradation.

4. Electrode reaction mechanism on a partially-amorphous LSC oxygen electrode

The transport of charges at the oxygen electrode in MIEC (Mixed Ionic-Electronic Conductor) materials, such as LSC, proceeds through three steps: the adsorption of oxygen molecules followed by their dissociation, the reduction of oxygen ions leading to their ionisation, and the integration of oxygen ions into the surface of the oxygen electrode [53]. In the following step, the oxygen ion undergoes either bulk diffusion or surface diffusion, and ultimately, in the final step, it reaches the interface between the oxygen electrode and the electrolyte.

Amorphous or partially amorphous materials exhibit unique properties that allow for electrochemical enhancement and catalytic activity. These materials show a short-range order, but on a larger scale, along-range disorder should be considered. For those material a reduction of electronic conductivity, increase in the occurrence of defects and vacancies, and possible faster ionic diffusion is observed [54]. In amorphous or partially-amorphous material, the movement of oxygen occurs through a "saddle point" located between two A-site cations and one B-site cation, instead of directly jumping from one site to the adjacent vacancy along the anion octahedra edge. The larger volume of the perovskite cell in the amorphous oxygen electrode material, along with its lower density, may cause a decrease in the amount of energy required for oxygen to move into a neighbouring oxygen vacancy. Similarly, the pathway through which oxygen moves in an amorphous 'pre'-perovskite

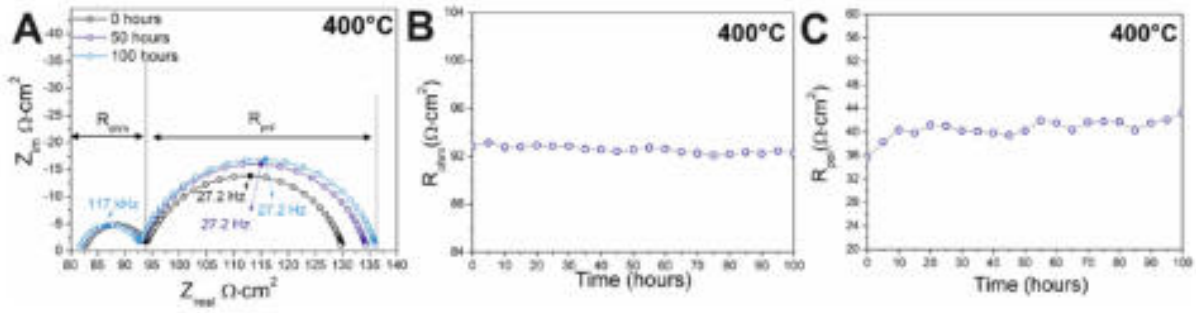


Fig. 6. Impedance spectra at 0, 50, and 100 h for a sample subjected to 100-hour ageing tests in 400 °C (A); change of ohmic resistance (B), and polarisation resistance during ageing measurements (C).

structure is likely to be distinct, resulting in a reduced activation energy for oxygen diffusion [55–57]. The combination of various sharing geometries also affects the properties. Amorphous materials are created by stacking distorted metal–oxygen polyhedra to create lattice arrays in a random arrangement. The oxygen atoms of multiple polyhedra are connected to each other through various sharing configurations, including edge sharing, corner sharing, and face sharing. The presence of extensive structural disturbances in amorphous materials reduces the mean free scattering path, while the absence of grain boundaries leads to the uniformity of electronic properties over large areas [54]. The improvement obtained in the catalytic properties of LSC in the partially amorphous form indicates that the greater number of defects and vacancies produced is responsible for this effect.

Annealing at 400 °C results in a reduction in polarisation resistance due to a high active surface area, a larger number of defects and vacancies, and extremely small grains, but at the same time increases ohmic resistance. Higher annealing temperatures lead to larger grain sizes, crystallisation of LSC, and a reduction in the number of defects and vacancies compared to the partially amorphous form. This outcome exhibits reduced ohmic resistance while also demonstrating notably higher polarisation resistance.

4.1. Literature comparison of electrochemical performance of oxygen electrodes at low temperatures

Among cited works an introduction part, for improve the discussion the result obtainsed in this study was compared with other works The obtained results were compared with the data available in the literature, not only for LSC but also for other promising oxygen electrode materials. Fig. 7A presents Arrhenius plots for cited works and a comparison with this work. Delving deeper into the topic, Fig. 7B presents the R_{pol} values obtained over the last 15 years. This chart also includes a division into the use of a single material and the composites.

For example Kamecki et al. describe the use of LSC oxygen electrode layer deposited with spray pyrolysis method. The electrode thickness was set as 400 nm. The symmetrical cell showed very low value of the polarisation resistance in 400 °C as −10 Ω·cm^2. The fuel cell with this electrode show high stability over the long time of stability experiment (around 1000 h) [40]. Very promising results were also achieved in the work of Nicolett et al. where they studied a CGO-based cathode infiltrated by praseodymium oxide. The polarization resistance value was −2 Ω·cm^2 at 400 °C[6]. Hu et al. described the use of $SrCo_{1-x}Sb_xO_{3-\delta}$ as a potential cathode. At 500 °C, the polarisation resistance for the $SrCo_{0.8125}Sb_{0.1875}O_{3-\delta}$ sample was −1.7 Ω·cm^2. Additionally, this work demonstrated an improvement in CO_2 tolerance [7]. Samat et al. described the use of single-phase, submicron LSC synthesized via a polymeric complexation method as an oxygen electrode in proton-conducting fuel cells. Symmetric samples were sintered at 900 °C. EIS measurements at 400 °C showed an R_{pol} value of approximately 32 Ω·cm^2 [18]. Noh et al. prepared a cell with an LSC oxygen electrode approximately 1 μm thick. At a temperature of 400 °C, the ASR value was 17.7 Ω·cm^2 [58].

There are very few works describing the use of non-crystalline LSC. However, the comparison with them is the most meaningful. In the work of Cavallaro et al. a PLD-deposited layer with a thickness of approximately 300 nm was used and heat treated from room temperature to 750 °C, with an intermediate step at 200 °C. At a temperature of 415 °C, the R_{pol} value reached 850 Ω·cm^2 [20]. In a separate study, Evans et al. employed partially amorphous LSC as an oxygen electrode in micro-solid oxide fuel cells. They investigated electrode thicknesses of 100

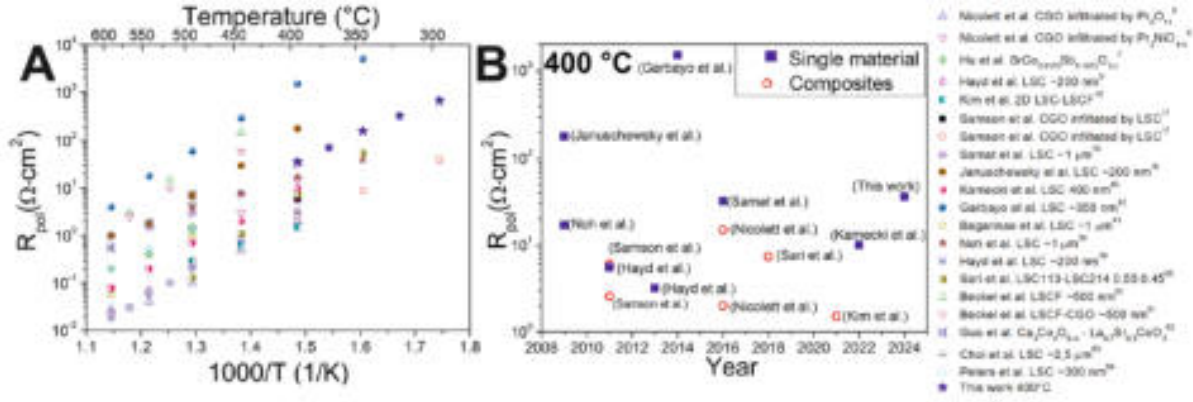


Fig. 7. Arrhenius plot of the polarization resistance of symmetrical half-cells in tests of cathodes that can be used in SOCs technology from literature data [6,7,9,16–19,40,42,43,58–64].

nm and 200 nm. For the 200 nm thickness at 400 °C, fuel cell measurements indicated an ASR value for the oxygen electrode not exceeding 0.3 $\Omega \cdot cm^2$ [12].

The values obtained in this work are in the middle of the polarization resistance values obtained in other works. This means that further development of partially amorphous oxygen electrode materials is needed. It is worth noting that in the case of single materials, better results are generally achieved with composites. Of the cited works, only one included temperature as low as 300 °C.

5. Conclusions

In this work, an oxygen electrode in the form of $La_{0.6}Sr_{0.4}CoO_{3-\delta}$ was deposited on $Ce_{0.8}Gd_{0.2}O_{2-\delta}$ pellets using the spin-coating technique. A new method for preparing the LSC precursor using UV radiation has been used. The structural analysis was based on tests such as XRD, HT-XRD, RAMAN spectra, FTIR, XANES, EXAFS, and WT as a function of annealing temperature in the range of 400–1000 °C. Electrochemical impedance spectroscopy allowed to determine the optimal range of oxygen electrode thickness (~500 nm) and to determine the optimal annealing temperature (400 °C).It has been shown that the partially amorphous LSC has significantly higher electrochemical activity. The partially amorphous nature of the material is indicated by the presence of characteristic bonds (typical for crystalline LSC, but lower intensity of the signal) with identified using Raman and FTIR spectroscopy. This is also indicated by the Bode characteristic in EIS measurements. Moreover, XRD and HT-XRD measurements indicate that the minimum crystallization temperature is approximately 600 °C (nanocrystalline).

The increase in electrochemical activity of partially amorphous LSC is probably due to the decreased oxidation state (from 3.4 to 2.9) of cobalt in partially amorphous LSC. This change is combined with a visibly lower coordination number of oxygen near the central atom. All this, combined with the irregular spatial structure, increases the number of defects in the material and oxygen vacancies.

Stability tests and post-mortem analysis of samples indicate adequate stability of the material combined with the lack of observations of oxides indicating material decomposition ($SrCO_3$ or Co_3O_4) indicate the potential use of partially amorphous LSC as an oxygen electrode in SOCs.

To the best of our knowledge, this work is the first to describe in a comprehensive study the electrochemical and structural properties of perovskite-based oxygen electrodes in SOC technology, focusing on such a low temperature. Attempts to describe partially amorphous material and demonstrate similarities and differences using multiple techniques are also worth noting.

CRediT authorship contribution statement

Bartłomiej Lemieszek: Writing – review & editing, Writing – original draft, Validation, Methodology, Investigation, Formal analysis, Data curation, Conceptualization. **Mindaugas Ilickas:** Writing – review & editing, Methodology, Investigation. **Jan Jamroz:** Writing – review & editing, Methodology, Investigation. **Asta Tamulevičienė:** Writing – review & editing, Methodology, Investigation. **Jakub Karczewski:** Writing – review & editing, Methodology, Investigation. **Patryk Błaszczak:** Writing – review & editing, Methodology, Investigation. **Alexey Maximenko:** Writing – review & editing, Supervision, Methodology, Investigation, Data curation. **Brigita Abakevičienė:** Writing – review & editing, Supervision, Methodology, Investigation. **Marcin Małys:** Writing – review & editing, Methodology, Investigation. **Sigitas Tamulevičius:** Writing – review & editing, Supervision, Resources, Methodology. **Piotr Jasiński:** Writing – review & editing, Supervision, Methodology. **Sebastian Molin:** Writing – review & editing, Supervision, Resources, Methodology, Data curation, Conceptualization.

Declaration of competing interest

The authors declare that they have no known competing financial interests or personal relationships that could have appeared to influence the work reported in this paper.

Data availability

Data will be made available on request.

Acknowledgements

This research has been supported by the National Science Centre (NCN) DAINA 2 project number UMO-2020/38/L/ST8/00513 and the Lithuanian Research Council (LMLT) project S-LL-21-8: "Porous metal supported micro-scale solid oxide fuel cells: fundamentals, fabrication and testing". The XAFS measurements at ASTRA beamline at NSRC SOLARIS were made under the provision of the Polish Ministry and Higher Education project "Support for research and development with the use of research infra-structure of the National Synchrotron Radiation Centre SOLARIS" under contract Nr 1/SOL/2021/2. The further development of ASTRA beamline at NSRC SOLARIS was supported within the EU Horizon2020 program (952148-Sylinda).

Appendix A. Supplementary data

Supplementary data to this article can be found online at https://doi.org/10.1016/j.apsusc.2024.160620.

References

[1] A. Tarancón, Strategies for lowering solid oxide fuel cells operating temperature, Energies 2 (4) (2009) 1130–1150, https://doi.org/10.3390/en20401130.
[2] A. Alaswad, A. Baroutaji, A. Rezk, M. Ramadan, A.G. Olabi, Advances in Solid Oxide Fuel Cell Materials, Elsevier Ltd., 2021, https://doi.org/10.1016/B978-0-12-803581-8.11743-6.
[3] J.C.W. Mah, A. Muchtar, M.R. Somalu, M.J. Ghazali, Metallic interconnects for solid oxide fuel cell: a review on protective coating and deposition techniques, Int. J. Hydrogen Energy 42 (14) (2017) 9219–9229, https://doi.org/10.1016/J.IJHYDENE.2016.03.195.
[4] M.F. Vostakola, B.A. Horri, Progress in material development for low-temperature solid oxide fuel cells: a review, Energies 14 (5) (2021), https://doi.org/10.3390/en14051280.
[5] L. Yefsah, J. Laurencin, M. Hubert, et al., Electrochemical performance and stability of $PrO_{1.833}$ as an oxygen electrode for solid oxide electrolysis cells, Solid State Ion. 399 (March) (2023) 1–14, https://doi.org/10.1016/j.ssi.2023.116316.
[6] C. Nicollet, A. Flura, V. Vibhu, A. Rougier, J.M. Bassat, J.C. Grenier, An innovative efficient oxygen electrode for SOFC: Pr_6O_{11} infiltrated into Gd-doped ceria backbone, Int. J. Hydrogen Energy 41 (34) (2016) 15538–15544, https://doi.org/10.1016/j.ijhydene.2016.04.024.
[7] X. Hu, Y. Xie, Y. Wan, Y. Yang, X. Wu, C. Xia, Antimony-doped strontium cobalt oxide as promising cathode for low-temperature solid oxide fuel cell with excellent carbon dioxide tolerance, Appl. Catal. B Environ. 286 (2021) 119901, https://doi.org/10.1016/J.APCATB.2021.119901.
[8] Yi-Ching Chen, Masamoto Yashima, Takashi Ohta, Kenji Ohoyama, S. Yamamoto, Crystal Structure, Oxygen Deficiency, and Oxygen Diffusion Path of Perovskite-Type Lanthanum Cobaltites $La_{1-x}Ba_{0.5}CoO_{3-\delta}$ and $La_{0.6}Sr_{0.4}CoO_{3-\delta}$, J. Phys. Chem. C 116 (2012) 5246–5254.
[9] J. Hayd, H. Yokokawa, E. Ivers-Tiffée, Hetero-interfaces at nanoscaled (La, Sr) $CoO_{3-\delta}$ thin-film cathodes enhancing oxygen surface-exchange properties, J. Electrochem. Soc. 160 (4) (2013) F351–F359, https://doi.org/10.1149/2.017304jes.
[10] L. Dieterle, P. Bockstaller, D. Gerthsen, J. Hayd, E. Ivers-tiffée, Microstructure of nanoscaled $La_{0.6}Sr_{0.4}CoO_{3-\delta}$ cathodes for intermediate-temperature solid oxide fuel cells, Published Online (2011) 249–258, https://doi.org/10.1002/aenm.201000036.
[11] J. Janaschewsky, M. Kubicek, M. Stöger-Pollach, J. Bernardi, J. Fleig, Structural and chemical investigations of (La, Sr)$CoO_{3-\delta}$, Trans E C S Soc. Electrochem. 25 (2) (2009) 2397–2402, https://doi.org/10.1149/MA2009-02/12/1474.
[12] A. Evans, J. Maetynczuk, D. Stender, C.W. Schneider, T. Lippert, M. Prestat, Low-temperature micro-solid oxide fuel cells with partially amorphous $La_{0.6}Sr_{0.4}CoO_{3-\delta}$ cathodes, Adv. Energy Mater. 5 (1) (2015) 1–9, https://doi.org/10.1002/aenm.201400747.
[13] M. Søgaard, P.V. Hendriksen, M. Mogensen, F.W. Poulsen, E. Skou, Oxygen nonstoichiometry and transport properties of strontium substituted lanthanum cobaltite, Solid State Ion. 177 (37–38) (2006) 3285–3296, https://doi.org/10.1016/J.SSI.2006.09.005.

[14] Y.T. Kim, N. Shikazono, Evaluation of electrochemical reaction mechanisms of $La_{0.6}Sr_{0.4}CoO_{3-\delta}$-$Gd_{0.2}Ce_{0.8}O_{2-\delta}$ composite cathodes by 3D numerical simulation, Solid State Ion. 319 (2018) 162–169, https://doi.org/10.1016/J.SSI.2018.02.014.
[15] R. Vinoth Kumar, A.P. Khandale, A review on recent progress and selection of cobalt-based cathode materials for low temperature-solid oxide fuel cells, Renew. Sustain. Energy Rev. 156 (2022) 111985, https://doi.org/10.1016/J.RSER.2021.111985.
[16] C. Kim, H. Lee, I. Jang, et al., Subcontinuous 2D $La_{0.6}Sr_{0.4}CoO_{3-\delta}$ nanosheet as an efficient charge conductor for boosting the cathodic activity of solid oxide fuel cells, Electrochim. Acta 366 (2021) 137371, https://doi.org/10.1016/J.ELECTACTA.2020.137371.
[17] A. Samson, M. Søgaard, R. Knibbe, N. Bonanos, High performance cathodes for solid oxide fuel cells prepared by infiltration of $La_{0.6}Sr_{0.4}CoO_{3-\delta}$ into Gd-Doped Ceria, J. Electrochem. Soc. 158(6) (2011), https://doi.org/10.1149/1.3571249.
[18] A. Abdul Samat, M.R. Somalu, A. Muchtar, O.H. Hasan, N. Osman, LSC cathode prepared by polymeric complexation method for proton-conducting SOFC application, J. Sol-Gel Sci. Technol. 78 (2) (2016) 382–393, https://doi.org/10.1007/s10971-015-3945-4.
[19] J. Janarchewsky, M. Ahrens, A. Opitz, F. Kubel, J. Fleig, Optimized $La_{0.6}Sr_{0.4}CoO_{3-\delta}$ thin-film electrodes with extremely fast oxygen-reduction kinetics, Adv. Funct. Mater. 19 (19) (2009) 3151–3156, https://doi.org/10.1002/adfm.200900362.
[20] A. Cavallaro, P.C. Sherrell, E. Ware, A. Kilner, S.J. Skinner, Amorphous-cathode-route towards low temperature, Sust. Energy Fuels. 2 (2018) 862–875, https://doi.org/10.1039/c7se00606c.
[21] H. Funke, A.C. Scheinost, M. Chukalina, Wavelet analysis of extended x-ray absorption fine structure data, Phys Rev B - Condens Matter Mater Phys. 71 (9) (2005) 1–7, https://doi.org/10.1103/PhysRevB.71.094110.
[22] H. Funke, M. Chukalina, A.C. Scheinost, A new FEFF-based wavelet for EXAFS data analysis, J. Synchrotron Radiat. 14 (5) (2007) 426–432, https://doi.org/10.1107/S0909049507031901.
[23] T.H. Wan, M. Saccoccio, C. Chen, F. Ciucci, Influence of the discretization methods on the distribution of relaxation times deconvolution: implementing radial basis functions with DRTtools, Electrochim. Acta 184 (2015) 483–499, https://doi.org/10.1016/J.ELECTACTA.2015.09.097.
[24] M.P. Pechini, Method of Pre Paring Lead and Alkaline Earth Titanates and Niobates and Coat, US Pat 3,330,697. Published online 1967:2.
[25] M. Kim, D.H. Kim, G.D. Han, H.J. Choi, H.R. Choi, J.H. Shim, Lanthanum strontium cobaltite-infiltrated lanthanum strontium cobalt ferrite cathodes fabricated by inkjet printing for high-performance solid oxide fuel cells, J. Alloy. Compd. 843 (2020) 155806, https://doi.org/10.1016/J.JALLCOM.2020.155806.
[26] T. Yamamoto, Assignment of pre-edge peaks in K-edge x-ray absorption spectra of 3d transition metal compounds: electric dipole or quadrupole? Published Online (2008) 572–584, https://doi.org/10.1002/xrs.
[27] J. Choy, H. Jung, J. Yoon, N. Nanohybrid, N. Co-doped-sio, N.C. Sio, catalysis Co K-edge XAS study on a new cobalt, Published Online (2001) 599–601, https://doi.org/10.1107/S0909049500015480.
[28] F. De Groot, G. Vankó, P. Glatzel, The 1s x-ray absorption pre-edge structures in transition metal oxides, J. Phys. Condens. Matter 21 (10) (2009), https://doi.org/10.1088/0953-8984/21/10/104207.
[29] W.W. Zhang, E. Povoden-Karadeniz, Y. Shang, P.V. Hendriksen, M. Chen, Phase equilibria and defect chemistry of the La-Sr-Co-O system, J. Eur. Ceram. Soc. 43 (10) (2023) 4419–4430, https://doi.org/10.1016/j.jeurceramsoc.2023.03.026.
[30] X. Wang, Z. Pan, X. Chu, et al., Atomic-scale insights into surface lattice oxygen activation at the spinel/perovskite interface of Co_3O_4/$La_{0.5}Sr_{0.5}CoO_{3-\delta}$, Angew. Chem. 58 (2019) 11720–11725, https://doi.org/10.1002/anie.201905843.
[31] O. Celikbilek, A. Cavallaro, G. Kerherve, et al., Surface restructuring of thin-film electrodes based on thermal history and its significance for the catalytic activity and stability at the gas/solid and solid/solid interfaces, ACS Appl. Mater. Interf. 12 (30) (2020) 34388–34401, https://doi.org/10.1021/acsami.0c08308.
[32] A. Ishikawa, J. Nohara, S. Sugai, Raman study of the orbital-phonon coupling in $LaCoO_3$, Phys. Rev. Lett. 93 (13) (2004) 1–4, https://doi.org/10.1103/PhysRevLett.93.136401.
[33] N. Orlovskaya, D. Steinmetz, S. Yarmolenko, D. Pai, J. Sankar, J. Goodenough, Detection of temperature- and stress-induced modifications of $LaCoO_3$ by micro-Raman spectroscopy, Phys. Rev. B – Condens. Matter. Mater. Phys. 72 (1) (2005) 1–7, https://doi.org/10.1103/PhysRevB.72.014122.
[34] X. Li, Z. Peng, W. Pan, et al., Raman spectra study of nanocrystalline composite oxides, Mater. Chem. Phys. 46 (1) (1996) 50–54, https://doi.org/10.1016/0254-0584(96)80129-5.
[35] A.H. El, J.F. Pierson, M. Chaik, et al., Evolution of the structural, morphological, optical and electrical properties of reactively RF-sputtered cobalt oxide thin fi lms with oxygen pressure, Vacuum 2019 (159) (2018) 346–352, https://doi.org/10.1016/j.vacuum.2018.10.065.
[36] T. Ghorbani-Moghadam, A. Kompany, M. Golmohammad, The comparative study of doping Cu and Fe on the cathodic properties of $La_{0.7}Sr_{1.3}CoO_4$ layered perovskite compound: to be used in IT-SOFC, J. Alloy. Compd. 926 (2022) 166928, https://doi.org/10.1016/J.JALLCOM.2022.166928.
[37] T. Ghorbani-Moghadam, A. Kompany, M.M. Bagheri-Mohagheghi, M.E. Abrishami, Cobalt spin states investigation of Ruddlesden-Popper $La_{2-x}Sr_xCoO_4$, using X-ray diffraction and infrared spectroscopy, J. Magn. Magn. Mater. 465 (2018) 766–774, https://doi.org/10.1016/J.JMMM.2018.06.062.
[38] M. Sivakumar, M. Sakthivel, S.M. Chen, P. Veerakumar, L.S. Bin, Sol-gel synthesis of carbon-coated $LaCoO_3$ for effective electrocatalytic oxidation of salicylic acid, ChemElectroChem 4 (4) (2017) 935–940, https://doi.org/10.1002/celc.201600714.
[39] L. Garces, M. Lopez-Medina, K.P. Padmasree, et al., A parchment-like supercapacitor made with sustainable graphene electrodes and its enhanced capacitance by incorporation of the LaSrCoO 3 perovskite, ChemistrySelect 7 (36) (2022), https://doi.org/10.1002/slct.202202199.
[40] B. Kamecki, G. Cempura, P. Jasiński, S.-P. Wang, S. Molin, Tuning electrochemical performance by microstructural optimization of the nanocrystalline functional oxygen electrode layer for solid oxide cells, ACS Appl. Mater. Interf. 14 (51) (2022) 57449–57459, https://doi.org/10.1021/acsami.2c18951.
[41] K. Develos-Bagarinao, O. Celikbilek, R.A. Budiman, et al., electrochemical performance and long-term, Published Online (2022) 2445–2459, https://doi.org/10.1039/d1ta07235b.
[42] I. Garbayo, V. Esposito, S. Sanna, et al., Porous $La_{0.6}Sr_{0.4}CoO_{3-\delta}$ thin film cathodes for large area micro solid oxide fuel cell power generators, J. Power Sources 248 (2014) 1042–1049, https://doi.org/10.1016/j.jpowsour.2013.10.038.
[43] K. Develos-Bagarinao, K. Yamaji, H. Kishimoto, H. Shimada, K. Yamaji, Nanoengineering of cathode layers for solid oxide fuel cells to achieve superior power densities, Nat. Commun. 12 (2021) 3979, https://doi.org/10.1038/s41467-021-24255-w.
[44] S.B. Adler, Factors governing oxygen reduction in solid oxide fuel cell cathodes, Chem. Rev. 104 (10) (2004) 4791–4843, https://doi.org/10.1021/cr020724o.
[45] C. Pu, K. Sun, N. Zhang, X. Chen, D. Zhou, Electrochemical characteristics of LSCF–SDC composite cathode for intermediate temperature SOFC, Electrochim. Acta 52 (13) (2007) 4589–4594, https://doi.org/10.1016/J.ELECTACTA.2007.01.001.
[46] T. Jacobsen, P.V. Hendriksen, S. Koch, Diffusion and conversion impedance in solid oxide fuel cells, Electrochim. Acta 53 (25) (2008) 7500–7508, https://doi.org/10.1016/J.ELECTACTA.2008.02.019.
[47] B.A. Boukamp, H.J.M. Bouwmeester, Interpretation of the Gerischer impedance in solid state ionics, Solid State Ion. 157 (2003) 29–33, https://doi.org/10.1016/S0167-2738(02)00185-6.
[48] A. Esquirol, N.P. Brandon, J.A. Kilner, M. Mogensen, Electrochemical characterization of $La_{0.6}Sr_{0.4}Co_{0.2}Fe_{0.8}O_{3-\delta}$ cathodes for intermediate-temperature SOFCs, J. Electrochem. Soc. 151 (2004) 1847–1855, https://doi.org/10.1149/1.1799391.
[49] A. Mroziński, S. Molin, J. Karczewski, T. Miruszewski, P. Jasiński, Electrochemical properties of porous $Sr_{0.85}Ti_{0.35}Fe_{0.35}O_3$ oxygen electrodes in solid oxide cells: impedance study of symmetrical electrodes, Int. J. Hydrogen Energy 44 (2018) 1827–1839, https://doi.org/10.1016/j.ijhydene.2018.11.205.
[50] B.A. Boukamp, A linear Kronig-Kramers transform test for immittance data validation, J. Electrochem. Soc. 142 (6) (1995) 1885–1894, https://doi.org/10.1149/1.2044210.
[51] M. Schönleber, D. Klotz, E. Ivers-Tiffée, A method for improving the robustness of linear kramers-kronig validity tests, Electrochim. Acta 131 (2014) 20–27, https://doi.org/10.1016/J.ELECTACTA.2014.01.034.
[52] T. Zhang, Y. Zhao, X. Zhang, et al., Thermal stability of an in situ exsolved metallic nanoparticle structured perovskite type hydrogen electrode for solid oxide cells, Published Online (2019), https://doi.org/10.1021/acsaem.9b04350.
[53] A. Endo, H. Fukunaga, C. Wen, K. Yamada, Cathodic reaction mechanism of dense $La_{0.6}Sr_{0.4}CoO_{3-\delta}$ and $La_{0.85}Sr_{0.15}MnO_3$ electrodes for solid oxide fuel cells, Solid State Ion. 135 (1–4) (2000) 353–358, https://doi.org/10.1016/S0167-2738(00)00466-5.
[54] S. Yan, K.P. Abhilash, L. Tang, et al., Research advances of amorphous metal oxides in electrochemical energy storage and conversion, Small 15 (4) (2019) 1–30, https://doi.org/10.1002/smll.201804371.
[55] J.A. Kilner, R.J. Brook, A study of oxygen ion conductivity in doped non-stoichiometric oxides, Solid State Ion. 6 (3) (1982) 237–252, https://doi.org/10.1016/0167-2738(82)90045-5.
[56] M.S. Islam, M. Cherry, C.R.A. Catlow, Oxygen diffusion in $LaMnO_3$ and $LaCoO_3$ perovskite-type oxides: a molecular dynamics study, J. Solid State Chem. 124 (2) (1996) 230–237, https://doi.org/10.1006/JSSC.1996.0231.
[57] M. Cherry, M.S. Islam, C.R.A. Catlow, Oxygen ion migration in perovskite-type oxides, J. Solid State Chem. 118 (1) (1995) 125–132, https://doi.org/10.1006/JSSC.1995.1320.
[58] H. Noh, J. Son, H. Lee, H. Song, H.-W. Lee, J. Lee, Low temperature performance improvement of SOFC with thin film electrolyte and electrodes fabricated by pulsed laser deposition, J. Electrochem. Soc. 156 (12) (2009) B1484, https://doi.org/10.1149/1.3243859.
[59] J. Hayd, L. Dieterle, U. Guntow, D. Gerthsen, E. Ivers-Tiffée, Nanoscaled $La_{0.6}Sr_{0.4}CoO_{3-\delta}$ as intermediate temperature solid oxide fuel cell cathode: microstructure and electrochemical performance, J. Power Sources. 196 (17) (2011) 7263–7270, https://doi.org/10.1016/J.JPOWSOUR.2010.11.147.
[60] D. Sari, F. Fiskin, Z.C. Torunoglu, B. Yasar, Y.E. Kalay, T. Ozturk, Combinatorial development of nanocrystalline/amorphous (La, Sr)CoO_3-(La, Sr)$_2CoO_4$ composite cathodes for IT-SOFCs, Solid State Ion. 326 (October) (2018) 124–130, https://doi.org/10.1016/j.ssi.2018.10.003.
[61] D. Beckel, U.P. Muecke, T. Gyger, G. Florey, A. Infortuna, L.J. Gauckler, Electrochemical performance of LSCF based thin film cathodes prepared by spray pyrolysis, Solid State Ion. 178 (2007) 407–415, https://doi.org/10.1016/j.ssi.2007.01.019.

[62] P. Guo, X. Huang, X. Zhu, et al., A new composite material $Ca_2Co_4O_{9+\delta}$-$La_{0.5}Sr_{0.5}CoO_3$ developed for intermediate-temperature SOFC cathode, Fuel Cells 13 (5) (2013) 666–672, https://doi.org/10.1002/fuce.201300031.
[63] S. Choi, S. Yoo, J. Shin, G. Kim, J.E. Soc, P. B-b, High Performance SOFC cathode prepared by infiltration of $La_{n+1}Ni_nO_{3n+1}$ (n = 1, 2, and 3) in porous YSZ high performance SOFC cathode prepared by infiltration, J. Electrochem. Soc. 158 (8) (2011) B995–B999, https://doi.org/10.1149/1.3598170.
[64] C. Peters, A. Weber, E. Ivers-tiffée, Nanoscaled $La_{0.5}Sr_{0.5}CoO_{3-\delta}$ thin film cathodes for SOFC application at 500°C < T < 700°C, Published Online (2008:) 730–737, https://doi.org/10.1149/1.2909552.

Supporting Information

Enhanced electrochemical performance of partially amorphous $La_{0.6}Sr_{0.4}CoO_{3-\delta}$ oxygen electrode materials for low-temperature solid oxide cells operating at 400°C

Bartłomiej Lemieszek[a], Mindaugas Ilickas[b], Jan Jamroz[c], Asta Tamulevičienė[b], Jakub Karczewski[d], Patryk Błaszczak[d], Alexey Maximenko[e], Brigita Abakevičienė[b], Marcin Małys[c], Sigitas Tamulevičius[b], Piotr Jasiński[a], Sebastian Molin[a]

[a] Advanced Materials Centre, Faculty of Electronics, Telecommunications and Informatics, Gdańsk University of Technology, ul. G. Narutowicza 11/12, 80-233 Gdańsk, Poland
[b] Institute of Materials Science of Kaunas University of Technology, K. Baršausko str. 59, Kaunas LT-51423, Lithuania Lithuania
[c] Warsaw University of Technology, Faculty of Physics, Koszykowa 75, 00-662 Warsaw, Poland
[d] Advanced Materials Centre, Faculty of Applied Physics and Mathematics, Gdańsk University of Technology, ul. G. Narutowicza 11/12, 80-233 Gdańsk, Poland
[e] National Synchrotron Radiation Centre SOLARIS, Jagiellonian University, Czerwone Maki 98, 30-392, Kraków, Poland

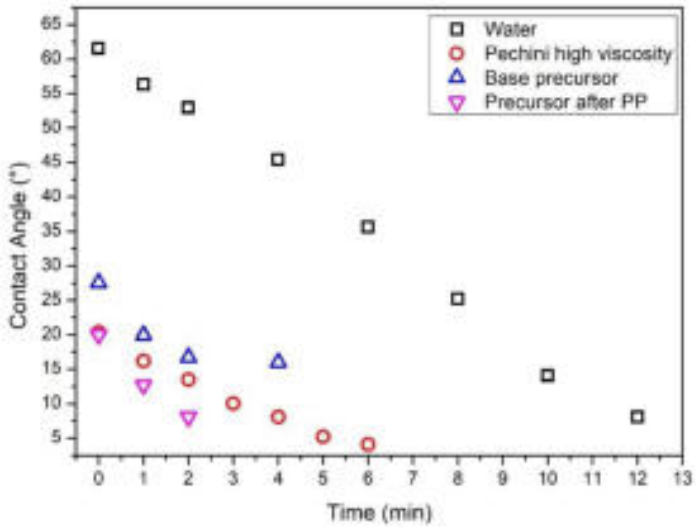


Figure S1. A relationship showing changes in the contact angle over time for different types of precursors and water as a reference sample.

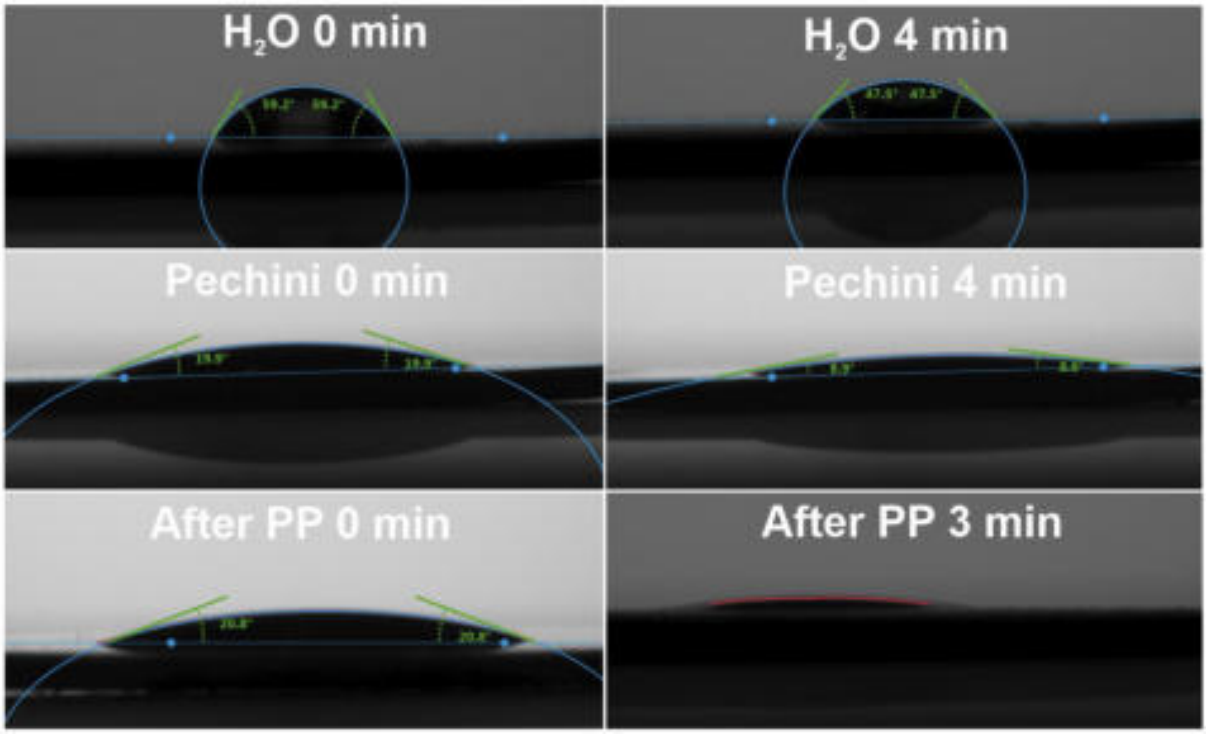


Figure S2. Photos presenting the determined contact angles for various types of precursors at the initial moment and after 4 minutes (3 minutes for the proposed precursor).

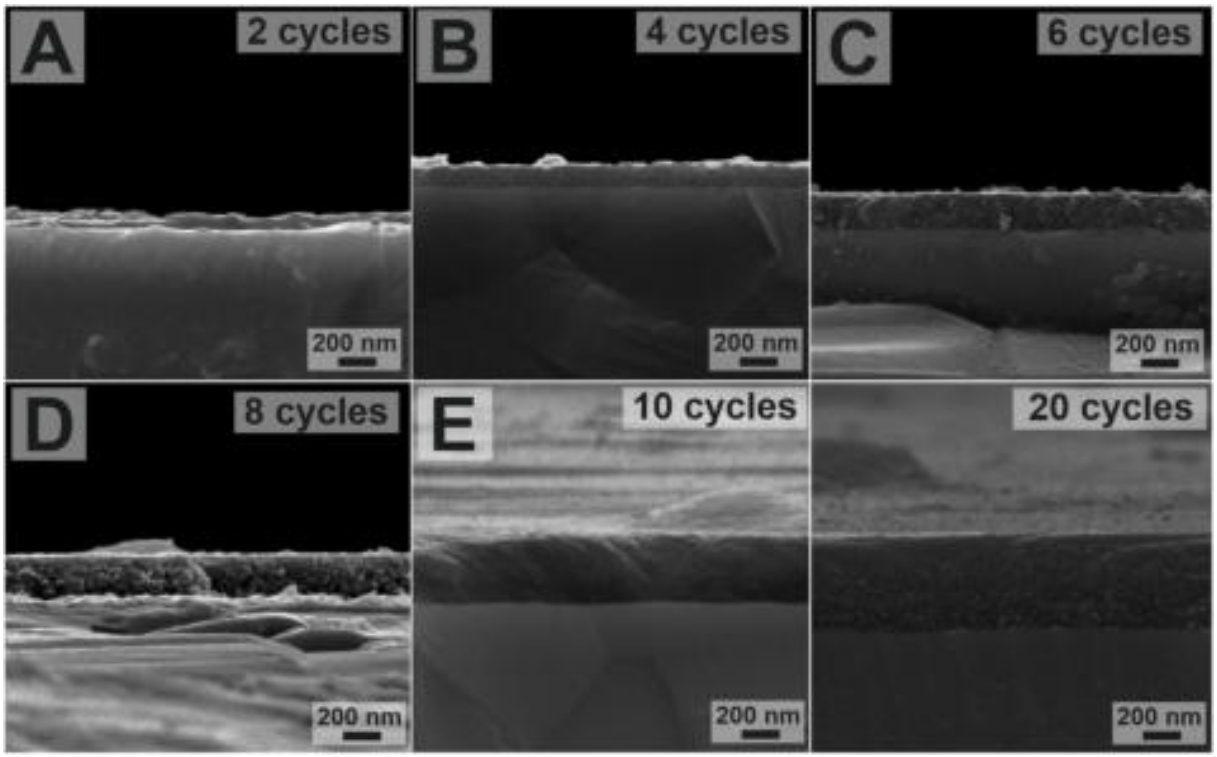


Figure S3. Fractures of CGO pellets with a LSC layer deposited by spin-coating show an increase in layer thickness with successive cycles of deposition.

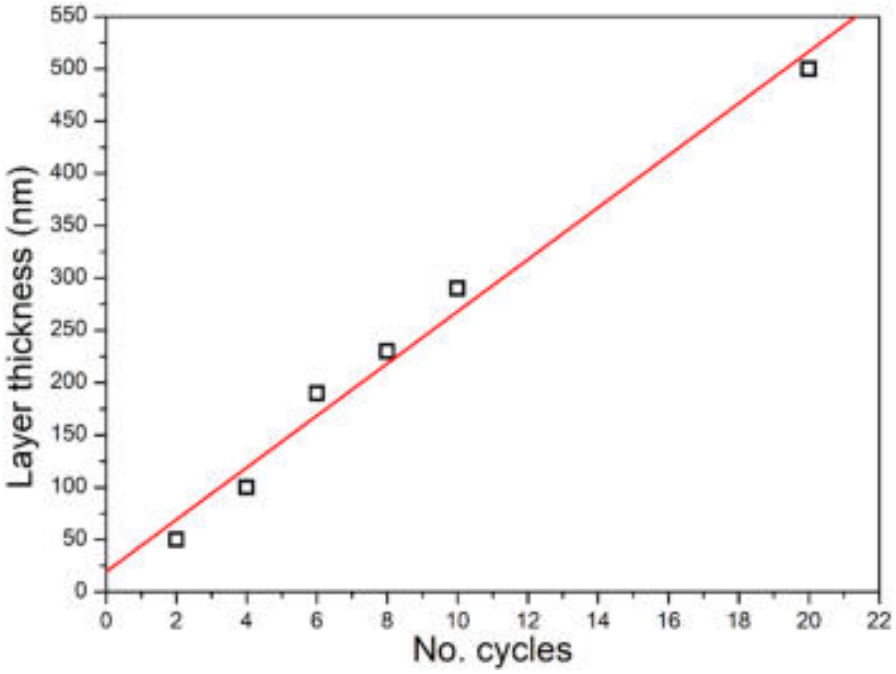


Figure S4. Calibration curve of the dependence of the change in layer thickness on the number of spin coating application cycles.

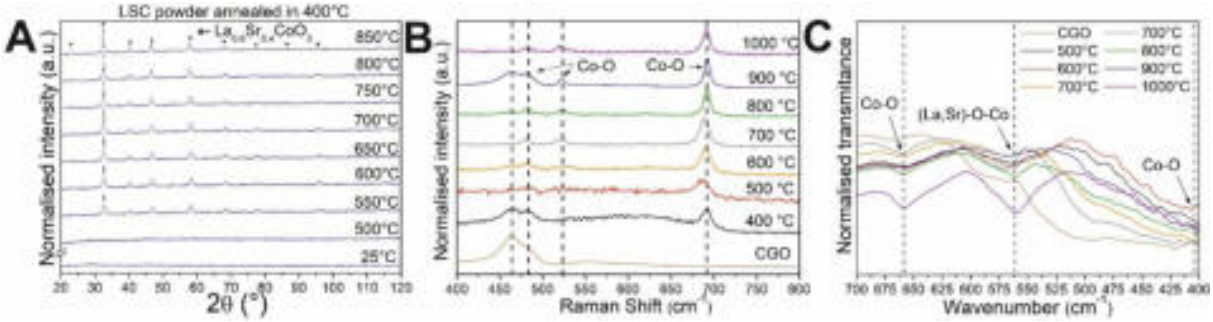


Figure S5. High-temperature diffractogram taken for LSC powder annealed at 400°C (A), Raman spectroscopy for LSC layers deposited on CGO (B); FTIR spectra for LSC layers (C).

Table S4. Fourier transform fit values for best fit.

$La_{0.6}Sr_{0.4}CoO_{3-\delta}$	Shell	N	sigma^2	R	R-factor
400 °C	Co-O	3.8 (0.5)	0.0018 (0.0022)	1.91 (0.001)	0.013
500 °C	Co-O	4.0 (0.4)	0.0014 (0.0014)	1.90 (0.006)	0.009
600 °C	Co-O	4.8 (0.5)	0.0034 (0.0017)	1.92 (0.006)	0.012
700 °C	Co-O	5.0 (0.4)	0.0027 (0.0011)	1.92 (0.006)	0.005
800 °C	Co-O	5.0 (0.4)	0.0026 (0.0010)	1.92 (0.005)	0.004
900 °C	Co-O	4.6 (0.6)	0.0027 (0.0018)	1.91 (0.01)	0.017
1000 °C	Co-O	4.7(0.5)	0.0016 (0.0014)	1.92 (0.007)	0.009

N - coordination number; R - interatomic distance; sigma^2- disorder parameter. All the fitting analysis were performed in the R space, ΔR = 1.0−2.1 and ΔK = 2.1−11.

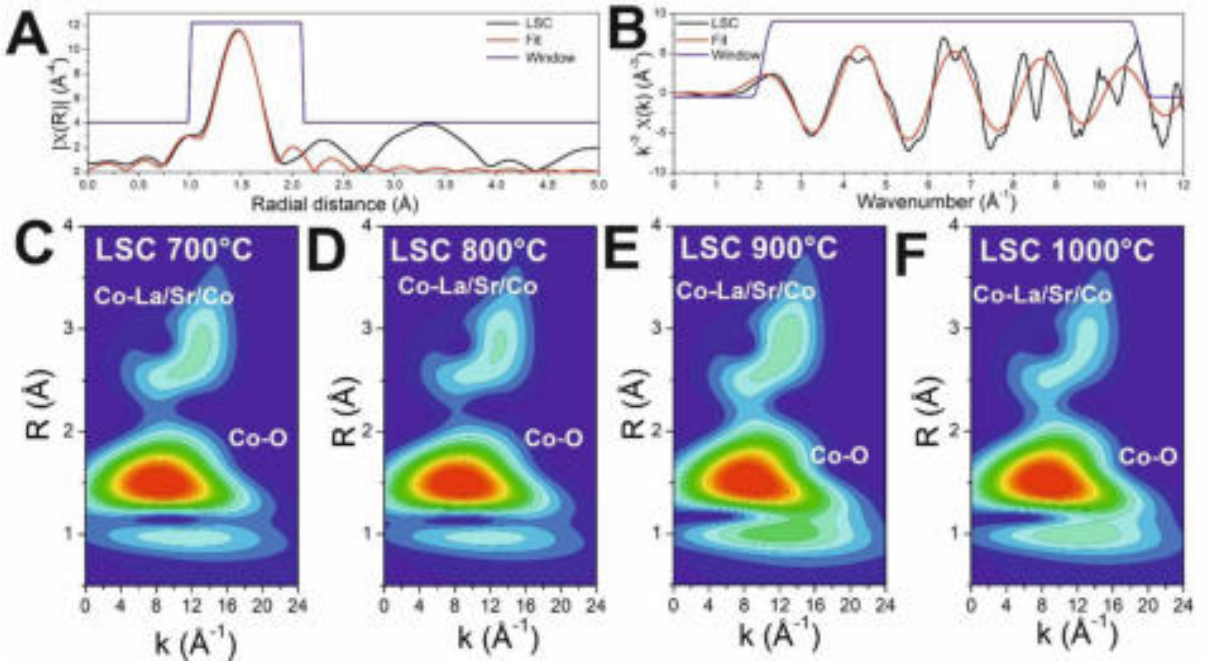


Figure S6. Determined vibration spectra |X(R)| (Å^{-3}) in k-space (A) and k2 X(k)(Å^{-2}) in q-space for LSC (B) and a fit allowing the identification of bonds in the crystal structure of LSC; maps determined using the wavelet transform for LSC with an annealing temperature in the range of 700°C–1000°C (C-F).

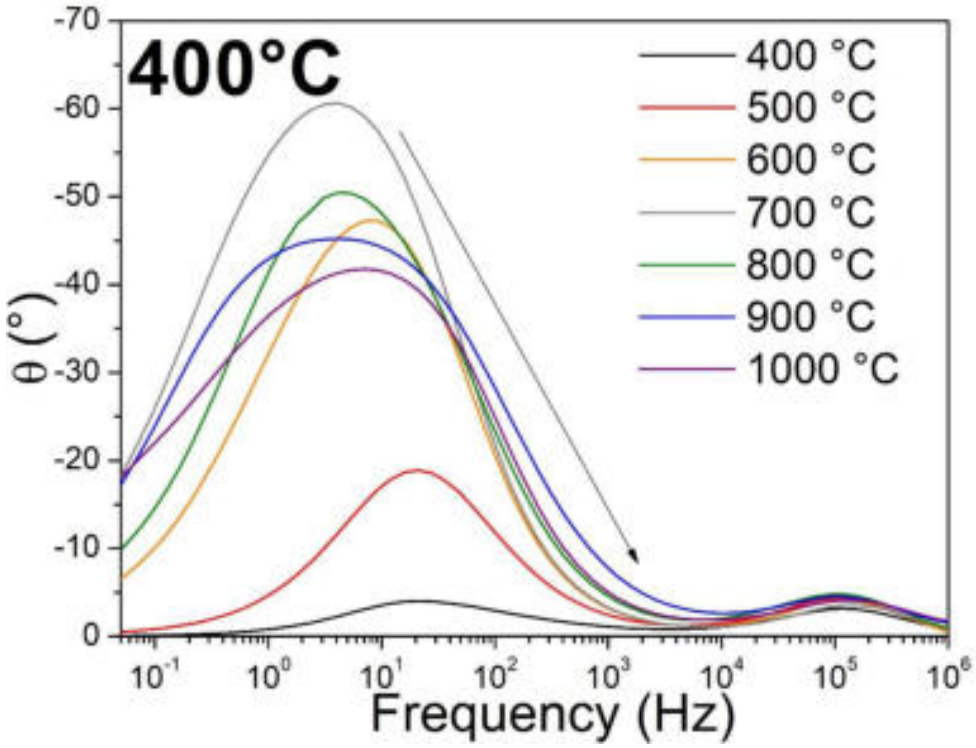


Figure S7. Bode plot showing the differences towards different annealing temperatures. The data shown was measured at 400°C.

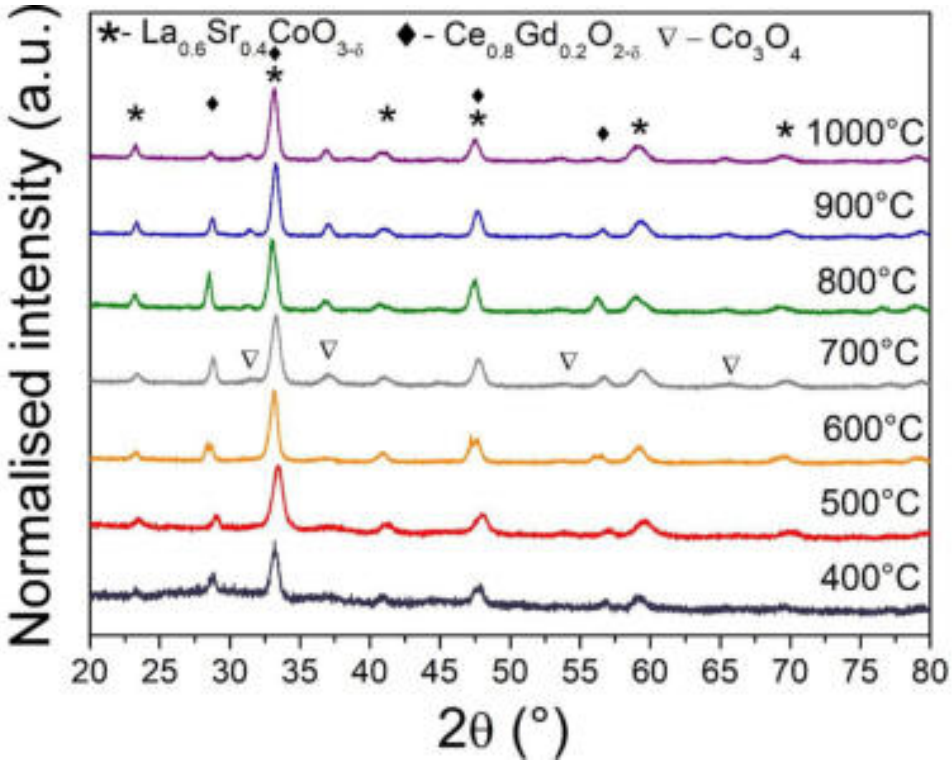


Figure S8. XRD diffraction pattern collected for samples after impedance measurements.

10.4. Developing high-performance oxygen electrodes for intermediate solid oxide cells (SOC) prepared by $Ce_{0.8}Gd_{0.2}O_{2-\delta}$ backbone infiltration

Authors: Ömer Faruk Aksoy, **Bartłomiej Lemieszek**, Murat Murutoğlu, Jakub Karczewski, Piotr Jasiński, Sebastian Molin

Applied Physics A, vol. 130, issue 11, pages 779, 2024, https://doi.org/10.1007/s00339-024-07939-0

IF = 2.8 (2024), MSHE points 70, Citations: 1

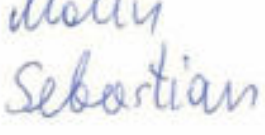
Article 4 describes research on the infiltration of a porous CGO backbone with oxygen electrode materials in the form of LSC, PrO_x, and a composite of the two (PrO_x:LSC). Among the tested infiltration procedure, nine cycles of immersion yielded the best electrocatalytic performance. Symmetrical measurements demonstrated that CGO–LSC exhibited the lowest polarization resistance, followed by the PrO_x:LSC composite, and finally CGO–PrO_x. Based on these results, CGO–LSC samples were selected for further investigation. Stability tests revealed an initial decrease in ohmic resistance, followed by a linear increase in polarization resistance over a 100-hour experiment. Fuel cell measurements with the proposed oxygen electrode achieved a peak power density of 0.53 $W \cdot cm^{-2}$ at 600 °C, representing an 8% improvement compared to the reference cell. Importantly, the cell maintained stable performance in an atmosphere containing 50% water vapour and 50% hydrogen, delivering nearly identical power output. Additionally, electrolyser-mode testing showed improved efficiency, confirming that the proposed electrode configuration enhances performance in both operating modes.

The novelty of this work lies in the systematic investigation of porous CGO backbones infiltrated with LSC, PrO_x, and composite infiltrates. In addition the PrO_x–LSC composite as a novel infiltrated electrode material. A direct side-by-side comparison of single-phase and composite infiltrates within the same porous backbone enabled a comprehensive evaluation of their electrochemical performance toward the oxygen reduction reaction, particularly at relatively low operating temperatures. The work further demonstrated the practical relevance of the proposed approach through validation in a commercial Elcogen cell.

The main achievement of this work was demonstrating improved efficiency while significantly reducing the amount of electrochemically active material required, thereby lowering cell cost. Furthermore, two promising cathode materials for low-temperature cells were directly compared, and it was shown that the relatively low annealing temperature of 600 °C did not cause a substantial increase in ohmic resistance or a decrease in overall efficiency.

My contributions included conducting part of symmetrical measurements to identify the optimal electrode configuration for subsequent tests, as well as performing and analysing long-term stability measurements. In addition, I was responsible for writing the manuscript and, as the corresponding author, submitting the article to the journal and preparing responses to reviewer comments.

Declaration of co-authors on their contribution to the publication: "Developing high-performance oxygen electrodes for intermediate solid oxide cells (SOC) prepared by $Ce_{0.8}Gd_{0.2}O_{2-\delta}$ backbone infiltration".

Name and Surname	Contribution	Signature
Ömer Faruk Aksoy	Writing – original draft, Writing - review & editing, Validation, Methodology, Investigation (Sample preparation, symmetrical cells measurements), Formal analysis, Data curation, Visualization.	
Bartłomiej Lemieszek	Writing – original draft, Writing - review & editing, Validation, Methodology, Investigation (symmetrical cells measurements), Formal analysis, Data curation	
Murat Murutoğlu	Writing - review & editing, Methodology, Investigation (Full cells measurements), Formal analysis, Data curation.	
Jakub Karczewski	Writing – review & editing, Methodology, Investigation (SEM).	
Piotr Jasiński	Writing – review & editing, Methodology.	
Sebastian Molin	Writing – review & editing, Supervision, Funding acquisition, Methodology, Conceptualization.	

Applied Physics A (2024) 130:779
https://doi.org/10.1007/s00339-024-07939-0

S.I. : XVI POLISH CONFERENCE FOR FAST IONIC CONDUCTORS

Developing high-performance oxygen electrodes for intermediate solid oxide cells (SOC) prepared by $Ce_{0.8}Gd_{0.2}O_{2-\delta}$ backbone infiltration

Ömer Faruk Aksoy[1] · Bartłomiej Lemieszek[2] · Murat Murutoğlu[1] · Jakub Karczewski[3] · Piotr Jasiński[2] · Sebastian Molin[2]

Received: 4 July 2024 / Accepted: 25 September 2024 / Published online: 7 October 2024
© The Author(s) 2024

Abstract

$Gd_{0.2}Ce_{0.8}O_{2-\delta}$ (GDC) porous backbone infiltration with $La_{0.6}Sr_{0.4}CoO_{3-\delta}$ (LSC), PrOx and LSC: PrOx as a composite oxygen electrode for intermediate solid oxide cells are conducted within the scope of this work. Samples were characterized using scanning electron microscopy (SEM), energy dispersive X-ray spectroscopy (EDX), and electrochemical impedance spectroscopy (EIS). A uniform distribution of the infiltrated material inside the backbone and at the electrolyte-backbone interface was achieved. EIS measurements on the prepared symmetrical samples showed electrode polarization resistance (R_p) values of 0.029 Ω.cm², 0.23 Ω.cm², and 0.44 Ω.cm² for LSC, LSC: PrOx, and PrOx at 600 °C, respectively. Long-term stability measurements at 600 °C for 100 h showed a slight increase in polarization resistance during the measurement period. Fuel cell measurements of commercial cells (Elcogen) with porous oxygen electrode consisting of GDC infiltrated with LSC showed an increase in power density compared to the reference cell with a value of 0.53 W. cm^{-2} obtained at 600 °C. It is proven that infiltration via polymeric precursor into porous scaffolds as backbone oxygen electrode layer is effective and convenient method to develop high performance and stable solid oxide cells.

Keywords Solid oxide cells · Oxygen electrode · Infiltration · LSC · Praseodymium oxide

1 Introduction

Solid oxide cells (SOCs) are one of the promising technologies that are a potentially important part of energy transformation [1]. Typically, SOCs can operate in two modes: fuel cell - solid oxide fuel cell (SOFC) and electrolyzer - solid oxide electrolysis cell (SOEC) [2].

Originally, SOCs operated at temperatures above 1000 °C, and it immediately became obvious that to implement the technology, a significant reduction in the system's operating temperature was needed. The current rent objective is to provide efficient cells operating in the intermediate temperature range to reduce cost significantly [3, 4]. To achieve this goal, improvements in oxygen electrode development must take place. The reason for this is the polarization resistance of this electrode, which is responsible for a significant part of the resistance of the entire cell [5]. Therefore, in recent years, there has been an intensification of research on effective materials for oxygen electrodes operating at low temperatures. Among the analyzed materials, mixed ionic-electronic conductors (MIECs) have gained popularity, as the oxygen reduction reaction takes place at triple phase boundaries where both the presence of electrons and the transport of ions in the material are possible [6]. The materials analyzed for use as an oxygen electrode in cells include perovskite oxides such as $La_{1-x}Sr_xMnO_{3-\delta}$ (LSM) [7, 8], $La_{1-x}Sr_xCoO_{3-\delta}$ (LSC) [6, 9–13], or $La_{1-x}Sr_xCo_{1-y}Fe_yO_{3-\delta}$ (LSCF) [14–17]. Additionally, materials such as PrOx and Ruddlesden-Popper phase $Pr_2NiO_{4+\delta}$ are currently gaining popularity [18, 19].

The efficiency of the oxygen electrode is also influenced by its manufacturing technique. The most popular techniques used to prepare these electrodes include screen-printing [20], tape-casting [21–24], spin-coating [25–27],

[1] Department of Material Science and Engineering, Gebze Technical University, Kocaeli 41400, Turkey

[2] Advanced Materials Centre, Faculty of Electronics, Telecommunications and Informatics, Gdańsk University of Technology, ul. G. Narutowicza 11/12, Gdańsk 80-233, Poland

[3] Advanced Materials Centre, Faculty of Applied Physics and Mathematics, Gdańsk University of Technology, ul. G. Narutowicza 11/12, Gdańsk 80-233, Poland

dip-coating [28], and more advanced techniques such as pulsed laser deposition (PLD) [29], atomic layer deposition (ALD) [30, 31], spray pyrolysis [6, 10], or chemical vapor deposition (CVD) [32]. Furthermore, the infiltration technique is increasingly used, in which a porous backbone made of an electrolyte material with high ionic conductivity is impregnated with a material with high electronic conductivity [33–36].

For example, in the work of Choi et al., described the infiltration of $La_{n+1}Ni_nO_{3n+1}$ material ($n = 1,2,3$) into the porous structure of YSZ (yttria-stabilized zirconia). A porous backbone with a thickness of about 50 µm was infiltrated with the prepared precursor until the loading reached 45 wt%, then the prepared oxygen electrode was annealed at 850 °C. Electrochemical Impedance Spectroscopy (EIS) measurements showed polarization resistance values of 0.120 Ω.cm^2 for La_2NiO_4, 0.112 Ω.cm^2 for $La_3Ni_2O_7$, and 0.068 Ω.cm^2 for $La_4Ni_3O_{10}$ at a temperature of 750 °C. The full cell measurements, with the $La_4Ni_3O_{10}$ as an oxygen electrode, reached 0.889 W·cm^{-2} at 750 °C [37]. Shah et al. described the infiltration of $La_{0.6}Sr_{0.4}Co_{0.2}Fe_{0.8}O_{3-\delta}$ into porous GDC (gadolinium-doped ceria). It has been shown that the optimal sintering temperature for GDC backbone is between 1100 °C and 1200 °C. Loading of 12.5 wt%, of material into the porous backbone showed the lowest polarization resistance (R_p) equal to 0.24 Ω.cm^2 at a temperature of 600 °C [38]. Huang et al. described the infiltration of the porous YSZ backbone with LSM ($La_{0.8}Sr_{0.2}MnO_{3-\delta}$) material as a potential oxygen electrode. All tested combinations showed similar catalytic properties, and the polarization resistance values were approximately 0.4 Ω.cm^2 at 700 °C [39]. Cheng et al. described the process of infiltration of the composite YSZ: $La_{0.8}Sr_{0.2}FeO_{3-\delta}$ (1:1 ratio) with LSCF ($La_{0.6}Sr_{0.4}Co_{0.2}Fe_{0.8}O_{3-\delta}$) material. With only two infiltration cycles of LSCF, decrease in polarization resistance from 1.4 Ω.cm^2 (for sample without infiltration) to 0.16 Ω.cm^2 at a temperature of 700 °C, was observed. The prepared cell with the proposed oxygen electrode showed a power density of 0.4 W·cm^{-2} at 700 °C [40]. Samson et al. described the infiltration of a porous $Ce_{0.9}Gd_{0.1}O_{2-\delta}$ backbone with a thickness of approximately 25 µm with LSC as a potential oxygen electrode for intermediate-temperature solid oxide fuel cells. It was found that for a precursor solution with a concentration of approximately 1 M, the optimal number of infiltration cycles was 9. It was also shown that the optimal annealing temperature was set at 600 °C. The polarization resistance of the obtained oxygen electrode at 600 °C was 0.044 Ω.cm^2 [34]. Nicollet et al. proposed infiltration porous GDC with Pr_6O_{11} material. It has been shown that the optimal backbone thickness was determined as 14 µm. Infiltration with the Pr_6O_{11} precursor continued until a loading of 30 wt% was achieved (3–4 cycles). After the preparation process, the samples were annealed at 600 °C. EIS measurements showed a very low value of polarization resistance, equal to 0.028 Ω.cm^2 at the same temperature. The cell with the described oxygen electrode showed a power density of 0.825 W.cm^{-2} at 600 °C compared to about 0.4 W.cm^{-2} for a commercial cell [18].

In this work investigation on the process of infiltration of a porous GDC (gadolinium-doped ceria) backbone with materials such as LSC, PrOx, and the LSC: PrOx composite were described. The infiltration process allows for the steady distribution of nanoparticles of the impregnated material throughout the structure of the backbone material. Electrochemical activity measurements showed very good oxygen reduction reaction (ORR) properties of the materials. Among the three materials discussed, LSC turned out to be the most promising. The use of the best combination as the oxygen electrode in the solid oxide fuel cell showed an increase in power density of the infiltrated commercial Elcogen cell compared to the plain Elcogen cell as reference sample which is denoted as EL throughout the paper.

2 Experimental

In this work, infiltration of porous air electrodes made of $Ce_{0.8}Gd_{0.2}O_{2-\delta}$ (GDC) backbone with $La_{0.6}Sr_{0.4}CoO_{3-\delta}$ (LSC), PrOx and LSC: PrOx (1:1 by precursor vol.) were performed. Various characterization techniques have been done, such as Electrochemical Impedance Spectroscopy (EIS), Scanning Electron Microscopy with Energy Dispersive X-ray Spectroscopy (SEM-EDS) and X-ray diffraction (XRD).

2.1 Sample preparation

Polymeric precursors for infiltration were prepared with the Pechini method [41]. Nitrate salts in the form of $La(NO_3)_3{\cdot}6H_2O$ (purity 99.9%, Alfa Aesar), $Sr(NO_3)_2$ (purity 99%, Sigma Aldrich), $Co(NO_3)_3{\cdot}6H_2O$ (purity 99%, Sigma Aldrich), or $Pr(NO_3)_3{\cdot}6H_2O$ (99.9% of purity, Alfa Aesar) were dissolved in the appropriate stoichiometry in distilled water with a total molar concentration of 0.2 M (or nitrates as 0.04 M of ethylene glycol). Ethylene glycol was then added to perform the polymerization process with heating at 80 °C on a hotplate with continuous stirring. Heating was continued until all the water had evaporated from the solution. The completion of this process was determined by the decrease in the mass of the solution by the mass of water measured at the initial stage.

0.8 g of commercially available GDC powder (GDC-20 K, Daiichi Kigenso Kagaku Kogyo, Japan) was placed in a mould with a diameter of 16 mm and pressed at 98 MPa

for 1 min. Sintering was carried out at 1400 °C for 10 h to obtain a dense structure. After sintering, the pellets shrank to an average diameter of 13 mm with a thickness of around 0.6 mm.

The next step was preparation a porous backbone with a porosity of approximately 50%. Prepared slurry, for wet-powder spraying, consisting of toluene, ethanol, (with ratio toluene to ethanol 1:4) binder (Heraeus) and GDC powder (3 wt%), sprayed using an airbrush (Paasche VLS) onto GDC pellets on a hot plate heated to 250 °C. The slurry was kept in an ultrasonic bath for homogenization before spraying. As a result of contact with the hot surface, the solvents evaporated instantaneously, leaving the scaffold structure. Porous backbone was prepared on both sides of the dense GDC pellets. After spraying, sintering was carried out, at a temperature of 1150 °C for 2 h in order to obtain adequate mechanical properties and a good connection between the dense electrolyte surface and the backbone. Prepared pellets with a porous backbone were used for infiltration. Wet-powder spraying and post-sintering infiltration are graphically shown in Fig. 1.

The infiltration process was carried out by immersing pellets with a porous backbone into the prepared precursor solution (1 ml) and then removing the air remaining from the pores using a vacuum chamber (0.08 Pa) for 10 min. Excess solution was then gently removed with a paper towel. The utilization of the immersion technique permitted the simultaneous and uniform application of the precursor solution to both sides of the sample. The samples prepared in this way were then pre-annealed on a hotplate at a temperature of 400 °C. The pre-annealing process took place in 3 stages: 90 °C–15 min, 180 °C–15 min and 400 °C–15 min. The optimum loading volume of the porous material with the impregnated material was determined using electrochemical impedance spectroscopy (EIS). It was found that the lowest values of the polarization resistance were obtained for the samples that were infiltrated for 6 cycles. After completing the procedure, the samples were annealed in a muffle furnace (Carbolyte RHF 16/8 box furnace) at 600 °C for 2 h. The samples prepared in this way were used for further research.

2.2 Characterization

Electrochemical impedance spectroscopy (EIS) measurements were conducted on the prepared symmetrical cells, to evaluate the ohmic and polarization resistance (R_{ohm} and R_p). An LSC paste (Fiaxell) current collector layer was applied to both side of the pellets and annealed at 600 °C for two hours. The samples were placed in a compression cell where the electrical contact was a gold mesh connected to platinum wires on both sides of the sample. These wires were led outside the furnace where they were connected to the Novocontrol Alpha-A potentiostat, which was used to perform the measurements. For EIS measurements, an excitation amplitude of 25 mV and in frequency range of 3 MHz to 50 mHz were used. Measurements were performed in the temperature range from 600 °C to 300 °C, every 50 °C in the range of 600 °C–400 °C, and every 25 °C in the range of 400 °C–300 °C. An atmosphere of synthetic air was used with a controlled flow of 50 ml min^{-1}.

SEM-EDS analysis of fractures, with appropriate materials was performed using a field emission scanning electron microscope (FEI Quanta FEG250) equipped with a secondary ET detector. The accelerating voltage was maintained at 10 keV.

Commercial half-cells (ASC-400B, Elcogen), comprising a NiO-YSZ (fuel electrode), YSZ/GDC (electrolyte), without an oxygen electrode, were used for the full cell measurements. Infiltrated samples were labeled as EL-9 C-LSC and EL-12 C-LSC respectively depending on their infiltration cycle as 9 or 12 times. The porous backbone was prepared in the same procedure as for symmetrical measurements. The infiltration process was conducted by applying the precursor to the surface of the porous GDC and subjecting it to pre-annealing at 400 °C on a hot plate. Once the

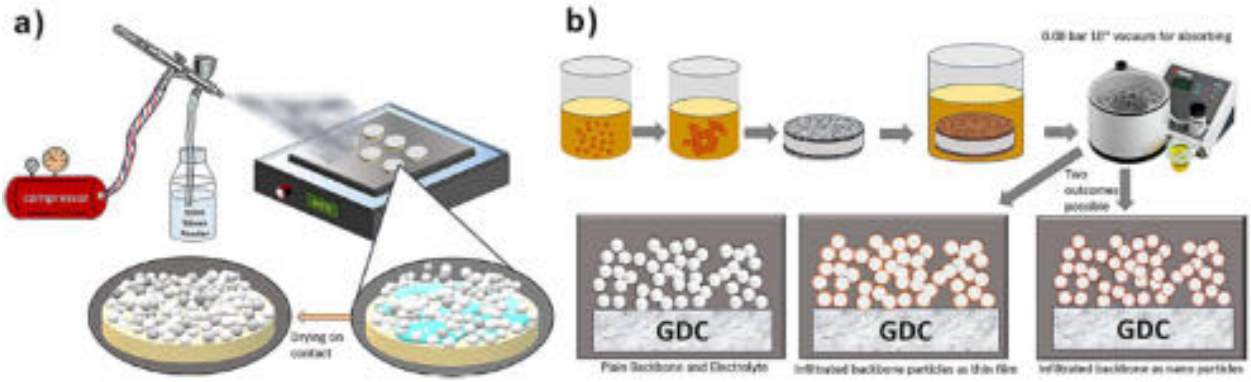


Fig. 1 Graphical representation of a) GDC backbone spraying on to GDC pellets and b) infiltration of porous GDC backbones with solutions

optimal loading of the GDC backbone had been achieved, the samples were annealed at 600 °C for two hours. The reference sample was a commercial full cell (Elcogen) with an LSC oxygen electrode.

The fuel cell characterization was performed using an Open Flanges V5 test setup (Fiaxell Sàrl Technologies). The prepared cell was electrically connected on the fuel side by a nickel foam and on the air side by a gold mesh. The cell was placed in a Kittec furnace equipped with a PID temperature controller. The wires were connected to a Solartron 1260/1287 frequency analyzer for impedance and current-voltage characterization. The cell was heated to 600 °C and held isothermally. The fuel electrode was reduced in dry hydrogen gas (100 ml min^{-1}), which was supplied as fuel, while synthetic air was delivered to the oxygen electrode as the oxidant (200 ml min^{-1}). To characterize the cell, impedance spectra were measured at open-circuit voltage (OCV) conditions in the frequency range of 100 kHz–0.1 Hz. For evaluating the cell performance, current-voltage characteristics were performed.

3 Results and discussion

3.1 Sample preparation

Following the infiltration process, the prepared samples were subjected to SEM-EDX analysis to confirm the uniform distribution of the infiltrated material within the backbone structure. The SEM images in Fig. 2 show the fractures of the samples after infiltration for LSC, LSC: PrOx, and PrOx. The backbone structure is well formed, despite the presence of heterogeneities, segregation and flake structure, and the pore size is relatively small. Nevertheless, the presence of nanoparticles derived from the respective materials was discerned in all three infiltrated precursors (LSC, PrOx and LSC: PrOx) (red circles). Concurrently, the loading level is relatively low.

An EDX analysis was conducted to ascertain the distribution of materials within the porous backbone. Spot EDX analysis was performed on the fractures of samples immersed in LSC, LSC: PrOx and PrOx alone. Figure 3 shows the distribution of measurement spots. Figure 4 shows EDX spectra with elements identified at point 4, closest to the electrolyte. The elements expected to be introduced into the backbone by the immersion technique were identified.

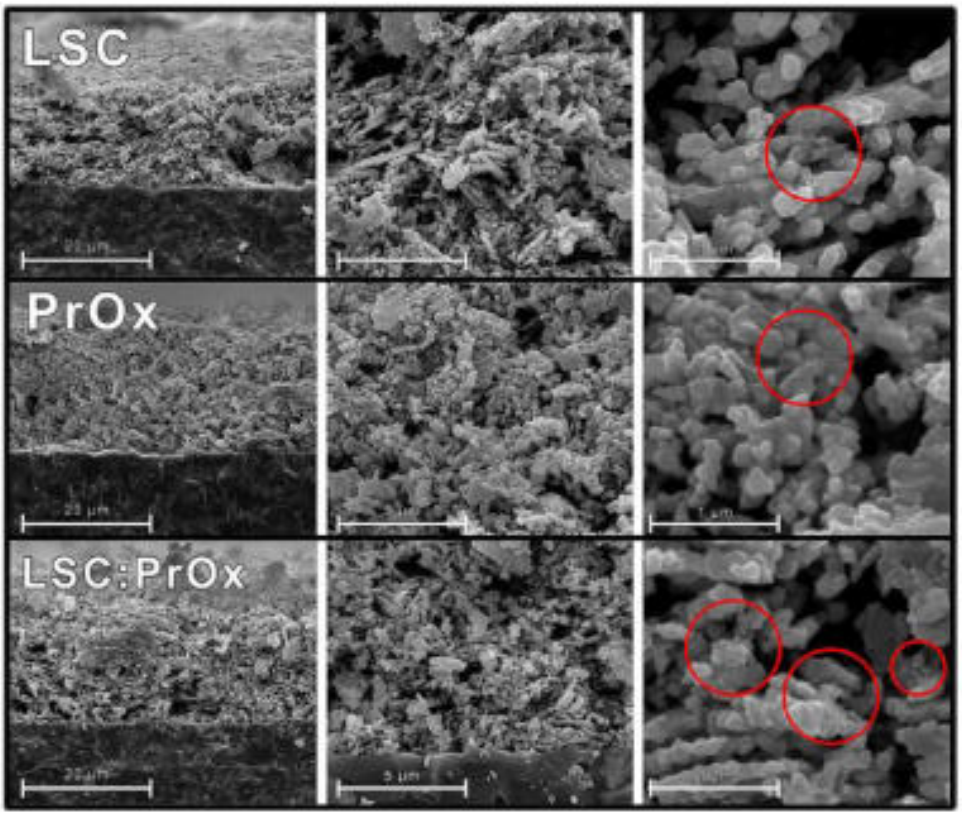


Fig. 2 SEM images of LSC, LSC: PrOx and PrOx infiltrated backbones

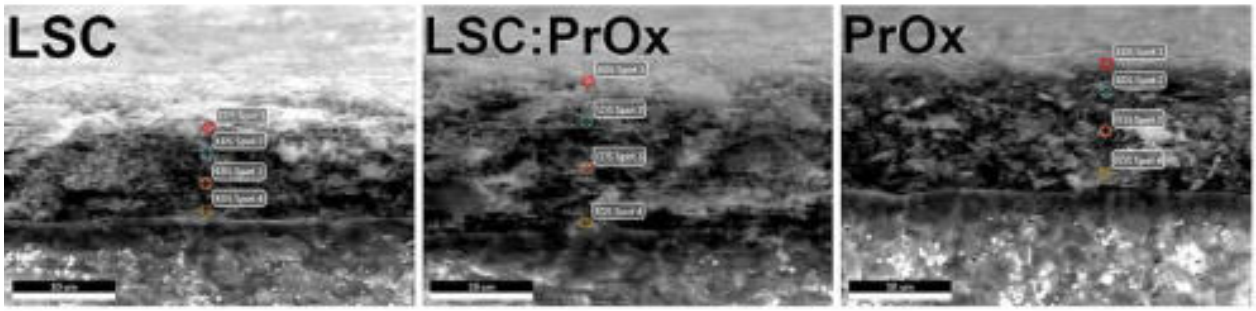


Fig. 3 Location spots of EDX responses from infiltrated symmetrical cells in the backbone

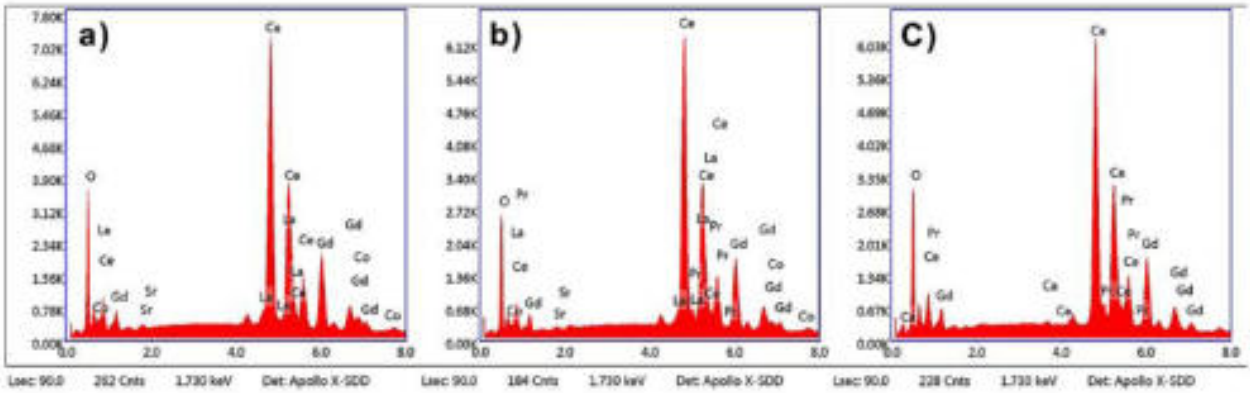


Fig. 4 EDX analysis of a) LSC, b) LSC: PrOx and c) PrOx infiltrated backbones at spot 4

Table 1 presents the atomic concentration of indentified cations obtained at each of the analysed points. Moreover, no segregation of strontium or other elements was identified, and the atomic distribution was found to be consistent with the expected pattern. Furthermore, a markedly higher loading of LSC in comparison to PrOx was discerned. This result was unexpected, given that the total cation concentration was identical in both precursors. The LSC was responsible for approximately 14% of the total signal, while PrOx accounted for approximately 4.5%. In the case of the composite-infiltrated sample, the signal ratio of LSC to PrOx was, on average, 3:1 at points 2, 3, and 4. However, at point 1, the ratio was higher, amounting to 5.4:1.

The EDX analysis performed was mainly for qualitative analysis, i.e. to demonstrate the presence of specific elements in the porous GDC backbone and for rough comparison of values. This was due to the high quantitative inaccuracy of EDX for atomic concentrations below 5%. An effective and uniform distribution of the impregnated materials in the porous GDC backbone was demonstrated by SEM-EDX analysis.

3.2 Electrochemical impedance spectroscopy

A series of measurements were conducted using electrochemical impedance spectroscopy on symmetrical samples with an electrode layer on either side of the electrolyte. The objective was to determine the electrochemical performance of the proposed oxygen electrode.

Figure 5a and b show the area specific resistance (ASR) dependence as a function of temperature for three types of samples, including ohmic resistance and electrode polarization.

The analysis demonstrated that the lowest ohmic resistance values were observed in samples infiltrated with an LSC: PrOx composite, followed by samples infiltrated with LSC. Conversely, the highest ohmic resistance values were observed in samples that had been infiltrated with PrOx alone. The activation energy values (Ea) were also determined for the aforementioned data set. Furthermore, the lowest activation energy at higher temperatures was identified for samples infiltrated in PrOx. Similar Ea values were obtained at lower temperatures for all three tested types of specimens.

In terms of polarization resistance, the LSC-infiltrated sample obtain the lowest polarization resistance at a temperature of 600 °C, followed by the GDC-LSC: PrOx-infiltrated

Table 1 EDX output as atomic percentage values of all samples

	LSC				LSC: PrOx				PrOx			
Spot number	1	2	3	4	1	2	3	4	1	2	3	4
La L	3.53	4.09	4.30	3.44	1.78	2.05	1.61	2.87	-	-	-	-
Sr L	4.03	3.88	4.16	4.30	5.96	2.44	3.11	1.77	-	-	-	-
Co L	6.69	7.04	6.82	5.66	3.19	3.81	3.25	3.58	-	-	-	-
Ce L	68.93	68.22	68.00	69.12	69.90	71.68	72.38	71.44	77.76	77.42	76.24	76.32
Gd K	16.81	16.78	16.72	17.49	17.13	16.87	17.08	17.50	19.11	18.31	18.13	18.65
Pr L	-	-	-	-	2.04	3.15	2.58	2.83	3.13	4.27	5.63	5.03

sample, and the GDC-infiltrated PrOx-infiltrated sample had the highest values. The polarization resistance for the oxygen electrode in the form of porous GDC immersed in LSC was 0.029 $\Omega.cm^2$, 0.68 $\Omega.cm^2$ and 7.89 $\Omega.cm^2$ at temperatures of 600 °C, 500 °C and 400 °C respectively. In the case of the LSC: PrOx sample, it was 0.23 $\Omega.cm^2$, 0.93 $\Omega.cm^2$ and 9.75 $\Omega.cm^2$, respectively, and for the samples with GDC backbone infiltrated in PrOx alone, it was 0.42 $\Omega.cm^2$, 2.95 $\Omega.cm^2$ and 17.38 $\Omega.cm^2$, respectively, at the same temperatures. Significant differences in activation energy at higher temperatures was noticeable. The sample infiltrated with the LSC: PrOx composite has a significantly lower Ea value than the others. This outcome is likely attributable to the combination of the properties of the two materials. It is also noteworthy that the Ea value of 1.523 eV for LSC in the temperature range between 600 °C and 450 °C is considerably higher than the data presented in the literature, for example, the value of 1.099 eV reported in the study conducted by Samson A. et al. [42]. At lower temperatures it was noticeable that the Ea for LSC and LSC: PrOx are almost identical. This was most likely due to the high electical conductivity of LSC compared to PrOx, which dominates over praseodymium oxide at lower temperatures in the composite. The significantly higher value of polarization resistance for PrOx was the result of the low electrical conductivity of the material at low temperatures [43]. Figure 6 shows the Nyquist plots obtain for the samples tested at different temperatures. The ohmic resistance part has been subtracted to compare the electrode performance only. At 600 °C, high frequencies are related to charge transfer and transport of oxide ions through the composite to the electrolyte interface in TPB (triple-phase boundary), medium frequencies are related to diffusion of adsorbed oxygen and finally low frequencies were related to the oxygen reduction reaction (conversion). Two different impedance semicircles were observed at 400 °C and 500 °C. The semicirle in higher frequencies was related to the grain boundary polarization and the semicircle in lower frequencies was related to the oxygen electrode polarization mentioned above. The polarization value of the oxygen electrode (hereafter referred to as R_p) was the diameter of the semi-circle on the real impedance axis, multiplied by the area of the active electrode surface and divided by two to obtain the ASR of one side of the electrode, due to the symmetrical nature of the samples tested.

3.3 Long-term stability

Figure 7a illustrates the EIS spectra recalculated to the active area of the oxygen electrode. Figure 7b depicts the change in ohmic resistance calculated throughout the experiment, while Fig. 7c illustrates the change in polarization

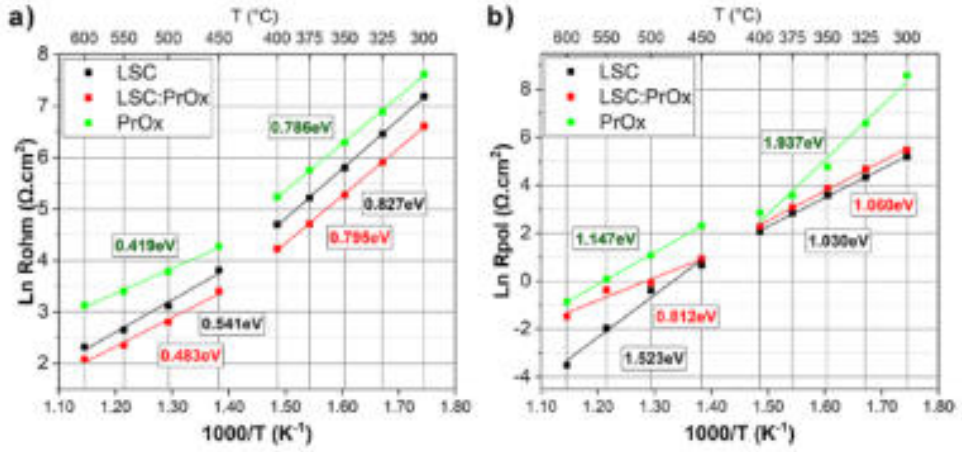


Fig. 5 ASR vs. temperature plots of infiltrated symmetrical cells as a) R_{ohm} and b) R_p with calculated activation energy

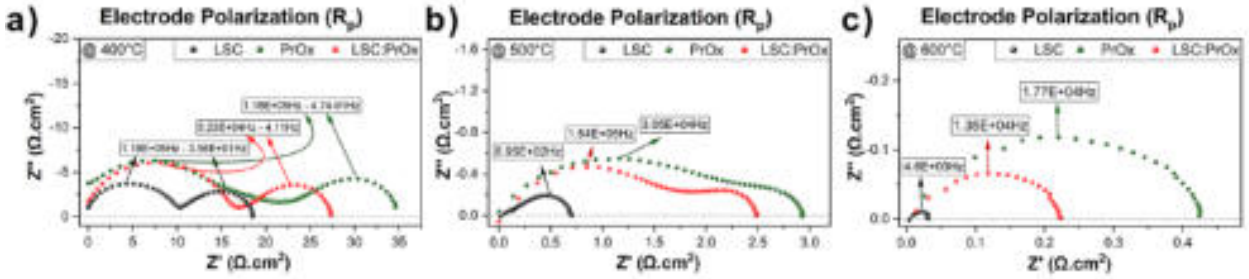


Fig. 6 Nyquist plots of infiltrated symmetrical cells at a) 400 °C, b) 500 °C and c) 600 °C

resistance. The initial decline was followed by a period of stabilisation, which commenced after 30 h. The initial R_{ohm} value was determined to be 10.58 Ω.cm², and after 50 h of the experiment, a decrease of approximately 0.19 Ω.cm² was observed. Between 50 and 100 h, a slight increase in ohmic resistance was noted, amounting to 0.005 Ω.cm². The reduction in R_{ohm} observed during the experiment may be attributed to minor microstructural alterations at the LSC-GDC interphase, including alterations in porosity, grain size of the LSC nanoparticles, and the number and length of TPBs. The electrode polarization resistance exhibited an increase from an initial value of 0.0375 Ω.cm² to 0.0464 Ω.cm², representing a 24% change in ΔASR after 100 h in LSC. This phenomenon is a common occurrence in literature, with a threefold increase in polarization resistance achieved when screen-printed and deposited films are used in comparison to the conventional methods described in literature [47, 48]. The observed increase in R_p with the passage of time is attributed to grain coarsening, which was a consequence of a reduction in the electronically active areas and length of TPB.

3.4 Fuel cell testing

Analysis of the oxygen electrode in the form of symmetrical measurements using electrochemical impedance spectroscopy gives a general overview of the material's properties. For a more comprehensive characterization, measurements were performed on full cells. The described combination of a porous GDC backbone infiltrated with LSC was used as the oxygen electrode. Porous GDC backbone on commercially available half cells was prepared in the same procedure as symmetrical cells and infiltrated with the LSC precursor. In this case it was necessary to change the method from immersing to dropping due to the nature of the samples. It was found that this method gave similar results after 12 infiltration cycles. The reference was a commercial cell with an oxygen electrode in the form of LSC. Figure 8a and b, show the I-V curves and Fig. 8c and d EIS graphs obtained for cells with the proposed solution for 9 and 12 infiltrations and the reference sample in both dry and humidified H2 (50% H_2:50%H_2O) at a temperature of 600 °C. The 12 C infiltrated sample show a power density of 0.53 W.cm^{-2} at 600 °C, an increase of 8% over the reference sample. Fuel mode measurements also showed an increase in current density at the same potential for the 12 C LSC

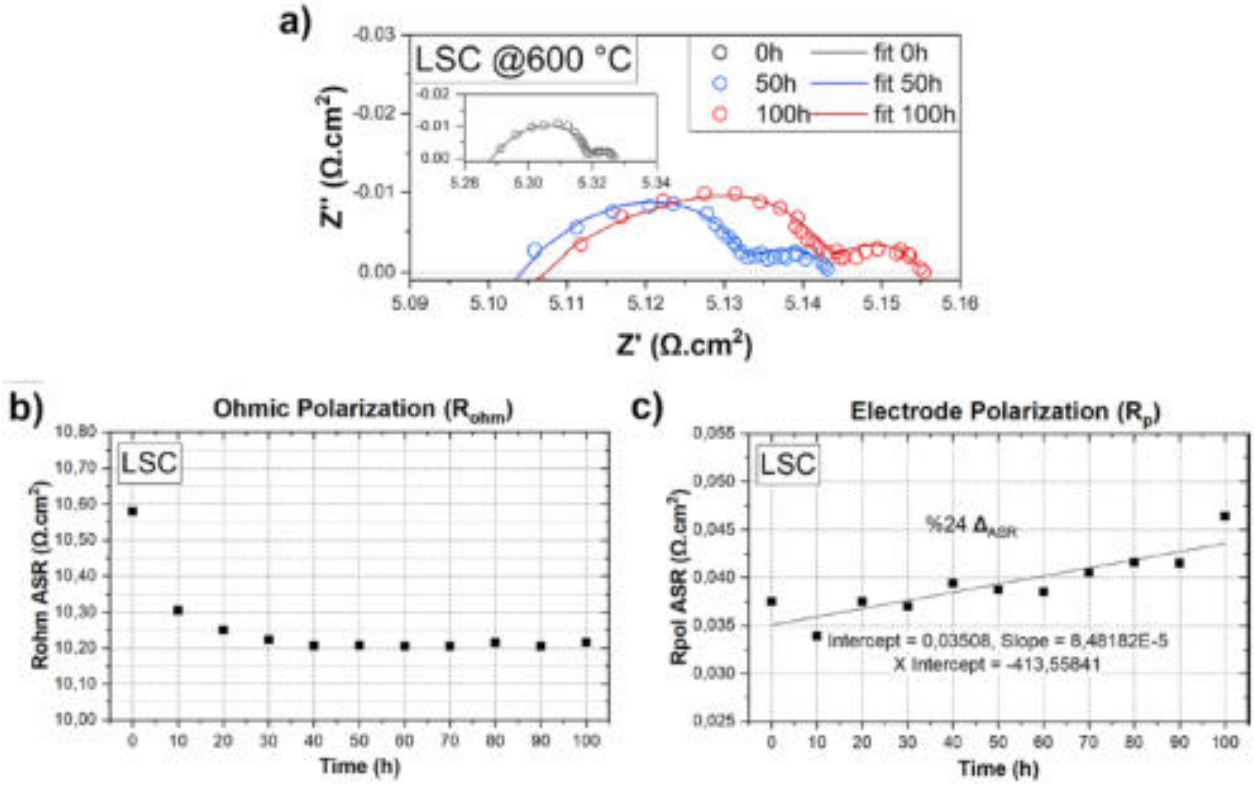


Fig. 7 Long-term ASR values of a) R_{ohm} and c) R_p of LSC at 600 °C

infiltrated sample compared to the reference. The increase was analyzed using the potential of 0.7 V, which yielded a value of 0.62 A.cm^{-2} to 0.7 A·cm^{-2} for the reference sample and 12 C LSC, respectively. Furthermore, a lower slope was observed in the electrolysis mode, confirming the trend above. This observation indicates an increase in the electrochemical activity of the cell. It has been shown that due to the identical fuel electrode and electrolyte, the obtained increase in power density was related to the increased electrochemical efficiency of the oxygen electrode. At the same time, a reduction in the polarization resistance of the cell was observed for both dry and wet hydrogen. In the case of dry hydrogen, R_p was 1.8 Ω.cm^2 compared to 2.3 Ω.cm^2 for the reference sample, a reduction of approximately 22% compared to the reference sample. A similar relationship occurs in the case of wet hydrogen where the R_p for the 12 C LSC impregnated sample was 0.47 Ω.cm^2 compared to 0.55 Ω.cm^2 for the reference sample, a reduction of approximately 15%.

4 Discussion and literature comparison

4.1 Symmetrical cells

To facilitate a more comprehensive interpretation of the results, a comparative analysis was conducted to identify any potential discrepancies between the findings and the existing literature. In the present study, the oxygen electrode formed of a porous backbone of GDC immersed in LSC exhibited the most promising electrochemical performance. The polarization resistance was observed to be 0.029 Ω.cm² and 7.89 Ω.cm² at 600 °C and 400 °C, respectively. The LSC: PrOx composite infiltration exhibits an intermediate performance compared to single phase compositions, with R_p values of 0.23 Ω.cm² and 9.75 Ω.cm² at 600 °C and 400 °C, respectively. The highest R_p values were observed for samples immersed in PrOx alone, with polarization resistance at 600 °C and 400 °C being 0.42 Ω.cm² and 17.38 Ω.cm², respectively.

In a similar study, A. Samson et al. examined the infiltration of the same composition (LSC64) into a screen-printed porous GDC backbone on a sintered GDC electrolyte at 1050 °C. They observed a polarization resistance of 0.044 Ω.cm² and 6.04 Ω.cm² at 600 °C and 400 °C respectively. Despite the use of a very thin electrolyte (180 µm), an

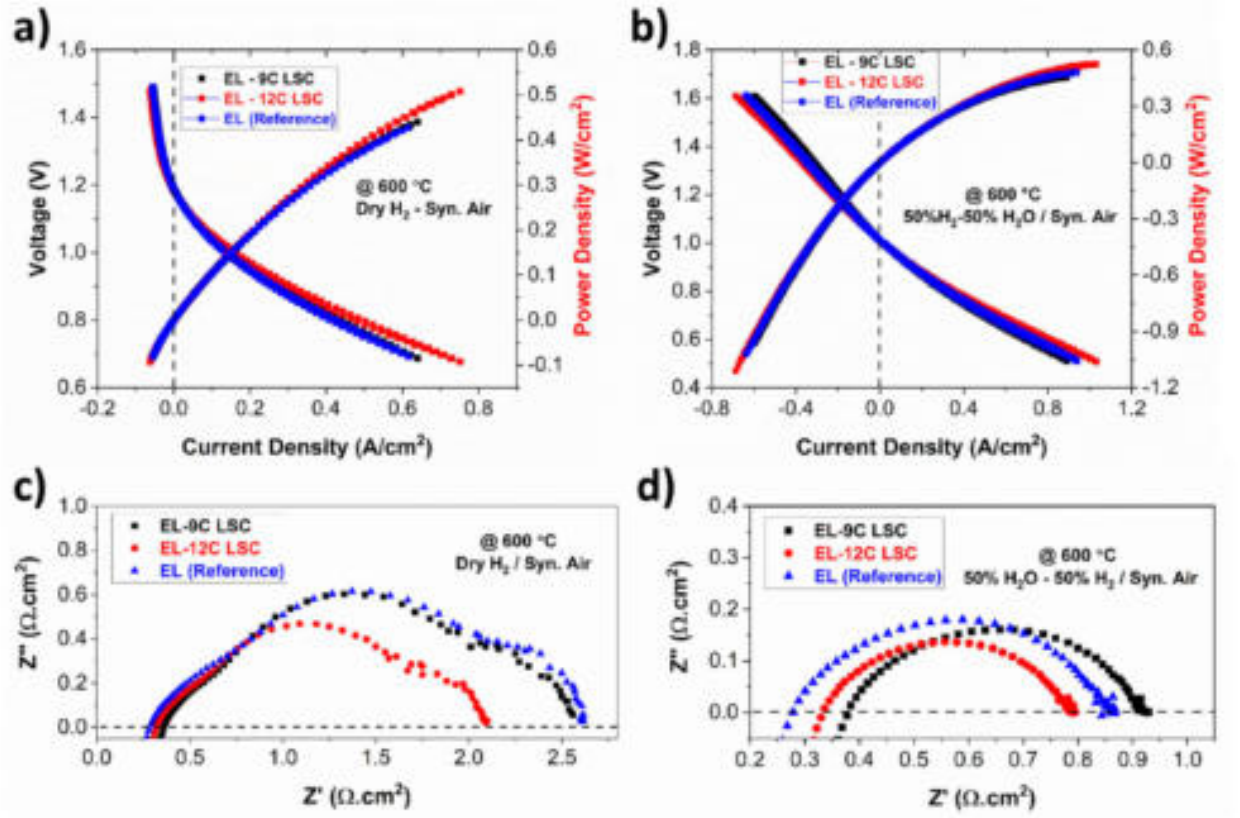


Fig. 8 Power, I-V curve and EIS data of infiltrated commercial fuel cells in dry (a, c), and 50% humidified fuel conditions (b, d)

infiltration loading of 9 times that used in this study, and a polymeric precursor concentration of 1 M, which is 5 times higher than that used in this study [34]. In the latter work, the same group achieved a value of 0.062 Ω.cm² with the six cycles of infiltration of the LSC [42]. Ovtar S. et al. achieved a R_p value of 0.031 Ω.cm² at a temperature of 700 °C. The electrode was produced through a process of infiltration, whereby a YSZ backbone was subjected to six layers of GDC and subsequently nine layers of LSC [44]. In the work of Zhao Fei et al., the infiltration of LSC into samaria-doped ceria (SDC, $Sm_{0.2}Ce_{0.8}O_{2-\delta}$) backbone onto SDC electrolyte has been conducted, resulting in an R_p of 0.281 Ω.cm² after subjecting the material to various thermal cycling regimes [45]. In a study conducted by Chrzan A. et al., symmetrical cells infiltrated with $La_{0.6}Sr_{0.4}Co_{0.2}Fe_{0.8}O_{3-\delta}$ were prepared. The objective was to investigate the effects of sintering temperature, thickness of the backbone and electrolyte, and the number of infiltration cycles on the polarization resistance. Additionally, the molarity of the infiltration solution was varied. At 600 °C, the polarization resistance achieved was 0.16 Ω.cm². The inferior performance observed in this study may be attributed to the use of coarser GDC particles, which result in diminished electrocatalytic activity due to the shortened TPB and reduced active area [46].

Nicollet C et al. conducted an infiltration process of Pr_6O_{11} into screen-printed 10 µm $LaNi_{0.6}Fe_{0.4}O_{3-\delta}$ (LNF) or GDC backbone (7–14 µm) onto a commercially available 100 µm 3% YSZ dense electrolyte. Notably, the polarization resistance was found to be 0.028 Ω.cm² at 600 °C. The molar concentration of Pr nitrate was 2 M, which is tenfold higher than that used in our work [18]. In a recent study, Caizán-Juanarena et al. investigated the potential of Pr_6O_{11}-infiltrated LSM-GDC backbone prepared by spray pyrolysis as an efficient oxygen electrode for solid oxide fuel cells. Electrochemical impedance spectroscopy measurements revealed a polarization resistance of 0.3 Ω.cm² and 44.5 Ω.cm² R_{ohm} at 650 °C [47]. In our work, 22.84 Ω.cm² of R_{ohm} was obtained for samples infiltrated with PrOx itself at 600 °C.

The values obtained for the sample immersed in PrOx: LSC composite exhibit a higher polarization resistance than those reported by Xiaofeng T. et al. for Pr-doped GDC (CGPO) and LSC, which is not a composite mixture, but a comparison in terms of Pr involvement may be reasonable. The composite mixture was infiltrated twice with CGPO and nine times with LSC into the GDC backbone, resulting in an R_p of 0.104 Ω.cm² at 700 °C [48].

4.2 Full cells

As previously stated, the infiltration of oxygen electrodes has been identified as a popular method for enhancing cell performance in the literature. However, the majority of these studies reported the performance of cells measured above 700 °C [44, 49–56]. The utilisation of anode-supported solid oxide cells at such low temperatures remains a relatively uncommon practice, although this operating temperature is gaining in popularity. For example, Samson A.C. et al. reported 1.28 $\Omega.cm^2$ total polarization of a similar cell with an LSC-infiltrated GDC oxygen electrode at 650 °C [57]. The anode was fueled by humidified H_2 (80%H_2:20%H_2O). In another study with a similar cell structure, Rehman S.U. et al. showed that infiltrating LSC into a porous GDC decreased the total polarization from 2.11 $\Omega.cm^2$ to 1.32 $\Omega.cm^2$ when compared to the conventionally fabricated LSC-GDC oxygen electrode [58]. The study reported an increase in power density from 0.48 $W.cm^{-2}$ to 0.82 $W.cm^{-2}$. The measurements were carried out at 650 °C with dry H_2 as fuel. Huang et al. studied LSC infiltration into an LSCF-SDC cathode integrated with a Ni-GDC anode-supported GDC electrolyte cell and claimed maximum power densities of 0.8 and 0.4 $W.cm^{-2}$ at 600 and 550 °C, respectively [59]. In this current study, similar to the literature, a trend to increase performance with the infiltration method was demonstrated, and a power density of 0.53 $W.cm^{-2}$ was obtained at 600 °C.

5 Conclusion

Infiltration process of LSC, LSC: PrOx and PrOx into the porous backbone GDC was prepared with wet powder spraying, as an porous oxygen electrode for intermediate solid oxide cells. It was found that an effective infiltration process was carried out by the immersion method. SEM-EDX analysis showed a uniform distribution of the immerse material in the porous backbone, both on the surface and in the electrolyte. In addition, the LSC infiltration was shown to be more effective than the PrOx infiltration.

Electrochemical impedance spectroscopy measurements showed a very low value of polarization resistance for LSC-immersed samples (0.029 $\Omega.cm^2$ at 600 °C). Specimens infiltrated with the LSC: PrOx composite showed intermediate values (0.23 $\Omega.cm^2$ at the same temperature), and the worst results were obtained with samples infiltrated with only PrOx (0.42 $\Omega.cm^2$ at the same temperature°C).

Long-term stability measurements showed a slight increase in the polarization resistance of the LSC-immersed sample. This value changed by 24% in 100 h. A decrease and stabilization of the ohmic resistance was also observed.

Measurements of full cells showed a high power density of 0.53 $W.cm^{-2}$ at a temperature of 600 °C, an increase of 8% compared to the reference sample. Improvement was also demonstrated in all cell operating modes, both fuel and electrolyser. EIS measurements performed on the cells showed a reduction in polarization resistance for the LSC-infiltrated samples compared to the reference.

Acknowledgements This research has been supported by National Science Centre (NCN) DAINA 2 project number UMO-2020/38/L/ST8/00513: "Porous metal supported micro-scale solid oxide fuel cells: fundamentals, fabrication and testing".

Authors contribution Ömer Faruk Aksoy - Writing – original draft, Writing - review & editing, Validation, Methodology, Investigation (Sample preparation, symmetrical cells measurements), Formal analysis, Data curation. Bartłomiej Lemieszek: Writing – original draft, Writing - review & editing, Validation, Methodology, Investigation (symmetrical cells measurements), Formal analysis, Data curation. Murat Murutoğlu – Writing - review & editing, Methodology, Investigation (Full cells measurements), Formal analysis, Data curation. Jakub Karczewski - Writing – review & editing, Methodology, Investigation. Piotr Jasiński - Writing – review & editing, Methodology. Sebastian Molin - Writing – review & editing, Supervision, Funding acquisition, Methodology, Conceptualization.

Data availability The raw/processed data from this study will be available on request from the corresponding author.

Declarations

Competing interests The authors declare that they have no known competing financial interests or personal relationships that could have appeared to influence the work reported in this paper.

Open Access This article is licensed under a Creative Commons Attribution 4.0 International License, which permits use, sharing, adaptation, distribution and reproduction in any medium or format, as long as you give appropriate credit to the original author(s) and the source, provide a link to the Creative Commons licence, and indicate if changes were made. The images or other third party material in this article are included in the article's Creative Commons licence, unless indicated otherwise in a credit line to the material. If material is not included in the article's Creative Commons licence and your intended use is not permitted by statutory regulation or exceeds the permitted use, you will need to obtain permission directly from the copyright holder. To view a copy of this licence, visit http://creativecommons.org/licenses/by/4.0/.

References

1. A. Alaswad, A. Baroutaji, A. Rezk, M. Ramadan, A.G. Olabi, *Advances in Solid Oxide Fuel Cell Materials. In Encyclopedia of Smart Materials*, pp. 334–340 (2020). https://doi.org/10.1016/B978-0-12-803581-8.11743-6
2. M. Ghamarinia, A. Babaei, C. Zamani, H. Aslannejad, Application of the distribution of relaxation time method in electrochemical analysis of the air electrodes in the SOFC/SOEC devices: a review. Chem. Eng. J. Adv. **15**, 100503 (2023). https://doi.org/10.1016/J.CEJA.2023.100503

3. A. Tarancón, Strategies for lowering solid oxide fuel cells operating temperature. Energies. 2(4), 1130–1150 (2009). https://doi.org/10.3390/en20401130
4. J.C.W. Mah, A. Muchtar, M.R. Somalu, M.J. Ghazali, Metallic interconnects for solid oxide fuel cell: a review on protective coating and deposition techniques. Int. J. Hydrogen Energy. 42(14), 9219–9229 (2017). https://doi.org/10.1016/j.ijhydene.2016.03.195
5. S. Chen, H. Zhang, C. Yao et al., Review of SOFC Cathode performance enhancement by surface modifications: recent advances and future directions. Energy Fuels. 37(5), 3470–3487 (2023). https://doi.org/10.1021/acs.energyfuels.2c03934
6. B. Kamecki, G. Cempura, P. Jasiński, S.-F. Wang, S. Molin, Tuning Electrochemical performance by Microstructural Optimization of the Nanocrystalline Functional Oxygen Electrode Layer for Solid Oxide cells. ACS Appl. Mater. Interfaces. 14(51), 57449–57459 (2022). https://doi.org/10.1021/acsami.2c18951
7. Z. Wang, X. Wang, Z. Xu et al., Semiconductor-ionic nanocomposite La0.1Sr0.9MnO3-δ-Ce0.8Sm0.2O2-δ functional layer for high performance low temperature SOFC. Mater. (Basel). 11(9) (2018). https://doi.org/10.3390/MA11091549
8. Z. Li, M. Li, Z. Zhu, Perovskite Cathode materials for low-temperature solid oxide fuel cells: fundamentals to optimization STO SrTiO 3 TEM transmission electron microscopy YSZ Yttria-stabilized zirconia. 1918;5:263–311. https://doi.org/10.1007/s41918-021-00098-3
9. A. Evans, J. Martynczuk, D. Stender, C.W. Schneider, T. Lippert, M. Prestat, Low-temperature micro-solid oxide fuel cells with partially amorphous la0.6Sr0.4CoO3-δ cathodes. Adv. Energy Mater. 5(1), 1–9 (2015). https://doi.org/10.1002/aenm.201400747
10. B. Kamecki, J. Karczewski, H. Abdoli et al., Deposition and Electrical and Structural properties of $La_{0.6}Sr_{0.4}CoO_3$ thin films for Application in High-Temperature Electrochemical cells. J. Electron. Mater. 48(9), 5428–5441 (2019). https://doi.org/10.1007/s11664-019-07372-7
11. J. Hayd, L. Dieterle, U. Guntow, D. Gerthsen, E. Ivers-Tiffée, Nanoscaled $La_{0.6}Sr_{0.4}CoO_{3-\delta}$ as intermediate temperature solid oxide fuel cell cathode: microstructure and electrochemical performance. J. Power Sources. 196(17), 7263–7270 (2011). https://doi.org/10.1016/J.JPOWSOUR.2010.11.147
12. C. Kim, H. Lee, I. Jang et al., Subcontinuous 2D $La_{0.6}Sr_{0.4}CoO_{3-\delta}$ nanosheet as an efficient charge conductor for boosting the cathodic activity of solid oxide fuel cells. Electrochim. Acta. 366, 137371 (2021). https://doi.org/10.1016/J.ELECTACTA.2020.137371
13. Y.T. Kim, N. Shikazono, Investigation of $La_{0.6}Sr_{0.4}CoO_{3-\delta}$-$Gd_{0.1}Ce_{0.9}O_{2-\delta}$ composite cathodes with different volume ratios by three-dimensional reconstruction. Solid State Ionics. 309, 77–85 (2017). https://doi.org/10.1016/J.SSI.2017.07.010
14. Y.J. Jin, Z.G. Liu, Z.Y. Ding, G. Cao, J.H. Ouyang, Preparation, microstructure and electrical property of $GdSmZr_2O_7$-$(Li_{0.52}Na_{0.48})_2CO_3$ composite electrolyte via carbonate infiltration. Ceram. Int. 46(5), 5689–5694 (2020). https://doi.org/10.1016/J.CERAMINT.2019.11.016
15. Y.T. Kim, A. Ohi, A. He et al., Microstructure and polarization characteristics of LSCF-GDC composite cathode with different volume fractions. ECS Trans. 68(1), 757–762 (2015). https://doi.org/10.1149/06801.0757ecst
16. A. Donazzi, G. Cordaro, A. Baricci, Z. Ding, M. Bin, Maestri, A detailed kinetic model for the reduction of oxygen on LSCF-GDC composite cathodes. Electrochim. Acta. 335, 135620 (2020). https://doi.org/10.1016/J.ELECTACTA.2020.135620
17. C. Fu, K. Sun, N. Zhang, X. Chen, D. Zhou, Electrochemical characteristics of LSCF–SDC composite cathode for intermediate temperature SOFC. Electrochim. Acta. 52(13), 4589–4594 (2007). https://doi.org/10.1016/J.ELECTACTA.2007.01.001
18. C. Nicollet, A. Flura, V. Vibhu, A. Rougier, J.M. Bassat, J.C. Grenier, An innovative efficient oxygen electrode for SOFC: Pr_6O_{11} infiltrated into Gd-doped ceria backbone. Int. J. Hydrogen Energy. 41(34), 15538–15544 (2016). https://doi.org/10.1016/j.ijhydene.2016.04.024
19. L. Yefsah, J. Laurencin, M. Hubert et al., Electrochemical performance and stability of $PrO_{1.833}$ as an oxygen electrode for solid oxide electrolysis cells. Solid State Ionics. 399(March), 1–14 (2023). https://doi.org/10.1016/j.ssi.2023.116316
20. M.R. Somalu, A. Muchtar, W.R.W. Daud, N.P. Brandon, Screen-printing inks for the fabrication of solid oxide fuel cell films: a review. Renew. Sustain. Energy Rev. 75(December 2015), 426–439 (2017). https://doi.org/10.1016/j.rser.2016.11.008
21. H. Zhang, T. Chen, Z. Huang, G. Hu, J. Zhou, S. Wang, A cathode-supported solid oxide fuel cell prepared by the phase-inversion tape casting and impregnating method. Int. J. Hydrogen Energy. 47(43), 18810–18819 (2022). https://doi.org/10.1016/j.ijhydene.2022.04.021
22. J.H. Myung, H.J. Ko, H.G. Park, M. Hwan, S.H. Hyun, Fabrication and characterization of planar-type SOFC unit cells using the tape-casting/lamination/co-firing method. Int. J. Hydrogen Energy. 37(1), 498–504 (2012). https://doi.org/10.1016/J.IJHYDENE.2011.09.011
23. C. Yuan, Y. Liu, Y. Zhou, Z. Zhan, S. Wang, Fabrication and characterization of a cathode-support solid oxide fuel cell by tape casting and lamination. Int. J. Hydrogen Energy. 38(36), 16584–16589 (2013). https://doi.org/10.1016/J.IJHYDENE.2013.08.146
24. S. Zhang, L. Bi, L. Zhang, C. Yang, H. Wang, W. Liu, Fabrication of cathode supported solid oxide fuel cell by multi-layer tape casting and co-firing method. Int. J. Hydrogen Energy. 34(18), 7789–7794 (2009). https://doi.org/10.1016/J.IJHYDENE.2009.07.081
25. A. Evans, C. Benel, A.J. Darbandi et al., Integration of spin-coated nanoparticulate-based $La_{0.6}Sr_{0.4}CoO_{3-\delta}$ cathodes into micro-solid oxide fuel cell membranes. Fuel Cells. 13(3), 441–444 (2013). https://doi.org/10.1002/fuce.201300020
26. Z. Wang, W. Weng, K. Chen, G. Shen, P. Du, G. Han, Preparation and performance of nanostructured porous thin cathode for low-temperature solid oxide fuel cells by spin-coating method. J. Power Sources. 175(1), 430–435 (2008). https://doi.org/10.1016/J.JPOWSOUR.2007.09.092
27. B. Lemieszek, M. Ilickas, J. Jamroz et al., Enhanced electrochemical performance of partially amorphous $La_{0.6}Sr_{0.4}CoO_{3-\delta}$ oxygen electrode materials for low-temperature solid oxide cells operating at 400°C. Appl. Surf. Sci. 670 (2024). https://doi.org/10.1016/j.apsusc.2024.160620
28. L. Baqué, A. Serquis, Microstructural characterization of $La_{0.4}Sr_{0.6}Co_{0.8}Fe_{0.2}O_{3-\delta}$ films deposited by dip coating. Appl. Surf. Sci. 254(1), 213–218 (2007). (SPEC. ISS.). https://doi.org/10.1016/j.apsusc.2007.07.033
29. M. Xu, J. Yu, Y. Song, R. Ran, W. Wang, Z. Shao, Advances in Ceramic Thin films fabricated by Pulsed Laser Deposition for Intermediate-Temperature Solid Oxide fuel cells. Energy Fuels. 34(9), 10568–10582 (2020). https://doi.org/10.1021/acs.energyfuels.0c02338
30. Y. Chen, L. Liang, S.A. Paredes Navia, A. Hinerman, K. Gerdes, X. Song, Synergetic Interaction of Additive Dual nanocatalysts to accelerate Oxygen reduction reaction in fuel cell cathodes. ACS Catal. 9(8), 6664–6671 (2019). https://doi.org/10.1021/acscatal.9b00811
31. A. Seong, J. Kim, O. Kwon et al., Self-reconstructed interlayer derived by in-situ mn diffusion from $La_{0.5}Sr_{0.5}MnO_3$ via atomic layer deposition for an efficient bi-functional electrocatalyst. Nano Energy. 71(January), 104564 (2020). https://doi.org/10.1016/j.nanoen.2020.104564
32. C. Xiong, S. Xu, X. Li et al., Surface regulating and hetero-interface engineering of an LSCF cathode by CVD for solid oxide fuel

cells: integration of improved electrochemical performance and Cr-tolerance. J. Mater. Chem. A **11**(29), 15760–15768 (2023). https://doi.org/10.1039/d3ta02249h
33. F.L.W.C. Jung, F.L.J.J. Kim, F.L.H.L. Tuller, Investigation of nanoporous platinum thin films fabricated by reactive sputtering: application as micro-SOFC electrode. J. Power Sources. **275**, 860–865 (2015). https://doi.org/10.1016/j.jpowsour.2014.11.084
34. A. Samson, M. Søgaard, R. Knibbe, N. Bonanos, High performance cathodes for solid oxide fuel cells prepared by infiltration of $La_{0.6}Sr_{0.4}CoO_{3-\delta}$ into Gd-Doped Ceria. J. Electrochem. Soc. **158**(6), B650 (2011). https://doi.org/10.1149/1.3571249
35. R. Zeng, Y. Huang, Enhancing surface activity of $La_{0.6}Sr_{0.4}CoO_{3-\delta}$ cathode by a simple infiltration process. Int. J. Hydrogen Energy. **42**(10), 7220–7225 (2017). https://doi.org/10.1016/J.IJHYDENE.2016.04.014
36. D. Ding, M. Liu, M. Liu, S.O.F.C. Enhancing, Electrode Performance through Surface Modification. ECS Trans. **57**(1), 1801–1810 (2013). https://doi.org/10.1149/05701.1801ecst
37. S. Choi, S. Yoo, J. Shin, G. Kim, J.E. Soc, B-b P. High Performance SOFC Cathode prepared by infiltration of $La_{n+1}Ni_nO_{3n+1}$ (n = 1, 2, and 3) in porous YSZ High Performance SOFC Cathode prepared by infiltration. J. Electrochem. Soc. **158**(8), B995–B999 (2011). https://doi.org/10.1149/1.3598170
38. M. Shah, S.A. Barnett, Solid oxide fuel cell cathodes by infiltration of $La_{0.5}Sr_{0.4}Co_{0.2}Fe_{0.8}O_{3-\delta}$ into Gd-Doped Ceria. Solid State Ionics. **179**(35–36), 2059–2064 (2008). https://doi.org/10.1016/J.SSI.2008.07.002
39. Y. Huang, J.M. Vohs, R.J. Gorte, SOFC cathodes prepared by infiltration with various LSM precursors. Electrochem. Solid-State Lett. **9**(5), 237–240 (2006). https://doi.org/10.1149/1.2183867
40. Y. Cheng, A.S. Yu, X. Li, T. Oh, J.M. Vohs, R.J. Gorte, Preparation of SOFC cathodes by infiltration into LSF-YSZ composite scaffolds. J. Electrochem. Soc. **163**(2), 54–58 (2016). https://doi.org/10.1149/2.0171602jes
41. M.P. Pechini, Method of Preparing Lead and Alkaline Earth Titanates and Niobates and coating method using the same to form a Capacitor, *US Pat 3,330,697*. Published online 1967:2
42. A.J. Samson, M. Sgaard, N. Bonanos, Electrodes for solid oxide fuel cells based on infiltration of co-based materials. Electrochem. Solid-State Lett. **15**(4), 54–56 (2012). https://doi.org/10.1149/2.020204esl
43. V. Thangadurai, R.A. Huggins, W. Weppner, Mixed ionic-electronic conductivity in phases in the praseodymium oxide system. J. Solid State Electrochem. **5**, 531–537 (2001). https://doi.org/10.1007/s100080000187
44. S. Ovtar, A. Hauch, S. Veltzé, M. Chen, Comparison between $La_{0.6}Sr_{0.4}CoO_{3-\delta}$ and $LaNi_{0.6}Co_{0.4}O_{3-\delta}$ infiltrated oxygen electrodes for long-term durable solid oxide fuel cells. Electrochim. Acta. **266**, 293–304 (2018). https://doi.org/10.1016/j.electacta.2018.02.022
45. F. Zhao, R. Peng, C. Xia, A $La_{0.6}Sr_{0.4}CoO_{3-\delta}$-based electrode with high durability for intermediate temperature solid oxide fuel cells. Mater. Res. Bull. **43**(2), 370–376 (2008). https://doi.org/10.1016/j.materresbull.2007.03.006
46. A. Chrzan, J. Karczewski, M. Gazda, D. Szymczewska, P. Jasinski, $La_{0.6}Sr_{0.4}Co_{0.2}Fe_{0.8}O_{3-\delta}$ oxygen electrodes for solid oxide cells prepared by polymer precursor and nitrates solution infiltration into gadolinium doped ceria backbone. J. Eur. Ceram. Soc. **37**(11), 3559–3564 (2017). https://doi.org/10.1016/j.jeurceramsoc.2017.04.032
47. L. Caizán-Juanarena, J. Zamudio-García, D. Marrero-López, Electrochemical investigation of Pr_6O_{11} infiltration into $La_{0.8}Sr_{0.2}MnO_{3-\delta}$-$Ce_{0.9}Gd_{0.1}O_{1.95}$ cathodes for IT-SOFC. Ceram. Int. **49**(21), 33717–33724 (2023). https://doi.org/10.1016/j.ceramint.2023.08.060
48. X. Tong, C. Li, K. Xu et al., Nanoengineering of electrodes via infiltration: an opportunity for developing large-area solid oxide fuel cells with high power density. Nanoscale. **15**(40), 16362–16370 (2023). https://doi.org/10.1039/d3nr02704j
49. H. Fan, M. Keane, N. Li, D. Tang, P. Singh, ScienceDirect infiltrated YSZ oxygen electrode for reversible solid oxide fuel cells. 2014;**9**. https://doi.org/10.1016/j.ijhydene.2014.05.149
50. X. Tong, S. Ovtar, K. Brodersen, P.V. Hendriksen, M. Chen, A 4 × 4 cm 2 Nanoengineered Solid Oxide Electrolysis Cell for E ffi cient and Durable Hydrogen Production. Published online 2019. https://doi.org/10.1021/acsami.9b07749
51. S. Ur, H. Song, H. Kim et al., A dynamic infiltration technique to synthesize nanolayered cathodes for high performance and robust solid oxide fuel cells. J. Energy Chem. **70**, 201–210 (2022). https://doi.org/10.1016/j.jechem.2022.02.052
52. Y. Namgung, J. Hong, A. Kumar, D.K. Lim, S.J. Song, One step infiltration induced multi-cation oxide nanocatalyst for load proof SOFC application. Appl. Catal. B Environ. **267**(November 2019), 118374 (2020). https://doi.org/10.1016/j.apcatb.2019.118374
53. Song YH, Rehman SU, Kim HS et al., Facile surface modification of LSCF/GDC cathodes by epitaxial deposition of $Sm_{0.5}Sr_{0.5}CoO_3$ via ultrasonic spray infiltration. J. Mater Chem. A. **8**(7), 3967–3977 (2020). https://doi.org/10.1039/c9ta11704k
54. L. Sr, H. Ahmad, M. Zubair et al., ScienceDirect Boosting performance of the solid oxide fuel cell by. Int. J. Hydrogen Energy. **47**(88), 37587–37598 (2021). https://doi.org/10.1016/j.ijhydene.2021.11.109
55. Z. Zheng, J. Jing, Z. Lei, Z. Wang, Z. Yang, ScienceDirect Performance and DRT analysis of infiltrated functional cathode based on the anode supported SOFCs with long-term stability. Int. J. Hydrogen Energy. **47**(41), 18139–18147 (2022). https://doi.org/10.1016/j.ijhydene.2022.03.289
56. Samson AJ, Søgaard M, Hjalmarsson P et al., Durability and performance of high performance infiltration cathodes. **13**(4), 511–519 (2013). https://doi.org/10.1002/fuce.201200183
57. A.J. Samson, P. Hjalmarsson, M. Søgaard, J. Hjelm, N. Bonanos, Highly durable anode supported solid oxide fuel cell with an in fi ltrated cathode. 2012;**216**:124–130. https://doi.org/10.1016/j.jpowsour.2012.05.040
58. S. Ur, M. Haseeb, H. Kim et al., Applied Catalysis B: Environmental Designing the nano-scale architecture of the air electrode for high-performance and robust reversible solid oxide cells. Appl. Catal. B Environ. **333**(December 2022), 122784 (2023). https://doi.org/10.1016/j.apcatb.2023.122784
59. Y. Huang, A.M. Hussain, E.D. Wachsman, Nano Energy Nanoscale cathode modi fi cation for high performance and stable low- temperature solid oxide fuel cells (SOFCs). Nano Energy. **49**(March), 186–192 (2018). https://doi.org/10.1016/j.nanoen.2018.04.028

Publisher's note Springer Nature remains neutral with regard to jurisdictional claims in published maps and institutional affiliations.

10.5. Unveiling the Potential of Praseodymium Oxide as Efficient Oxygen Electrode for Low-Temperature Solid Oxide Cell Applications.

Authors: **Bartłomiej Lemieszek**, Lulu Alluhaibi, Alexey Maximenko, Łukasz Gaweł, Aleksandra Mielewczyk-Gryń, Michał Struzik, Marcin Małys, Muhammad Imran Asghar, Grzegorz Cempura, Piotr Jasiński, Sebastian Molin
https://doi.org/10.1016/j.cej.2026.173949
Chemical Engineering Journal, vol. 531, pages 173949, 2026,
IF = 13.2 (2024), MSHE points 200, Citations: 0

The final article investigates the potential of praseodymium oxide as an oxygen electrode material for low-temperature solid oxide cells. The electrode was deposited by spin coating using a newly developed precursor, and only three deposition cycles (~200 nm) were sufficient to achieve very high electrochemical efficiency. The material was characterized by HT-XRD, Raman spectroscopy, XPS, XAFS, and DC conductivity measurements. Structural studies highlighted the complex nature of praseodymium oxide, showing that several PrO_x phases may coexist within narrow temperature ranges. The average oxidation state of praseodymium strongly depended on annealing temperature, and EXAFS analysis further confirmed the coexistence of multiple phases.

Electrochemical characterization on symmetrical cells showed that the previously unexplored annealing temperature of 500 °C gave the lowest polarization resistance and the best performance. Measurements at different oxygen partial pressures indicated stable operation down to 10% pO_2, below which polarization resistance increased significantly. The material also showed reversible interactions with H_2O and CO_2, which is advantageous compared with conventional electrodes such as LSC, LSCF, and LSM. Long-term stability was confirmed over 225 hours. Fuel cell tests demonstrated that cells with the PrO_x electrode achieved about 40% higher power density than a commercial reference cell and nearly four times higher power density than a similar cell without the PrO_x layer at 500 °C.

The novelty of this work lies in demonstrating that praseodymium oxide is an effective, stand-alone oxide electrode material for low-temperature oxide

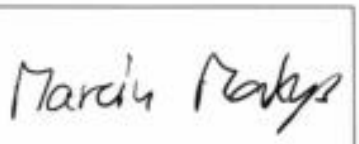
cells operating at temperatures below 600 °C. The study combines systematic optimization of spin-coated PrO_x thin films with detailed structural and electronic characterization, enabling correlation of electrochemical performance with the oxidation state and phase composition of PrO_x. An additional, novel aspect is the evaluation of the electrode's stability in the presence of H_2O and CO_2, along with validation in a full cell at 500°C.

The main achievements of this study include a comprehensive structural characterization of praseodymium oxide using multiple complementary techniques, which enabled determination of the average oxidation state and confirmation of the simultaneous presence of several PrO_x phases. Symmetric-cell measurements yielded some of the best results reported in the literature, obtained with a low-cost deposition method. The work also established 500 °C as the optimal annealing temperature, lower than the previously assumed 600 °C. Furthermore, the study demonstrated that PrO_x electrodes can recover full efficiency after exposure to H_2O and CO_2, highlighting their robustness. Finally, a cell operating at 500 °C was developed, outperforming state-of-the-art commercial product by nearly 40%.

My original contributions included developing the new precursor recipe, depositing electrode layers, and performing conductivity measurements using the Van der Pauw technique. I also carried out XAFS measurements (XANES and EXAFS), symmetric-cell studies at varying annealing temperatures and gas compositions (pO_2, pH_2O, pCO_2), and long-term stability tests. In addition, I prepared cells and performed corresponding electrochemical measurements. I analysed the XRD, XAFS, and XPS data, wrote the manuscript as first author, prepared all figures except the Raman spectra, submitted the article to the journal, and prepared responses to reviewer comments.

Declaration of co-authors on their contribution to the publication: "Unveiling the Potential of Praseodymium Oxide as Efficient Oxygen Electrode for Low-Temperature Solid Oxide Cell Applications".

Name and Surname	Contribution	Signature
Bartłomiej Lemieszek	Conceptualization, Writing – original draft, Writing - review & editing, Validation, Methodology, Investigation (Sample preparation, symmetrical cells measurements, Fuel cell measurements, DC conductivity, XAFS), Formal analysis, Data curation, Visualization.	
Lulu Alluhaibi	Writing - review & editing, Methodology, Investigation (XAFS), Data curation	
Alexey Maximenko	Writing - review & editing, Methodology, Investigation (XAFS), Data curation.	
Łukasz Gaweł	Writing – review & editing, Methodology, Investigation (XPS).	
Aleksandra Mielewczyk-Gryń	Writing – review & editing, Methodology, Investigation (Water uptake).	
Michał Struzik	Writing – original draft, Writing – review & editing, Methodology, Investigation (in-situ Raman spectroscopy).	

Marcin Małys	Writing – review & editing, Methodology, Investigation (HT-XRD).	
Muhammad Imran Asghar	Writing – review & editing, Methodology, Investigation (HT-XRD).	
Grzegorz Cempura	Writing – review & editing, Methodology, Investigation (SEM-EDS).	
Piotr Jasiński	Writing – review & editing, Methodology.	
Sebastian Molin	Writing – review & editing, Supervision, Funding acquisition, Methodology, Conceptualization.	

Chemical Engineering Journal 531 (2026) 173949

Contents lists available at ScienceDirect

Chemical Engineering Journal

journal homepage: www.elsevier.com/locate/cej

Unveiling the potential of praseodymium oxide as efficient oxygen electrode for low-temperature solid oxide cell applications

Bartłomiej Lemieszek [a,*], Lulu Alluhaibi [b], Alexey Maximenko [b], Łukasz Gaweł [d], Aleksandra Mielewczyk-Gryń [c], Michał Struzik [e], Marcin Małys [e], Muhammad Imran Asghar [f], Grzegorz Cempura [g], Piotr Jasiński [a], Sebastian Molin [a]

[a] Advanced Materials Centre, Faculty of Electronics, Telecommunications and Informatics, Gdańsk University of Technology, ul. G. Narutowicza 11/12, 80-233, Gdańsk, Poland
[b] National Synchrotron Radiation Centre SOLARIS, Jagiellonian University, Czerwone Maki 98, 30-392, Kraków, Poland
[c] Institute of Nanotechnology and Materials Engineering, Faculty of Applied Physics and Mathematics and Advanced Materials Centre, Gdańsk University of Technology, Gdańsk, Poland
[d] Department of Electrochemistry Corrosion and Materials Engineering, Faculty of Chemistry, Gdansk University of Technology, 11/12 Narutowicza Street, 80-233, Gdansk, Poland
[e] Warsaw University of Technology, Faculty of Physics, Koszykowa 75, 00-662, Warsaw, Poland
[f] Renewable Energy Technologies Group, Faculty of Engineering and Natural Sciences, Tampere University, FI-33014, Tampere, Finland
[g] International Centre for Electron Microscopy, Faculty of Metals Engineering and Industrial Computer Science, AGH University of Science and Technology, 30-059, Kraków, Poland

ARTICLE INFO

Dataset link: EIS measurements for the PrOx oxygen electrode as a function of annealing temperature (Original data), EIS measurements at different pO2 for PrOx oxygen electrode - symmetrical measurements (Original data), Measurements of fuel cells with an oxygen electrode in the form of PrOx - I-V and EIS (Original data), XAFS spectra for praseodymium oxide annealed at temperatures from 400 °C to 1000 °C (Original data)

Keywords:
Praseodymium oxide
Low-temperature solid oxide cells
Oxygen electrode
XAFS
EIS

ABSTRACT

This study investigates praseodymium oxide (PrO_x) as a promising oxygen electrode material for solid oxide cells operating below 600 °C. The electrode was fabricated using the spin-coating technique and characterized by XRD, XPS, XAFS, and DC conductivity measurements. Structural analysis enabled precise determination of the average oxidation state of praseodymium, revealing the presence of multiple PrO_y phases, which significantly affect the material's electrochemical properties. Electrochemical impedance spectroscopy (EIS) indicated that a 200 nm electrode thickness yields optimal performance. The highest electrocatalytic activity for the oxygen reduction reaction was observed at an annealing temperature of 500 °C. The impact of water vapor (pH_2O) and carbon dioxide (pCO_2) on electrode performance was also examined. Both gases induced reversible changes, with the electrode retaining its activity—demonstrating superior stability compared to state-of-the-art materials. This change results from different structure and chemistry compared to perovskite oxides, higher redox activity associated with greater mobility of the Pr cation oxidation state, and lower basicity, which influences the formation of less stable carbonates and hydroxides. Full cell tests conducted at 500 °C yielded a power density of 95 mW·cm^{-2} - over four times higher and 39% greater than that of reference cells. These results highlight the potential of PrO_x for use in solid oxide cells, proton-conducting cell technologies, and broader electrochemical applications.

1. Introduction

Solid Oxide Cells (SOCs) have emerged as one of the most promising technologies in the next generation of potentially emission-free energy sources. This technology allows the use of hydrogen as a fuel (solid oxide fuel cell) and the effect of the electrochemical reaction is environmentally neutral water. In addition, the technology can operate in reverse mode (solid oxide electrolyser cell), allowing excess energy to be used for direct fuel production [1]. Despite its potential, this technology requires further advancements to enable effective commercialization. Achieving these targets leads to improvements in efficiency and a reduction in stack costs. It was hypothesized that lowering the operating temperature below 500 °C, even to 350 °C, could lower the costs of metallic interconnects, extend the operational lifespan, and contribute

* Corresponding author.
E-mail address: bartlomiej.lemieszek@pg.edu.pl (B. Lemieszek).

https://doi.org/10.1016/j.cej.2026.173949
Received 14 November 2025; Received in revised form 30 December 2025; Accepted 8 February 2026
Available online 9 February 2026
1385-8947/© 2026 The Authors. Published by Elsevier B.V. This is an open access article under the CC BY-NC license (http://creativecommons.org/licenses/by-nc/4.0/).

to the commercial availability [2–4]. To enable operation under these conditions, advanced research is required to optimize the properties and enhance the electrical and electrochemical efficiency. This trend encompasses all components of the cell and stack, including the oxygen electrode [5–7], electrolyte [8–10], fuel electrode [11–13], potential additional layers [14], as well as interconnects and their protective coatings [15–17].

For oxygen electrodes, high-performance solutions operating at low temperatures ($\leq$ 600 °C) are needed. Current state-of-the-art materials include mixed ionic-electronic conductor (MIEC) perovskite oxides, such as $La_{1-x}Sr_xCoO_{3-\delta}$ (LSC) and $La_{1-x}Sr_xCo_{1-y}Fe_yO_{3-\delta}$ (LSCF). These materials exhibit high electronic and ionic conductivity together with low polarization resistance in the intermediate range [18,19].

However, the quest for efficient cells in the low temperature range is contributing to the increased search for new materials for oxygen electrodes. Currently, in addition to the materials mentioned above, particular attention is being paid to praseodymium oxide. Although this material has been known for years, it has recently gained interest as a potentially more effective material for catalysing the electrochemical reduction of oxygen in fuel cells [20,21]. Praseodymium oxide (PrO_x) represents an interesting subject within the domain of binary oxides, exhibiting a broad spectrum of stoichiometries that deviate from the conventional model predicated on randomly dispersed isolated point defects. These structures exhibit a high degree of interconnectedness, thereby creating a complex and intricate network of relationships [22].

The literature indicates that the most electrochemically active form of praseodymium oxide is the cubic β-phase, Pr_6O_{11} ($PrO_{1.833}$). This phase is characterized by a total conductivity of $6.77 \cdot 10^{-2}$ S·cm^{-1} at 400 °C, with an activation energy of 0.52 eV per atom [22]. Notably, this phase exhibits stability at relatively low temperatures - 430 °C. A small increase in temperature (up to 470 °C) induces a phase transition to the δ-phase, $Pr_{11}O_{20}$. At temperatures approaching 490 °C, the ε-phase, Pr_5O_9, becomes apparent (up to 520 °C), while at temperatures up to 700 °C, the rhombohedral ι-phase, Pr_7O_{12}, is observed [21,22]. The ι-phase is distinguished by a markedly lower total conductivity compared to the aforementioned phases [21]. Despite this variability, these structures demonstrate a high degree of similarity to one another and to the underlying basic lattice structure [22]. The high phase variability and the resulting different physicochemical properties require detailed parameter optimisation for the effective use of PrO_x in solid oxide cell technology.

Phase variation can be particularly critical when PrO_x is implemented as a thin functional layer, with a thickness of 200 nm. Similar thin-layer concepts have already been reported for other oxygen-electrode materials and have been shown to improve performance by tailoring the interfacial reaction zone [14]. This approach is especially relevant in light of recent findings suggesting that the electrochemically active region of the oxygen electrode may be confined to a near-interface zone. Recent work of Fujimaki et al. using operando micro-XAS indicates that the electrochemically active reaction zone in porous SOC oxygen electrodes can be confined to a characteristic length of approximately 1 μm from the electrode-electrolyte interface under cathodic polarization. This means that the active thickness is not necessarily several micrometres but can be limited to the region near the interface [23]. Therefore, the use of thin functional layers may be a promising approach both for lowering the effective operating temperature of SOCs and for enabling alternative architectures, such as metal-supported SOCs or micro-SOCs.

In the context of SOC research, there are limited examples in the literature of the use of praseodymium oxide as an oxygen electrode. Typically, symmetric measurements for tested material for oxygen electrodes are made with a constant gas flow – synthetic air or atmospheric air – within a fixed temperature range. Kamecki et al. investigated the effect of interlayer application on the performance of oxygen electrodes in the intermediate temperature range of Solid Oxide Cells. Oxygen electrodes made of $Sm_{0.5}Sr_{0.5}CoO_{3-\delta}$ (SSC), $La_{0.6}Sr_{0.4}CoO_{3-\delta}$ (LSC), $La_{0.6}Sr_{0.4}Co_{0.2}Fe_{0.8}O_{3-\delta}$ (LSCF), or Pr_6O_{11} (PrO_x), with thicknesses ranging from 400 nm to 600 nm, were prepared using the spray pyrolysis technique. In this study, the effect of annealing temperature was also evaluated within the range of 600 °C to 700 °C. Except for SSC, the remaining samples exhibited the lowest ASR (Area Specific Resistance) at an annealing temperature of 600 °C. Among the tested materials, praseodymium oxide showed the highest ASR values, though still approximately twice lower than the reference sample. These values were 0.245, 0.833, and 1.65 Ω·cm^2 at 600 °C, 550 °C, and 500 °C, respectively [24]. Aksoy et al. proposed the infiltration of a porous GDC ($Ce_{0.8}Gd_{0.2}O_{2-\delta}$) backbone with materials such as LSC, PrO_x, and an LSC: PrO_y composite in a 1:1 ratio. It was demonstrated that six infiltration cycles were optimal for achieving the best electrochemical performance, as determined by electrochemical impedance spectroscopy (EIS). For samples modified with praseodymium oxide and the PrO_y-LSC composite, the polarization resistance at 600 °C was 0.42 Ω·cm^2 for PrO_x, and 0.23 Ω·cm^2 for the composite of these two materials [25]. Nicollet et al. described an oxygen electrode based on a porous GDC backbone infiltrated with Pr_6O_{11} for intermediate SOCs. Infiltration was carried out by applying a 2 M PrO_x precursor solution to the electrode surface and placing it under vacuum for 2 min. This process was repeated until 30 wt% of the backbone was infiltrated (3–4 cycles). The final step involved annealing the samples at 600 °C for 2 h. The polarization resistance values obtained from symmetric measurements were 0.028 Ω·cm^2, 0.14 Ω·cm^2, and 3.5 Ω·cm^2 at 600 °C, 500 °C, and 400 °C, respectively [26]. Sharma et al. investigated the effect of sintering temperature on the microstructure of oxygen electrodes composed of Pr_6O_{11}, deposited via electrostatic spray deposition, for applications in intermediate-temperature solid oxide cells. Symmetrical studies revealed that the lowest polarization resistance at 600 °C was observed in samples where Pr_6O_{11} was annealed at 600 °C for two hours, with an LSM current collector (CC) layer of 30 μm thickness, yielding a value of 0.02 Ω·cm^2. Additionally, the sample annealed at 700 °C for two hours, with an LSCF current collector layer of 30 μm thickness, also exhibited low polarization resistance, measuring 0.022 Ω·cm^2 at the same temperature [27]. Nam et al. described the electrochemical deposition of PrO_x and (Pr,Ce)O_x nanoparticles as a method to enhance the performance of the LSM-YSZ composite electrode for intermediate temperatures fuel cells. Symmetrical measurements revealed that the lowest polarization resistance values were obtained for samples modified with PrO_x, followed by samples modified with (Pr,Ce)O_x, while the reference sample exhibited the highest polarization resistance. For the sample modified with PrO_x, a value of approximately 0.6 Ω·cm^2 was obtained, for the sample modified with (Pr,Ce)O_x, this value was around 2 Ω·cm^2, and for the reference sample, it was approximately 5 Ω·cm^2 at 650 °C [28]. Ge et al. demonstrated an enhancements in the performance of conventional oxygen electrodes (LSM, LSC, LSCF) after the addition of praseodymium oxide nanoparticles. These electrodes were modified with Pr_6O_{11} using the infiltration technique and then sintered at 800 °C for 2 h. The ASR values for unmodified electrodes were 2.46 ± 0.201, 1.103 ± 0.082, and 0.763 ± 0.011 Ω·cm^2 for LSM, LSCF, and LSC at 600 °C, respectively. For Pr_6O_{11}-infiltrated samples, these values were 0.284 ± 0.013, 0.482 ± 0.032, and 0.273 ± 0.011 Ω·cm^2, respectively, at the same temperature [29]. Kane et al. described the precise modification of the surface of an oxygen electrode made from LSCF with PrO_x using sol-gel deposition to form a bilayer. The best results were achieved after 75 cycles of PrO_x deposition. The polarization resistance (R_{pol}) at 600 °C for the modified sample was 0.117 Ω·cm^2, compared to 1.136 Ω·cm^2 for the LSCF alone. At 500 °C, the value was 0.991 Ω·cm^2, compared to 27.41 Ω·cm^2 for the reference sample. Samples subjected to 30 to 75 cycles also demonstrated the best stability during long-term measurements (220h) [30]. Lu et al. studied the infiltration of LSCF and STFC ($SrTi_{0.3}Fe_{0.55}Co_{0.15}O_{3-\delta}$) with PrO_x for intermediate- and low-temperature solid oxide cell applications. Symmetrical measurements demonstrated that modification with praseodymium oxide significantly enhanced the electrochemical performance of oxygen electrodes. For

unmodified LSCF, the R_{pol} values at 650 °C and 550 °C were determined to be 0.220 Ω·cm^2 and 2.05 Ω·cm^2, respectively. Infiltration improved these values to 0.556 Ω·cm^2 and 0.099 Ω·cm^2, respectively, at the same temperatures. For the STFC reference, the polarization resistance values were recorded as 0.552 Ω·cm^2 and 0.088 Ω·cm^2 at 550 °C and 650 °C, respectively. Modification with PrO_x reduced these values to 0.202 Ω·cm^2 and 0.067 Ω·cm^2 at the same temperatures, respectively. The oxygen electrodes exhibited very good stability over almost 1000 h at 550 °C and more than 1000 h at 650 °C [31]. Caizan-Juanarena et al. examined the influence of Pr_6O_{11} infiltration on the $La_{0.8}Sr_{0.2}MnO_{3-\delta}$-$Ce_{0.9}Gd_{0.1}O_{1.95}$ (LSM-CGO) oxygen electrode. At 650 °C, the polarization resistance for PrO_x-infiltrated samples was determined to be 0.03 Ω·cm^2 for CGO, 0.06 Ω·cm^2 for LSM-CGO, and 0.1 Ω·cm^2 for LSM alone. For Pr_6O_{11} directly deposited on CGO, this value was 0.125 Ω·cm^2, while for pure LSM, it was approximately 0.7 Ω·cm^2 at the same temperature [32]. As summarized in Table 1, the direct use of praseodymium oxide in research remains relatively uncommon. In most cases, PrO_x was employed as an infiltrating material for other oxygen electrode materials, while studies focusing on the pure/single-phase PrO_x electrode—particularly regarding its intrinsic electrochemical properties and activity in the oxygen reduction reaction (ORR)—are limited. Only rarely PrO_x were employed as the primary electrochemically active component of an oxygen electrode (e.g., Nicollet et al. and Aksoy et al.), and reports where PrO_x is used as a standalone oxygen-electrode layer are also scarce (e.g., Kamecki et al., Sharma et al. and Caizán-Juanarena et al.). The remaining cited studies—including those by Sharma et al., Caizán-Juanarena and Aksoy—use PrO_x as an admixture or as part of a composite electrode.

Comprehensive optimization of annealing temperature and thickness (or, in the case of infiltration, mass loading) for PrO_x is rarely reported in the literature. This is important because, as shown above, phase variability strongly influences the material's properties; therefore, controlling the thermal history may be crucial when PrO_x is used as a thin functional layer. Thickness optimization is also essential, both to maximize performance and to minimize material usage, given that PrO_x is relatively costly yet highly promising for intermediate- and low-temperature SOCs. This represents a notable gap in the current literature. Moreover, to the best of our knowledge, there are no systematic reports on the impact of humidity or CO_2 on PrO_x-based electrode performance, including resistance to poisoning and the ability to recover upon returning to initial conditions. Such data are highly relevant for practical deployment, as commercial systems typically operate on atmospheric air containing variable levels of H_2O and often non-negligible concentrations of CO_2.

This paper describes the research on the oxygen electrode in the form of praseodymium oxide thin film (200 nm). The material was characterized for electrical, electrochemical and structural properties. The electrode thickness was optimized, the effect of annealing temperature was investigated, the catalytic properties were thoroughly examined, and the impact of moisture on efficiency and stability was also evaluated.

Table 1
Comparison of polarization resistance values obtained in the literature using praseodymium oxide as material for oxygen electrode or for boosting electrode performance.

Material	Polarization resistance [Ω·cm^2]	Temperature [°C]	Reference
Pr_6O_{11}	0.245	600	[24]
PrO_x-CGO	0.42	600	[25]
LSC:PrO_x-CGO	0.23		
Pr_6O_{11}-CGO	0.028	600	[26]
	0.14	500	
Pr_6O_{11} with LSM as CC	0.02	600	[27]
	0.022		
Pr_6O_{11} with LSCF as CC			
LSM-YSZ – PrO_x	0.6	650	[28]
LSM-YSZ – (Pr,Ce)O_x	2		
LSM-PrO_x	0.284 ± 0.013	600	[29]
LSC-PrO_x	0.273 ± 0.011		
LSCF-PrO_x	0.482 ± 0.032		
LSCF-PrO_x	0.991	500	[30]
LSCF – PrO_x	0.556	650	[31]
STFC – PrO_x	0.067		
PrO_x	0.125	650	[32]
PrO_x – CGO	0.03		
PrO_x LSM-CGO	0.06		
PrO-LSM	0.1		
PrO_x	0.021	600	This work
	0.254	500	

2. Experimental

2.1. Sample preparation

The substrate for the deposition of the oxygen electrode layer consisted of pellets fabricated from $Ce_{0.8}Gd_{0.2}O_{2-\delta}$ (GDC-20 K or CGO, Daiichi Kigenso Kagaku Kogyo, Japan) powder. To prepare the pellets, 0.8 g of CGO powder was placed in a mold with a 16 mm diameter and compressed at a pressure of 98 MPa for 1 min. The resulting pellets were subsequently sintered in a box furnace at 1450 °C for 10 h. Following the sintering process, the pellets exhibited an average diameter reduction to around 13 mm. Both surfaces of the samples were polished using a semi-automatic polisher (Struers Tergamin-20) and then subjected to an additional annealing step at 1200 °C for 2 h.

The PrO_x precursor was prepared by dissolving $Pr(NO_3)_3{\cdot}6H_2O$ (99.9% purity, Alfa Aesar) in distilled water to achieve a concentration of 0.25 mol·dm^{-3}. To this solution, 2-butoxyethanol (99% purity, Sigma Aldrich) in a 1:1 volume ratio with water, and citric acid (99% purity, Chempur) at a molar ratio of 1:2 (TMI), were added. Additionally, 5 wt% of ethanol (99.8% purity, POCH) was incorporated. The mixture was heated on a hotplate at 100 °C with continuous stirring for approximately 15 min to evaporate most of the water and ethanol, reducing the solution volume by half. Prolonged heating was avoided to prevent the formation of a white precipitate. Once cooled to room temperature, the prepared precursor was used to synthesize powders for HT-XRD, XPS, XAFS and water uptake analyses and to fabricate PrO_x layers.

The deposition of the PrO_x oxygen electrode onto the pre-prepared CGO pellets was achieved using the spin-coating method (Laurell spin coater, model WS-400B-6NPP/LITE). A 6 µl of the PrO_x precursor was applied to the CGO surface, and excess solution was removed by employing a three-stage rotational speed sequence: 1000 rpm for 20 s, 3000 rpm for 30 s, and 5000 rpm for 30 s. After each layer application, the pellets underwent heat treatment on a hotplate, where they were sequentially heated at 90 °C, 180 °C, and up to 400 °C, with each temperature maintained for 15 min.

To investigate the effect of application cycles on layer thickness, samples were prepared with cycle counts ranging from 1 to 4. It was determined that 1 cycles results an oxygen electrode layer approximately 70 nm thick, while 3 cycles yielded a thickness of about 200 nm. Once the desired oxygen electrode thickness was achieved, the edges of the half-cells were polished to remove any residual PrO_x. The samples were then annealed in a box furnace (Carbolite RHF 16/8) at temperatures ranging from 400 to 900 °C for 2 h. A layer of LSC paste (Fiaxell) was applied to each pellet as a current collector and subsequently annealed at 400 °C for 2 h. The symmetrical cells thus prepared, featuring PrO_x oxygen electrodes on both sides, were utilized for further analysis.

2.2. Measurement methods

High-temperature X-ray powder diffraction data were collected using a Philips X'Pert Pro diffractometer equipped with an X'Celerator

detector. The measurements employed Ni-filtered Cu-Kα radiation, with wavelengths λ_1 = 1.54056 Å and λ_2 = 1.54439 Å, in flat-plate Bragg-Brentano geometry over the 2θ range 5–125°, in steps of 0.033°, with an effective count time of 50 s per step. High-temperature experiments were conducted using an Anton-Paar HTK 1200 high-temperature camera. Calibration was performed with a LaB_6 standard. Diffraction patterns were recorded in air at room temperature and at 50 °C intervals from room temperature up to 800 °C.

The temperature-dependent evolution of the local structure was monitored by in situ Raman spectroscopy. Measurements were conducted using a Renishaw inVia Reflex spectrometer equipped with an 1800 lines mm^{-1} grating. A 532 nm excitation laser was focused onto the sample through a 50× long working distance objective, yielding a spot size of approximately 1.5 μm. The laser power was limited to ~5 mW to minimize local heating. Spectra were acquired under a constant flow of dry synthetic air, while the sample was heated from 25 °C to 900 °C using a Linkam temperature-controlled stage.

The chemical composition of the surface of praseodymium oxide samples was analysed using High-Resolution X-ray Photoelectron Spectroscopy (XPS). The measurements were carried out using a Thermo Fisher Scientific Escalab 250 Xi spectrometer, equipped with a monochromatic Al Kα X-ray source. The pass energy was set to 20 eV, and the analysed area had a spot size of 650 μm in diameter. Charge compensation during measurement was achieved using a flood gun, which emitted low-energy electrons and Ar^+ ions (emission current: 150 μA; beam voltage: 2.1 V; filament current: 3.5 A). Spectral deconvolution and peak fitting were performed using the integrated Avantage software package (Thermo Fisher Scientific).

The X-ray absorption spectroscopy measurements at the Pr L_3-edge were conducted at the ASTRA beamline at the SOLARIS National Synchrotron Radiation Centre in Cracow, Poland. The white beam from the 1.3 bending magnet was monochromatized by a modified Lemonnier-type double crystal monochromator equipped with a Ge(220) crystal pair. At the sample position, the monochromatized beam had a size of 7 × 1 mm. The XANES and EXAFS spectra were collected in transmission mode, with the sample chamber and ionisation chambers filled with air at atmospheric pressure. The monochromator at the Pr L_3-edge was calibrated using a Cr foil from Exafs Company. During the set of the measurements of the samples of interest, the Cr foil was also measured as a reference sample in order to control the alignment of the collected spectra. For the measurements, the PrO_x powder was mixed with microcrystalline cellulose (Warchem, Zakręt, Poland) and uniform pellets of a diameter of 16 mm were made. In order to get a good edge step, the mass of the powders before mixing with cellulose was evaluated using the XAFSmass program. A further analysis of the spectra was performed using the Athena and Artemis software [33]. The crystallography data used to fit the calculated Fourier transform (FT) spectra was taken from the Crystallography Open Database (COD). FEFF files for fitting into the Artemis software have been prepared on the WebAtoms website.

The average oxidation state of praseodymium in PrO_x was determined using peak-area integration. The energy threshold E_0, incorporated within an arctangent function, was set at the inflection point—identified as the global maximum of the first derivative. The central point of the edge was located at the inflection point of the main absorption edge. The procedure and formulas used for determining the average oxidation state of the praseodymium cation is described in the supplementary materials.

DC electrical conductivity measurements of PrO_x material were conducted using the van der Pauw method. A thin praseodymium oxide layer, ~200 nm thick, was deposited on a quartz substrate via the spin-coating technique, similarly to the process used for samples prepared for symmetric measurements. Platinum wires were affixed to the outer edges of the sample using silver paste (DuPont 4922 N, USA). The measurements were carried out with a Keithley 2400 instrument (Cleveland, USA) and an automated data acquisition system. Two types of measurements were performed. The first set of measurements, to determine electrical conductivity, was conducted in a dry synthetic air atmosphere with a flow rate of 50 ml·min^{-1} across an annealing temperature range of 400 °C to 900 °C. Measurements were performed from the highest annealing temperature down to 300 °C in 50 °C steps. The second set investigated the effect of water vapor on the material's conductivity. In this case, measurements were performed at 500 °C at varying pH_2O levels of 0.1%, 0.5%, 1%, 2%, and 2.77% with the same gas flow level.

SEM investigations were performed using a Zeiss Merlin Gemini 2 high-resolution FEG-SEM microscope equipped with a Quantax 800 characteristic X-ray spectroscope (Bruker) with the use of secondary electron detector.

HT-XRD measurements were performed on a praseodymium oxide layer deposited on a CGO substrate using an X'Pert Pro MPD powder diffractometer (Malvern Panalytical) equipped with a Pixcel 1D detector. Cu Kα radiation was used as the X-ray source throughout the experiment. The instrument was configured with a Cu X-ray tube, a beta filter, and a monochromator optimized specifically for Cu radiation. The 2θ resolution was better than 0.089°, ensuring high precision in phase identification. Measurements were performed using both flat and spinner sample holders. An Anton Paar HTK 1200 N high-temperature stage was used to conduct in situ XRD analysis under ambient air conditions. Data were collected over a temperature range from room temperature to 800 °C in 50 °C increments. The heating rate was set to 6 °C/min.

Electrochemical impedance spectroscopy was used to measure the ohmic resistance (R_{ohm}) and polarization resistance (R_{pol}) of the symmetrical cells (PrO_x|CGO|PrO_x). The experiments were performed using Novocontrol Alpha-A mainframe with a 4-wire ZG4 interface (Montabaur, Germany). The measurements were conducted using an excitation amplitude of 25 mV across a frequency range from 3 MHz to 50 mHz. The samples were positioned in a compression cell, with gold meshes on either side ensuring electrical contact to platinum wires extending beyond the furnace. This technique was aimed to investigate the influence of the annealing temperature (AT), pO_2 and pCO_2.

The influence of annealing temperature within the range of 400 °C to 900 °C was examined through impedance measurements conducted between 600 °C and 300 °C in a synthetic air atmosphere, maintained at a flow rate of 50 ml·min^{-1}. For samples annealed at 500 °C, the maximum testing temperature was limited to 500 °C (500–300 °C) to avoid inducing additional changes or phase transitions during measurement. Similarly, the sample annealed at 400 °C was measured only in the range 400–300 °C. Two temperature ranges were identified within this measurement: from 600 °C to 400 °C, measurements were taken at 50 °C intervals, while from 400 °C to 300 °C, measurements were conducted at 25 °C intervals.

Measurements were also conducted at varying partial oxygen pressures (pO_2) of 1%, 3%, 5%, 10%, and 20%, maintaining a constant flow rate of 40 ml·min^{-1}. Prior to each measurement, the samples were stabilized in the selected pO_2 atmosphere for 3 h.

The Distribution of Relaxation Times (DRT) method was used for detailed analysis. For this purpose, the DRTtool Matlab GUI was used [34]. The DRT analysis was performed by choosing the C4 Matern method of discretization utilizing the 2nd order of the regularization derivative and a regularization parameter (λ) of 10^{-4}.

In addition, measurements were conducted at varying CO_2 concentrations (pCO_2). The experiments were performed at carbon dioxide levels of 0.04%, 0.1%, 0.5%, 1%, 2%, 3% and 5%, maintaining a constant flow rate of 50 ml·min^{-1}. Measurements were taken every 12 min, with gas compositions being changed every 2 h.

Thermogravimetric analysis (TGA) was used to determine the water uptake of praseodymium oxide. Measurements were performed using a Netzsch Jupiter® 449 F1 instrument (Selb, Germany) under a controlled humid atmosphere. A gas mixer equipped with humidifying and drying modules was used to precisely control the atmospheric composition. Prior to each measurement, a blank run was performed in both dry and

humid conditions to allow for accurate baseline correction. The procedure began by heating the sample (powder) to 700 °C at a rate of 5 °C·min^{-1} in 40 ml·min^{-1} air as purge gas and 20 ml·min^{-1} nitrogen as protective gas, and hold at this temperature for 300 min in dry air to remove any physically adsorbed water and carbon dioxide from the sample surface. The sample was then cooled to 500 °C in the dry atmosphere. After an 80-minute stabilization period, the purge gas was replaced with humidified air ($pH_2O = 2.3{\cdot}10^{-2}$ atm) for two hours of exposure. The last step of the measurement was performed after switching back to dry air.

The characterisation of the fuel cell was conducted within an Open Flanges V5 test configuration (Fiaxell Sàrl Technologies). The cell, was electrically interconnected by a nickel mesh from the fuel side and by a Au mesh from the oxygen electrode side. Subsequently, the cell was positioned within a Kittec furnace, which was equipped with a temperature controller with feedback control. The wires were connected to an IVIUM Vertex.2A for impedance and current–voltage (I-V) characterisation. The cell was heated to 600 °C for the reduction step and initial characterisation, after which it was cooled down to 500 °C and isothermally held. The fuel electrode was reduced in wet H_2 (100 ml·min^{-1}) which was used as a fuel supplied from the fuel side, and synthetic air (200 ml·min^{-1}) was delivered to the oxygen electrode as an oxidant. The cell's characterisation involved the measurement of Nyquist plots at OCV within a frequency range of 100 kHz – 0.1 Hz with an excitation potential of 25 mV. The assessment of cell performance entailed the measurement of current–voltage characteristics, while the cell's short-term stability was evaluated in galvanostatic mode at current densities of 100 mA·cm^{-2}. Commercial planar cells and half-cells from Elcogen were used in this study. Both the cells and the half-cells were anode-supported and consisted of a Ni–YSZ fuel electrode and an approximately 3 μm thick YSZ electrolyte. The full cell additionally included a CGO barrier layer and an LSC oxygen electrode.

3. Results

3.1. Structural characterisation

3.1.1. X-ray diffractometry

Fig. 1A presents the diffraction pattern obtained from high-temperature XRD measurements of PrO_x powder. The primary peaks were observed at 28° (111), 32.5° (200), 46.5° (220), 55° (311), 58° (222), 67.5° (400), 75° (331), and 78° (420), which were characteristic of all phases, but can be connected with cubic (*Fm-3m*) β-phase - Pr_6O_{11}. At room temperature, the presence of several phases was shown by the presence of longer tails at higher angular values in the main peaks at 28°, 33°, and 55°. This asymmetric broadening indicates the presence of the cubic (*Fm-3m*) α-phase – PrO_2 in samples annealed at temperatures not exceeding 400 °C. The remaining peaks were associated with the β-phase – Pr_6O_{11}. Additionally, the higher intensity than for the background at around 30° at low temperature range can suggest the existence of $Pr_2O_2CO_3$ [35]. Reaching temperature 300 °C results in the disappearance of this asymmetric broadening. Subsequently, at temperatures exceeding 500 °C, the Δ- and ε-phases should become detectable. However, the diffraction patterns of Δ- and ε-phases exhibit a shifts due to a smaller or irregular lattice constant, complicating their accurate identification due to temperature-induced spectral changes. Due to the high similarity of these phases of lattice constant, their precise identification relies on analysing specific peaks that serve as unique fingerprints. At the maximum temperature of 800 °C, additional peaks appear at 38°, 41°, 51.5°, 64.3°, and 65.7°. Although these peaks were of low intensity, they suggest the start of formation of the ι-phase (Pr_7O_{12}). Although XRD measurements provide qualitative information about the material, the changes occurring between successive phases were so small that a complete description of praseodymium oxide cannot be obtained. XRD indicates temperature-driven phase evolution of PrO_x at elevated temperatures. In particular, additional praseodymium oxide phases become detectable above ~500 °C and are present in a clearly

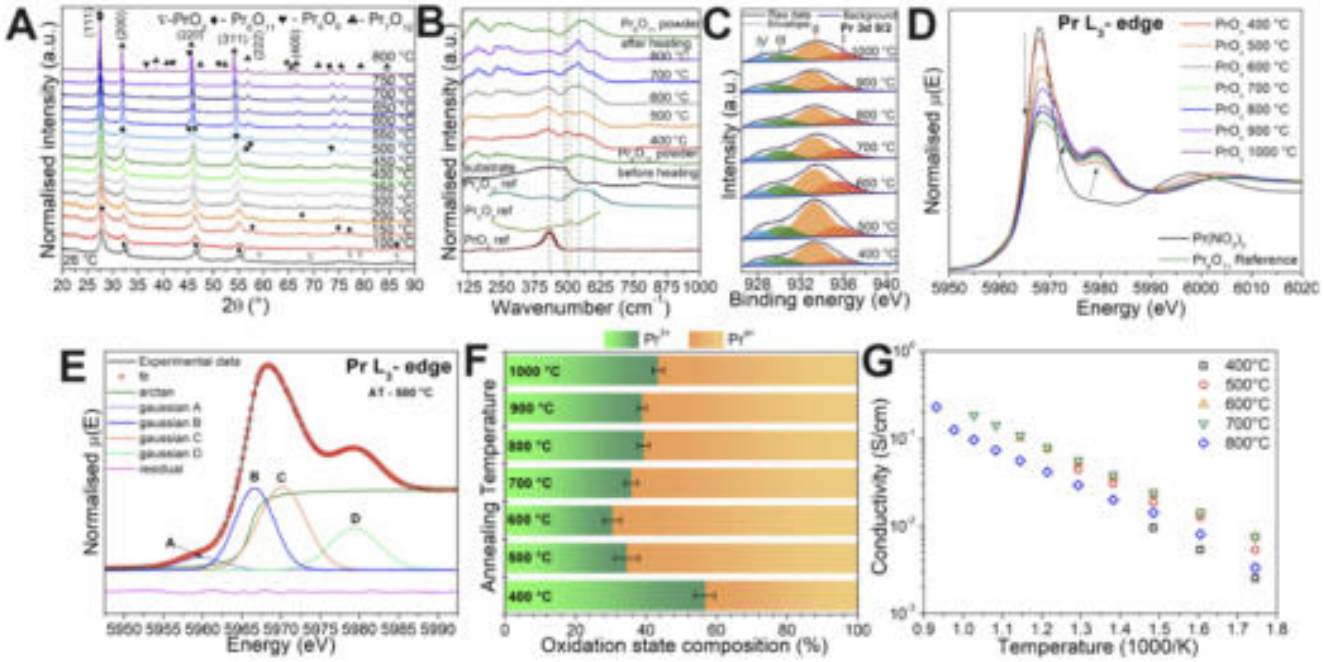


Fig. 1. High-temperature XRD of PrO_x powder annealed at 400 °C (A); Raman spectra for a praseodymium oxide layer deposited on fused silica and annealed to 800 °C, along with reference materials PrO_2, Pr_6O_{11} and Pr_2O_3 (B) XPS spectra for PrO_x powder annealed at various temperatures in the range from 400 to 1000 °C (C), Xanes spectrum collected for PrO_x powders annealed in the temperature range from 400 °C to 1000 °C (D); Example of fitting for Pr L_3-edge XANES spectrum using the peak fitting method (E); composition of praseodymium cations in the 3^+ and 4^+ oxidation state in the material (F); the total conductivity measured at various temperatures using the van der Pauw method (G).

observable amount at 800–850 °C. Such phase changes may modify the defect chemistry and transport properties of the electrode and can also affect microstructure (e.g., densification tendency), which may reduce the effective active surface area and diminish the beneficial impact of PrO_x on oxygen reduction properties.

3.1.2. Raman spectroscopy

Fig. 1B presents the thermal evolution of the Raman spectra of deposited praseodymium oxide layers recorded in the temperature range of 400–800 °C, alongside reference spectra of PrO_2, Pr_2O_3, and Pr_6O_{11}. The reference spectra were acquired from powder samples before and after annealing and are included for comparison.

At 400 °C, the spectrum consists of three broad vibrational bands centred at approximately 428, 499, and 555 cm^{-1}. The band near 428 cm^{-1} can be attributed to a Pr–O–Pr vibrational mode characteristic of PrO_2. Upon increasing temperature, the intensity of this mode progressively decreases, while features at ~540 and ~ 595 cm^{-1} become more pronounced—these are consistent with vibrational signatures observed in the spectra of Pr_6O_{11} powders. Concurrently, two distinct groups of broad modes become evident at lower Raman shifts: four modes below 200 cm^{-1}, and three in the 200–350 cm^{-1} range. These features have not been previously assigned in the literature and may be associated with defect-induced or symmetry-lowered vibrational modes.

3.1.3. X-ray photoelectron spectroscopy

To complement the data regarding the praseodymium oxide system, a series of XPS measurements were conducted for the Pr $3d_{5/2}$ (Fig. 1C) and O 1 *s* (Fig. S1A) regions on samples annealed within the temperature range of 400 °C to 1000 °C. Given the oxygen deficiency in PrO_x, and assuming a simplified model in which Pr ions are either eightfold or sevenfold coordinated by oxygen atoms, only three Pr ions per unit cell would exhibit full (eightfold) coordination. This highlights the inherent complexity of the praseodymium oxide system, stemming from the coexistence of multiple oxidation states and structural configurations [36]. The maxima observed at 928.1 eV (marked as IV), 930.25 eV (III), and 933.25 eV (II) correspond to intra-atomic interactions involving the $3d^94f^3$ and $3d^94f^2$ final states. These features were characteristic of both Pr^{4+} (as in PrO_2) and Pr^{3+} (as in Pr_2O_3) oxidation states [37]. Additionally, a peak at 935.6 eV (I) was observed. The survey XPS spectrum with focus on Pr $3d_{5/2}$ and Pr $3d_{3/2}$ region with peak and satellite structures labelled according to their electronic origin as according to work Seifarth et al. [38] was presented in Fig. S1B and C. This reveals a further maximum at approximately 944 eV and 968.1 eV, corresponding to the duplet $3d^94f^1$ state configuration. Although this feature was not specific to a single oxidation state, its intensity increases with a higher concentration of Pr^{4+} species [38,39]. For the O 1 s spectra recorded for the same samples, the main features were observed at 528.5 eV (marked as I), which, according to the literature, may be associated with a mixed oxidation state of praseodymium, although a clear mechanistic explanation for this binding energy remains unexplained. Additional peaks were present at 531.3 eV (marked as II), typically attributed to praseodymium oxide [36], and at 532.9 eV, which corresponds to O—H bonds (marked as III) [37]. All of the spectra obtained correspond to those observed in the literature [36–40]. Notably, the signal at 532.9 eV, attributed to surface hydroxyl groups, shows a distinct increase in intensity for the sample annealed at 1000 °C, whereas it remains relatively constant across the remaining temperature conditions. Observed a weak peak for $3d_{3/2}4f^1\underline{L}$ at 968 eV that can be observed only when praseodymium exists in the 4^+ oxidation state, on mixed oxidation states of praseodymium and PrO_2, suggesting the existence of many oxygen vacancies in the analysed material. XPS measurements give a deeper understanding of praseodymium oxide, with the detection of additional compounds that coexist with the final material. That provided important information for further research, especially in the electrochemical studies.

3.1.4. X-ray absorption fine structure

To precisely determine the effect of the annealing temperature and to accurately describe the material, XAFS measurements were performed on the same powders. Fig. 1D presents the XANES spectra at the Pr L_3 edge for PrO_x samples annealed at temperatures ranging from 400 °C to 1000 °C. For comparison, reference spectra of $Pr(NO_3)_3$, where praseodymium exists only in the 3^+ oxidation state, and Pr_6O_{11}, where Pr should exhibits an average oxidation state of 3.67^+, are also included.

In the case of the praseodymium nitrate reference, a distinct peak at 5966 eV was observed, indicative of Pr^{3+}. All PrO_x samples exhibit a slight shift towards higher energies, which was expected due to the coexistence of both Pr^{3+} and Pr^{4+} within the compound's structure. Additionally, a component (a peak at 5970–5971 eV) emerges on the high-energy slope, alongside a third contribution appearing at 5979 eV. These features were characteristic of Pr^{4+} states, specifically associated with the $4f^1$ and $4f^2\underline{L}$ electronic configurations. Initially, as the annealing temperature increases, the intensity of the first peak, corresponding to Pr^{3+}, decreases, while the second and third peaks, associated with Pr^{4+}, become more pronounced. This trend continues up to an annealing temperature of 800 °C, beyond which the intensity of the first peak begins to rise again. Determination of average oxidations states of praseodymium cations were modelled by the sum of three Gaussian functions and an arctangent function representing the stepped edge of the continuum excitations. The edge position E_0 was defined as the inflection point of the absorption edge, i.e., the maximum of the first derivative $d\mu/dE$, consistent with the arctangent function - description of the edge step. The Gaussian A corresponds to the pre-edge region. The Gaussian B (peak: 5966 eV) shows the excitation from $2p_{3/2}$ to $4f^2$ $5d^*$, representing Pr^{3+} ions. $5d^*$ refers to the presence of an excited electron in the 5d band [41]. The remaining Gaussian C and D (peak 5970–5971 eV and peak 5979 eV) show excitations from $2p_{3/2}$ to $4f^2\underline{L}$ $5d^*$ and to $4f^3$ $5d^*$, $\underline{L}$ being a ligand hole in the O 2p orbital, both representing Pr^{4+} ions [42–45]. Table S1 shows the results values of the average Pr oxidation state obtained for the fitting method used. Example fit obtained using the peak fitting function for PrO_x annealing temperature of 500 °C shown in Fig. 1E. In addition, Fig. S2 shows the fits performed on each type of the XANES spectra analysed, and Fig. 1F shows the oxidation state composition for praseodymium. At the annealing temperature of 400 °C, the average oxidation state was determined as $3.433^+ \pm 0.144$. This value differs significantly from the literature suggestions and the possible occurrence of the α-phase PrO_2 mixed with β-phase Pr_6O_{11}. This may be due to the occurrence of the $Pr_2O_2CO_3$, $Pr(OH)_3$ compounds (confirmed with XRD and XPS measurements), described in the literature as impurities present after synthesis at such low temperatures, where the Pr cation occurs in the 3^+ oxidation state together with the presence of the target Pr_6O_{11} and probably PrO_2 oxides [46,47]. This means that the temperature of 400 °C may not be sufficient for fully efficient synthesis of pure praseodymium oxide. At an annealing temperature of 500 °C, the average Pr oxidation state was $3.655^+ \pm 0.171$, which was almost nominal and consistent with the literature [36]. A slow decrease in the average oxidation state was observed above the AT above 600 °C and at an annealing temperature of 1000 °C the average oxidation state was already $3.566^+ \pm 0.080$. This was probably due to the formation of the new phases described above, such as the δ-phase Pr_3O_9 (average oxidation state 3.6^+) and ι-phase Pr_7O_{12} (3.43^+), and the existence of a high content of $Pr(OH)_3$ confirmed by XPS. The results obtained also indicate the simultaneous occurrence of many phases, since no straightforward results were obtained by XRD and XAS, and the occurrence of different phases was allowed.

Fig. S3 shows the k-space oscillation and Fourier transform (FT) ($k^2\chi(k)$) EXAFS spectra for the reference materials and PrO_x samples annealed at different temperatures (with phase correction), along with the spectral fit for the annealing temperature of 500 °C (B—C). For comparison, Fig. S3D shows the fit obtained when attempting the same

procedure with the scattering path data for the Pr_6O_{11} phase only. The first maximum, corresponding to the nearest oxygen atom, appears at a radial distance of approximately 2.2 Å. The asymmetrical shape of this peak indicates that the Pr—O bond was not only associated with Pr_6O_{11} phase but also with other phases presence in the material. The distinct tail observed in samples annealed at 400 °C and 500 °C—indicating a bond length shorter than predicted by theoretical models—may result from multipath scattering effects. The second peak, located at approximately 2.7 Å, was well-defined and has been associated with the presence of a Pr—O bond in the form of Pr_2O_3, indicating the presence of praseodymium in the 3^+ oxidation state. A trend of increasing intensity with rising annealing temperature can be observed, indicating the increase of Pr^{3+} content in the material. A subsequent peak at 3.9 Å was identified and designated as the Pr—Pr bond. Also in this case, the peak was also comprised of multiple peaks, as evidenced by the presence of an extended tail at higher radial distances. These findings support the hypothesis of the simultaneous presence of multiple praseodymium oxide phases, emphasizing the importance of precise control over the composition of the material.

3.1.5. DC conductivity

The DC electrical conductivity of the praseodymium oxide was measured for a PrO_y layer approximately 200 nm thick, deposited on a quartz substrate. The measurements were conducted in the temperature range from the maximum tested temperature down to 300 °C in an air atmosphere (e.g. sample annealed at 500 °C was tested in the range of 500–300 °C). The results were presented in Fig. 1G, alongside a comparison of the values obtained at the lowest maximum temperature of 400 °C (Fig. S4). The lowest conductivity, $9.58{\cdot}10^{-3}$ S·cm^{-1}, was observed for the sample annealed at 400 °C. With increasing annealing temperatures, the conductivity systematically increased, reaching a maximum value of $2.41{\cdot}10^{-2}$ S·cm^{-1} for a sample annealed at 700 °C. At the same time, at a temperature of 700 °C, the electrical conductivity of this material was $1.84{\cdot}10^{-1}$ S·cm^{-1}. Notably, a significant decrease in conductivity was observed at 800 °C, which was likely attributable to start the formation of the ι-phase (Pr_7O_{12}). According to the literature, this phase exhibits lower conductivity compared to other praseodymium oxide phases [21]. Attempts to measure conductivity at 900 °C revealed a pronounced and consistent reduction in conductivity, to the extent that noise rendered reliable calculations infeasible. The highest activation energy value was obtained for the sample annealed at 400 °C and it was 0.44 eV. For the remaining annealing temperatures this value was 0.40 eV, 0.38 eV, 0.38 eV and 0.39 eV for 500 °C, 600 °C, 700 °C and 800 °C, respectively.

The achieved values were compared with the literature. Thangadurai et al. reported a total 1.4 S·cm^{-1} at 850 °C for a pellet made of commercial Pr_6O_{11} annealed at 1000 °C for 24 h and then annealed at 350 °C for additional 24 h. The corresponding activation energy was 0.52 eV/per atom. Moreover, it was assumed that β-phase has a total conductivity of $6.77{\cdot}10^{-2}$ S·cm^{-1} at 400 °C [22]. Hassan et al. reported a conductivity of 0.954 S·cm^{-1} at 850 °C for PrO_y samples prepared from nanorods. These nanorods were synthesized at 500 °C for 2 h. The activation energy was determined to be 0.504 eV [48]. Vshivkova et al. demonstrated a conductivity of approximately 1 S·cm^{-1} at around 800 °C for praseodymium oxide, both in the ceramic sample and in the film. The activation energies were 0.44 eV and 0.42 eV, respectively [49]. Abu-Zied investigated the effect of annealing temperature on the electrical conductivity of praseodymium oxide. Based on the available data, the highest conductivity value, approximately $1{\cdot}10^{-2}$ S·cm^{-1}, was observed at 400 °C for a sample annealed at 500 °C [50]. Arakawa et al. reported an electrical conductivity of approximately $1{\cdot}10^{-2}$ S·cm^{-1} at a temperature slightly below 400 °C and approximately $1.8{\cdot}10^{-1}$ S·cm^{-1} at a temperature slightly above 700 °C. The measurements were conducted on a PrO_x layer with a thickness of 1 μm [51].

The obtained results are consistent with the data available in the literature. A slightly lower activation energy was observed compared to those reported in the mentioned studies, with the value approaching those described in Vshivkova's work [49]. The electrical conductivity values at 700 °C are also in close agreement with those reported, for instance, by Arakawa and Abu-Zied [50,51]. The only notable discrepancy was observed in the high-temperature range (above 800 °C), where values of approximately 1 S·cm^{-1} were reported, which probably were not be achieved in this case. Nevertheless, both the activation energies and the conductivity values below 800 °C were similar to those obtained in the cited works.

3.2. Thickness optimization

The optimization of parameters for the oxygen electrode based on praseodymium oxide began with determining the optimal electrode thickness. For this purpose, samples with thicknesses of approximately 70 nm, 100 nm, 200 nm, and 300 nm were prepared, corresponding to 1, 2, 3, and 4 spin-coating cycles, respectively. The samples were annealed at 600 °C for two hours, according to the description of sample preparation available in the literature [24,26]. The effect of layer thickness on the electrochemical reaction efficiency was assessed through a series of symmetric measurements using electrochemical impedance spectroscopy (EIS).

Fig. S5 illustrates the calculated values of ohmic resistance (Fig. S5A) and polarization resistance (Fig. S5B), alongside Nyquist plots for individual samples (Fig. S5C) and a comparative analysis of polarization resistance as a function of electrode thickness (Fig. S5D). The measured ohmic resistance values were 41.88, 28.24, 24.56, and 24.97 Ω·cm^2 for samples with thicknesses of 70 nm, 100 nm, 200 nm, and 300 nm, respectively measured at 500 °C. The sample with the lowest electrode thickness (70 nm) exhibited the highest ohmic resistance, while the remaining samples showed relatively similar values, with the lowest ohmic resistance observed for the sample with the electrode thickness of 200 nm.

At 500 °C, the polarization resistance values were determined as 14.74, 0.774, 0.446, and 0.917 Ω·cm^2 for samples with electrode thicknesses of 70 nm, 100 nm, 200 nm, and 300 nm, respectively. The highest polarization resistance was observed for the sample with the thinnest oxygen electrode, mirroring the trend observed for ohmic resistance. A reduction in polarization resistance was noted with increasing thickness, reaching its minimum value at 200 nm. This trend may be attributed to an increase in the active surface area of the electrode. However, further increasing the electrode thickness beyond 200 nm did not yield additional improvements; instead, the polarization resistance increased. This behaviour may be associated with the low electrical conductivity of the material, combined with the attainment of maximum transference numbers at relatively low temperatures for electrolyte material - CGO.

3.3. Annealing temperature optimization

The next step involved determining the optimum annealing temperature, a parameter that significantly influences grain size and, consequently, the active surface area and porosity of the electrode. Furthermore, as previously demonstrated, the annealing temperature also affects the electrical and structural properties of the material.

Fig. 2 presents the Arrhenius plot for ohmic resistance, shown as the average value obtained from three samples (A), the Arrhenius plot for polarization resistance (B), Nyquist plots measured at 400 °C (2C), and a comparison of R_{pol} values determined at 400 °C as a function of annealing temperature (D). In symmetric cell stability tests, the R_{ohm} value is dominated by the electrolyte, however, the EIS-derived real intercept represents the effective series resistance and may contain additional components such as electrode contact/interface resistance and collector/current lead resistance. To enable comparison across all tested AT temperatures, the measurements were compared at 400 °C, the lowest tested annealing temperature. The highest ohmic resistance

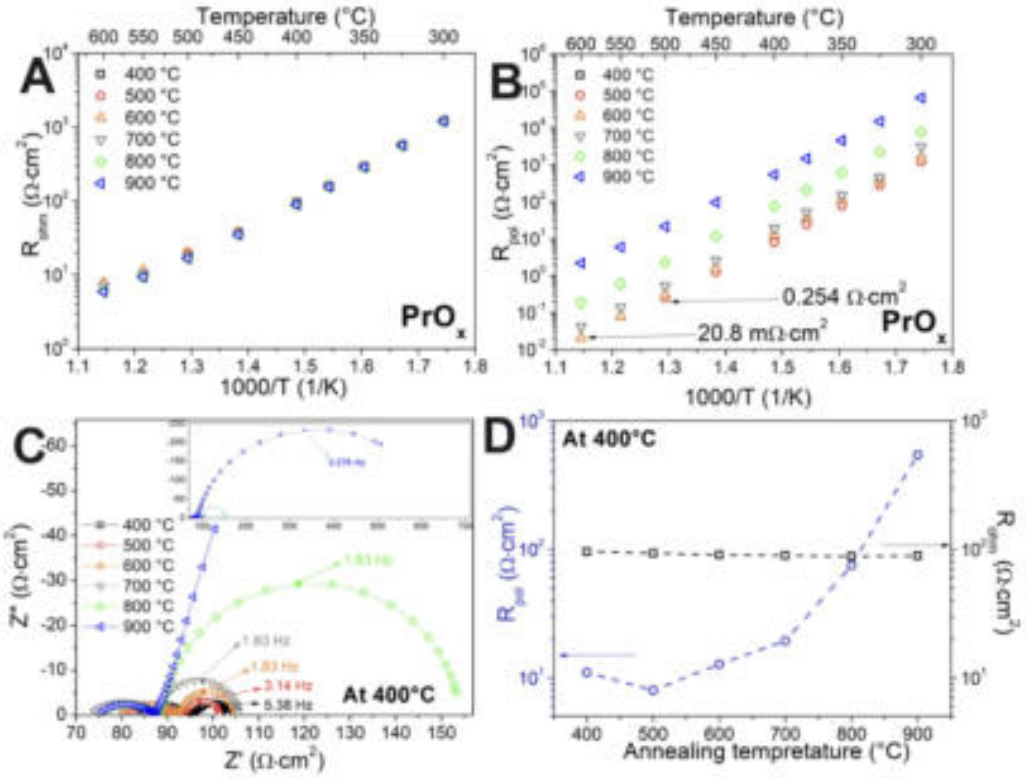


Fig. 2. The Arrhenius plot of the ohmic resistance (A) and polarization resistance (B) obtained from symmetric measurements of half-cells with annealing temperatures. Additionally, the Nyquist plots collected at 400 °C (C), along with a comparative analysis of R_{ohm} and R_{pol} values as a function of annealing temperature (D).

was observed for the sample annealed at 400 °C, with a value of 96.26 Ω·cm^2. As the annealing temperature increased, the R_{ohm} values decreased, measuring 93.37, 90.70, 89.68, 88.26, and 89.12 Ω·cm^2 for annealing temperatures (AT) of 500, 600, 700, 800, and 900 °C, respectively. This trend is commonly observed and can be attributed to improved bonding between the electrode and electrolyte at higher annealing temperatures.

For polarization resistance, the measured values (at 400°C) 11, 8.02, 12.76, 19.37, 75.05, and 545.91 Ω·cm^2 for ATs of 400, 500, 600, 700, 800, and 900 °C, respectively. These results indicate that the optimal annealing temperature was determined as 500 °C, corresponding to the presence of β and δ phases—recognized as the most active forms of praseodymium oxide. Beyond 700 °C, a significant increase in R_{pol} was observed, likely due to the formation of the ι-phase, which exhibits considerably lower conductivity. Particularly noteworthy were the polarization resistance values obtained at 500 °C (AT 500 °C) and 600 °C (AT 600 °C), measured at 0.254 Ω·cm^2 and 0.0208 Ω·cm^2, respectively. These values are comparable to the best results for PrO_x described in Nicollet et al.'s work [26] and Sharma et al.'s work [27].

Additionally, Fig. S6 presents SEM images of the sample surfaces annealed at temperatures ranging from 400 °C to 900 °C. Given the low thickness of the oxygen electrode, electrolyte grains are also visible in the SEM images. In the annealing temperature range of 400 to 600 °C, no significant structural changes were observed. Grain growth was not detected, and the grains remain indistinguishable due to their very small size. Significant structural changes in the electrode become apparent starting at an annealing temperature of 700 °C. At this temperature, the electrode densifies, and small voids appear at the grain boundaries of the underlying electrolyte grains. At 800 °C, these grain boundaries become clearly visible, and the PrO_x layer begins to rupture. Despite this, agglomerates of electrode material remain visible. By 900 °C, the grain boundaries are barely discernible, and the electrode layer was completely degraded. This degradation was attributed to the dissolution of praseodymium oxide into ceria. Initial signs of this phenomenon were evident at 700 °C, though it could also occur at lower temperatures at a much slower rate. Changes in the oxygen electrode's microstructure have a substantial impact on its efficiency. The observed increase in polarization resistance, particularly at higher temperatures, can be also explained by the material's dissolution into the electrolyte.

To validate the hypothesis, high-temperature XRD measurements were conducted on the PrO_x layer deposited on a CGO pellet. Fig. S7 presents the diffraction patterns obtained for heated sample, with focusing on the range between 25° and 35°. The peaks from CGO closely align with those from PrO_y, resulting in significant overlap. Below 50°, the peaks exhibit asymmetry, further supporting the overlap of these signals. However, above 50°, the peaks begin to separate, making their identification more straightforward.

No significant changes in the diffraction pattern were observed up to 500 °C. However, at 600 °C, new diffraction peaks begin to emerge. In particular, a peak at 32.5° becomes visible, and its intensity increases substantially, reaching a level comparable to that of the peak at 33° (indexed as 200) by 1000 °C. This 33° peak reflects contributions from both CGO and PrO_x phases. Notably, the relative intensity of this peak decreases progressively with increasing temperature. Additionally, from 700 °C onwards, new peaks appear at 29.5° and 28°. The emergence of these peaks at lower angles than the primary ones indicates the formation of a distorted CGO unit cell, characterized by enlarged lattice parameters. Analysis of the unit cell size reveals an increase from 5.4228 Å for CGO substrate to 5.5103 Å upon the dissolution of PrO_x into the ceria. The increase in unit cell size results from replacing Gd^{3+} gadolinium cations with Pr^{3+} cations because the atomic radius of the trivalent praseodymium cation (1.13 Å) is larger than that of gadolinium (1.05 Å). This difference in atomic radius arises from the lanthanide contraction, a phenomenon in which the atomic radius decreases with

increasing atomic number across the lanthanide series, while the cation valence remains constant. These findings are consistent with the majority of existing literature [52,53]. However, some reports have observed the opposite trend [54–56]. This discrepancy is likely related to the specific synthesis method employed and the availability of praseodymium cations in either the 3^+ or 4^+ oxidation state [52].

These observations suggest that high-temperature annealing induces crystallographic heterogeneity within the material. Although PrO_x–CGO interdiffusion is expected to be thermally activated and therefore much slower at 500 °C than at higher temperatures, it cannot be excluded over very long operation times. Consequently, at least two factors appear to contribute to the observed increase in polarization resistance: structural degradation and phase dissolution.

Furthermore, regardless of the substrate—whether the samples were deposited on CGO or quartz for conductivity measurements—a characteristic feature of PrO_x was its inability to create porosity. Interestingly, lower annealing temperatures appear to have a beneficial effect on this property, as naturally occurring microporosity enhances electrode performance.

Taking all factors into consideration, samples annealed at 500 °C were chosen for further investigation. Nevertheless, additional measurements were also conducted at 600 °C to provide a basis for comparison and to enable a more comprehensive discussion.

Taking the structural and electrochemical results together, several conclusions can be drawn. As noted above, the most electrochemically active PrO_x material is obtained for the β- phase assemblage, which is stable up to approximately 470 °C. With increasing annealing temperature, further phase evolution occurs (e.g., towards the ι-phase), accompanied by a decrease in electrical conductivity. XRD provides qualitative evidence of these changes up to 800 °C: the first indications of additional phase formation are already observed at 500 °C, while the iota-related reflections become clearly visible at 800 °C. These trends are consistent with Raman spectroscopy. The samples annealed at 400 and 500 °C show the strongest band at 428 cm^{-1}, indicating the highest PrO_2-related contribution, which gradually diminishes at higher temperatures. In addition, a noticeable Pr_2O_3 contribution is present in the 400 and 500 °C samples and becomes less pronounced upon annealing at higher temperatures, consistent with phase re-equilibration. The evolution of phase composition is further supported by XAS: in the 500–600 °C range the highest average Pr oxidation state is observed, and it decreases progressively with increasing annealing temperature. For the 400 °C sample, the PrO_x powder may not be fully equilibrated and may contain additional short-range ordered or poorly crystalline components not resolved by XRD; this is consistent with a lower average Pr oxidation state (higher Pr^{3+} fraction) and a more defect-rich, chemically complex system. The trend in average Pr oxidation state, approaching the value expected for Pr_7O_{12} at high annealing temperature, correlates well with the conductivity results. Above 700 °C, the electrical conductivity decreases significantly, deviating from the initial increase observed at lower annealing temperatures. These structural and transport changes are also reflected in the EIS data: the best electrochemical performance is obtained for the 500 °C annealed sample, with comparable but inferior results for 400 and 600 °C. Above 500 °C, R_{pol} increases systematically, which is consistent with the phase transformations evidenced by the structural characterisation and may also be exacerbated by partial dissolution and densification of the PrO_x layer on the CGO surface. All these conclusions are consistent with the assumption that the effect of the annealing temperature is very important for the structural structure of PrO_x and, consequently, for the electrochemical activity of the material in terms of oxygen reduction reactions.

3.4. Detailed EIS analysis

3.4.1. pO_2 influence

A detailed analysis of Nyquist plots was conducted to identify the factors limiting the efficiency of the PrO_x oxygen electrode. Fig. 3A presents the values of ohmic resistance, while Fig. 3B depicts the polarization resistance values obtained from measurements performed at oxygen partial pressures (pO_2) ranging from 1% to 20%. Fig. 3C illustrates the Nyquist plots measured at 500 °C, excluding ohmic resistance. The polarization resistance values were determined to be 0.41, 0.42, 0.65, 0.83, and 1.33 Ω·cm^2 for pO_2 levels of 20%, 10%, 5%, 3%, and 1%, respectively. Notably, there was no significant change in R_{pol} values between 10% and 20% pO_2. However, at lower pO_2 levels, a marked increase in polarization resistance was observed.

Fig. 3D–F presents the DRT analysis for spectra collected at 500 °C, 450 °C, and 400 °C. According to the literature, in the case of mixed ionic-electronic conductors, DRT analysis allows for the identification of at least three subprocesses occurring at the oxygen electrode. These include charge transfer at the electrode/electrolyte interface, which typically occurs at high frequencies and was designated as P1. The P2 process encompasses various electrode phenomena associated with surface oxygen exchange kinetics and oxygen ion diffusion, including the adsorption of molecular oxygen, O_2 dissociation, and charge transfer diffusion, predominantly occurring in the medium-frequency range. The P3 process, observed at the lowest frequencies, is attributed to gas diffusion within the porous oxygen electrode [14,57–60]. Importantly, P1–P3 are assigned based on their high−/medium−/low-frequency character, and their peak positions may shift with temperature and gas composition due to changes in the characteristic relaxation times.

For measurements conducted at 500 °C, well-separated peaks corresponding to the aforementioned P1, P2, and P3 processes can be distinguished. The P1 subprocess, associated with charge transfer at the electrode/electrolyte interface, shifts towards higher frequencies as pO_2 increases. Similar trends are observed at 450 °C, albeit to a lesser extent at 400 °C. In addition to peak-position shifts, changes in peak intensities are observed. In particular, the P1 intensity/area shows only a weak dependence on pO_2 and temperature, consistent with a predominantly thermally activated interfacial process. Conversely, the P2 process involves the adsorption of molecular oxygen. This is reflected in a significant decrease in peak intensity with increasing pO_2. Additionally, this process exhibits a pronounced temperature dependence. These measurements suggest the presence of complex processes that can be described by the de Levie element, incorporating diffusion impedance. This phenomenon occurs in porous electrodes and describes diffusion in finite pores, where mass transport is more intricate [61–63]. The P3 process, predominantly associated with gas diffusion, was most prominent at 500 °C, where a strong dependence on pO_2 is observed; at the highest oxygen concentrations, this value was significantly reduced. At a temperature 50 °C lower, the gas diffusion peak becomes nearly imperceptible and has a negligible impact on the efficiency of the oxygen electrode. At 400 °C, this process is no longer detectable within the measured frequency window. The absence of a gas diffusion component at lower temperatures can be correlated with the limited catalytic activity of the electrode material, which causes the rate-limiting electrochemical reaction to occur only on the electrode surface. Additionally, this may be influenced by the limited ionic conductivity of the electrolyte and possibly masked by other processes, which may shift the process to frequencies lower than the measurement range.

3.5. pH_2O influence

Praseodymium oxide was also examined regarding the effect of water as a poisoning factor for the oxygen electrode. This material, particularly in its beta form, exhibits a strong affinity for binding water at low temperatures, as reported in the literature [47,64]. According to Netz et al., this process is reversible, and water is released from the oxide structure at 350 °C [47]. In most studies, the loss of water was discussed primarily in the context of material synthesis [21,47,64]. However, Kim et al. described a gas sensor (designed for acetone detection) based on iridium oxide with added praseodymium oxide that demonstrated

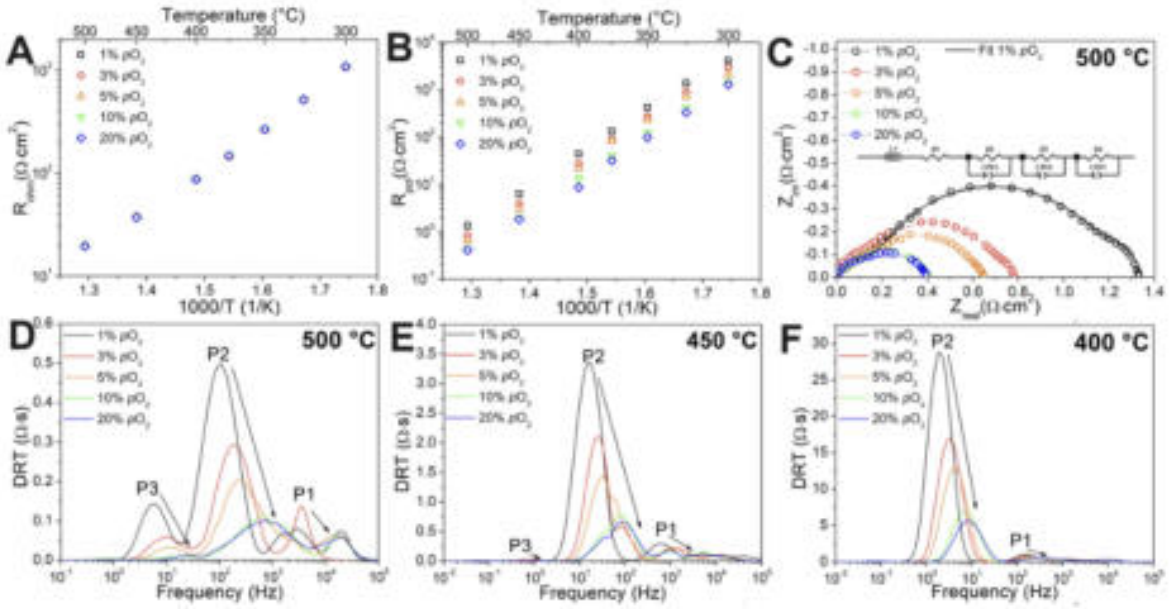


Fig. 3. Arrhenius plots of ohmic resistance (A) and polarization resistance (B) measured at different pO_2, along with Nyquist plots excluding ohmic resistance, along with the equivalent circuit used to fit the Nyquist spectra in this work and an example of the fit (C), and graphs presenting the DRT analysis at 500 °C (D), 450 °C (E), and 400 °C (F).

insensitivity to water poisoning [65]. Nevertheless, there is no information regarding the high-temperature effects of water vapor on this material. This is a critical gap, as atmospheric air, rather than synthetic air, is typically used in practical applications such as SOCs stacks.

The sensitivity of the state of the art materials commonly used as oxygen electrodes, such as LSM and LSC to the presence of water vapor was already confirmed in the literature. As demonstrated in the study by Nielsen et al., investigating the effect of moisture on the degradation of LSM:YSZ cathodes, the changes induced by exposure to water vapor were partially irreversible. This degradation manifests as an increase in the polarization resistance associated with the high-frequency semicircle, accompanied by a decrease in the corresponding capacitance. Such behaviour indicates impaired oxide ion transfer at the LSM/YSZ interface, most likely due to the initial stages of LSM decomposition. During long-term operation under humid conditions, interfacial degradation progresses to the point where a permanent loss of contact between the LSM and YSZ phases is observed. This is accompanied by a significant increase in ohmic resistance as well as in the resistances of both the high- and low-frequency semicircles. Upon the removal of moisture, a partial reversal of these effects occurs, reflected in a decrease in the resistance of the high-frequency semicircle and a partial recovery of the lost performance [66].

A similar phenomenon has been reported for LSC electrodes. In the study by Hayd et al., the influence of water vapor and CO_2—factors known to inhibit electrochemical oxygen reduction—was investigated. For exposure to CO_2, full reversibility of performance degradation was demonstrated after 10 h. However, as in the case of LSM, exposure to water vapor resulted only in partial reversibility of the degradation process [67]. Hjalmarsson et al. suggested that this behaviour may be attributed to the formation of strontium hydroxide ($Sr(OH)_2$) on the electrode surface. The formation of such species leads to the occupation of active sites by hydroxyl groups, thereby reducing the number of sites available for oxygen reduction and accelerating the overall degradation of the electrode. This irreversible binding with hydroxyl ions clearly compromises electrochemical efficiency and limits the extent of performance recovery after moisture exposure [68].

Fig. 4A illustrates the dependence of the PrO_x electrical conductivity on pH_2O. The gas compositions were alternated every 2 h to properly see the effect of water vapor. The initial conductivity of approximately $2.7 \cdot 10^{-2}$ S·cm^{-1} gradually increased, and switching to 0.1% or even 0.5%pH_2O did not significantly impact the conductivity, despite a slight decrease observed after the 0.1% stage. A pronounced and nearly immediate reduction in conductivity, to $1.7 \cdot 10^{-2}$ S·cm^{-1}, occurred only upon switching to 1%pH_2O. Following this, a gradual increase in

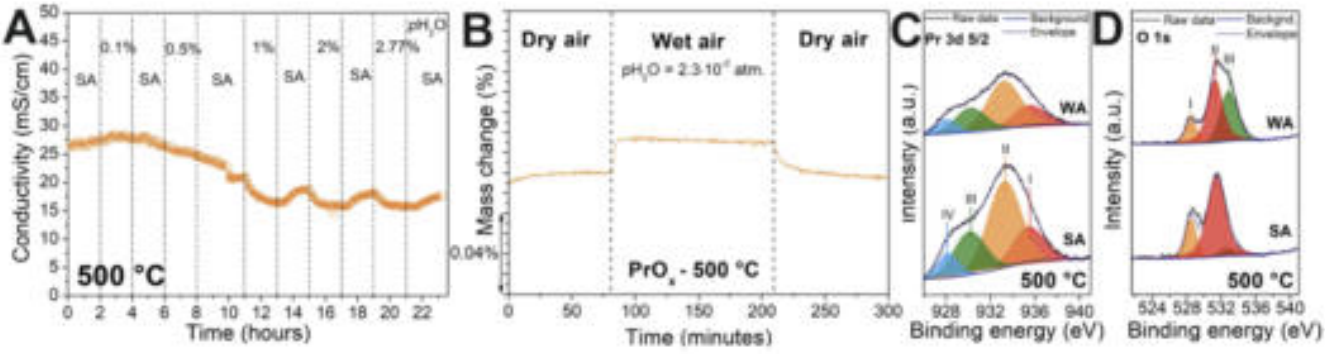


Fig. 4. DC electrical conductivity at 500 °C, determined by the Van der Pauw method at varying pH_2O (A), water uptake measurement made for praseodymium oxide powder at 500 °C (B) and XPS spectra for Pr $3d_{5/2}$ (C) and O 1s (D) after exposure to humid air for 10 h and drying for another 10 h.

conductivity was observed after switching to synthetic air. Interestingly, the transition to SA did not result in an immediate effect. Instead, the change in conductivity occurred only after a significant delay. Notably, the conductivity did not return to its initial value, likely due to the delayed release of water from the praseodymium oxide structure.

pH_2O concentrations of 2% and 2.77% caused no substantial changes in conductivity. Although the measured values were slightly lower, the differences were minimal, within $1{\cdot}10^{-3}$ S·cm^{-1}. However, an extended delay in the onset of water molecule release from the PrO_x structure was observed.

These findings suggest the occurrence of local chemical reactions involving water, which may simultaneously affect electron carriers. Additionally, water absorption on the material's surface cannot be excluded, potentially forming a slightly more resistive layer.

To further investigate the effect of water vapor on the material, thermogravimetric measurements were performed. Fig. 4B presents the result obtained at 500 °C. Upon the introduction of water vapor, a mass increase of approximately 0.02% was observed for praseodymium oxide, which quickly stabilized. Switching back to dry air led to a relatively rapid removal of the attached water molecules, and after about one hour, the mass returned to its initial value. These findings suggest that the process is dominated by hydration rather than hydrogenation. In order to assess whether the measured mass gain corresponds to a physically reasonable amount of water uptake, the TGA result $\frac{\Delta m}{m_0} = 0.02$ wt% was converted into an apparent adsorption capacity of 0.2 mg·g^{-1}, which gives a value of 11.1 $\mu mol_{H2O}{\cdot}g^{-1}$. Using the calculated value of average praseodymium oxidation state at 500 °C ($3.655^{+} \pm 0.171$), this uptake corresponds to $\frac{n_{H_2O}}{n_{Pr}} \approx 1.89{\cdot}10^{-3}$(≈1 molecule of H_2O per ~529 Pr cations), which is a very small fraction of the available lattice-defect sides. Approximating the oxide as $PrO_{2-\delta}$ gives $\delta = 2 - \left(\frac{3.655}{2}\right) = 0.1725$, i.e., on the order of 0.17 oxygen vacancies per Pr, such that the experimentally observed uptake would account for only ~1.1% of a one-to-one "H_2O-per-vacancy" upper bound. This order-of-magnitude comparison indicates that the measured mass gain is fully compatible with the defect chemistry of PrO_x and suggests that a limited, reversible uptake associated predominantly with surface/near-surface adsorption and hydroxylation rather than bulk hydration or phase degradation.

To further verify this hypothesis, XPS measurements were carried out on PrO_x powder annealed at 500 °C for 10 h in a humid atmosphere (2.77 wt% of pH_2O). A portion of the powder was subsequently re-annealed for an additional 10 h in dry air at the same temperature to assess the reversibility of the process. The results of the Pr $3d_{5/2}$ XPS measurements are shown in Fig. 4C, while those for O 1 s are presented in Fig. 4D. Similar to the XPS measurements described above, the peaks corresponding to the Pr $3d_{5/2}$ $4f^{\underline{0}}\underline{v}^2\underline{c}$ transition at 930.25 eV and the $3d_{5/2}$ $f^{\underline{2}}\underline{vc}$ transition at 933.3 eV were observed. A decrease in the contribution from the II Pr $3d_{5/2}$ state associated with mixed praseodymium oxidation state was also noted, in favour of the remaining oxidation states, when comparing the samples after annealing in humid and dry air. Much more pronounced changes were observed for the oxygen signal. In the dry air conditions, three states were identified, consistent with earlier observations: at 535.5 eV (corresponding to O—H bonds), at 531.5 eV and at 528.4 eV. Under dry conditions, the signal corresponding to O—H bonds was weak and of little significance. However, after exposure to humid air, a substantial increase in this signal was observed, with its intensity approaching that of the most prominent peak at 531.5 eV. Importantly, after drying the sample, a comparably low signal from the O—H bond was obtained.

Considering the application of LSC as a current collector and its behaviour in water vapor-rich environments, a series of impedance measurements were conducted at varying H_2O partial pressures. This approach accounts for the partially irreversible interaction between LSC and water, acknowledging the potential inability to restore the original polarization resistance values. Fig. S8A and B illustrates the determined R_{ohm} values for measurements conducted at various pH_2O levels at 500 °C (A) alongside the corresponding polarization resistance R_{pol} values (B). The R_{ohm} values exhibit minor changes across the entire range. Although some correlations can be observed, the variations are so minimal that it was challenging to clearly determine the extent to which the presence of water vapor influences this parameter. The situation was more evident in the case of polarization resistance. The initial R_{pol} value of approximately 0.25 Ω·cm^2 increases marginally by changing to 0.1% pH_2O, reaching 0.26 Ω·cm^2. Upon transitioning to dry air, the value reverts to 0.25 Ω·cm^2. Introducing 0.5% water content causes an immediate increase to 0.35 Ω·cm^2, followed by stabilization at roughly 0.44 Ω·cm^2. When dry air was reintroduced, a reduction in R_{pol} was observed; however, after two hours, the value stabilizes at 0.28 Ω·cm^2. Introducing 1% water content causes a sudden rise in R_{pol} to 0.49 Ω·cm^2—higher than the value after two hours of exposure to 0.5% pH_2O. Stabilization was achieved shortly thereafter, with a final value of approximately 0.56 Ω·cm^2. Returning to synthetic air results in a decrease to 0.34 Ω·cm^2. At 2% pH_2O, a jump to 0.62 Ω·cm^2 occurs, followed by a linear increase in R_{pol} without signs of stabilization. After two hours under these conditions, the value reaches 0.91 Ω·cm^2. Transitioning back to synthetic air initially results in a significant drop in R_{pol}, which stabilizes at 0.55 Ω·cm^2 after two additional hours. At the highest possible pH_2O concentration (at 23 °C) tested, an even more rapid increase in R_{pol} was observed. Within two hours, the value raised to 1.72 Ω·cm^2—more than three times the initial value. Switching to synthetic air again causes an initial sharp drop in R_{pol}, which stabilizes at approximately 1.12 Ω·cm^2.

The results obtained were similar to those in Hayd et al.'s work for LSC as oxygen electrode. For a measurement temperature of 500 °C, they also observed an initial sudden increase and subsequent slowdown after switching to dry air. Then, an initial decrease in the value of R_{pol} was observed, followed by stabilization. The difference lies in the magnitude of the observed changes. In the described work, the maximum ratio of the R_{pol} value to the original value was approximately 1.3 after 10 h in 2% of water content and approximately 1.2 after 10 h in dry air [67]. In our case, the ratio was above 3.1 for two hours in 2% pH_2O content and around 1.9 in dry air. Therefore, it seems that using PrO_x as a readily water-binding material contributes to a sharp change in polarization resistance and an equally pronounced decrease in it. These results clearly indicate the formation of reversible, weak bonds between PrO_x and water. The reversibility of this process is crucial, as it confirms that water uptake, while influencing electrode performance—as evidenced by changes in AC measurements and DC conductivity—does not cause permanent inhibition of the electrochemical reaction. Additionally, the presence of weak bonds between PrO_y and water warrants further investigation, particularly in the context of proton-conducting fuel cells. The inhibitory effect of water vapor on the electrochemical reaction in the PrO_x oxygen-electrode layer is mainly attributed to reversible near-surface changes, arising from the adsorption and partial dissociation of H_2O at oxygen-defect sites. This results in a transient increase in O—H species (evidenced by XPS and the small mass increase in the water-uptake test), which temporarily modifies the near-surface electronic structure and reduces the availability of active sites involved in the surface steps of ORR. These changes manifest as a decrease in electrical conductivity and an increase in polarization resistance. The limited mass increase (0.02%) and around 1.1% of totally available water uptake capacity, and the complete recovery of both the O—H signal and conductivity after switching back to dry conditions indicate that the interaction of H_2O with PrO_x is reversible and confined to the surface (or, at most, a shallow subsurface region), rather than being associated with permanent bulk hydration or phase degradation. Moreover, with respect to the ease of removing adsorbed water, the redox flexibility of PrO_x—i.e., its ability to readily change the praseodymium oxidation state – also can play an important role. Similar to its strong capability to

accommodate and release oxygen, this redox adaptability facilitates faster desorption of water-derived species compared with state-of-the-art oxide electrodes.

3.6. pCO_2 influence

Carbon dioxide is also one of the key factors influencing the efficiency of oxygen electrodes. As mentioned before, for state of the art materials, CO_2 can reversible react with electrode material and blocking the active sides [67]. Furthermore long exposure to can cause the formation additional compounds e.g. $SrCO_3$ that permanently decrease the electrode efficiency [69]. To assess its impact on the proposed electrode material, a series of EIS measurements were conducted at different partial pressures of CO_2. Considering that using LSC as current collector did not cause irreversible degradation and that polarization resistance regenerates to its initial value after switching back to the synthetic air environment, the possible observation of different behaviour will be straightforwardly connected with the PrO_x material. Fig. S9A presents the determined values of R_{ohm} while Fig. S9B shows R_{pol} values determined during measurement. Regarding ohmic resistance, similar to the pH_2O measurements, no specific trend was observed. In the case of polarization resistance, no significant changes were detected up to 1% pCO_2, indicating that the oxygen electrode was not sensitive to CO_2 under standard atmospheric conditions (0.04%) or even with a multiple increase in concentration. However, above 1% pCO_2, a substantial increase in polarization resistance was observed, reaching 1.11 Ω·cm^2. Importantly, the R_{pol} value returns to its initial state. At 2% pCO_2, a maximum value of 3.46 Ω·cm^2 was recorded, followed by the onset of stabilization. At higher CO_2 concentrations, polarization resistance values of 5.03 Ω·cm^2 and 7.99 Ω·cm^2 were obtained for 3% and 5% pCO_2, respectively, with an initial stabilization phase noticeable in both cases. At the final stage, the polarization resistance returns to its initial value, suggesting that the electrochemical reaction inhibition was transient and reversible.

3.7. Long-term stability

Long-term stability measurements were conducted to evaluate the usability of the PrO_x oxygen electrode in the context of its application in solid oxide cell technology. The low operating temperature employed during these experiments could help to mitigate the degradation rate of the material and potentially extend its operational lifespan. Additionally, it facilitates the identification of degradation mechanisms and the quantification of the degree of degradation.

Fig. 5A depicts the Nyquist plots of the polarization resistance (ohmic resistance subtracted) at three distinct stages of the experiment Fig. 5B shows the values of ohmic resistance obtained during a 225-hour measurement in a synthetic air atmosphere, while Fig. 5C presents the polarization resistance values recorded during the same experiment.

In the case of ohmic resistance, the initial value was 18.6 Ω·cm^2. Following an initial decrease, a relative stabilization of this parameter was observed. The decrease in ohmic resistance is a phenomenon reported in several studies and was attributed to the formation of improved connectivity between the electrode and the electrolyte due to prolonged exposure to high temperatures. After 65 h, a sudden increase in ohmic resistance was observed, followed by a return to a value of approximately 18.0 Ω·cm^2. This value was maintained till the end of the measurement. Monitoring the R_{ohm} value during long-term operation is important for diagnosing cell integrity and interface stability and helps separate true polarization changes from artifacts related to contact evolution. A decreasing R_{ohm} value over time, especially in the initial stages, indicates gradual conditioning/improvement of the electrical contact (e.g., thermally activated relaxation and increase in the actual contact area at the electrode-electrolyte), rather than contact degradation.

Polarization resistance, which characterizes the efficiency of the electrochemical reaction, is influenced by material degradation through various surface processes or, as described in earlier sections, interactions between the electrode layer and the substrate. At 500 °C, the polarization resistance remained relatively stable. Starting at an initial value of 0.35 Ω·cm^2, it reached 0.34 Ω·cm^2 after both 100 and 225 h. Similar to ohmic resistance, an initial decrease in R_{pol} was followed by a very gradual increase over time.

To better capture the non-linear time evolution of R_{pol} value, the data were fitted using a dynamic model combining an initial relaxation term and a long-term increase of R_{pol} value:

$$R(t) = R_{base} + Ae^{\frac{-t}{\tau}} + kt \quad (1)$$

The exponential term accounts for the early conditioning stage, whereas k quantifies the long-term degradation rate. For measurement performed at 500 °C, the fit yielded is presented in Table 2.

This provides a more general description than piecewise-linear rates and separates the short-time transient from the long-term degradation trend. The short-time exponential component ($\tau \approx 4.2$ h) can be attributed to an initial conditioning/relaxation stage, such as equilibration of surface coverage and near-surface defect chemistry (e.g., redistribution of oxygen vacancies and associated Pr^{3+}/Pr^{4+} states), which temporarily modifies the kinetics of the surface oxygen reduction reaction steps. In contrast, the long-term linear drift quantified by k is consistent with slower, cumulative degradation processes, for example

Table 2
Fitting parameters obtained from the dynamic model for the long-term measurement of the oxygen electrode PrO_x at 500 °C.

Parameter	R_{base} [Ω·cm^2]	A [Ω·cm^2]	τ [h]	k [Ω·cm^2 h^{-1}]
Value	0.2976 ± 0.0029	0.0491 ± 0.0089	4.19 ± 1.90	(2.08 ± 0.22)·10-4

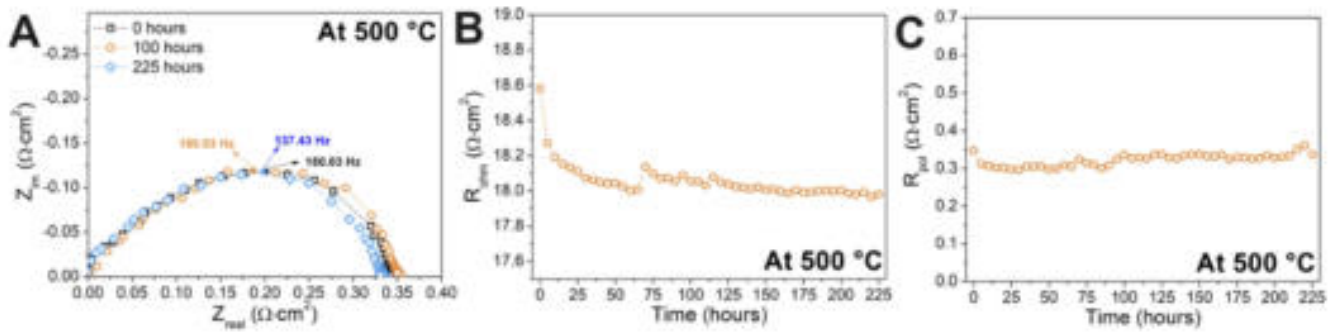


Fig. 5. Nyquist plots recorded after 0, 100, and 225 h with subtracted ohmic resistance at 500 °C (A); changes in ohmic resistance (B) as well as polarization resistance (C) during long-term stability measurements.

gradual microstructural coarsening, evolution of interfacial resistance, or progressive surface degradation effects. These results indicate an initial and relatively short conditioning stage (up to ~17 h according to the model) followed by a slow and long-lasting degradation process of the material. Good material stability over time and a low degradation rate according to the model of ~0.021 Ω·cm^2 within 100 h was determined.

Fig. S10 illustrates the values of ohmic and polarization resistance obtained during a similar 100-h measurement conducted at a temperature of 600 °C. For ohmic resistance, a significant decrease was observed, similar to the results at 500 °C. Starting from an initial value of 8.72 Ω·cm^2, the resistance decreased to 8.27 Ω·cm^2 after 50 h and further to 8.21 Ω·cm^2 after 100 h, representing a reduction of 0.51 Ω·cm^2 over 100 h.

A more pronounced change was observed for polarization resistance at 600 °C. The initial value of 0.038 Ω·cm^2 increased to 0.075 Ω·cm^2 after 50 h and reached 0.106 Ω·cm^2 after 100 h. This substantial and linear increase suggests a rapid degradation process. The Nyquist plots recorded at 0, 50, and 100 h show a marked increase in the low-frequency semicircle, which can be associated with gas diffusion within the electrode. This behaviour may result from either densification of the electrode material or the dissolution of the electrode into the electrolyte. Based on previous studies, the latter process was more likely. This finding provides additional evidence to suggest that 600 °C could be too high temperature for the PrO_x material deposited on CGO.

3.8. Fuel cells measurements

To analyse the performance of the proposed oxygen electrode under operating conditions, a series of measurements was conducted on an anode-supported fuel cell with a PrO_x layer. Fig. 6A presents the current-voltage (I-V) characterisation obtained at 600 °C, 550 °C, and 500 °C. Fig. 6B compares the I-V characteristics at 500 °C for the cell with the PrO_x electrode and a reference commercial cell. Additionally, Fig. 6C illustrates the Nyquist plots recorded at 500 °C at open-circuit voltage (OCV) for the reference sample and the tested cell, both in its initial state and after 87 h of operation under a 100 mA·cm^{-2} applied current.

Two type of the reference samples were prepared to evaluate the proposed design. The first type was fabricated identically to the studied cell, with the exception of the praseodymium oxide layer. This sample underwent the same sintering and reduction treatment as the research sample. The second type was a commercially available cell supplied by Elcogen Company, featuring an LSC oxygen electrode. This cell differed from the other two in that it incorporated a thicker CGO layer and was subjected to a higher sintering temperature during its production process.

The measured OCV at 500 °C for the cell with the PrO_x electrode was 1.13 V, closely matching the reference samples, which exhibited a value of 1.12 V. The maximum power density values obtained for the cell with the PrO_x layer were 280 mW·cm^{-2}, 170 mW·cm^{-2}, and 95 mW·cm^{-2} at 600 °C, 550 °C, and 500 °C, respectively. For the first reference sample, a maximum power density of 22 mW·cm^{-2} was achieved. This meant that the use of praseodymium oxide as the oxygen electrode increased the cell power density by more than four times. In contrast, the reference Elcogen cell demonstrated a power density of 69 mW·cm^{-2} at 500 °C, corresponding to an approximate 39% increase for the modified electrode.

Moreover, the initial segment of the I-V curves appears nearly identical for the studied cell and the Elcogen cell, indicating similar activation losses for both cells. However, a significant divergence was observed in the higher current range, primarily due to differences in ohmic losses. The key advantage of the tested cell was its substantially reduced ohmic losses. This conclusion was further supported by impedance spectroscopy, which reveals an exceptionally low ohmic resistance of 0.52 Ω·cm^2 at 500 °C. In comparison, the reference sample exhibited an ohmic resistance of 2.11 Ω·cm^2 and 1.41 Ω·cm^2 for the Elcogen cell at the same temperature, representing a reduction of approximately 75% and 63%. The high ohmic resistance value obtained for the reference sample with a deposited CGO layer may be due to the use of an unusually low sintering temperature. This temperature did not allow for proper connection between the oxygen electrode and the electrolyte. Using thin-film techniques and preparing the PrO_x electrode also had a beneficial effect in this regard.

Simultaneously, the initial polarization resistance of the modified cell was 10.8 Ω·cm^2, decreasing to 8.4 Ω·cm^2 after 87 h of operation. For the reference sample, this value was around 20 Ω·cm^2 and 7.74 Ω·cm^2, corresponding to decrease of around 50% for the reference cell and an increase of 39.5% and 8.5% in comparison with the Elcogen sample. However, measurements performed at OCV do not fully capture the cell's performance under load. Thus, despite the higher R_{pol} observed for the modified cell, this does not directly correlate with its power density capabilities. Therefore, short-term stability tests were performed and after 87 h of operation, the measured power density remained almost unchanged, indicating short-term cell stability. Fig. S11 presents the voltage evolution under a constant load of 100 mA·cm^{-2} over the 87 h test. While a slight voltage drift was observed, EIS indicates stable ohmic resistance and a decrease in polarization resistance (from 10.8 to 8.4 Ω·cm^2), together with a small increase in OCV (from 1.13 to ~1.14 V), which is consistent with a mild conditioning effect rather than degradation. The small voltage drift is therefore most likely related to minor variations in the fuel humidification (e.g., changes in the water level in the humidifier bottle during operation), rather than to a deterioration of the cell components.

The obtained results were compared with the data available in the literature. The data were divided into the intermediate range (> 600 °C) and the low temperature range (≤ 600 °C). In the intermediate range, Nam et al. studied fuel cells with oxygen electrodes composed of LSM-YSZ – PrO_x and LSM-YSZ – $(Pr,Ce)O_x$. At 650 °C, the power density

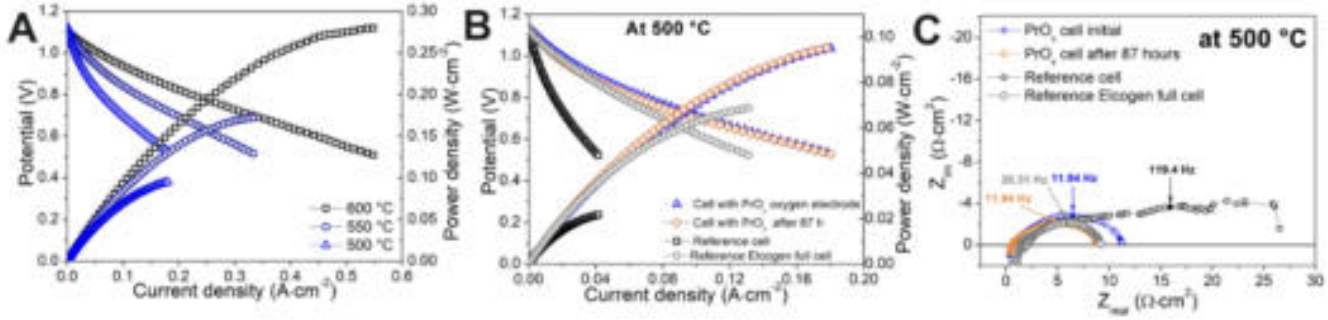


Fig. 6. Current-voltage characteristics in the temperature range of 600–500 °C (A). Comparison of the I-V characteristics of a cell with a PrO_x-based oxygen electrode and the reference cells (B). Nyquist plot measured at OCV at 500 °C for the reference samples, as well as for the modified cell in its initial state and after short-term stabilization (87 h) (C).

was 418 mW·cm^{-2} for the PrO_x-modified sample, 342 mW·cm^{-2} for the $(Pr,Ce)O_x$-modified sample, and 142 mW·cm^{-2} for the reference sample [28]. Dogdibegovic et al. described high-performance metal-supported solid oxide fuel cells and investigated the effect of infiltrating the oxygen electrode (porous YSZ backbone) with PrO_x. Their study achieved the highest power density reported to date compared to previously investigated materials, reaching 1.3 W·cm^{-2} at 700 °C [70].

In the low temperature range, for example Nicollet et al. tested a cell with a Pr_6O_{11} oxygen electrode, achieving a power density of 825 mW·cm^{-2} at 600 °C and demonstrating good stability over 840 h of measurement. In contrast, the commercial reference cell did not exceed a power density of 400 mW·cm^{-2} [26]. Ge et al. measured full cells with both PrO_x-modified and unmodified electrodes (LSM, LSCF, LSC). The obtained power densities for unmodified cells were 73 ± 18, 155 ± 13, and 279 ± 17 mW·cm^{-2} for LSM, LSCF, and LSC at 600 °C, respectively. For cells infiltrated with praseodymium oxide nanoparticles, these values increased to 505 ± 35, 344 ± 46, and 531 ± 23 mW·cm^{-2} under the same conditions [29]. Kane et al. analysed a full cell with a modified oxygen electrode made of LSCF, where 45 cycles of PrO_x deposition resulted in a power density of 220 mW·cm^{-2} at 600 °C [30]. Lu et al. conducted tests on STFC-PrO_x oxygen electrode fuel cells, which exhibited high power densities—approximately 0.28 W·cm^{-2} at 550 °C and nearly 1 W·cm^{-2} at 650 °C. In the case of the LSCF-PrO_x oxygen electrode, the maximum power density was approximately 0.08 W·cm^{-2} at 550 °C and about 0.42 W·cm^{-2} at 650 °C [31]. So far, Lu et al. were the only study to investigate a praseodymium oxide-modified oxygen electrode below 600 °C. The power densities obtained at 550 °C for STFC-PrO_x were higher than those we obtained for PrO_x alone. However, at the same time, the power density obtained for LSCF-PrO_x was lower than the power density obtained in our work at a temperature 50 °C lower. To the best of our knowledge, no one before has investigated praseodymium oxide in fuel cells at temperatures as low as 500 °C.

Fig. 7A presents an SEM image of the cross-section of the fuel cell taken after the measurements. Additionally, Fig. 7B displays EDX maps illustrating the distribution of elements within the fuel cell. The commercial half-cell consisted of a fuel electrode composed of Ni-YSZ and an electrolyte in the form of YSZ. Notably, the CGO layer, deposited via spray pyrolysis, exhibits an average thickness of approximately 600 nm and was dense and well-adhered to the YSZ. The CGO surface is well-defined, without significant irregularities, while the visible cracks were likely a result of the sample preparation and polishing processes. Above this layer, a porous oxygen electrode with a thickness of approximately 200 nm, deposited using the spin-coating method, was clearly visible. Furthermore, the small grain size was noteworthy, as it positively influences the active surface of the electrode. Above this, a CC layer composed of LSC, characterized by significant grain diversity, was observed. The EDX maps confirm the proper distribution of cerium and gadolinium within the applied barrier layer. Additionally, a thin PrO_x layer appears as a distinct line. No visible changes were observed within this layer—no signs of reactions or diffusion with either CGO or LSC were detected.

4. Conclusions

This paper investigates the potential application of PrO_x material as an effective oxide electrode in low-temperature solid-oxide cells (SOCs). The material's structure was studied using different techniques, such as XRD, Raman spectroscopy, XPS, and XAS.

The variability of the PrO_x material was demonstrated using several techniques, including XRD, Raman spectroscopy, XPS, and XAS. These studies revealed the formation of new phases that impacted the material's electrocatalytic properties. In-situ Raman and XAS measurements showed the highest Pr^{4+} content for the praseodymium cation at annealing temperatures of 500 and 600 °C. However, a noticeably lower average oxidation state was observed at an annealing temperature of 400 °C for XAS. The presence of PrO_2 in this composition, confirmed by Raman and XRD, indicates the complexity of the analysed system.

Analysis of the effect of annealing temperature revealed that the lowest polarization resistance was achieved at 500 °C, which was a value lower than those previously used, resulting in an R_{pol} value of 0.254 Ω cm^2. Furthermore, electrode degradation was observed at higher temperatures due to the dissolution of PrO_x into CGO above 600 °C. Interdiffusion between the PrO_x electrode and the CGO electrolyte was observed using HT-XRD, resulting in CGO lattice expansion and degradation of electrode performance. This was also due to the electrode densification and the lack of porosity formation, as observed for perovskite oxides. Thanks to the use of thin layers, this process was visible in a relatively short time, enabling faster observation of the phenomenon, not described in such details in previous works on praseodymium oxide. Therefore, to optimize material utilization while maintaining efficiency, it is necessary to carefully select the operating conditions for the material in question.

Measurements performed at different oxygen partial pressures revealed that the adsorption of molecular oxygen onto the catalytic material was the main factor limiting the electrode efficiency. Furthermore, the shape of the obtained spectra, especially in the high-frequency range, suggests that a complex diffusion process was occurred in the electrode and was probably influenced by the intrinsic properties of

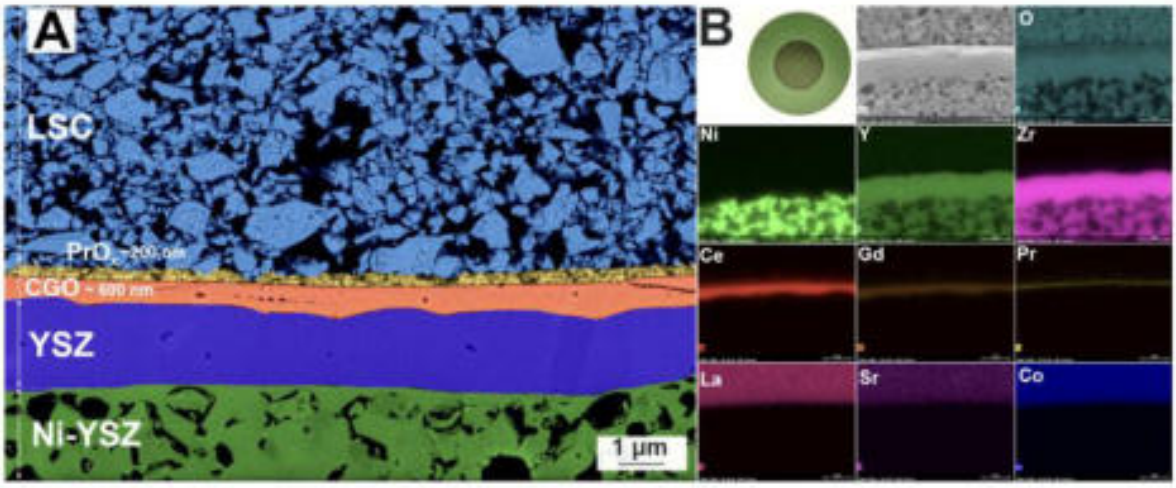


Fig. 7. Cross-section of the full cell after testing, with layers and materials labelled (A). Cell with a deposited PrO_x oxygen electrode before the testing, and EDX maps showing the elements distribution in the solid oxide cell (B).

PrO_x. The material's high phase variation indicates that oxygen ion transport does not occur exclusively via isolated point defects, as observed in standard materials.

The influence of water vapor as a potential inhibitor of the electrochemical oxygen reduction reaction demonstrated the material's dependence on water vapor. Electrical conductivity decreased in the presence of water due to binding in the hydration process. However, this process was fully reversible; using dry air reversed the process, as confirmed by XPS and water uptake.

No negative effects were observed for the second potential inhibitor of electrochemical reactions, CO_2, at concentrations up to 1%. However, above this threshold, polarization resistance increased significantly. These changes were found to be fully reversible, and the material's sensitivity to CO_2 remained well below atmospheric levels. Improved resistance to CO_2- and H_2O-induced poisoning, the advantages of PrO_x over commonly used perovskite cathode materials such as LSC or LSCF arise from several factors. The non-stoichiometric character of praseodymium oxide, its high redox flexibility between Pr^{3+} and Pr^{4+}, and the large number of active adsorption sites can facilitate the uptake of impurities and their subsequent removal. Moreover, compared with strontium located on the perovskite A-site-widely regarded as a major contributor to CO_2/H_2O sensitivity-praseodymium exhibits lower basicity. As a result, CO_2 and H_2O tend to bind more strongly and often partially irreversibly to Sr, promoting the formation of stable surface phases such as $SrCO_3$ and $Sr(OH)_2$, whereas analogous praseodymium-containing species are comparatively less stable. In addition, perovskites such as LSC and LSCF are prone to strontium surface segregation, a well-known degradation pathway that further increases the local reactivity and accelerates carbonate/hydroxide formation. This phenomenon did not occur in PrO_x-based oxygen electrode. While the observed recovery of R_{pol} indicates reversibility under small-signal symmetric-cell conditions, full-cell under-load cyclic gas-switching tests are required to confirm reversible performance under practical operating conditions.

Stability measurements performed at 500 °C in synthetic air demonstrated excellent long-term performance over 225 h. The degradation rate was determined as 18.88% per 100 h from 30 to 100 h and decreased significantly to 0.15% per 100 h after 100 h. However, significant degradation of the material was observed at 600 °C, as evidenced by a clear increase in R_{pol}.

Fuel cell measurements with PrO_x as the oxygen electrode showed a power density increase of more than four times compared to the reference cell and a 39% increase compared to the commercial Elcogen cell. Additionally, the prepared cell exhibited exceptionally low ohmic resistance at 500 °C: 0.52 Ω cm^2, compared to 2.11 and 1.41 Ω cm^2 in the reference cells.

In conclusion, praseodymium oxide appears to be a highly promising material for oxygen electrodes in low-temperature solid oxide cells operating below 600 °C. Material characterized by low R_{pol} value (0.021 Ω cm^2 at 600 °C and 0.254 Ω cm^2 at 500 °C) and even outperforms LSC. However, to ensure its effective use, special attention must be paid to factors discussed in this work, such as electrode temperature and annealing. The material's key advantage over LSC and LSCF lies in its reversible reaction with atmospheric compounds like H_2O or CO_2. This feature opens up the potential for effective utilization of the material in the future.

Beyond the specific performance parameters presented here, our results point to broader design principles for oxygen electrodes operating in low-temperature SOCs. The high tolerance of PrO_x to H_2O and CO_2 arises from its defect-flexible oxide chemistry, including an oxygen sublattice that can accommodate non-stoichiometry and the Pr^{3+}/Pr^{4+} redox couple, which enables largely reversible adjustment of surface and near-surface states. Consequently, poisoning manifests primarily as reversible surface effects rather than irreversible bulk degradation, consistent with the observed recovery in impedance, conductivity, and surface-sensitive measurements. These attributes make PrO_x particularly attractive for oxygen electrodes in SOCs operating in the 500–600 °C range. Moreover, commercial systems typically use atmospheric air rather than synthetic gas mixtures, and thus operate under humid, CO_2-containing conditions. In this context, PrO_x may be relevant not only for intermediate-temperature SOFCs but also for proton-conducting fuel cells and related electrochemical devices (e.g., electrolyzers), where cathode stability under humid conditions is critical. From a fabrication perspective, the proposed PrO_x thin functional layer at the electrode/electrolyte interface performs best when combined with a conductive, porous current-collection scaffold. Spin coating is convenient for laboratory optimization, whereas scalable spray-based methods (e.g., spray pyrolysis) offer a viable route to large-area, thickness-controlled coatings for practical cells and stacks.

CRediT authorship contribution statement

Bartłomiej Lemieszek: Writing – review & editing, Writing – original draft, Visualization, Validation, Methodology, Investigation, Formal analysis, Data curation, Conceptualization. **Lulu Alluhaibi:** Writing – review & editing, Methodology, Investigation, Data curation. **Alexey Maximenko:** Writing – review & editing, Methodology, Investigation, Data curation. **Łukasz Gawel:** Writing – review & editing, Methodology, Investigation. **Aleksandra Mielewczyk-Gryń:** Writing – review & editing, Methodology, Investigation. **Michał Struzik:** Writing – review & editing, Writing – original draft, Methodology, Investigation. **Marcin Małys:** Writing – review & editing, Methodology, Investigation. **Muhammad Imran Asghar:** Writing – review & editing, Methodology, Investigation. **Grzegorz Cempura:** Writing – review & editing, Methodology, Investigation. **Piotr Jasiński:** Writing – review & editing, Methodology. **Sebastian Molin:** Writing – review & editing, Supervision, Methodology, Funding acquisition, Conceptualization.

Declaration of competing interest

The authors declare the following financial interests/personal relationships which may be considered as potential competing interests: Sebastian Molin reports financial support was provided by National Science Centre Poland. If there are other authors, they declare that they have no known competing financial interests or personal relationships that could have appeared to influence the work reported in this paper.

Acknowledgements

This research has been supported by the National Science Centre (NCN) DAINA 2 project number UMO-2020/38/L/ST8/00513 "Porous metal supported micro-scale solid oxide fuel cells: fundamentals, fabrication and testing". The XAFS measurements at ASTRA beamline at NSRC SOLARIS were made under the provision of the Polish Ministry and Higher Education project "Support for research and development with the use of research infra-structure of the National Synchrotron Radiation Centre SOLARIS" under contract Nr 1/SOL/2021/2. The further development of ASTRA beamline at NSRC SOLARIS was supported within the EU Horizon2020 program (952148-Sylinda).

Appendix A. Supplementary data

Supplementary data to this article can be found online at https://doi.org/10.1016/j.cej.2026.173949.

Data availability

The data has been partially made available on the Bridge of Knowledge Repository of the Gdańsk University of Technology - https://mostwiedzy.pl/pl/bartlomiej-lemieszek,1100677-1/research-data

EIS measurements for the PrOx oxygen electrode as a function of annealing temperature (Original data) (Brigde of Knowledge)

EIS measurements at different pO2 for PrOx oxygen electrode -

symmetrical measurements (Original data) (Brigde of Knowledge)

Measurements of fuel cells with an oxygen electrode in the form of PrOx - I-V and EIS (Original data) (Brigde of Knowledge)

XAFS spectra for praseodymium oxide annealed at temperatures from 400 °C to 1000 °C (Original data) (Brigde of Knowledge)

References

[1] M. Singh, D. Zappa, E. Comini, Solid oxide fuel cell: decade of progress, future perspectives and challenges, Int. J. Hydrog. Energy 46 (54) (2021) 27643–27674, https://doi.org/10.1016/j.ijhydene.2021.06.020.

[2] E.D. Wachsman, K.T. Lee, Lowering the temperature of solid oxide fuel cells, Science 334 (6058) (2011) 935–939, https://doi.org/10.1126/science.1204090 (80-).

[3] M. Yousaf, Y. Lu, M. Akbar, L. Lei, S. Jing, Y. Tao, Advances in solid oxide fuel cell technologies: lowering the operating temperatures through material innovations, Mater. Today Energy. 44 (2024) 101633, https://doi.org/10.1016/j.mtener.2024.101633.

[4] A. Tarancón, Strategies for lowering solid oxide fuel cells operating temperature, Energies 2 (4) (2009) 1130–1150, https://doi.org/10.3390/en20401130.

[5] B. Lemieszek, M. Ilickas, J. Jamroz, et al., Enhanced electrochemical performance of partially amorphous La0.6Sr0.4CoO3-δ oxygen electrode materials for low-temperature solid oxide cells operating at 400°C, Appl. Surf. Sci. 670 (2024), https://doi.org/10.1016/j.apsusc.2024.160620.

[6] J. Gao, Z. Wei, M. Yuan, et al., Boosting oxygen reduction activity and CO2 resistance on bismuth ferrite-based perovskite cathode for low-temperature solid oxide fuel cells below 600°C, J. Energy Chem. 90 (2024) 600–609, https://doi.org/10.1016/j.jechem.2023.12.004.

[7] Y. Meng, W. Zhang, Z. He, et al., Partially reduced Ni0.8Co0.15Al0.05LiO2-δ for low-temperature SOFC cathode, Int. J. Hydrog. Energy 46 (15) (2021) 9874–9881, https://doi.org/10.1016/j.ijhydene.2020.05.150.

[8] A. Pesaran, A. Jaiswal, Y. Ren, E.D. Wachsman, Development of a new ceria/yttria-ceria double-doped bismuth oxide bilayer electrolyte low-temperature SOFC with higher stability, Ionics (Kiel). 25 (7) (2019) 3153–3164, https://doi.org/10.1007/s11581-019-02838-4.

[9] B. Singh, S. Ghosh, S. Aich, B. Roy, Low temperature solid oxide electrolytes (LT-SOE): a review, J. Power Sources 339 (2017) 103–135, https://doi.org/10.1016/j.jpowsour.2016.11.019.

[10] J. Zhang, C. Lenser, N.H. Menzler, O. Guillon, Comparison of solid oxide fuel cell (SOFC) electrolyte materials for operation at 500 °C, Solid State Ionics 344 (October 2019) (2020) 115138, https://doi.org/10.1016/j.ssi.2019.115138.

[11] G. Abbas, R. Raza, M.A. Khan, et al., Synthesize and characterization of nanocomposite anodes for low temperature solid oxide fuel cell, Int. J. Hydrog. Energy 40 (1) (2015) 891–897, https://doi.org/10.1016/j.ijhydene.2014.10.119.

[12] F.S. Toranik, M. Keyanpour-Rad, A. Maghsoudipour, G.M. Choi, Effect of microstructure refinement on performance of Ni/Ce 0.8Gd0.2O1.9 anodes for low temperature solid oxide fuel cell, Ceram. Int. 40 (1 PART B) (2014) 1341–1350, https://doi.org/10.1016/j.ceramint.2013.07.015.

[13] J.H. Park, S.M. Han, K.J. Yoon, et al., Impact of nanostructured anode on low-temperature performance of thin-film-based anode-supported solid oxide fuel cells, J. Power Sources 315 (2016) 324–330, https://doi.org/10.1016/j.jpowsour.2016.03.055.

[14] B. Kamecki, G. Cempura, P. Jasiński, S.-F. Wang, S. Molin, Tuning electrochemical performance by microstructural optimization of the nanocrystalline functional oxygen electrode layer for solid oxide cells, ACS Appl. Mater. Interfaces 14 (51) (2022) 57449–57459, https://doi.org/10.1021/acsami.2c18951.

[15] J. Ignaczak, L. Zeng, D.F. Sanchez, et al., Fe-modified Mn2CuO4 spinel oxides: coatings based on abundant elements for solid oxide cell interconnects, Int. J. Hydrog. Energy 48 (92) (2023) 36076–36093, https://doi.org/10.1016/j.ijhydene.2023.06.041.

[16] O.P. Ostash, T.O. Prikhna, V.Y. Podhurska, et al., Light interconnects for medium-temperature (550–650°C) solid-oxide fuel cells, Mater. Sci. 57 (2) (2021) 215–220, https://doi.org/10.1007/s11003-021-00534-1.

[17] J. Mao, E. Wang, H. Wang, et al., Experimental investigation of the initial stage of the oxidation mechanism of Co coating for solid oxide fuel cell interconnects at 650°C, Coatings 13 (7) (2023), https://doi.org/10.3390/coatings13071144.

[18] M.Z. Ahmad, S.H. Ahmad, R.S. Chen, A.F. Ismail, R. Hazan, N.A. Baharuddin, Review on recent advancement in cathode material for lower and intermediate temperature solid oxide fuel cells application, Int. J. Hydrog. Energy 47 (2) (2022) 1103–1120, https://doi.org/10.1016/j.ijhydene.2021.10.094.

[19] J. Zhang, S. Ricote, P.V. Hendriksen, Y. Chen, Advanced materials for thin-film solid oxide fuel cells: recent progress and challenges in boosting the device performance at low temperatures, Adv. Funct. Mater. 32 (22) (2022), https://doi.org/10.1002/adfm.202111205.

[20] E.S. Putna, J.M. Vohs, R.J. Gorte, G.W. Graham, An examination of praseodymia as an oxygen-storage component in three-way catalysts, Catal. Lett. 54 (1) (1998) 17–21, https://doi.org/10.1023/a:1019059401500.

[21] S. Ferro, Physicochemical and electrical properties of praseodymium oxides, Int. J. Electrochem. 2011 (2011) 1–7, https://doi.org/10.4061/2011/561204.

[22] V. Thangadurai, R.A. Huggins, W. Weppner, Mixed ionic-electronic conductivity in phases in the praseodymium oxide system, J. Solid State Electrochem. 5 (2001) 531–537, https://doi.org/10.1007/s100080000187.

[23] Y. Fujimaki, T. Nakamura, Y. Kimura, et al., Operando evaluation of the electrochemically active area in a solid oxide fuel cell porous electrode by micro X-ray absorption spectroscopy, J. Phys. Chem. Lett. 16 (37) (2025) 9599–9605, https://doi.org/10.1021/acs.jpclett.5c02422.

[24] B. Kamecki, J. Karczewski, P. Jasiński, S. Molin, Improvement of oxygen electrode performance of intermediate temperature solid oxide cells by spray pyrolysis deposited active layers, Adv. Mater. Interfaces 8 (9) (2021) 1–11, https://doi.org/10.1002/admi.202002227.

[25] O. Faruk Aksoy, L. Bartłomiej, M. Murat, K. Jakub, J. Piotr, M. Sebastian, Developing high-performance oxygen electrodes for intermediate, Appl. Phys. A Mater. Sci. Process. (2024), https://doi.org/10.1007/s00339-024-07939-0 (Published online).

[26] C. Nicollet, A. Flura, V. Vibhu, A. Rougier, J.M. Bassat, J.C. Grenier, An innovative efficient oxygen electrode for SOFC: Pr6O11 infiltrated into Gd-doped ceria backbone, Int. J. Hydrog. Energy 41 (34) (2016) 15538–15544, https://doi.org/10.1016/j.ijhydene.2016.04.024.

[27] R.K. Sharma, N.I. Khamidy, L. Rapenne, et al., Highly efficient architectured Pr6O11 oxygen electrode for solid oxide fuel cell, J. Power Sources 419 (February) (2019) 171–180, https://doi.org/10.1016/j.jpowsour.2019.02.077.

[28] S. Nam, J. Kim, H. Kim, et al., Revitalizing oxygen reduction reactivity of composite oxide electrodes via electrochemically deposited PrOx nanocatalysts, Adv. Mater. 36 (25) (2024) 1–11, https://doi.org/10.1002/adma.202307286.

[29] L. Ge, K. Sun, Y. Gu, Q. Ni, X. Huang, Boosting the performance of conventional air electrodes for solid oxide cells by in-situ loading of nano praseodymium oxide, Energy Convers. Manag. 249 (September) (2021) 114873, https://doi.org/10.1016/j.enconman.2021.114873.

[30] N. Kane, Y. Zhou, W. Zhang, et al., Precision surface modification of solid oxide fuel cells via layer-by-layer surface sol-gel deposition, Published online, J. Mater. Chem. A (2022) 8798–8806, https://doi.org/10.1039/d2ta00458e.

[31] M.Y. Lu, R. Scipioni, B.K. Park, T. Yang, Y.A. Chart, S.A. Barnett, Mechanisms of PrOx performance enhancement of oxygen electrodes for low and intermediate temperature solid oxide fuel cells, Mater. Today Energy. 14 (2019) 100362, https://doi.org/10.1016/j.mtener.2019.100362.

[32] L. Caizán-Juanarena, J. Zamudio-García, D. Marrero-López, Electrochemical investigation of Pr6O11 infiltration into La0.8Sr0.2MnO3-δ-Ce0.9Gd0.1O1.95 cathodes for IT-SOFC, Ceram. Int. 49 (21) (2023) 33717–33724, https://doi.org/10.1016/j.ceramint.2023.08.060.

[33] B. Ravel, M. Newville, ATHENA, ARTEMIS, HEPHAESTUS: data analysis for X-ray absorption spectroscopy using IFEFFIT, J. Synchrotron Radiat. 12 (4) (2005) 537–541, https://doi.org/10.1107/S0909049505012719.

[34] T.H. Wan, M. Saccoccio, C. Chen, F. Ciucci, Influence of the discretization methods on the distribution of relaxation times deconvolution: implementing radial basis functions with DRTtools, Electrochim. Acta 184 (2015) 483–499, https://doi.org/10.1016/J.ELECTACTA.2015.09.097.

[35] P. Lv, L. Zhang, S. Koppala, et al., Decomposition study of praseodymium oxalate as a precursor for praseodymium oxide in the microwave field, ACS Omega 5 (34) (2020) 21338–21344, https://doi.org/10.1021/acsomega.0c00505.

[36] S. Lütkehoff, M. Neumann, A. Šlebarski, 3d and 4d x-ray-photoelectron spectra of Pr under gradual oxidation, Phys. Rev. B 52 (19) (1995) 13808–13811, https://doi.org/10.1103/PhysRevB.52.13808.

[37] K. Dzierzgowski, S. Wachowski, M. Łapiński, A. Mielewczyk-Gryń, M. Gazda, Praseodymium orthoniobate and praseodymium substituted lanthanum orthoniobate: electrical and structural properties, Materials (Basel). 15 (6) (2022), https://doi.org/10.3390/ma15062267.

[38] O. Seifarth, J. Dabrowski, P. Zaumseil, et al., On the band gaps and electronic structure of thin single crystalline praseodymium oxide layers on Si(111), J. Vac. Sci. Technol. B Microelectron. Nanometer Struct. 27 (1) (2009) 271–276, https://doi.org/10.1116/1.3021047.

[39] H. Ogasawara, A. Kotani, R. Potze, G. Sawatzky, B. Thole, Praseodymium 3d- and 4d-core photoemission spectra of Pr2O3, Phys. Rev. B 44 (11) (1991) 5465–5469.

[40] M. Kruczek, E. Talik, D. Pawlak, T. Łukaniewicz, X-ray photoelectron spectroscopy studies of PrAlO3 crystals before and after thermal treatment, Opt. Appl. 35 (3) (2005) 347–354.

[41] T.S. Wu, Y. Zhou, R.F. Sabirianov, W.N. Mei, Y.L. Soo, C.L. Cheung, X-ray absorption study of ceria nanorods promoting the disproportionation of hydrogen peroxide, Chem. Commun. 52 (28) (2016) 5003–5006, https://doi.org/10.1039/c5cc10643e.

[42] H. Fujishiro, T. Naito, D. Takeda, et al., Simultaneous valence shift of Pr and Tb ions at the spin-state transition in (Pr1-yTby)0.7Ca0.3CoO3, Phys. Rev. B Condens. Matter Mater. Phys. 87 (15) (2013) 1–7, https://doi.org/10.1103/PhysRevB.87.155153.

[43] A. Bianconi, A. Marcelli, H. Dexpert, et al., Specific intermediate-valence state of insulating 4f compounds detected by L3 x-ray absorption, Phys. Rev. B 35 (2) (1987) 806–812, https://doi.org/10.1103/PhysRevB.35.806.

[44] H. Yamaoka, H. Oohashi, I. Jarrige, et al., X-ray spectroscopic study of the electronic structure of Y1-x Prx Ba2 Cu3 O7, Phys. Rev. B 77 (4) (2008) 1–7, https://doi.org/10.1103/PhysRevB.77.045135.

[45] H. Fujishiro, T. Naito, S. Ogawa, et al., Valence shift of Pr ion from 3+ to 4+ in (Pr1-y) 0.7Ca0.3CoO3 estimated by X-ray absorption spectroscopy, J. Phys. Soc. Jpn. 81 (6) (2012) 2–6, https://doi.org/10.1143/JPSJ.81.064709.

[46] Y. Borchert, P. Sonström, M. Wilhelm, H. Borchert, M. Bäumer, Nanostructured praseodymium oxide: preparation, structure, and catalytic properties, J. Phys. Chem. C 112 (8) (2008) 3054–3063, https://doi.org/10.1021/jp0768524.

[47] A. Netz, W.F. Chu, V. Thangadurai, R.A. Huggins, W. Weppner, Investigations of praseodymium oxide electrodes in lithium concentration cells, Ionics 5 (1999) 426–433.

[48] M.S. Hassan, M.S. Akhtar, K.B. Shim, O.B. Yang, Morphological and electrochemical properties of crystalline praseodymium oxide nanorods, Nanoscale Res. Lett. 5 (4) (2010) 735–740, https://doi.org/10.1007/s11671-010-9547-8.
[49] A.I. Vshivkova, V.P. Gorelov, A.V. Kuz'Min, S.V. Plaksin, A.A. Pankratov, T. V. Yaroslavtseva, Preparation and physicochemical properties of praseodymium oxide films and ceramics, Inorg. Mater. 51 (11) (2015) 1168–1176, https://doi.org/10.1134/S0020168515100179.
[50] B.M. Abu-Zied, Controlled synthesis of praseodymium oxide nanoparticles obtained by combustion route: effect of calcination temperature and fuel to oxidizer ratio, Appl. Surf. Sci. 2019 (471) (December 2018) 246–255, https://doi.org/10.1016/j.apsusc.2018.12.007.
[51] T. Arakawa, A. Kabumoto, J. Shiokawa, Some electrical properties of praseodymium oxide films produced by oxidation of thin metal films, J. Less Common Met. 115 (2) (1986) 281–286, https://doi.org/10.1016/0022-5088(86)90150-5.
[52] P. Shuk, M. Greenblatt, Hydrothermal synthesis and properties of mixed conductors based on Ce1−xPrxO2−δ solid solutions, Solid State Ionics 116 (3–4) (1999) 217–223, https://doi.org/10.1016/S0167-2738(98)00345-2.
[53] R.D. Shannon, Revised effective ionic radii and systematic studies of interatomic distances in halides and chalcogenides, Acta Crystallogr. Sect. A. 32 (1976) 751–767, https://doi.org/10.1107/S0567739476001551.
[54] Y. Takasu, T. Sugino, Y. Matsuda, Electrical conductivity of praseodymia doped ceria, J. Appl. Electrochem. 14 (1) (1984) 79–81, https://doi.org/10.1007/BF00611261.
[55] M. Nauer, C. Ftikos, B.C.H. Steele, An evaluation of Ce-Pr oxides and Ce-Pr-Nb oxides mixed conductors for cathodes of solid oxide fuel cells: Structure, thermal expansion and electrical conductivity, J. Eur. Ceram. Soc. 14 (6) (1994) 493–499, https://doi.org/10.1016/0955-2219(94)90118-X.
[56] R. Chockalingam, A.K. Ganguli, S. Basu, Praseodymium and gadolinium doped ceria as a cathode material for low temperature solid oxide fuel cells, J. Power Sources 250 (2014) 80–89, https://doi.org/10.1016/J.JPOWSOUR.2013.10.105.
[57] K. Develos-Bagarinao, K. Yamaji, H. Kishimoto, H. Shimada, K. Yamaji, Nanoengineering of cathode layers for solid oxide fuel cells to achieve superior power densities, Nat. Commun. 12 (2021) 3979, https://doi.org/10.1038/s41467-021-24255-w.
[58] S.B. Adler, Factors governing oxygen reduction in solid oxide fuel cell cathodes, Chem. Rev. 104 (10) (2004) 4791–4843, https://doi.org/10.1021/cr020724o.
[59] T. Jacobsen, P.V. Hendriksen, S. Koch, Diffusion and conversion impedance in solid oxide fuel cells, Electrochim. Acta 53 (25) (2008) 7500–7508, https://doi.org/10.1016/J.ELECTACTA.2008.02.019.
[60] A. Maradesa, B. Py, J. Huang, et al., Advancing electrochemical impedance analysis through innovations in the distribution of relaxation times methods, Joule (2024) 1–24, https://doi.org/10.1016/j.joule.2024.05.008 (Published online).
[61] R. De Levie, The influence of surface roughness of solid electrodes on electrochemical measurements, Electrochim. Acta 10 (2) (1965) 113–130, https://doi.org/10.1016/0013-4686(65)87012-8.
[62] J. Gunning, The exact impedance of the de Levie grooved electrode, J. Electroanal. Chem. 392 (1–2) (1995) 1–11, https://doi.org/10.1016/0022-0728(95)03951-C.
[63] A. Lasia, Electrochemical Impedance Spectroscopy and Its Applications 9781461489, 2014, https://doi.org/10.1007/978-1-4614-8933-7.
[64] M.F. Gazulla, M.J. Ventura, C. Andreu, J. Gilabert, M. Orduña, M. Rodrigo, Praseodymium oxides., Complete characterization by determining oxygen content, Microchem. J. 148 (May) (2019) 291–298, https://doi.org/10.1016/j.microc.2019.05.013.
[65] J.S. Kim, C.W. Na, C.H. Kwak, et al., Humidity-independent gas sensors using Pr-doped In2O3 macroporous spheres: role of cyclic Pr3+/Pr4+ redox reactions in suppression of water-poisoning effect, ACS Appl. Mater. Interfaces 11 (28) (2019) 25322–25329, https://doi.org/10.1021/acsami.9b06386.
[66] J. Nielsen, M. Mogensen, SOFC LSM:YSZ cathode degradation induced by moisture: an impedance spectroscopy study, Solid State Ionics 189 (1) (2011) 74–81, https://doi.org/10.1016/j.ssi.2011.02.019.
[67] J. Hayd, E. Ivers-Tiffée, Detailed electrochemical study on nanoscaled La 0.6 Sr 0.4 CoO 3-δ SOFC thin-film cathodes in dry, humid and CO 2-containing atmospheres, J. Electrochem. Soc. 160 (11) (2013) F1197–F1206, https://doi.org/10.1149/2.026311jes.
[68] P. Hjalmarsson, M. Søgaard, M. Mogensen, Electrochemical performance and degradation of (La0.6Sr0.4)0.99CoO3-δ as porous SOFC-cathode, Solid State Ionics 179 (27–32) (2008) 1422–1426, https://doi.org/10.1016/j.ssi.2007.11.010.
[69] Z. Zhao, L. Liu, X. Zhang, et al., High- and low- temperature behaviors of La0.6Sr0.4Co0.2Fe0.8O3−δ cathode operating under CO2/H2O-containing atmosphere, Int. J. Hydrog. Energy 38 (35) (2013) 15361–15370, https://doi.org/10.1016/J.IJHYDENE.2013.09.089.
[70] E. Dogdibegovic, R. Wang, G.Y. Lau, M.C. Tucker, High performance metal-supported solid oxide fuel cells with infiltrated electrodes, J. Power Sources 2019 (410–411) (October 2018) 91–98, https://doi.org/10.1016/j.jpowsour.2018.11.004.

Supporting information

Unveiling the Potential of Praseodymium Oxide as Efficient Oxygen Electrode for Low-Temperature Solid Oxide Cell Applications.

Bartłomiej Lemieszek[a]*, Lulu Alluhaibi[b], Alexey Maximenko[b], Łukasz Gaweł[c], Aleksandra Mielewczyk-Gryń[d], Michał Struzik[e], Marcin Małys[e], Muhammad Imran Asghar[f], Grzegorz Cempura[g], Piotr Jasiński[a], Sebastian Molin[a]

[a] Advanced Materials Centre, Faculty of Electronics, Telecommunications and Informatics, Gdańsk University of Technology, ul. G. Narutowicza 11/12, 80-233 Gdańsk, Poland

[b] National Synchrotron Radiation Centre SOLARIS, Jagiellonian University, Czerwone Maki 98, 30-392, Kraków, Poland

[c] Institute of Nanotechnology and Materials Engineering, Faculty of Applied Physics and Mathematics, and Advanced Materials Centre, Gdańsk University of Technology, Gdańsk, Poland

[d] Department of Electrochemistry Corrosion and Materials Engineering, Faculty of Chemistry, Gdansk University of Technology, 11/12 Narutowicza Street, 80-233, Gdansk, Poland

[e] Warsaw University of Technology, Faculty of Physics, Koszykowa 75, 00-662 Warsaw, Poland

[f] Renewable Energy Technologies Group, Faculty of Engineering and Natural Sciences, Tampere University, FI-33014, Tampere, Finland

[g] International Centre for Electron Microscopy, Faculty of Metals Engineering and Industrial Computer Science, AGH University of Science and Technology, 30-059 Kraków, Poland

Corresponding author: bartlomiej.lemieszek@pg.edu.pl

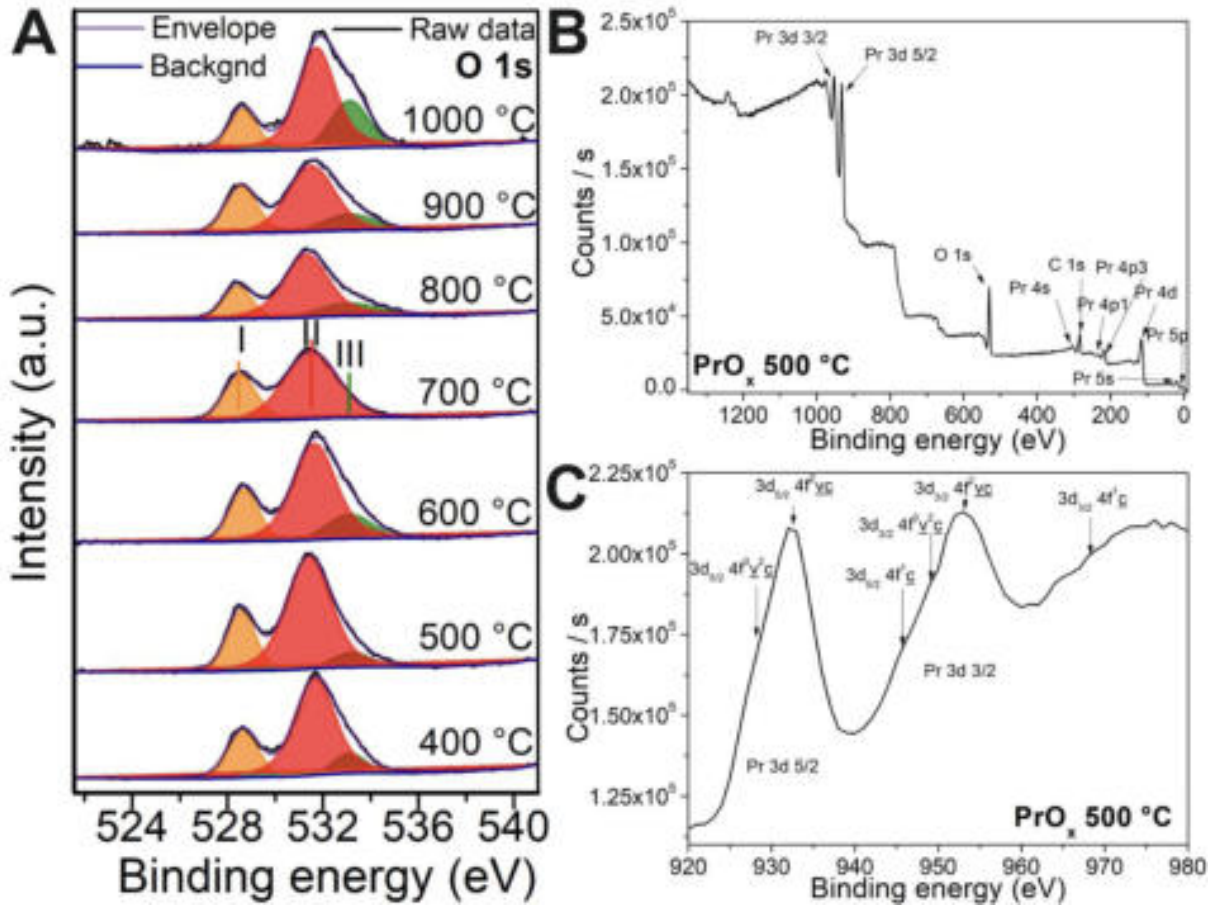


Figure S1. XPS survey example collected for a praseodymium oxide sample annealed at 500 °C (A), with detailed the Pr $3d_{5/2}$ and Pr $3d_{3/2}$ range (B).

The integrated areas of the characteristic electronic-transition peaks—labelled B (Pr^{3+}), C, and D (Pr^{4+})—were used to calculate the praseodymium cation's average oxidation state according to the equation:

$$\mathrm{Pr}_{average} = 3 \cdot \frac{A(Pr^{3+})}{A(Pr^{3+}) + A_1(Pr^{4+}) + A_2(Pr^{4+})} 4 \cdot \frac{A_1(Pr^{4+}) + A_2(Pr^{4+})}{A(Pr^{3+}) + A_1(Pr^{4+}) + A_2(Pr^{4+})}$$

Where: A(Pr^{3+}) corresponds to the area under the gaussian obtained for a given fitted peak.

The fractional content of each oxidation state was calculated using formula:

$$\mathrm{Pr}^{4+}\ (\%) = \frac{A_1(Pr^{4+}) + A_2(Pr^{4+})}{A(Pr^{3+}) + A_1(Pr^{4+}) + A_2(Pr^{4+})} \cdot 100\%$$

Fractional content uncertainties were evaluated via a variance-based method, using following formula:

$$\Delta Pr^{3+} = \sqrt{\left(\frac{A_1(Pr^{4+}) + A_2(Pr^{4+})}{A(Pr^{3+}) + A_1(Pr^{4+}) + A_2(Pr^{4+})} \cdot \Delta A(Pr^{3+})\right)^2 + \left(\frac{-A(Pr^{3+})}{A(Pr^{3+}) + A_1(Pr^{4+}) + A_2(Pr^{4+})} \cdot \Delta A(Pr^{4+}_{total})\right)^2}$$

Where:

$\Delta A(Pr^{3+})$ and $\Delta A_{1,2}(Pr^{4+})$ represent the uncertainties of the determined peak areas corresponding to Pr^{3+} and Pr^{4+}, and:

$$\Delta A(Pr^{4+}_{total}) = \sqrt{\Delta A_1(Pr^{4+})^2 + \Delta A_2(Pr^{4+})^2}$$

The uncertainties of the average oxidation state were determined using the following formula:

$$\Delta Pr_{average} = \sqrt{(3 \cdot \Delta Pr^{3+})^2 + (4 \cdot \Delta Pr^{4+})^2 + 2 \cdot 3 \cdot 4 \cdot Cov(Pr^{3+}, Pr^{4+})}$$

Where *Cov(Pr^{3+},Pr^{4+})* denotes the covariance, applied as a result of the anticorrelation between the Pr^{3+} and Pr^{4+} cations. This results from the fact that the sum of the constituent oxidation states is always equal to 1.

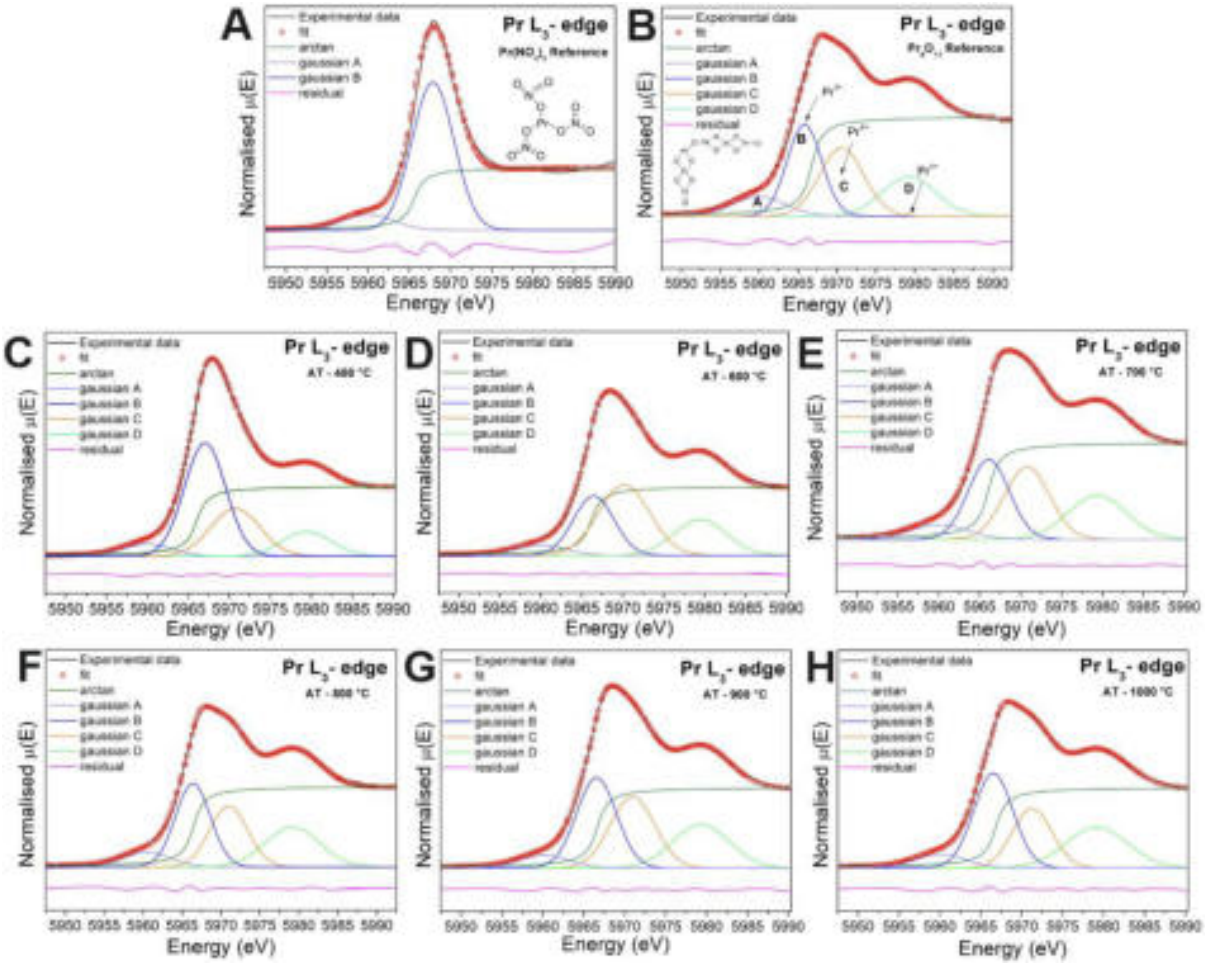


Figure S2. Fits of individual type of spectra using the peak fitting function for: reference samples $Pr(NO_3)_3$ (A) and Pr_6O_{11} (B) and research samples PrO_x as a function of annealing temperature from 400 °C to 1000 °C (C-H).

Table S5. Calculated values from the peak fitting used to determine the average oxidation state of the praseodymium cation.

	Peak A			Peak B			Peak C		
PrO_x	**height**	**Position**	**sigma**	**height**	**Position**	**sigma**	**height**	**Position**	**sigma**
400	1.212±0.030	5959.986	2.933±0.072	9.625±0.617	5967.031±0.20	2.527±0.011	4.853±0.713	5970.721±0.22	3.021±0.239
500	1.011±0.028	5959.830	2.810±0.074	5.798±0.755	5966.647±0.36	2.473±0.014	7.173±0.849	5970.167±0.12	3.018±0.185
600	1.043±0.026	5960.055	3.212±0.086	4.937±0.523	5966.455±0.28	2.468±0.014	7.430±0.624	5970.163±0.12	3.132±0.142
700	1.231±0.034	5960.088	3.485±0.100	4.814±0.281	5966.100±0.35	2.513±0.024	4.818±0.467	5970.780±0.12	2.771±0.074
800	1.261±0.036	5960.499	3.022±0.084	5.381±0.212	5966.403±0.23	2.238±0.018	4.295±0.437	5970.996±0.11	2.449±0.058
900	1.094±0.027	5960.200	3.474±0.113	6.319±0.179	5966.557±0.15	2.430±0.014	5.583±0.370	5970.948±0.08	2.715±0.057
1000	1.173±0.033	5960.118	3.014±0.081	6.516±0.250	5966.524±0.23	2.391±0.081	4.109±0.427	5971.260±0.12	2.404±0.056
Reference									
$Pr(NO_3)_3$	1.611±0.092	5960.010	3.098±0.200	12.687±0.356	5967.870±0.04	2.553±0.020	-	-	-
Pr_6O_{11}	1.578±0.043	5959.986	3.351±0.097	4.865±0.489	5965.826±0.19	2.211±0.020	4.644±0.489	5970.603±0.16	2.837±0.104

	Peak D			Arctan.			
PrO_x	**height**	**Position**	**sigma**	**height**	**Posit.**	**sigma**	**Av. Oxidation state**
400	2.496±0.123	5979.445±0.28	3.017±0.119	0.945±0.010	5966.014±0.26	1.000	3.433±0.144
500	3.825±0.114	5979.385±0.22	3.185±0.095	0.926±0.010	5966.042±0.25	1.000	3.655±0.171
600	3.887±0.120	5979.460±0.22	3.212±0.086	0.930±0.011	5966.139±0.20	1.000	3.696±0.127
700	3.806±0.145	5979.377±0.43	3.598±0.174	0.931±0.017	5966.028±0.24	1.000	3.642±0.094
800	4.010±0.148	5979.187±0.35	3.496±0.143	0.929±0.016	5966.455±0.28	1.000	3.607±0.081
900	4.348±0.115	5979.335±0.27	3.475±0.113	0.930±0.012	5966.631±0.21	1.000	3.611±0.057
1000	4.394±0.136	5979.132±0.43	3.785±0.194	0.926±0.016	5966.811±0.12	1.000	3.566±0.080
Reference							
$Pr(NO_3)_3$	-	-	-	0.844±0.006	5965.588±0.42	1.000	3.000
Pr_6O_{11}	3.251±0.176	5979.259±0.52	3.446±0.204	0.955±0.019	5966.749±0.29	1.000	3.619±0.028

Each line shape has an independent centroid, height, and width. Peak shapes are unit normalized, meaning the height is uniquely the area under the peak. Sigma is the width of the gaussian and the position is the centre of the specific peak.

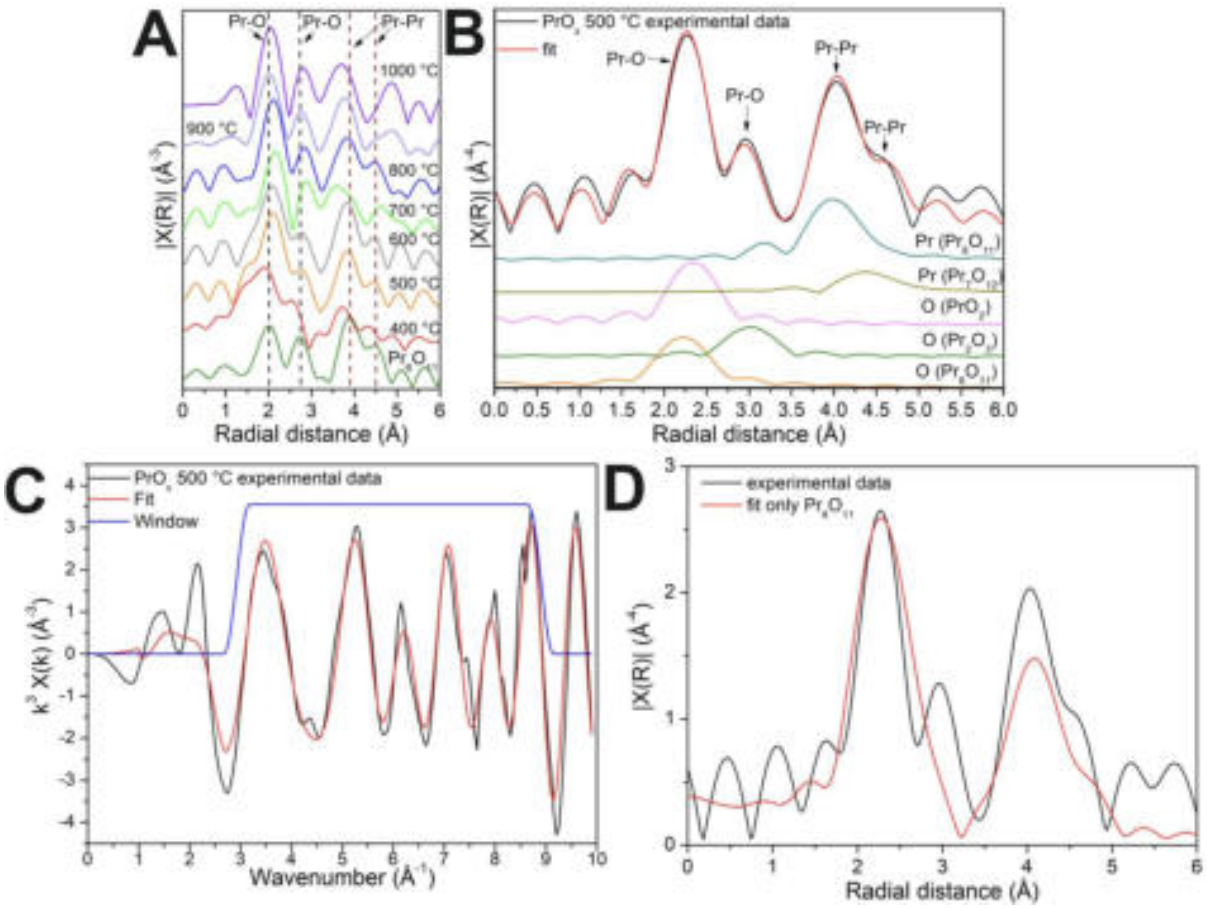


Figure S3. R-space oscillations Fourier transform (FT) ($k^2\chi(k)$) EXAFS spectra for the reference materials and PrO_x (A); . determined the vibration spectra $|X(R)|$ ($Å^{-4}$) in k-space with a fit allowing the identification of specific bonds (B) and k^3 $X(k)(Å^{-3}$ for PrO_x annealed at 500 °C (C) and best fit obtained using only data for the Pr_6O_{11} phase (D).

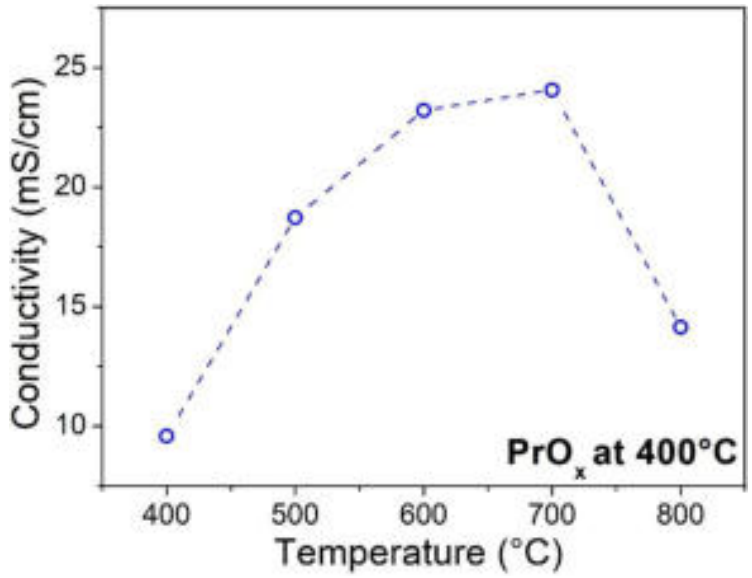


Figure S4. Comparison of the electrical conductivity values obtained for PrO_x layer at the temperature of 400 °C.

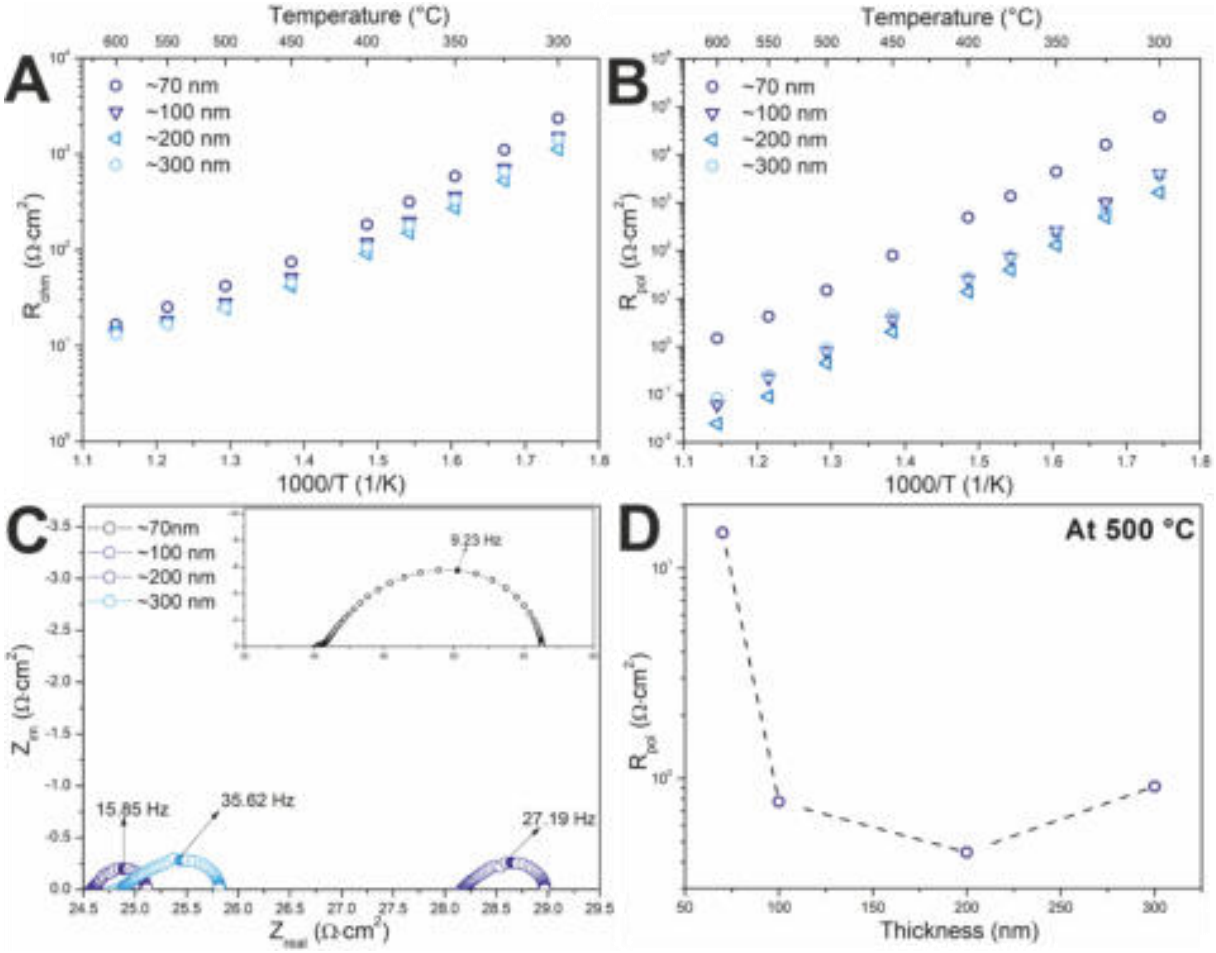


Figure S5. The Arrhenius plot of the ohmic resistance (A) and polarization resistance (B) obtained from symmetric measurements of half-cells with varying electrode thicknesses. Additionally, the Nyquist plots recorded at 500 °C (C), along with a comparative analysis of R_{pol} values as a function of electrode thickness (D).

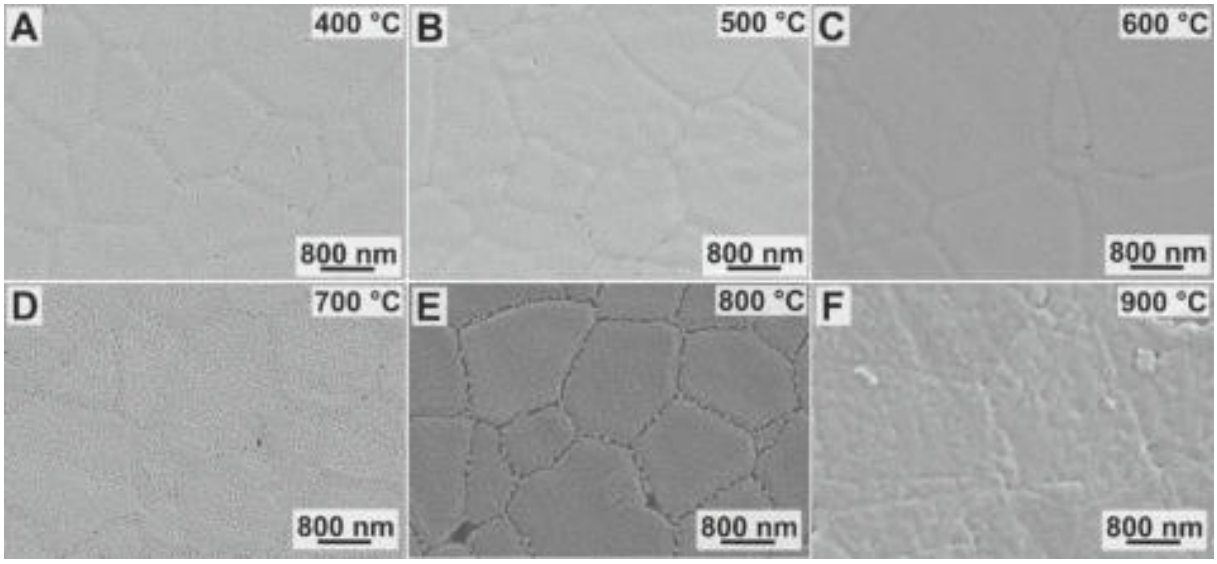


Figure S6. SEM images of the surface of PrO_x oxygen electrodes deposited on CGO and annealed at temperatures ranging from 400 to 900 °C (A-F).

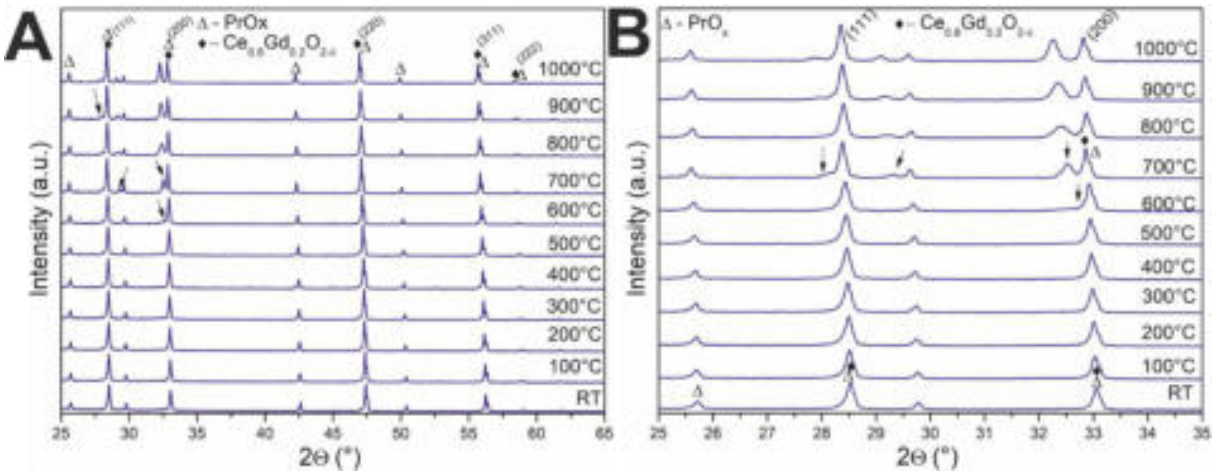


Figure S7. Diffraction patterns obtained from high-temperature XRD measurement of PrO_x layer deposited on CGO (A) with a focus on the 25° to 35° region (B).

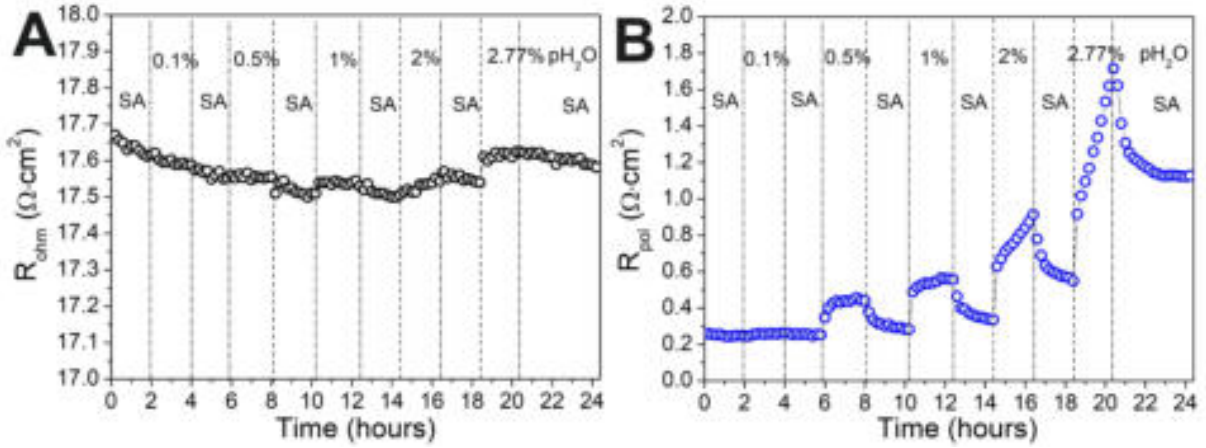


Figure S8. Results of impedance analysis illustrating the influence of different pH_2O levels on R_{ohm} (A) and R_{pol} (B) values measured at 500 °C.

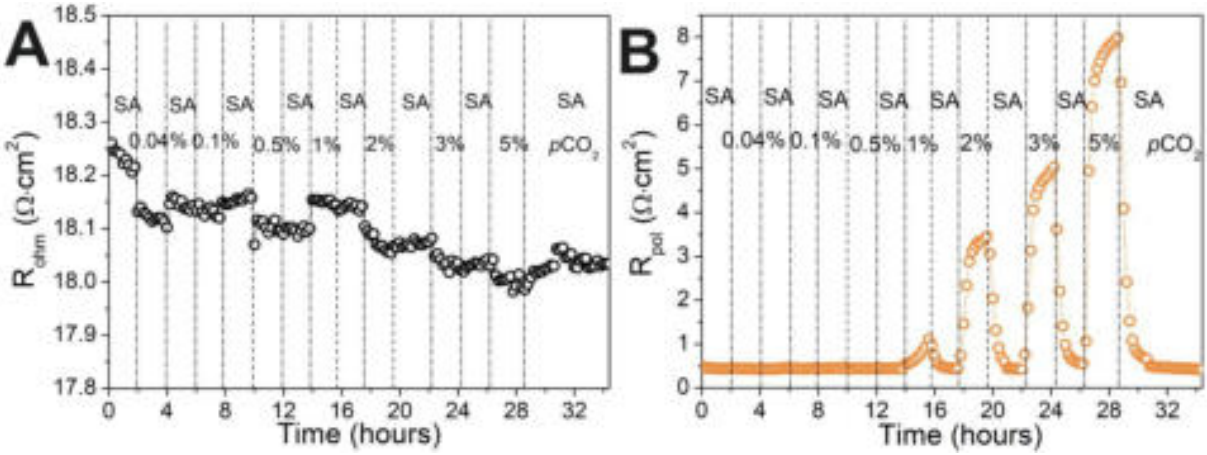


Figure S9. Results of impedance analysis illustrating the influence of different pCO_2 levels on R_{ohm} (A) and R_{pol} (B) values measured at 500 °C.

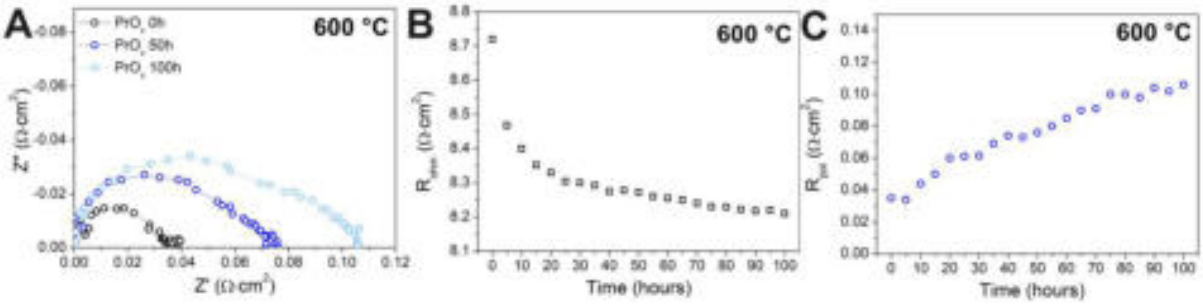


Figure S10. Nyquist plots of impedance spectra recorded after 0. 50. and 100 hours with subtracted ohmic resistance at 600 °C (A), with changes in ohmic resistance (B) and polarization resistance (C) recorded during experiment.

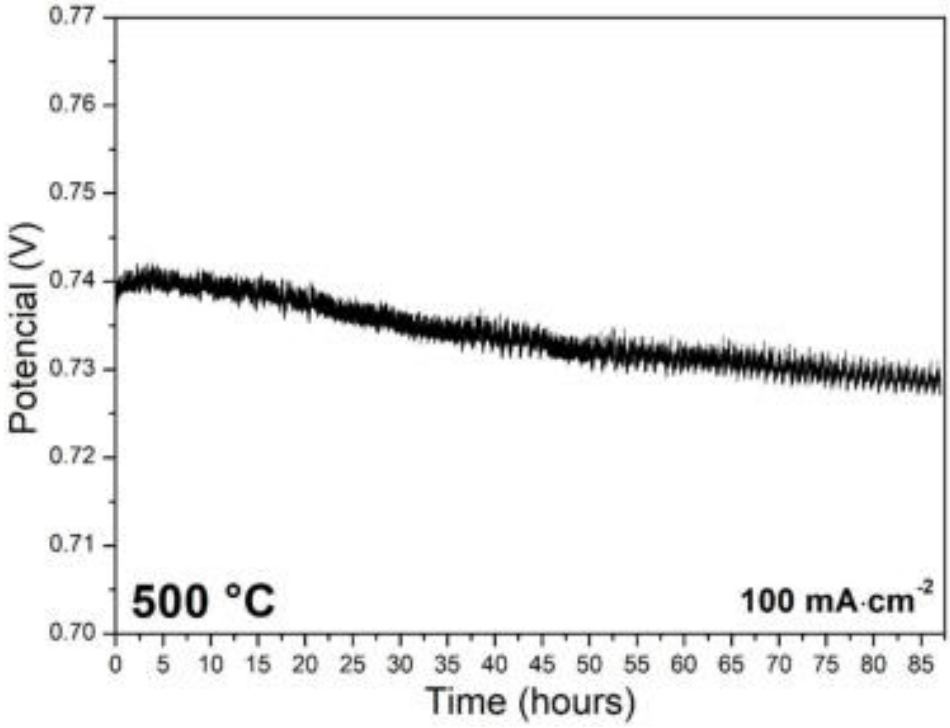


Figure S11. Real-time potential change during an 87-hour measurement in fuel cell mode at a load of 100 mA·cm^{-2} at 500 °C

11. Conclusions

This dissertation explores the potential of various materials and design strategies that could support the next generation of solid oxide cells. Efficient hydrogen-based energy production may become a serious alternative within the evolving energy mix, particularly during the ongoing energy transition. In this context, effective solutions must enable lower SOC operating temperatures, which would simultaneously reduce stack costs. Such advances would improve economic feasibility and establish SOCs as a stable complement to intermittent renewable energy sources, such as wind and photovoltaic systems, thereby strengthening modern power networks.

Achieving this goal requires a significant reduction in energy production costs. A central strategy is to lower the operating temperature of the cells, allowing the use of less expensive metallic alloys. This is particularly important because interconnects and current leads account for a large share of system costs. Several approaches are being developed to address this challenge, including the introduction of new low-cost coating materials with high electrochemical performance, as well as modification of existing materials to improve their properties. Such modifications may involve doping, grain size control, or optimized electrode architectures. Progress in these areas depends on a thorough understanding of the materials and their behaviour, enabling the extraction of maximum information from structural, chemical, and electrochemical studies.

Within this thesis, research was carried out to assess the feasibility of using cobalt-free materials as protective layers for metallic interconnects in systems operating at 700 °C. In addition, selected materials were investigated for efficient oxygen reduction reactions in low-temperature SOCs operating at or below 600 °C.

The results are presented in Chapter 10. The first two articles support Hypothesis 1 and demonstrate that cobalt-free materials, specifically rare-earth oxides and the spinel $CuMn_{1.7}Fe_{0.3}O_4$, provide a novel solution for protective coatings on interconnects. The inclusion of rare-earth oxides enhances the chromium diffusion-blocking capability of CMFO, providing an effective alternative to the state-of-the-art MCO. Moreover, the complementary

advantages of these materials—higher electrical conductivity in the case of CMFO and effective corrosion inhibition by rare-earth oxides—compensate for their individual limitations. The main achievements of these studies are:

• Development of effective protective layers based on rare-earth oxides and cobalt-free spinel $CuMn_{1.7}Fe_{0.3}O_4$.

• Significant reduction of ASR values after 2000 and 4000 hours of exposure to an oxidizing environment at 700 °C.

• Enhancement of the overall chromium diffusion-blocking ability of CMFO through the addition of thin (100 nm) rare-earth oxide layers by reducing the corrosion rate.

The following three articles support Hypothesis 2. Two materials - $La_{0.6}Sr_{0.4}CoO_{3-\delta}$ and praseodymium oxide - were investigated as promising oxygen electrode candidates for low-temperature solid oxide cells (≤600 °C). It was shown that partially amorphous LSC exhibits better electrochemical performance than its crystalline counterpart, which is linked to a reduction in the average cobalt oxidation state. In addition, Article 4 reported the development of high-performance oxygen electrodes using infiltration of a porous CGO backbone, enabling efficient operation at 600 °C while reducing electrode fabrication costs through better use of electrochemically active material. Finally, the last article provided detailed insight into PrO_x as an oxygen electrode material. The study revealed its multiphase nature and emphasized the complexity of its structural characterization. XAFS analysis enabled precise determination of the oxidation state and local structure of praseodymium, which had not been sufficiently addressed in earlier literature. The main achievements of these studies can be summarized as follows:

• Development of two new precursor formulations for electrode deposition.

• Deposition of electrodes using low-cost techniques while achieving electrochemical performance comparable to more advanced methods reported in the literature, enabling scalability and cost reduction.

• Determination of optimal annealing temperatures for oxygen electrode materials, differing from those commonly used.

• Detailed insights into the structural and electrochemical behaviour of partially amorphous LSC, including the first observation of a 0.5-unit decrease in the average cobalt oxidation state compared with the crystalline phase.

• Determination of the average oxidation state of praseodymium at different annealing temperatures, revealing significant deviations from assumptions reported in the literature due to the coexistence of multiple PrO_x phases.

• Comprehensive electrochemical characterization of electrode materials using EIS under varying pO_2 conditions, identifying the limiting factors affecting oxygen reduction kinetics.

• Verification of the influence of H_2O and CO_2 on electrode performance, demonstrating that PrO_x exhibits greater tolerance to these species than state-of-the-art materials such as LSC.

• Experimental validation of the proposed oxygen electrode configurations in full fuel cells, achieving higher power densities than commercial reference cells.

The proposed and tested approaches provide alternatives to conventional solutions, enabling the replacement of costly materials and the reduction of associated expenses. This creates a pathway toward systems capable of efficient operation at lower temperatures. This thesis provides a foundation for further research on promising materials for low-temperature SOC applications. Future work will focus on the development of operando XAFS techniques for comprehensive structural characterization under operating conditions. This will be an important step toward a deeper understanding of electrochemical reactions and their underlying mechanisms.

Collectively, the articles included in this dissertation represent an important step toward the development of efficient SOC systems operating at lower temperatures. These advances not only contribute to meaningful cost reduction but also accelerate the path toward large-scale commercialization of these technologies.

Other publication record in journals from the JCR list:

1. Urbanowicz M, Sadowska K, **Lemieszek B**, et al. Effect of dendrimer-based interlayers for enzyme immobilization on a model electrochemical sensing system for glutamate. Bioelectrochemistry. 2023;152:108407. doi:10.1016/J.BIOELECHEM.2023.108407
2. Lankauf K, **Lemieszek B**, Górnicka K, et al. Enhanced Electrochemical Performance of MnCo1.5Fe0.5O4 Spinel for Oxygen Evolution Reaction through Heat Treatment. Energy & Fuels. 2024;38:1330-1336. doi:10.1021/acs.energyfuels.3c02875
3. Kabir A., **Lemieszek B.**, Karczewski J., et al. Ultrafast high-temperature sintering (UHS) of cerium oxide-based compound. Open Ceram. 2024;17:100551. doi:10.1016/J.OCERAM.2024.100551
4. Kabir A., **Lemieszek B.**, Varenik M., et al. Enhanced Mechanical and Electromechanical Properties of Compositionally Complex Zirconia Zr1−x(Gd1/5Pr1/5Nd1/5Sm1/5Y1/5)xO2−δ Ceramics. ACS Appl Mater Interfaces. 2024;16:12765-12772. doi:10.1021/acsami.3c17501
5. Baba MA, **Lemieszek B**, Sriubas M, et al. Femtosecond laser ablated trench array for improving performance of commercial solid oxide cell. J Power Sources. 2024;616:235128. doi:10.1016/j.jpowsour.2024.235128
6. Ur Rehman Z, **Lemieszek B**, Cempura G, et al. Solution combustion synthesis and electrospinning of storage performance. *J Energy Chem*. 2026;151:120645. doi:10.1016/j.est.2026.120645
7. Baba MA, **Lemieszek B**, Gaweł Ł, et al. Influence of femtosecond laser-generated LIPSS on corrosion behavior of Crofer 22 APU stainless steel for SOCs applications. *Opt Laser Technol*. Published online 2026. doi:10.1016/j.optlastec.2025.114596
8. Ignaczak J, Bik M, **Lemieszek B**, et al. Long-term stability and oxidation behavior of Mn2CuO4, Mn1.9Fe0.1CuO4, Mn1.7Fe0.3CuO4 coatings on SOFC interconnects: summary of a 10,000-h oxidation test. *J Power Sources*. 2026;674:239785. doi:10.1016/j.jpowsour.2026.239785

Conference attendance and lectures

2022:

- MSRC; VIIITH INTERNATIONAL SAMSONOV CONFERENCE "MATERIALS SCIENCE OF REFRACTORY COMPOUNDS" (MSRC-2022) 24-27 May 2022 Kyiv, Ukraine (online); Oral presentation: "Ceramic-Spinel Composite Layers As Effective Materials For Protective Interconnector Coatings For Solid Oxide Cells"; Authors: Bartłomiej Lemieszek, Sebastian Molin, date of presentation 26.05.2022.
- AMT 2022; ADVANCED MATERIALS AND TECHNOLOGIES 2022 24-th International Conference – School, 22 – 26 August, 2022, Palanga, Lithuania (poster). Functional oxygen electrode layers for Solid Oxide Cells by a spin-coating method using polymeric precursors. Authors: Bartłomiej Lemieszek, B. Kamecki, P. Jasiński, S. Molin
- 7 TH POLISH FORUM SMART ENERGY CONVERSION & STORAGE 4 – 6 September, 2022, Ogrodzieniec, Poland; Poster; "Functional oxygen electrode layers for Solid Oxide Cells by a spin-coating method using polymeric precursors"; Authors: Bartłomiej Lemieszek, B. Kamecki, P. Jasiński, S. Molin.

2023

- ISSFIT 15; 15th International Symposium on Systems with Fast Ionic Transport Dubrovnik, Croatia 18-22.04.2023; Oral presentation; "Development and performance of $La_{0.6}Sr_{0.4}CoO_{3-\delta}$ oxygen electrode for low-temperature (<500°C) Solid Oxide Cells" Authors: Bartłomiej Lemieszek , Mindaugas Ilickas, Jan Jamroz, Asta Tamulevičienė, Jakub Karczewski, Patryk Błaszczak, Brigita Abakevičienė, Marcin Małys, Sigitas Tamulevičius, Piotr Jasiński, Sebastian Molin; Date: 20.04.2023

2024

- International Symposium SYLINDA 7-8 March 2024 Kraków, Poland, Poster: Enhanced electrochemical performance of amorphous $La_{0.6}Sr_{0.4}CoO_{3-\delta}$ oxygen electrode materials for low temperature solid oxide cells operating at 400°C Bartłomiej Lemieszek, Jakub Karczewski, Alexey Maximenko, Piotr Jasiński, Sebastian Molin
- XVI SYMPOZJUM PRZEWODNIKI SZYBKICH JONÓW, AUGUSTÓW 16-19.IV.2024, 2 posters:
  "Development and characterization of the electrochemical properties of PrO_x as an efficient cathode for intermediate solid oxide cells." Authors: Bartłomiej Lemieszek, Piotr Jasiński, Sebastian Molin;

"High-performance oxygen electrodes for intermediate solid oxide cells (SOC) prepared by $Ce_{0.8}Gd_{0.2}O_{2-d}$ backbone infiltration." Authors: Ömer Faruk Aksoy, Bartłomiej Lemieszek, Murat Murutoglu, Piotr Jasiński, Sebastian Molin.

- PRIME 2024 6-11.10.2024 Honolulu, USA
  "A New Generation of Protective Coating Materials Based on $CuMn_{1.7}Fe_{0.3}O_4$-Me_2O_3 (Me=Y, Gd) Ceramic Bilayers for Solid Oxide Cells Interconnect" Authors: Bartłomiej Lemieszek, Justyna Ignaczak, Krystian Lankauf, Patryk Błaszczak, Maciej Bik, Marcin Zając, Maciej Sitarz, Piotr Jasiński, Sebastian Molin
  "Characterization of the Structural and Electrochemical Properties of Praseodymium Oxide as an Efficient Oxygen Electrode for Intermediate Solid Oxide Cells" Authors: Bartłomiej Lemieszek, Piotr Jasiński, Sebastian Molin.

2025

- 16th Pacific Rim Conference on Ceramic and Glass Technology including Glass & Optical Materials Division Meeting (GOMD 2025) 04-09.05.2025 - Oral presentation: Structural and Electrochemical Properties of Praseodymium Oxide as a High-Performance Oxygen Electrode for Low-temperature Solid Oxide Cells B. Lemieszek, A. Maximenko, Ł. Gaweł, A. Mielewczyk-Gryń, M. Struzik , G. Cempura, M. Malys, M. I. Asghar, P. Z. Jasinski, S. Molin
- LEAPS Meets Advanced Materials for Energy Conference 2025, Sopot 18-23.05.2025 Poster: "Advanced Characterization of LSC and PrOx Electrodes for Solid Oxide Cells: An XAFS study and importance." Bartłomiej Lemieszek, Alexey Maximenko, Piotr Jasiński, Sebastian Molin
- **Invited Lecture:** "Characterization of Oxygen Electrodes materials for low-temperature Solid Oxide Cells", X-ray Seminar, Institute of Physics, Polish Academy of Science, 17.06.2025

List of Figures

Figure 1. Global energy consumption by source of energy[3]. 16
Figure 2. Overview of fuel cell types in relation to operating temperature, efficiency, system complexity, fabrication cost, and material cost[23]. 19
Figure 3. Cross-section of a modern anode-supported solid oxide cell (SOC), highlighting individual components. 22
Figure 4. Generations of SOCs with support indication and operating temperature range. 24
Figure 5. Construction and operation of basic SOC system. 30
Figure 6. Activation, ohmic and mass losses plotted throughout the I–V curve[83]. 33
Figure 7. Example of an impedance spectrum with components listed. 37
Figure 8. The crystal structure of all three zirconia phases: (a) cubic, (b) tetragonal, and (c) monoclinic[105,106]. 40
Figure 9. Comparison of the ionic conductivity of different types of solid oxide materials[32]. 42
Figure 10. Arrhenius plots of electronic conductivity for various oxygen electrodes for SOCs[134]. 45
Figure 11. Variability of praseodymium oxides. 46
Figure 12. Sketch of deposition setup (A), and the example of samples after the deposition and annealing at 400 °C (B). 56
Figure 13. Sketch of deposition setup (A), and the example of sample with deposited spinel layer (B). 58
Figure 14. Graphic visualization of the process of deposition of ceramic layers by spin-coating technique. 59
Figure 15. Spin coater used to deposit PrOx layers on YSZ, CGO, and LSC substrates, along with the sample before and after deposition. 59
Figure 16. Bragg's Law. 61
Figure 17. Scheme of photoelectron and Auger electron process (A) and the construction of modern XPS (B)[196]. 63
Figure 18. an Omicron plate with powders of the reference materials applied (A), a loading station with plates on the PIRX beamline (B) and the end part of the ASTRA beamline with the marking of the measurement and reference chamber. 66
Figure 19. Energy level diagrams describing the physical phenomenon of Rayleigh scattering and Raman scattering[199]. 68
Figure 20. Schematic representation of the operating principle of an FTIR spectrometer using a Michelson interferometer[196]. 69
Figure 21. Principal function of the SEM-EDS analysis technique (A). Based on work[200]. A stand with a Phenom XL microscope, which is part of the equipment of Gdańsk University of Technology, that where a significant part of the performed microscopic analyses (B). 70

Figure 22. ASR measurement diagram for Crofer 22 APU steel samples after corrosion tests (A) and a measuring station for ASR measurements at the Gdańsk University of Technology (B). 73
Figure 23. Schematic diagram of the sample and electrical connections on which conductivity was measured (A) and a photo of the measurement system with the sample - PrO_x layer deposited on fused silica (B), and a measuring station for Van der Pauw measurements at the Gdańsk University of Technology (C). 74
Figure 24. Graphic diagram of the sample for symmetrical measurements and the measurement system (A) and a measuring station for EIS measurements at the Gdańsk University of Technology (B) along with a photo of the compression cell where the measurement samples are placed (C). 77
Figure 25. Prepared fuel cell with applied oxygen electrode (A), Fiaxell Open Flanges V5 test configuration with the cell after measurements (B) and cell connection diagram (C) and a measuring station for cell measurements at the Gdańsk University of Technology (D). 79

List of Tables

Table 1. Review of works related to rare earth metals and spinel derivatives $CuMn_2O_4$. 49
Table 2.Overview of the results obtained so far for LSC as an oxygen electrode. 50
Table 3. Overview of the results obtained so far for praseodymium as an part or functional oxygen electrode. 52
Table S1. Fourier transform fit values for best fit. 139
Table S1. Calculated values from the peak fitting used to determine the average oxidation state of the praseodymium cation. 180

12. Bibliography

[1] I. Tatarewicz *et al.*, “TRANSFORMACJA SEKTORA ENERGETYCZNEGO POLSKI I UE DO 2050 ROKU,” 2022.

[2] J. L. Holechek, H. M. E. Geli, M. N. Sawalhah, and R. Valdez, “A Global Assessment: Can Renewable Energy Replace Fossil Fuels by 2050?,” *Sustain.*, vol. 14, no. 8, pp. 1–22, 2022, doi: 10.3390/su14084792.

[3] M. Ritchie, Hannah; Roser, “Fossil Fuels; Our world in data,” *Our world in data*. p., 2018, [Online]. Available: https://ourworldindata.org/fossil-fuels.

[4] A. Zhang, J. Yang, Y. Luo, and S. Fan, “Forecasting the progression of human civilization on the Kardashev Scale through 2060 with a machine learning approach,” *Sci. Rep.*, vol. 13, no. 1, pp. 1–10, 2023, doi: 10.1038/s41598-023-38351-y.

[5] D. Gielen, F. Boshell, D. Saygin, M. D. Bazilian, N. Wagner, and R. Gorini, “The role of renewable energy in the global energy transformation,” *Energy Strateg. Rev.*, vol. 24, pp. 38–50, Apr. 2019, doi: 10.1016/J.ESR.2019.01.006.

[6] E. Rusu, “Evaluation of the wave energy conversion efficiency in various coastal environments,” *Energies*, vol. 7, no. 6, pp. 4002–4018, 2014, doi: 10.3390/en7064002.

[7] B. Igliński *et al.*, “Assessment of the Current Potential of Hydropower for Water Damming in Poland in the Context of Energy Transformation,” *Energies*, vol. 15, no. 3, 2022, doi: 10.3390/en15030922.

[8] M. Kaczmarczyk and A. Sowiżdżał, “Environmental and Social Dimensions of Energy Transformation Using Geothermal Energy,” *Energies*, vol. 18, no. 13, 2025, doi: 10.3390/en18133565.

[9] B. C. Tashie-Lewis and S. G. Nnabuife, “Hydrogen Production, Distribution, Storage and Power Conversion in a Hydrogen Economy - A Technology Review,” *Chem. Eng. J. Adv.*, vol. 8, p. 100172, Nov. 2021, doi: 10.1016/J.CEJA.2021.100172.

[10] H. van ‘t Noordende, F. van Berkel, and M. Stodolny, “Next Level Solid Oxide Electrolysis,” *Inst. Sustain. Process Technol.*, 2023.

[11] M. Seitz, H. von Storch, A. Nechache, and D. Bauer, “Techno economic design of a solid oxide electrolysis system with solar thermal steam supply and thermal energy storage for the generation of renewable hydrogen,” *Int. J. Hydrogen Energy*, vol. 42, no. 42, pp. 26192–26202, 2017, doi: 10.1016/j.ijhydene.2017.08.192.

[12] R. M. Nienhuis, M. van Rooij, W. A. Prins, B. Jayawardhana, and A. I. Vakis, “Investigating the efficiency of a novel offshore pumped hydro energy storage system: Experimental study on a scale prototype,” *J. Energy Storage*, vol. 74, p. 109374, Dec. 2023, doi: 10.1016/J.EST.2023.109374.

[13] B. Elmegaard and W. Brix, “Efficiency of compressed air energy storage,” *Proc. 24th Int. Conf. Effic. Cost, Optim. Simul. Environ. Impact Energy Syst. ECOS 2011*, pp. 2512–2523, 2011.

[14] A. A. Kebede, T. Kalogiannis, J. Van Mierlo, and M. Berecibar, “A comprehensive review of stationary energy storage devices for large scale renewable energy sources grid integration,” *Renew. Sustain. Energy Rev.*, vol. 159, p. 112213, May 2022, doi: 10.1016/J.RSER.2022.112213.

[15] P. Cosme and C. Vieira, “Infinite Universe in Time , Energy , Mass , and Space Infinite Universe in Time , Energy , Mass , and Space,” no. February, 2025, doi: 10.13140/RG.2.2.26158.42567.

[16] R. M. Macrae, “Isotopes and analogs of hydrogen - From fundamental investigations to practical applications,” *Sci. Prog.*, vol. 96, no. 3, pp. 237–293, 2013, doi: 10.3184/003685013X13722668590726.

[17] Royal Society of Chemistry (RSC), “Hydrogen - Element information, properties and uses | Periodic Table,” *Period Table*. pp. 1–5, 2017, [Online]. Available: http://www.rsc.org/periodic-table/element/1/hydrogen.

[18] K. Mazloomi and C. Gomes, “Hydrogen as an energy carrier: Prospects and challenges,” *Renew. Sustain. Energy Rev.*, vol. 16, no. 5, pp. 3024–3033, Jun. 2012, doi: 10.1016/J.RSER.2012.02.028.

[19] M. Sarikaya, “A view about the short histories of the mole and Avogadro’s number,” *Found. Chem.*, vol. 15, no. 1, pp. 79–91, 2013, doi: 10.1007/s10698-011-9128-7.

[20] S. K. Dash, S. Chakraborty, and D. Elangovan, “A Brief Review of Hydrogen Production Methods and Their Challenges,” *Energies*, vol. 16, no. 3, 2023, doi: 10.3390/en16031141.

[21] D. Vergara, P. Fernández-Arias, G. Lampropoulos, and Á. Antón-Sancho, “Hydrogen Revolution in Europe: Bibliometric Review of Industrial Hydrogen Applications for a Sustainable Future,” *Energies*, vol. 17, no. 15, 2024, doi: 10.3390/en17153658.

[22] S. Biswas, D. S. Dhawale, T. Hosseini, G. Kaur, S. Giddey, and N. Haque, “A Review on Critical Metals Used in Solid Oxide Cells for Power ↔ X Applications and Materials Recyclability,” *ACS Sustain. Chem. Eng.*, vol. 12, no. 16, pp.

6037–6058, 2024, doi: 10.1021/acssuschemeng.3c07934.

[23] S. Wang and S. P. Jiang, “Prospects of fuel cell technologies,” *Natl. Sci. Rev.*, vol. 4, no. 2, pp. 161–163, 2017, doi: 10.1093/nsr/nwx032.

[24] N. A. A. Qasem and G. A. Q. Abdulrahman, “A Recent Comprehensive Review of Fuel Cells: History, Types, and Applications,” *Int. J. Energy Res.*, vol. 2024, no. Figure 1, 2024, doi: 10.1155/2024/7271748.

[25] Y. Wang, D. Y. C. Leung, J. Xuan, and H. Wang, “A review on unitized regenerative fuel cell technologies, part B: Unitized regenerative alkaline fuel cell, solid oxide fuel cell, and microfluidic fuel cell,” *Renew. Sustain. Energy Rev.*, vol. 75, no. November 2015, pp. 775–795, 2017, doi: 10.1016/j.rser.2016.11.054.

[26] A. Tarancón, “Strategies for lowering solid oxide fuel cells operating temperature,” *Energies*, vol. 2, no. 4, pp. 1130–1150, 2009, doi: 10.3390/en20401130.

[27] V. Cigolotti and M. Genovese, “STATIONARY FUEL CELL APPLICATIONS: CURRENT AND FUTURE TECHNOLOGIES - COSTS, PERFORMANCES, AND POTENTIAL,” *Station. Fuel Cells*, 2007, doi: 10.1016/B978-0-08-045118-3.X5001-8.

[28] X. Zhang, “Current status of stationary fuel cells for coal power generation,” *Clean Energy*, vol. 2, no. 2, pp. 126–139, 2018, doi: 10.1093/ce/zky012.

[29] M. T. Mehran *et al.*, “A comprehensive review on durability improvement of solid oxide fuel cells for commercial stationary power generation systems,” *Appl. Energy*, vol. 352, no. August, p. 121864, 2023, doi: 10.1016/j.apenergy.2023.121864.

[30] D. Manzo, R. Thai, H. T. Le, and G. K. Venayagamoorthy, “Fuel cell technology review: Types, economy, applications, and vehicle-to-grid scheme,” *Sustain. Energy Technol. Assessments*, vol. 75, no. February, p. 104229, 2025, doi: 10.1016/j.seta.2025.104229.

[31] G. Yang *et al.*, “Toward reducing the operation temperature of solid oxide fuel cells: Our past 15 years of efforts in cathode development,” *Energy and Fuels*, vol. 34, no. 12, pp. 15169–15194, 2020, doi: 10.1021/acs.energyfuels.0c01887.

[32] E. D. Wachsman and K. T. Lee, “Lowering the temperature of solid oxide fuel cells,” *Science (80-.).*, vol. 334, no. 6058, pp. 935–939, 2011, doi: 10.1126/science.1204090.

[33] A. J. Appleby, “From Sir William Grove to today: fuel cells and the future,” *J. Power Sources*, vol. 29, no. 1–2, pp. 3–11, Jan. 1990, doi: 10.1016/0378-

7753(90)80002-U.

[34] E. Baur and H. Preis, “Uber brennstoff-ketten mit festleitern.,” *Zeitschrift für Elektrochemie und Angew. Phys. Chemie*, pp. 727–732, 1937.

[35] A. K. Padinjarethil, F. R. Bianchi, B. Bosio, and A. Hagen, “Electrochemical Characterization and Modelling of Anode and Electrolyte Supported Solid Oxide Fuel Cells,” *Front. Energy Res.*, vol. 9, 2021, doi: 10.3389/fenrg.2021.668964.

[36] S. Basu, *Recent Trends in Fuel Cell Science and Technology*, vol. 17. 2007.

[37] M. Chen, Y. L. Liu, A. Hagen, P. V. Hendriksen, and F. W. Poulsen, “LSM-YSZ reactions in different atmospheres,” *Fuel Cells*, vol. 9, no. 6, pp. 833–840, 2009, doi: 10.1002/fuce.200800129.

[38] P. Kopras, C. Tsanaktsidis, and N. Kiratzis, “Advanced ceramic materials for electrolytes and electrodes in reversible solid oxide cells,” *Acad. Green Energy*, vol. 1, no. 3, pp. 1–34, 2024, doi: 10.20935/acadenergy7390.

[39] Z. Zhou, V. K. Nadimpalli, D. B. Pedersen, and V. Esposito, “Degradation Mechanisms of Metal-Supported Solid Oxide Cells,” *Materials (Basel).*, vol. 14, no. 11, 2021.

[40] M. Tucker, G. Lau, C. P. Jacobson, L. C. DeJonghe, and S. J. Visco, “Metal Supported SOFCs,” *ECS Trans.*, vol. 7, no. 1, pp. 279–284, 2007, doi: 10.1149/1.2729102.

[41] A. Evans *et al.*, “Micro-solid oxide fuel cells: Status, challenges, and chances,” *Monatshefte fur Chemie*, vol. 140, no. 9, pp. 975–983, 2009, doi: 10.1007/s00706-009-0107-9.

[42] J. An, Y. B. Kim, J. Park, T. M. Gür, and F. B. Prinz, “Three-dimensional nanostructured bilayer solid oxide fuel cell with 1.3 W/cm2 at 450 C,” *Nano Lett.*, vol. 13, no. 9, pp. 4551–4555, 2013, doi: 10.1021/nl402661p.

[43] C. C. Chao, C. M. Hsu, Y. Cui, and F. B. Prinz, “Improved solid oxide fuel cell performance with nanostructured electrolytes,” *ACS Nano*, vol. 5, no. 7, pp. 5692–5696, 2011, doi: 10.1021/nn201354p.

[44] P. C. Su, C. C. Chao, J. H. Shim, R. Fasching, and F. B. Prinz, “Solid oxide fuel cell with corrugated thin film electrolyte,” *Nano Lett.*, vol. 8, no. 8, pp. 2289–2292, 2008, doi: 10.1021/nl800977z.

[45] A. S. Deepi, S. Dharani Priya, A. Samson Nesaraj, and A. I. Selvakumar, “Component fabrication techniques for solid oxide fuel cell (SOFC)–A comprehensive review and future prospects,” *Int. J. Green Energy*, vol. 00, no.

00, pp. 1–13, 2022, doi: 10.1080/15435075.2021.2018320.

[46] M. Gianni, A. Pietra, R. Taccani, and F. SpA, “Outlook of future implementation of PEMFC and SOFC onboard cruise ships,” doi: 10.1051/e3sconf/202123804004.

[47] R. O’Hayre, S.-W. Cha, W. Colella, and F. B. Prinz, “Chapter 4: Fuel Cell Charge Transport,” *Fuel Cell Fundam.*, pp. 117–166, 2016, doi: 10.1002/9781119191766.ch4.

[48] A. Chroneos, R. V. Vovk, I. L. Goulatis, and L. I. Goulatis, “Oxygen transport in perovskite and related oxides: A brief review,” *J. Alloys Compd.*, vol. 494, no. 1–2, pp. 190–195, Apr. 2010, doi: 10.1016/J.JALLCOM.2010.01.071.

[49] A. Chroneos, B. Yildiz, A. Tarancón, D. Parfitt, and J. A. Kilner, “Oxygen diffusion in solid oxide fuel cell cathode and electrolyte materials: Mechanistic insights from atomistic simulations,” *Energy Environ. Sci.*, vol. 4, no. 8, pp. 2774–2789, 2011, doi: 10.1039/c0ee00717j.

[50] F. Rahmawati, N. Zuhrini, K. D. Nugrahaningtyas, and S. K. Arifah, “Yttria-stabilized zirconia (YSZ) film produced from an aqueous nano-YSZ slurry: preparation and characterization,” *J. Mater. Res. Technol.*, vol. 8, no. 5, pp. 4425–4434, Sep. 2019, doi: 10.1016/J.JMRT.2019.07.054.

[51] A. R. Allnatt and E. L. Allnatt, “Correlation effects in atom transport by the interstitialcy mechanism,” *Philos. Mag. A Phys. Condens. Matter, Struct. Defects Mech. Prop.*, vol. 64, no. 4, pp. 777–786, 1991, doi: 10.1080/01418619108213947.

[52] A. Kushima, D. Parfitt, A. Chroneos, B. Yildiz, J. A. Kilner, and R. W. Grimes, “Interstitialcy diffusion of oxygen in tetragonal La2CoO 4+δ,” *Phys. Chem. Chem. Phys.*, vol. 13, no. 6, pp. 2242–2249, 2011, doi: 10.1039/c0cp01603a.

[53] M. Yashima, H. Yamada, S. Nuansaeng, and T. Ishihara, “Role of Ga3+ and Cu2+ in the High Interstitial Oxide-Ion Diffusivity of Pr2NiO4-Based Oxides: Design Concept of Interstitial Ion Conductors through the Higher-Valence d10 Dopant and Jahn−Teller Effect,” *Chem. Mater.*, vol. 24, pp. 4100–4113, 2012.

[54] A. M. Svensson, S. Sunde, and K. Nis ̧ancioĞlu, “Mathematical Modeling of Oxygen Exchange and Transport in Air-Perovskite-Yttria-Stabilized Zirconia Interface Regions: II. Direct Exchange of Oxygen Vacancies,” *J. Electrochem. Soc.*, vol. 145, no. 4, pp. 1390–1400, 1998, doi: 10.1149/1.1838471.

[55] R. Schaub, E. Wahlström, A. Rønnau, E. Lægsgaard, I. Stensgaard, and F. Besenbacher, “Oxygen-mediated diffusion of oxygen vacancies on the TiO2(110) surface,” *Science (80-.).*, vol. 299, no. 5605, pp. 377–379, 2003, doi:

10.1126/science.1078962.

[56] R. Pornprasertsuk, P. Ramanarayanan, C. B. Musgrave, and F. B. Prinz, “Predicting ionic conductivity of solid oxide fuel cell electrolyte from first principles,” *J. Appl. Phys.*, vol. 98, no. 10, 2005, doi: 10.1063/1.2135889.

[57] S. N. Rashkeev and M. V. Glazoff, “Atomic-scale mechanisms of oxygen electrode delamination in solid oxide electrolyzer cells,” *Int. J. Hydrogen Energy*, vol. 37, no. 2, pp. 1280–1291, Jan. 2012, doi: 10.1016/J.IJHYDENE.2011.09.117.

[58] E. A. Kotomin and A. I. Popov, “Radiation-induced point defects in simple oxides,” *Nucl. Instruments Methods Phys. Res. Sect. B Beam Interact. with Mater. Atoms*, vol. 141, no. 1–4, pp. 1–15, May 1998, doi: 10.1016/S0168-583X(98)00079-2.

[59] M. O. Keeffe and B. M. O. Keeffe, “DIFFUSION OF OXYGEN IN SINGLE CRYSTALS OF NICKEL OXIDE,” *J. Phys. Chem.*, vol. 65, pp. 1438–1439, 1961.

[60] R. O’Hayre, S.-W. Cha, W. Colella, and F. B. Prinz, “Chapter 3: Fuel Cell Reaction Kinetics,” *Fuel Cell Fundam.*, pp. 77–116, 2016, doi: 10.1002/9781119191766.ch3.

[61] M. Mogensen, “The Kinetics of Hydrogen Oxidation on a Ni-YSZ SOFC Electrode at 1000°C,” *ECS Proc. Vol.*, vol. 1993–4, no. 1, pp. 484–493, 1993, doi: 10.1149/199304.0484pv.

[62] J. H. Wang, M. L. Liu, and M. C. Lin, “Oxygen reduction reactions in the SOFC cathode of Ag/CeO2,” *Solid State Ionics*, vol. 177, no. 9–10, pp. 939–947, Mar. 2006, doi: 10.1016/J.SSI.2006.02.029.

[63] S. B. Adler, “Factors governing oxygen reduction in solid oxide fuel cell cathodes,” *Chem. Rev.*, vol. 104, no. 10, pp. 4791–4843, 2004, doi: 10.1021/cr020724o.

[64] W. Kong, Z. Han, S. Lu, X. Gao, and X. Wang, “A novel interconnector design of SOFC,” *Int. J. Hydrogen Energy*, vol. 45, no. 39, pp. 20329–20338, Aug. 2020, doi: 10.1016/J.IJHYDENE.2019.10.252.

[65] R. O’Hayre, S.-W. Cha, W. Colella, and F. B. Prinz, “Chapter 9: PEMFC and SOFC Materials,” *Fuel Cell Fundam.*, pp. 303–346, 2016, doi: 10.1002/9781119191766.ch9.

[66] J. C. W. Mah, A. Muchtar, M. R. Somalu, and M. J. Ghazali, “Metallic interconnects for solid oxide fuel cell: A review on protective coating and deposition techniques,” *Int. J. Hydrogen Energy*, vol. 42, no. 14, pp. 9219–9229, 2017, doi: 10.1016/j.ijhydene.2016.03.195.

[67] Ł. Mazur and T. Brylewski, “Electrophoretic Deposition and Physicochemical Properties of Ni- and Fe-Doped Cu–Mn Spinel Coatings Enhanced with Ce0.9Y0.1O2 Nanoparticles on Fe16Cr Ferritic Stainless Steel Interconnects for SOEC Applications,” *Metall. Mater. Trans. A Phys. Metall. Mater. Sci.*, vol. 55, no. 12, pp. 5100–5113, 2024, doi: 10.1007/s11661-024-07615-1.

[68] A. Holt and P. Kofstad, “Electrical conductivity and defect structure of Cr2O3. II. Reduced temperatures (<∼1000°C),” *Solid State Ionics*, vol. 69, no. 2, pp. 137–143, 1994, doi: 10.1016/0167-2738(94)90402-2.

[69] S. Fontana *et al.*, “Metallic interconnects for SOFC: Characterisation of corrosion resistance and conductivity evaluation at operating temperature of differently coated alloys,” *J. Power Sources*, vol. 171, no. 2, pp. 652–662, 2007, doi: 10.1016/j.jpowsour.2007.06.255.

[70] Y. P. Xiong *et al.*, “Electronic conductivity of CeO2: Its dependence on oxygen partial pressure and temperature,” *Electrochem. Solid-State Lett.*, vol. 13, no. 3, pp. 21–24, 2010, doi: 10.1149/1.3276731.

[71] T. NORBY and P. KOFSTAD, “Electrical Conductivity of Y2O3 as a Function of Oxygen Partial Pressure in Wet and Dry Atmospheres,” *J. Am. Ceram. Soc.*, vol. 69, no. 11, pp. 784–789, 1986, doi: 10.1111/j.1151-2916.1986.tb07360.x.

[72] A. Balland, P. Gannon, M. Deibert, S. Chevalier, G. Caboche, and S. Fontana, “Investigation of La2O3 and/or (Co,Mn)3O4 deposits on Crofer22APU for the SOFC interconnect application,” *Surf. Coatings Technol.*, vol. 203, no. 20–21, pp. 3291–3296, 2009, doi: 10.1016/j.surfcoat.2009.04.017.

[73] A. Bandyopadhyay, S. Sharma, M. Nath, A. Karmakar, K. Kumari, and S. Sutradhar, “Dielectric study and magnetic property analysis of Gd2O3 nanorods/nanowire in combination with Monte Carlo simulation,” *J. Alloys Compd.*, vol. 882, p. 160720, Nov. 2021, doi: 10.1016/J.JALLCOM.2021.160720.

[74] M. Stanislowski *et al.*, “Reduction of chromium vaporization from SOFC interconnectors by highly effective coatings,” *J. Power Sources*, vol. 164, no. 2, pp. 578–589, 2007, doi: 10.1016/j.jpowsour.2006.08.013.

[75] T. Brylewski and K. Przybylski, “Perovskite and spinel functional coatings for SOFC metallic interconnects,” *Mater. Sci. Forum*, vol. 595-598 PA, pp. 813–822, 2008, doi: 10.4028/www.scientific.net/msf.595-598.813.

[76] A. J. deBethune, “Fuel Cell Thermodynamics,” *J. Electrochem. Soc.*, vol. 107, no. 11, p. 937, 1960, doi: 10.1149/1.2427549.

[77] T. Yonekura, Y. Yachikawa, T. Yoshizuma, Y. Shiratori, K. Ito, and K. Sasaki,

“Cathode Electrolyte Anode,” *ECS Trans.*, vol. 35, no. 1, pp. 1007–1014, 2011.

[78] D. A. Noren and M. A. Hoffman, “Clarifying the Butler–Volmer equation and related approximations for calculating activation losses in solid oxide fuel cell models,” *J. Power Sources*, vol. 152, no. 1–2, pp. 175–181, Dec. 2005, doi: 10.1016/J.JPOWSOUR.2005.03.174.

[79] S. H. Chan, K. A. Khor, and Z. T. Xia, “A complete polarization model of a solid oxide fuel cell and its sensitivity to the change of cell component thickness,” *J. Power Sources*, vol. 93, no. 1–2, pp. 130–140, Feb. 2001, doi: 10.1016/S0378-7753(00)00556-5.

[80] A. Gebregergis, P. Pillay, D. Bhattacharyya, and R. Rengaswemy, “Solid Oxide Fuel Cell Modeling; Solid Oxide Fuel Cell Modeling,” *IEEE Trans. Ind. Electron.*, vol. 56, no. 1, 2009, doi: 10.1109/TIE.2008.2009516.

[81] Y. J. Leng, S. H. Chan, S. P. Jiang, and K. A. Khor, “Low-temperature SOFC with thin film GDC electrolyte prepared in situ by solid-state reaction,” *Solid State Ionics*, vol. 170, no. 1–2, pp. 9–15, May 2004, doi: 10.1016/J.SSI.2004.02.026.

[82] W. G. Bessler and S. Gewies, “Gas Concentration Impedance of Solid Oxide Fuel Cell Anodes,” *J. Electrochem. Soc.*, vol. 154, no. 6, p. B548, 2007, doi: 10.1149/1.2720639.

[83] R. O’Hayre, S.-W. Cha, W. G. Colella, and F. B. Prinz, “Fuel Cell Fundamentals: Third Edition; Chapter 1: Fuel Cell Principles,” 2016.

[84] J. Hjelm, M. Søgaard, M. Wandel, M. Menon, M. Mogensen, and A. Hagen, “Electrochemical Impedance Studies of SOFC Cathodes,” *ECS Trans.*, vol. 7, no. 1, pp. 1261–1270, 2007, doi: 10.1149/1.2729227.

[85] B. Kamecki, G. Cempura, P. Jasiński, S.-F. Wang, and S. Molin, “Tuning Electrochemical Performance by Microstructural Optimization of the Nanocrystalline Functional Oxygen Electrode Layer for Solid Oxide Cells,” *ACS Appl. Mater. & Interfaces*, vol. 14, no. 51, pp. 57449–57459, Dec. 2022, doi: 10.1021/acsami.2c18951.

[86] B. Lemieszek *et al.*, “Unveiling the potential of praseodymium oxide as efficient oxygen electrode for low-temperature solid oxide cell applications,” *Chem. Eng. J.*, vol. 531, p. 173949, 2026, doi: 10.1016/j.cej.2026.173949.

[87] B. Lemieszek *et al.*, “Enhanced electrochemical performance of partially amorphous La0.6Sr0.4CoO3-δ oxygen electrode materials for low-temperature solid oxide cells operating at 400 °C,” *Appl. Surf. Sci.*, vol. 670, 2024, doi: https://doi.org/10.1016/j.apsusc.2024.160620.

[88] A. Mroziński *et al.*, “Impact of strontium non-stoichiometry electrochemical

properties for potential oxygen electrode of intermediate temperature solid oxide cells," *Int. J. Hydrogen Energy*, no. xxxx, 2023, doi: 10.1016/j.ijhydene.2023.05.323.

[89] J. Hayd and E. Ivers-Tiffée, " Detailed Electrochemical Study on Nanoscaled La 0.6 Sr 0.4 CoO 3-δ SOFC Thin-Film Cathodes in Dry, Humid and CO 2 - Containing Atmospheres ," *J. Electrochem. Soc.*, vol. 160, no. 11, pp. F1197–F1206, 2013, doi: 10.1149/2.026311jes.

[90] C. Peters, A. Weber, and E. Ivers-tiffée, "Nanoscaled „La0.5Sr0.5…CoO3−ʕ Thin Film Cathodes for SOFC Application at 500°C ⬍ T ⬍ 700°C," pp. 730–737, 2008, doi: 10.1149/1.2909552.

[91] P. Hjalmarsson, M. Søgaard, and M. Mogensen, "Electrochemical performance and degradation of (La0.6Sr0.4)0.99CoO3 - δ as porous SOFC-cathode," *Solid State Ionics*, vol. 179, no. 27–32, pp. 1422–1426, 2008, doi: 10.1016/j.ssi.2007.11.010.

[92] N. Kane *et al.*, "Precision surface modification of solid oxide fuel cells via layer-by-layer surface sol-gel deposition," *J. Mater. Chem. A*, vol. 10, no. 16, pp. 8798–8806, 2022, doi: 10.1039/d2ta00458e.

[93] F. Yadollahi Farsani, M. Jafari, E. Shahsavari, H. Shakeripour, and H. Salamati, "Investigation of structural, electrical and electrochemical properties of La0.6Sr0.4Fe0.8Mn0.2O3-δ as an intermediate temperature solid oxide fuel cell cathode," *Int. J. Hydrogen Energy*, vol. 45, no. 15, pp. 8915–8929, 2020, doi: 10.1016/j.ijhydene.2020.01.030.

[94] F. Liu *et al.*, "CO2 Poisoning of Solid Oxide Fuel Cell Cathodes: Mechanisms, Solutions, and Progress," *Processes*, vol. 13, no. 12, pp. 1–22, 2025, doi: 10.3390/pr13123931.

[95] D. A. Osinkin, "Detailed analysis of electrochemical behavior of high–performance solid oxide fuel cell using DRT technique," *J. Power Sources*, vol. 527, p. 231120, Apr. 2022, doi: 10.1016/J.JPOWSOUR.2022.231120.

[96] H. Toraya, "Calibration Curve for Quantitative Analysis of the Monoclinic-Tetragonal Zr02 System by X-Ray Diffraction," *J. Am. Ceram. Soc.*, no. June, pp. 119–121, 1984.

[97] V. P. Gorelov, S. A. Belyakov, and R. K. Abdurakhimova, "Phase transitions in monoclinic ZrO2," *Phys. Solid State*, vol. 65, no. 3, pp. 461-, 2023, doi: 10.21883/PSS.2023.03.55589.541.

[98] J. C. Ray, R. K. Pati, and P. Pramanik, "Chemical synthesis and structural characterization of nanocrystalline powders of pure zirconia and yttria

stabilized zirconia (YSZ)," *J. Eur. Ceram. Soc.*, vol. 20, no. 9, pp. 1289–1295, Aug. 2000, doi: 10.1016/S0955-2219(99)00293-9.

[99] J. W. Fergus, "Electrolytes for solid oxide fuel cells," *J. Power Sources*, vol. 162, no. 1, pp. 30–40, 2006, doi: 10.1016/j.jpowsour.2006.06.062.

[100] D. W. STRICKLER and W. G. CARLSON, "Ionic Conductivity of Cubic Solid Solutions in the System CaO—Y2O3—ZrO2," *J. Am. Ceram. Soc.*, vol. 47, no. 3, pp. 122–127, 1964, doi: 10.1111/j.1151-2916.1964.tb14368.x.

[101] J. M. Dixon, L. D. LaGrange, U. Merten, C. F. Miller, and J. T. Porter, "Electrical Resistivity of Stabilized Zirconia at Elevated Temperatures," *J. Electrochem. Soc.*, vol. 110, no. 4, p. 276, 1963, doi: 10.1149/1.2425731.

[102] P. Khajavi, "Improving the mechanical properties and stability of solid oxide fuel and electrolysiscells," vol. 22, pp. 1–198, 2018.

[103] Y. Li *et al.*, "Effect of Two-Step Sintering on the Mechanical and Electrical Properties of 5YSZ and 8YSZ Ceramics," *Materials (Basel).*, vol. 16, no. 5, pp. 1–15, 2023, doi: 10.3390/ma16052019.

[104] Y. Xu *et al.*, "Thermal Properties and Microstructures Analysis of YSZ and YSZ-Al2O3 Thermal Barrier Coatings," *J. Therm. Spray Technol.*, vol. 29, no. 4, pp. 574–581, 2020, doi: 10.1007/s11666-020-00996-w.

[105] D. L. Porter, A. G. Evans, and A. H. Heuer, "Transformation-toughening in partially-stabilized zirconia (PSZ)," *Acta Metall.*, vol. 27, no. 10, pp. 1649–1654, 1979, doi: 10.1016/0001-6160(79)90046-4.

[106] P. Vinchhi, M. Khandla, K. Chaudhary, and R. Pati, "Recent advances on electrolyte materials for SOFC: A review," *Inorg. Chem. Commun.*, vol. 152, p. 110724, Jun. 2023, doi: 10.1016/J.INOCHE.2023.110724.

[107] T. H. Etsell and S. N. Flengas, "THE ELECTRICAL PROPERTIES OF SOLID OXIDE ELECTROLYTES," *Chem. Rev.*, vol. 70, no. 3, pp. 339–376, 1969.

[108] B. C. H. Steele, "Appraisal of Ce1−yGdyO2−y/2 electrolytes for IT-SOFC operation at 500°C," *Solid State Ionics*, vol. 129, no. 1–4, pp. 95–110, Apr. 2000, doi: 10.1016/S0167-2738(99)00319-7.

[109] D. Pérez-Coll, P. Núñez, J. R. Frade, and J. C. C. Abrantes, "Conductivity of CGO and CSO ceramics obtained from freeze-dried precursors," *Electrochim. Acta*, vol. 48, no. 11, pp. 1551–1557, 2003, doi: 10.1016/S0013-4686(03)00027-6.

[110] Z. He *et al.*, "Densification and grain growth during early-stage sintering of Ce0.9Gd0.1O1.95−δ in a reducing atmosphere," *Acta Mater.*, vol. 58, no. 11, pp. 3860–3866, Jun. 2010, doi: 10.1016/J.ACTAMAT.2010.03.046.

[111] D. P. Fagg *et al.*, “Ceria based mixed conductors with adjusted electronic conductivity in the bulk and/or along grain boundaries,” *Solid State Ionics*, vol. 180, no. 11–13, pp. 896–899, Jun. 2009, doi: 10.1016/J.SSI.2009.02.024.

[112] R. Chockalingam, A. K. Ganguli, and S. Basu, “Praseodymium and gadolinium doped ceria as a cathode material for low temperature solid oxide fuel cells,” *J. Power Sources*, vol. 250, pp. 80–89, 2014, doi: 10.1016/j.jpowsour.2013.10.105.

[113] B. Fan, J. Yan, and X. Yan, “The ionic conductivity, thermal expansion behavior, and chemical compatibility of La0.54Sr0.44Co0.2Fe0.8O3-δ as SOFC cathode material,” *Solid State Sci.*, vol. 13, no. 10, pp. 1835–1839, Oct. 2011, doi: 10.1016/J.SOLIDSTATESCIENCES.2011.07.007.

[114] S. Molin, J. Karczewski, B. Kamecki, A. Mroziński, S. F. Wang, and P. Jasiński, “Processing of Ce0.8Gd0.2O2-δ barrier layers for solid oxide cells: The effect of preparation method and thickness on the interdiffusion and electrochemical performance,” *J. Eur. Ceram. Soc.*, vol. 40, no. 15, pp. 5626–5633, Dec. 2020, doi: 10.1016/J.JEURCERAMSOC.2020.06.006.

[115] B. J. Kamecki, J. Karczewski, P. Jasinski, and S. Molin, “Evaluation of Praseodymium and Gadolinium Doped Ceria as a Possible Barrier Layer Material for Solid Oxide Cells,” *ECS Trans.*, vol. 91, no. 1, pp. 1165–1172, 2019, doi: 10.1149/09101.1165ecst.

[116] A. Sciazko, T. Shimura, Y. Komatsu, and N. Shikazono, “Ni-gdc and ni-ysz electrodes operated in solid oxide electrolysis and fuel cell modes,” *J. Therm. Sci. Technol.*, vol. 16, no. 1, pp. 1–10, 2021, doi: 10.1299/jtst.2021jtst0013.

[117] L. Zhang, S. P. Jiang, H. Q. He, X. Chen, J. Ma, and X. C. Song, “A comparative study of H2S poisoning on electrode behavior of Ni/YSZ and Ni/GDC anodes of solid oxide fuel cells,” *Int. J. Hydrogen Energy*, vol. 35, no. 22, pp. 12359–12368, Nov. 2010, doi: 10.1016/J.IJHYDENE.2010.08.067.

[118] J. H. Koh, Y. S. Yoo, J. W. Park, and H. C. Lim, “Carbon deposition and cell performance of Ni-YSZ anode support SOFC with methane fuel,” *Solid State Ionics*, vol. 149, no. 3–4, pp. 157–166, Aug. 2002, doi: 10.1016/S0167-2738(02)00243-6.

[119] B. Shri Prakash, S. Senthil Kumar, and S. T. Aruna, “Properties and development of Ni/YSZ as an anode material in solid oxide fuel cell: A review,” *Renew. Sustain. Energy Rev.*, vol. 36, pp. 149–179, Aug. 2014, doi: 10.1016/J.RSER.2014.04.043.

[120] V. Gil, J. Tartaj, and C. Moure, “Chemical and thermomechanical compatibility between Ni-GDC anode and electrolytes based on ceria,” *Ceram. Int.*, vol. 35,

no. 2, pp. 839–846, 2009, doi: 10.1016/j.ceramint.2008.03.004.

[121] A. Nenning, C. Bischof, J. Fleig, M. Bram, and A. K. Opitz, “The relation of microstructure, materials properties and impedance of SOFC electrodes: A case study of Ni/GDC anodes,” *Energies*, vol. 13, no. 4, pp. 5–9, 2020, doi: 10.3390/en13040987.

[122] S. Tao and J. T. S. Irvine, “Observed by in Situ High-Temperature Neutron Powder Diffraction,” no. 9, pp. 5453–5460, 2006.

[123] H. Dong, M. Wang, Y. Liu, and Z. Han, “Optimized Solid-State Synthesis of Sr2Fe1.5Mo0.5O6−δ Perovskite: Implications for Efficient Synthesis of Mo-Containing SOFC Electrodes,” *Crystals*, vol. 12, no. 11, pp. 1–9, 2022, doi: 10.3390/cryst12111533.

[124] V. A. Kolotygin *et al.*, “Functional properties of SOFC anode materials based on LaCrO3, La(Ti,Mn)O3 and Sr(Nb,Mn)O3 perovskites: A comparative analysis,” *Solid State Ionics*, vol. 251, pp. 28–33, Nov. 2013, doi: 10.1016/J.SSI.2013.01.005.

[125] S. P. Jiang, *Development of lanthanum strontium manganite perovskite cathode materials of solid oxide fuel cells: A review*, vol. 43, no. 21. 2008.

[126] J. Fleig, “Solid Oxide Fuel Cell Cathodes: Polarization Mechanisms and Modeling of the Electrochemical Performance,” *Annu. Rev. Mater. Res.*, vol. 33, pp. 361–382, 2003, doi: 10.1146/annurev.matsci.33.022802.093258.

[127] S. T. Aruna, M. Muthuraman, and K. C. Patil, “Combustion synthesis and properties of strontium substituted lanthanum manganites La1-xSrxMnO3 (0 ≤ x ≤ 0.3),” *J. Mater. Chem.*, vol. 7, no. 12, pp. 2499–2503, 1997, doi: 10.1039/a703901h.

[128] J. A. Kilner and M. Burriel, “Materials for intermediate-temperature solid-oxide fuel cells,” *Annu. Rev. Mater. Res.*, vol. 44, pp. 365–393, 2014, doi: 10.1146/annurev-matsci-070813-113426.

[129] B. Kamecki *et al.*, “Deposition and Electrical and Structural Properties of La0.6Sr0.4CoO3 Thin Films for Application in High-Temperature Electrochemical Cells,” *J. Electron. Mater.*, vol. 48, no. 9, pp. 5428–5441, 2019, doi: 10.1007/s11664-019-07372-7.

[130] F. Tietz, “Thermal expansion of SOFC materials,” *Ionics (Kiel).*, vol. 5, no. 1–2, pp. 129–139, 1999, doi: 10.1007/BF02375916.

[131] S. P. Jiang, “Development of lanthanum strontium cobalt ferrite perovskite electrodes of solid oxide fuel cells – A review,” *Int. J. Hydrogen Energy*, vol. 44, no. 14, pp. 7448–7493, Mar. 2019, doi: 10.1016/J.IJHYDENE.2019.01.212.

[132] H. J. M. Bouwmeester, M. W. Den Otter, and B. A. Boukamp, “Oxygen transport in La0.6Sr0.4Co1-yFe yO3-δ,” *J. Solid State Electrochem.*, vol. 8, no. 9, pp. 599–605, 2004, doi: 10.1007/s10008-003-0488-3.

[133] Y. Sun *et al.*, “Controllable Technology for Thermal Expansion Coefficient of Commercial Materials for Solid Oxide Electrolytic Cells,” *Materials (Basel).*, vol. 17, no. 5, 2024, doi: 10.3390/ma17051216.

[134] K. Singh, J. Nowotny, and V. Thangadurai, “Amphoteric oxide semiconductors for energy conversion devices: A tutorial review,” *Chem. Soc. Rev.*, vol. 42, no. 5, pp. 1961–1972, 2013, doi: 10.1039/c2cs35393h.

[135] A. Mroziński, S. Molin, J. Karczewski, T. Miruszewski, and P. Jasiński, “Electrochemical properties of porous Sr0.86Ti0.65Fe0.35O3 oxygen electrodes in solid oxide cells : Impedance study of symmetrical electrodes,” *Int. J. Hydrogen Energy*, vol. 44, pp. 1827–1839, 2018, doi: 10.1016/j.ijhydene.2018.11.203.

[136] V. V. Kharton *et al.*, “Mixed conductivity and stability of A-site-deficient Sr(Fe,Ti)O 3-δ perovskites,” *J. Solid State Electrochem.*, vol. 7, no. 1, pp. 30–36, 2002, doi: 10.1007/s10008-002-0286-3.

[137] M. B. Bellakki, C. Shivakumara, T. Baidya, A. S. Prakash, N. Y. Vasanthacharya, and M. S. Hegde, “Synthesis, structure and oxygen-storage capacity of Pr1-xZrxO2-d and Pr1-x-yPdyZrxO2-d,” *Mater. Res. Bull.*, vol. 43, pp. 2658–2667, 2008, doi: 10.1016/j.materresbull.2007.10.033.

[138] “Materials Data on Pr5O9 by Materials Project.” United States, 2020, doi: https://doi.org/10.17188/1277075.

[139] “Materials Data on Pr11O20 by Materials Project.” United States, 2020, doi: 10.17188/1673024.

[140] S. C. Atkinson, “CRYSTAL STRUCTURES AND PHASE TRANSITIONS IN THE RARE EARTH OXIDES,” no. July, 2013.

[141] “Materials Data on PrO2 by Materials Project.” United States, 2020, doi: https://doi.org/10.17188/1189331.

[142] V. Thangadurai, R. A. Huggins, and W. Weppner, “Mixed ionic-electronic conductivity in phases in the praseodymium oxide system,” *J. Solid State Electrochem.*, vol. 5, pp. 531–537, 2001, doi: 10.1007/s100080000187.

[143] S. Ferro, “Physicochemical and Electrical Properties of Praseodymium Oxides,” *Int. J. Electrochem.*, vol. 2011, pp. 1–7, 2011, doi: 10.4061/2011/561204.

[144] A. I. Vshivkova, V. P. Gorelov, A. V. Kuz'Min, S. V. Plaksin, A. A. Pankratov, and T. V. Yaroslavtseva, "Preparation and physicochemical properties of praseodymium oxide films and ceramics," *Inorg. Mater.*, vol. 51, no. 11, pp. 1168–1176, 2015, doi: 10.1134/S0020168515100179.

[145] B. M. Abu-Zied, "Controlled synthesis of praseodymium oxide nanoparticles obtained by combustion route: Effect of calcination temperature and fuel to oxidizer ratio," *Appl. Surf. Sci.*, vol. 471, no. December 2018, pp. 246–255, 2019, doi: 10.1016/j.apsusc.2018.12.007.

[146] B. Kamecki, J. Karczewski, P. Jasiński, and S. Molin, "Improvement of Oxygen Electrode Performance of Intermediate Temperature Solid Oxide Cells by Spray Pyrolysis Deposited Active Layers," *Adv. Mater. Interfaces*, vol. 8, no. 9, pp. 1–11, 2021, doi: 10.1002/admi.202002227.

[147] Ö. Faruk Aksoy, L. Bartłomiej, M. Murat, K. Jakub, J. Piotr, and M. Sebastian, "Developing high-performance oxygen electrodes for intermediate," *Appl. Phys. A Mater. Sci. Process.*, 2024, doi: https://doi.org/10.1007/s00339-024-07939-0.

[148] C. Nicollet, A. Flura, V. Vibhu, A. Rougier, J. M. Bassat, and J. C. Grenier, "An innovative efficient oxygen electrode for SOFC: Pr6O11 infiltrated into Gd-doped ceria backbone," *Int. J. Hydrogen Energy*, vol. 41, no. 34, pp. 15538–15544, 2016, doi: 10.1016/j.ijhydene.2016.04.024.

[149] R. K. Sharma *et al.*, "Highly efficient architectured Pr6O11 oxygen electrode for solid oxide fuel cell," *J. Power Sources*, vol. 419, no. February, pp. 171–180, 2019, doi: 10.1016/j.jpowsour.2019.02.077.

[150] S. Nam *et al.*, "Revitalizing Oxygen Reduction Reactivity of Composite Oxide Electrodes via Electrochemically Deposited PrOx Nanocatalysts," *Adv. Mater.*, vol. 36, no. 25, pp. 1–11, 2024, doi: 10.1002/adma.202307286.

[151] L. Ge, K. Sun, Y. Gu, Q. Ni, and X. Huang, "Boosting the performance of conventional air electrodes for solid oxide cells by in-situ loading of nano praseodymium oxide," *Energy Convers. Manag.*, vol. 249, no. September, p. 114873, 2021, doi: 10.1016/j.enconman.2021.114873.

[152] N. Kane *et al.*, "Precision surface modification of solid oxide fuel cells via layer-by-layer surface sol-gel deposition," *J. Mater. Chem. A*, pp. 8798–8806, 2022, doi: 10.1039/d2ta00458e.

[153] M. Y. Lu, R. Scipioni, B. K. Park, T. Yang, Y. A. Chart, and S. A. Barnett, "Mechanisms of PrOx performance enhancement of oxygen electrodes for low and intermediate temperature solid oxide fuel cells," *Mater. Today Energy*, vol. 14, p. 100362, 2019, doi: 10.1016/j.mtener.2019.100362.

[154] L. Caizán-Juanarena, J. Zamudio-García, and D. Marrero-López, “Electrochemical investigation of Pr6O11 infiltration into La0.8Sr0.2MnO3-δ-Ce0.9Gd0.1O1.95 cathodes for IT-SOFC,” *Ceram. Int.*, vol. 49, no. 21, pp. 33717–33724, 2023, doi: 10.1016/j.ceramint.2023.08.060.

[155] M. Rangarao, N. Gopikrishna, and S. Chandra Lingam, “Temperature dependence of density and thermal expansion of oxides of praseodymium and dysprosium in the temperature range 300 to 1000 K,” *J. Phys. Conf. Ser.*, vol. 1495, no. 1, 2020, doi: 10.1088/1742-6596/1495/1/012032.

[156] N. Shaigan, W. Qu, D. G. Ivey, and W. Chen, “A review of recent progress in coatings, surface modifications and alloy developments for solid oxide fuel cell ferritic stainless steel interconnects,” *J. Power Sources*, vol. 195, no. 6, pp. 1529–1542, Mar. 2010, doi: 10.1016/J.JPOWSOUR.2009.09.069.

[157] S. Chevalier, “What did we learn on the reactive element effect in chromia scale since Pfeil ’s patent?,” *Mater. Corros.*, vol. 65, no. 2, pp. 109–115, Feb. 2014, doi: 10.1002/maco.201307310.

[158] S. Chevalier and J. P. Larpin, “Formation of perovskite type phases during the high temperature oxidation of stainless steels coated with reactive element oxides,” *Acta Mater.*, vol. 50, no. 12, pp. 3107–3116, 2002, doi: 10.1016/s1359-6454(02)00106-4.

[159] B. Lemieszek *et al.*, “Electrolytic deposition of reactive element thin films on Crofer 22 APU and evaluation of the resulting high-temperature corrosion protection properties at 700 °C–900 °C,” *Int. J. Hydrogen Energy*, vol. 47, no. 78, pp. 33453–33465, Sep. 2022, doi: 10.1016/J.IJHYDENE.2022.07.220.

[160] A. Petric and H. Ling, “Electrical conductivity and thermal expansion of spinels at elevated temperatures,” *J. Am. Ceram. Soc.*, vol. 90, no. 5, pp. 1515–1520, 2007, doi: 10.1111/j.1551-2916.2007.01522.x.

[161] J. Ignaczak *et al.*, “Preparation and characterisation of iron substituted Mn1.7Cu1.3-xFexO4 spinel oxides (x = 0, 0.1, 0.3, 0.5),” *J. Eur. Ceram. Soc.*, vol. 40, no. 15, pp. 5920–5929, Dec. 2020, doi: 10.1016/j.jeurceramsoc.2020.07.001.

[162] N. Orlovskaya, A. Coratolo, C. Johnson, and R. Gemmen, “Structural Characterization of Lanthanum Chromite Perovskite Coating Deposited by Magnetron Sputtering on an Iron-Based Chromium-Containing Alloy as a Promising Interconnect Material for SOFCs.”

[163] M. J. REDDY, *Metallic materials for solid oxide fuel cells and electrolysers*. 2023.

[164] T. Brylewski, J. Dabek, K. Przybylski, J. Morgiel, and M. Rekas, “Screen-printed (La,Sr)CrO3 coatings on ferritic stainless steel interconnects for solid oxide fuel cells using nanopowders prepared by means of ultrasonic spray pyrolysis,” *J. Power Sources*, vol. 208, pp. 86–95, Jun. 2012, doi: 10.1016/J.JPOWSOUR.2012.02.015.

[165] K. Przybylski, T. Brylewski, E. Durda, R. Gawel, and A. Kruk, “Oxidation properties of the Crofer 22 APU steel coated with La 0.6Sr0.4Co0.2Fe0.8O3 for IT-SOFC interconnect applications,” *J. Therm. Anal. Calorim.*, vol. 116, no. 2, pp. 825–834, 2014, doi: 10.1007/s10973-013-3594-1.

[166] E. Durda and A. Kruk, “Physicochemical properties of the Crofer 22 APU steel with La0.6Sr0.4Co0.2Fe0.8O3-δ protective-conductive coatings prepared by pulsed laser deposition,” *Process. Appl. Ceram.*, vol. 17, no. 3, pp. 301–313, 2023, doi: 10.2298/PAC2303301D.

[167] J. Prażuch, M. Pyzalski, D. Fernández González, and T. Brylewski, “Physicochemical Properties of (La,Sr)CoO3 Thick Films on Fe-25Cr Steel under Exposure to SOFC Cathode Operating Conditions,” *Materials (Basel).*, vol. 17, no. 15, 2024, doi: 10.3390/ma17153791.

[168] M. De Angelis Korb *et al.*, “Modification of the La0.6Sr0.4CoO3 coating deposited on ferritic stainless steel by spray pyrolysis after oxidation in air at high temperature,” *Int. J. Hydrogen Energy*, vol. 38, no. 11, pp. 4760–4766, Apr. 2013, doi: 10.1016/J.IJHYDENE.2013.02.019.

[169] S. Molin *et al.*, “Effective yttrium based coating for steel interconnects of solid oxide cells: Corrosion evaluation in steam-hydrogen atmosphere,” *J. Power Sources*, vol. 440, no. September, 2019, doi: 10.1016/j.jpowsour.2019.226814.

[170] Ł. Mazur, K. Domaradzki, P. Winiarski, Ł. Zych, and T. Brylewski, “Optimization of electrophoretic deposition and thermal treatment of Cu–Mn spinel matrix for spinel/perovskite composite coating used as SOC metallic interconnect,” *Ceram. Int.*, vol. 50, no. 18, pp. 34017–34026, Sep. 2024, doi: 10.1016/J.CERAMINT.2024.06.221.

[171] T. Brylewski, K. Przybylski, and J. Morgiel, “Microstructure of Fe–25Cr/(La, Ca)CrO3 composite interconnector in solid oxide fuel cell operating conditions,” *Mater. Chem. Phys.*, vol. 81, no. 2–3, pp. 434–437, Aug. 2003, doi: 10.1016/S0254-0584(03)00041-5.

[172] B. Lemieszek *et al.*, “CuMn1.7Fe0.3O4 – RE2O3 (RE = Y, Gd) bilayers as protective interconnect coatings for solid oxide cells,” *J. Eur. Ceram. Soc.*, vol. 44, no. 15, 2024, doi: 10.1016/j.jeurceramsoc.2024.116743.

[173] Ł. Mazur *et al.*, “Effectiveness of a dual surface modification of metallic

interconnects for application in energy conversion devices," *Int. J. Hydrogen Energy*, vol. 47, no. 9, pp. 6295–6311, 2022, doi: 10.1016/j.ijhydene.2021.11.256.

[174] T. Brylewski *et al.*, "Improving the physicochemical properties of Fe-25Cr ferritic steel for SOFC interconnects via Y-implantation and Y2O3-deposition," *Oxid. Met.*, vol. 80, no. 1–2, pp. 83–111, 2013, doi: 10.1007/s11085-012-9345-z.

[175] J. W. Lee *et al.*, "Effects of La2O3 content and particle size on the long-term stability and thermal cycling property of La2O3-dispersed SUS430 alloys for SOFC interconnect materials," *Met. Mater. Int.*, vol. 23, no. 6, pp. 1250–1256, 2017, doi: 10.1007/s12540-017-7079-9.

[176] T. Brylewski *et al.*, "Influence of Gd deposition on the oxidation behavior and electrical properties of a layered system consisting of Crofer 22 APU and MnCo2O4 spinel," *Int. J. Hydrogen Energy*, vol. 46, no. 9, pp. 6775–6791, Feb. 2021, doi: 10.1016/j.ijhydene.2020.11.169.

[177] J. Ignaczak *et al.*, "Fe-modified Mn2CuO4 spinel oxides: coatings based on abundant elements for solid oxide cell interconnects," *Int. J. Hydrogen Energy*, Jun. 2023, doi: 10.1016/J.IJHYDENE.2023.06.041.

[178] J. Ignaczak *et al.*, "Development and evaluation of interconnect protective coatings based on commercial Mn1.9CuFe0.1O4 spinel powder," *J. Eur. Ceram. Soc.*, vol. 45, no. 7, p. 117259, Jul. 2025, doi: 10.1016/J.JEURCERAMSOC.2025.117259.

[179] A. Norouzi, M. Soltanieh, and S. Rastegari, "An electrophoretic co-deposition of metal oxides followed by in-situ copper manganese spinel synthesis on AISI-430 for application in SOFC interconnects," *Int. J. Hydrogen Energy*, vol. 47, no. 31, pp. 14346–14360, Apr. 2022, doi: 10.1016/J.IJHYDENE.2022.02.182.

[180] M. J. Reddy *et al.*, "Experimental review of the performances of protective coatings for interconnects in solid oxide fuel cells," *J. Power Sources*, vol. 568, p. 232831, Jun. 2023, doi: 10.1016/J.JPOWSOUR.2023.232831.

[181] W. Huang, S. Gopalan, U. B. Pal, and S. Basu, "Evaluation of Electrophoretically Deposited CuMn1.8O4 Spinel Coatings On Metallic Interconnects for SOFC Applications," *ECS Trans.*, vol. 13, no. 26, pp. 405–411, 2008, doi: 10.1149/1.3050411.

[182] Y. Jin *et al.*, "Investigation of CuxMn3-xO4 coatings for solid oxide fuel cell interconnect applications," *Ceram. Int.*, vol. 49, no. 17, pp. 27716–27723, Sep. 2023, doi: 10.1016/J.CERAMINT.2023.04.102.

[183] and S. Y. †Department Yi-Ching Chen,† Masatomo Yashima,*,†,‡ Takashi Ohta,† Kenji Ohoyama, “Crystal Structure, Oxygen Deficiency, and Oxygen Diffusion Path of Perovskite-Type Lanthanum Cobaltites La0.4Ba0.6CoO3−δ and La0.6Sr0.4CoO3−δ,” *journnal Phys. Chem. C*, vol. 116, pp. 5246–5254, 2012.

[184] J. Hayd, H. Yokokawa, and E. Ivers-Tiffée, “Hetero-Interfaces at Nanoscaled (La,Sr)CoO 3-δ Thin-Film Cathodes Enhancing Oxygen Surface-Exchange Properties,” *J. Electrochem. Soc.*, vol. 160, no. 4, pp. F351–F359, Feb. 2013, doi: 10.1149/2.017304jes.

[185] L. Dieterle, P. Bockstaller, D. Gerthsen, J. Hayd, and E. Ivers-tiffée, “Microstructure of Nanoscaled La 0 . 6 Sr 0 . 4 CoO 3 − δ Cathodes for Intermediate-Temperature Solid Oxide Fuel Cells,” pp. 249–258, 2011, doi: 10.1002/aenm.201000036.

[186] M. Søgaard, P. V. Hendriksen, M. Mogensen, F. W. Poulsen, and E. Skou, “Oxygen nonstoichiometry and transport properties of strontium substituted lanthanum cobaltite,” *Solid State Ionics*, vol. 177, no. 37–38, pp. 3285–3296, Dec. 2006, doi: 10.1016/J.SSI.2006.09.005.

[187] Y. T. Kim and N. Shikazono, “Evaluation of electrochemical reaction mechanisms of La0.6Sr0.4CoO3-δ-Gd0.1Ce0.9O2-δ composite cathodes by 3D numerical simulation,” *Solid State Ionics*, vol. 319, pp. 162–169, Jun. 2018, doi: 10.1016/J.SSI.2018.02.014.

[188] A. Samson, M. Søgaard, R. Knibbe, and N. Bonanos, “High Performance Cathodes for Solid Oxide Fuel Cells Prepared by Infiltration of La 0 . 6 Sr 0 . 4 CoO 3 − δ into Gd-Doped Ceria,” *J. Electrochem. Soc.*, vol. 158, no. 6, pp. B650–B659, 2011, doi: 10.1149/1.3571249.

[189] A. Abdul Samat, M. R. Somalu, A. Muchtar, O. H. Hassan, and N. Osman, “LSC cathode prepared by polymeric complexation method for proton-conducting SOFC application,” *J. Sol-Gel Sci. Technol.*, vol. 78, no. 2, pp. 382–393, 2016, doi: 10.1007/s10971-015-3945-4.

[190] J. Hayd, L. Dieterle, U. Guntow, D. Gerthsen, and E. Ivers-Tiffée, “Nanoscaled La0.6Sr0.4CoO3−δ as intermediate temperature solid oxide fuel cell cathode: Microstructure and electrochemical performance,” *J. Power Sources*, vol. 196, no. 17, pp. 7263–7270, Sep. 2011, doi: 10.1016/J.JPOWSOUR.2010.11.147.

[191] D. Sari, F. Piskin, Z. C. Torunoglu, B. Yasar, Y. E. Kalay, and T. Ozturk, “Combinatorial development of nanocrystalline/amorphous (La,Sr)CoO3-(La,Sr)2CoO4 composite cathodes for IT-SOFCs,” *Solid State Ionics*, vol. 326, no. October, pp. 124–130, Nov. 2018, doi: 10.1016/j.ssi.2018.10.003.

[192] J. Januschewsky, M. Ahrens, A. Opitz, F. Kubel, and J. Fleig, “Optimized La 0.6 Sr 0.4 CoO3- δ Thin-Film Electrodes with Extremely Fast Oxygen-Reduction Kinetics,” *Adv. Funct. Mater.*, vol. 19, no. 19, pp. 3151–3156, Oct. 2009, doi: 10.1002/adfm.200900362.

[193] C. Kim *et al.*, “Subcontinuous 2D La0.6Sr0.4CoO3-δ nanosheet as an efficient charge conductor for boosting the cathodic activity of solid oxide fuel cells,” *Electrochim. Acta*, vol. 366, p. 137371, Jan. 2021, doi: 10.1016/J.ELECTACTA.2020.137371.

[194] A. Cavallaro *et al.*, “Amorphous-cathode-route towards low temperature SOFC,” *Sustain. Energy Fuels*, vol. 2, no. 4, pp. 862–875, 2018, doi: 10.1039/C7SE00606C.

[195] A. Evans, J. Martynczuk, D. Stender, C. W. Schneider, T. Lippert, and M. Prestat, “Low-temperature micro-solid oxide fuel cells with partially amorphous la0.6Sr0.4CoO3-δ cathodes,” *Adv. Energy Mater.*, vol. 5, no. 1, pp. 1–9, 2015, doi: 10.1002/aenm.201400747.

[196] M. Sardela, *Practical materials characterization*. 2014.

[197] B. Ravel and M. Newville, “ATHENA, ARTEMIS, HEPHAESTUS: Data analysis for X-ray absorption spectroscopy using IFEFFIT,” *J. Synchrotron Radiat.*, vol. 12, no. 4, pp. 537–541, 2005, doi: 10.1107/S0909049505012719.

[198] H. Funke, A. C. Scheinost, and M. Chukalina, “Wavelet analysis of extended x-ray absorption fine structure data,” *Phys. Rev. B - Condens. Matter Mater. Phys.*, vol. 71, no. 9, pp. 1–7, 2005, doi: 10.1103/PhysRevB.71.094110.

[199] L. J. Bonales, J. M. Elorrieta, Á. Lobato, and J. Cobos, “Raman Spectroscopy, a Useful Tool to Study Nuclear Materials,” *Appl. Mol. Spectrosc. to Curr. Res. Chem. Biol. Sci.*, 2016, doi: 10.5772/64436.

[200] T. Leffler, H. Kassman, R. Norling, and A. Moya Núñez, “Experiences from eight years of firing demolition wood using ammonium sulphate to mitigate superheater corrosion,” no. September, 2022, [Online]. Available: https://www.researchgate.net/publication/383947172.

[201] Z. Yang, K. S. Weil, D. M. Paxton, and J. W. Stevenson, “Selection and Evaluation of Heat-Resistant Alloys for SOFC Interconnect Applications,” *J. Electrochem. Soc.*, vol. 150, no. 9, p. A1188, 2003, doi: 10.1149/1.1595659.

[202] T. H. Wan, M. Saccoccio, C. Chen, and F. Ciucci, “Influence of the Discretization Methods on the Distribution of Relaxation Times Deconvolution: Implementing Radial Basis Functions with DRTtools,” *Electrochim. Acta*, vol. 184, pp. 483–499, Dec. 2015, doi: 10.1016/J.ELECTACTA.2015.09.097.